Development of Fracture Based Geotechnical Design of Clay Barriers

by

Mohammad Zaid

A thesis
presented to the University of Waterloo
in fulfillment of the
thesis requirement for the degree of
Doctor of Philosophy
in
Civil Engineering

Waterloo, Ontario, Canada, 2026

© Mohammad Zaid 2026

Examining Committee Membership

The following served on the Examining Committee for this thesis.

External Examiner:	Dr. J. Carlos Santamarina G. Wayne Clough Chair and Professor, School of Civil and Environmental Engineering, Georgia Institute of Technology
Supervisor(s):	Dr. Dipanjan Basu Professor, Department of Civil and Environmental Engineering, University of Waterloo
	Dr.-Ing. Frank Wuttke Professor and Chair, Geomechanics and Geotechnics, Christian-Albrechts-Universität zu Kiel (Kiel University)
Internal Member:	Dr. Maurice B. Dusseault Professor Emeritus, Department of Earth and Environmental Sciences, University of Waterloo
Internal Member:	Dr. Pejoohan Tavassoti Assistant Professor, Jr. Norman W. McLeod Chair in Sustainable Pavement Engineering, Department of Civil and Environmental Engineering, University of Waterloo
Internal-External Member:	Dr. Hamid Jahed Professor, University Research Chair in Cold Spray Technology, Department of Mechanical and Mechatronics Engineering, University of Waterloo

Author's Declaration

I hereby declare that I am the sole author of this thesis. This is a true copy of the thesis, including any required final revisions, as accepted by my examiners.
I understand that my thesis may be made electronically available to the public.

Abstract

Compacted clay barriers are central components of landfill liners and covers, clay cores in embankment dams and tailings facilities, and other geoenvironmental containment systems. Their design is traditionally governed by classification, plasticity, compaction, hydraulic conductivity, shear strength, compressibility, and construction-quality requirements. These criteria are essential, but they do not directly measure the resistance of a compacted clay barrier to the initiation and extension of open-mode discontinuities and the subsequent formation of connected preferential flow paths. This omission is critical because an intact clay layer may meet the required low hydraulic conductivity, whereas the same layer can lose containment capacity when tensile cracks develop due to desiccation, differential settlement, shrinkage, hydraulic loading, or construction-induced fabric defects. The problem is particularly consequential for persistent contaminants such as per- and polyfluoroalkyl substances (PFAS), where landfill leachate can migrate through a liner with an open discontinuity, creating long-term exposure pathways to groundwater.

The present study develops a fracture based geotechnical design framework for compacted clay barriers by combining laboratory fracture testing, effective single edge notched beam (SENB) calibration, state-dependent geotechnical characterization, numerical comparison of crack-propagation formulations with selected experimental measures, and sequential one-way fracture-to-flow modelling. The work is organized around three connected technical questions. First, can Mode I fracture toughness of compacted clay be measured in a repeatable manner using a specimen geometry and loading system appropriate for weak, moisture-sensitive soils? Second, can the single edge notched beam (SENB) geometry correction function, $f(a/W)$, be derived for compacted soils rather than adopted directly from metallic fracture standards? Third, can the measured fracture parameters be incorporated into numerical crack propagation and hydraulic conductivity models to evaluate clay barrier performance as a sequential one-way mechanical-fracture-to-flow coupling problem rather than as an intact permeability problem alone?

A displacement-controlled SENB testing system is developed for compacted clayey soils. The system includes a low-load resolution load cell, vertical displacement measurement, dual crack mouth opening displacement measurement, roller supports, and machined moulds that produce repeatable notch depths during specimen preparation. The experimental matrix used laboratory-prepared kaolin and sand mixtures, denoted LS_0, LS_{15}, and LS_{25}, together with a field clay barrier soil, denoted FS. The tested SENB geometries were selected to match practical soil-sample dimensions while preserving fracture-mechanics similarity through $S/W = 4$, $L/W = 5$, and notch ratios $a/W = 0.45$, 0.50, and 0.55. A balanced geometry and replication programme showed that the $W = B = 50$ mm SENB specimen provides the most repeatable corrected fracture toughness response for the tested compacted soils, because it provides sufficient ligament size for a representative fracture process zone while remaining practical for soil preparation and handling.

The present study develops and cross-checks an effective SENB load-to-K_I correction within the tested geometry and material-state domain using three complementary routes: three-dimensional Abaqus® contour integral extraction, analytical derivation of the weight function, and experimental compliance validation. The finite element route first reproduced the ASTM metallic benchmark to verify mesh convergence and stress intensity extraction, and then used the measured soil elastic properties to evaluate finite body amplification in compacted soils. The analytical route preserved the LEFM crack-tip singularity and introduced soil-specific finite body scaling using measured the ranges of Poisson's ratio. The experimental route used the measured load-CMOD response as an independent compliance check. The three routes provide a cross-consistency assessment of the adopted load-to-K_I correction within the tested geometry and material-state domain; they do not establish a universal material-dependent geometry function.

The experimental results show that fracture toughness is governed by the coupled effects of water content, dry density, fabric, specimen geometry, and soil composition. Higher dry density was generally associated with higher apparent Mode-I initiation resistance, whereas higher water content was associated with lower resistance within the tested soil series; matric suction and contact-scale resistance were not measured independently. Near the representative design state, corrected Mode I fracture toughness values were approximately 0.86-0.87 kPam$^{0.5}$ for LS_0, 0.99-1.01 kPam$^{0.5}$ for LS_{15}, 0.51-0.62 kPam$^{0.5}$ for LS_{25}, and 1.70-1.83 kPam$^{0.5}$ for FS. These values demonstrate that the selection of clay barrier material cannot be based solely on hydraulic conductivity or fracture toughness. Clay-rich mixtures may provide excellent sealing but only moderate crack resistance, whereas field soils or modified mixtures may exhibit higher fracture resistance but different hydraulic and compressibility behaviour. Nanomaterial improvement is therefore assessed using fracture toughness, hydraulic conductivity, strength, and consolidation metrics together rather than through a single optimized property.

A proposed K_{Ic}-k-a_v interrelationship is developed to connect crack initiation resistance, saturated hydraulic conductivity, and coefficient of compressibility for clay barrier screening. For the investigated materials, a preliminary design screening space defined by $k \leq 1.0 \times 10^{-9}$ m/s and $K_{Ic} \geq 0.8$ kPam$^{0.5}$ identifies LS_0 and FS as the most favourable barrier candidates, classifies LS_{15} as fracture toughness favourable but hydraulically marginal, and identifies LS_{25} as unsuitable under the coupled criterion. This interpretation demonstrates that crack resistance, intact permeability, and compressibility are mutually constrained design variables.

The numerical part of the present study compares four fracture formulations: the extended finite element method, the space-time finite element method, the phase-field fracture method, and the lattice element method. All methods were evaluated using the same SENB cases and selected experimental response measures. For the examined cases, the lattice element method provided the closest combined agreement with the corrected apparent initiation-toughness trends and visible post-test paths and supplied the failed-link graph and displacement jumps required for hydraulic

mapping. The subsequent pore-network calculations predict changes in equivalent hydraulic conductivity from the mapped opening, throat conductance, and connectivity; these predictions were not independently validated against flow measurements on mechanically fractured specimens.

The final outcome is a design methodology in which conventional geotechnical tests remain the first screening level, but fracture toughness, the soil-specific SENB correction function, the K_{Ic}-k-a_{v} relationship, and sequential fracture-to-flow predictions provide the additional checks required for crack sensitive clay barriers. The proposed framework advances clay barrier design from intact-hydraulic conductivity acceptability to sequential one-way mechanical-fracture-to-flow coupling performance.

Acknowledgments

I am truly grateful to everyone who has supported, guided, and encouraged me throughout my PhD journey. Completing this thesis has been one of the most intellectually stimulating and personally rewarding experiences of my life, and I could not have done it without the incredible contributions of so many wonderful individuals. Thank you all!

I sincerely thank my supervisors, Dr. Dipanjan Basu and Dr.-Ing Frank Wuttke, for their invaluable guidance, constant encouragement, insightful feedback, and patience throughout my PhD journey. Their dedication, academic rigour, and pursuit of excellence significantly influenced this work and helped me grow as a researcher. I am especially grateful to Dr. Basu for his extraordinary commitment of time and effort, dedicating marathon sessions, sometimes lasting ten hours, to discussing my research and meticulously reviewing my papers. His ongoing encouragement led me to take on leadership roles, including President of the Civil and Environmental Engineering Graduate Association (CE2GA).

I would also like to thank the members of my supervisory committee, Prof. J. Carlos Santamarina, Prof. Maurice Dusseault, Prof. Pejoohan Tavassoti, and Prof. Hamid Jahed, for their constructive suggestions, critical insights, and thoughtful discussions, which enriched this thesis. Their expertise and encouragement were instrumental in refining my ideas and broadening my perspective. Additionally, I would like to acknowledge Prof. John Montesano for his valuable teachings in Fracture Mechanics and for his suggestions during the development of this work; his input significantly shaped the final outcome of this research.

My sincere thanks go to the faculty members, researchers, and administrative staff of the Department of Civil and Environmental Engineering at the University of Waterloo for providing an intellectually stimulating and supportive academic environment. I especially acknowledge the technical and administrative staff whose assistance made many aspects of my research smoother and more manageable.

I sincerely thank Anne M. Allen, Geotechnical Engineering Laboratory Technologist, for her ongoing support, readiness to assist whenever experimental issues emerged, and her practical guidance. Her patience, technical skills, and dedication were essential throughout my research. I especially appreciate the numerous instances she helped troubleshoot and quickly resolve laboratory and experimental problems. Her strong work ethic and commitment made a deep impression on me and played a crucial role in successfully completing my experimental research.

I sincerely thank all the friends I met at Waterloo for their companionship, encouragement, and the many meaningful conversations we have had over the years. The spirit of collaboration, idea sharing, and laughter with them made this journey both enriching and memorable. I am

particularly grateful to Dr. Zarghaam H. Rizvi for their support during difficult phases of my research.

My family is my greatest blessing, and I cannot fully express my thanks to them. To my parents, Abba and Amma, I thank you for your boundless love, sacrifices, and unwavering faith in my potential. I am truly thankful for the freedom you provided to explore my limits and for your consistent backing of every decision I have made. Your ongoing encouragement has been the backbone of my success. To my siblings and grandfather, Dr. Saud Parvez, I appreciate your patience, motivation, and emotional support.

Finally, I wish to thank everyone who contributed to this work and my journey in various ways, even if their names are not explicitly mentioned. Your kindness and support have left a lasting impact on my life and academic path.

I dedicate this thesis to all who believed in me and inspired me to persevere in the pursuit of knowledge and excellence. I also dedicate this work to everyone who finds strength in hard work and persistence, and who demonstrates that dedication is the ultimate path to discovery.

Dedicated to my love

Table of Contents

Examining Committee Membership ii

Author's Declaration iii

Abstract iv

Acknowledgments vii

Dedication ix

List of Figures xvi

List of Tables xx

List of Abbreviations xxiv

List of Symbols xxvi

1 Motivation and Background 1
- 1.1 PFAS: A containment problem . . . 1
- 1.2 Clay barriers as a geostructure . . . 2
- 1.3 Conventional clay barrier design checks . . . 3
- 1.4 Motivation for fracture based geotechnical design . . . 3
- 1.5 Research hypotheses, objectives and associated tasks . . . 5

2 Literature Review 9
- 2.1 Scope, review strategy, and synthesis logic . . . 9
- 2.2 Fracture mechanics as the missing design layer . . . 10
- 2.3 Evidence from crack-controlled geotechnical systems . . . 13
- 2.4 Fracture mechanics basis for crack controlled clay systems . . . 17

2.4.1 Crack modes and the priority of Mode I . . . 17
2.5 Classical soil models and the fracture limitation . . . 20
2.6 Experimental characterization of Mode-I fracture in clayey soils . . . 23
2.6.1 SENB/SECB as the historical reference geometry . . . 23
2.6.2 Alternative geometries and specimen preparation . . . 24
2.7 Hydromechanical coupling, hydraulic conductivity change, and hydraulic fracture 29
2.8 Material modification for fracture resistant clay barriers . . . 36
2.9 Fracture capable constitutive models and numerical methods . . . 37
2.9.1 Classical yield models and why crack capable extensions are required . . 39
2.9.2 Hydro-mechanical field equations required by any predictive crack model 40
2.9.3 Extended finite element method (XFEM) . . . 41
2.9.4 Space-time finite element method (STFEM) . . . 42
2.9.5 Phase-field modelling . . . 42
2.9.6 Lattice element method (LEM) . . . 43
2.9.7 Method comparison before coupled modelling . . . 45
2.10 Hydraulic conductivity, fracture toughness, and compressibility as coupled metrics 48
2.11 Research gaps . . . 49
2.12 Summary of literature review . . . 51

3 Experimental Investigation 53
3.1 Experimental programme . . . 54
3.2 Soil selection and conventional clay barrier properties . . . 56
3.3 Elastic characterization for fracture calculations . . . 60
3.4 Development of the SENB laboratory test setup . . . 63
3.4.1 Design of experiments for SENB . . . 66
3.5 Baseline load-CMOD response and crack morphology . . . 71
3.6 Development of the SENB geometry correction function $f(a/W)$ . . . 75
3.6.1 Governing LEFM form . . . 75
3.6.2 Numerical development using Abaqus® contour integrals . . . 75
3.6.3 Analytical weight function derivation . . . 79
3.6.4 Experimental compliance . . . 81
3.7 Mode I Fracture Toughness Results . . . 83
3.7.1 Maximum load as a geometry-dependent response . . . 83
3.7.2 Corrected Mode I fracture toughness and geometry robustness . . . 88
3.7.3 Water content, dry density, and soil fabric . . . 95
3.8 Compressibility and nanomaterial improvement metrics . . . 102
3.9 Proposed K_{Ic}-k-a_v interrelationship for clay barrier design . . . 108
3.10 Chapter summary . . . 113

4 Advanced Numerical and sequential mechanical-fracture and pore-network flow model **115**
4.1 Technical logic of the chapter . . . 115
4.2 SENB formulation common to all four fracture solvers . . . 117
4.2.1 Geometry, boundary conditions, and recorded quantities . . . 117
4.2.2 Constitutive and fracture models used . . . 119
4.2.3 Validation criteria . . . 121
4.3 Extended finite element method (XFEM) . . . 123
4.3.1 Historical background and mathematical formulation . . . 123
4.3.2 XFEM SENB model and interpretation . . . 124
4.3.3 XFEM crack propagation result . . . 124
4.4 Space-time finite element method (STFEM) . . . 127
4.4.1 Historical background and mathematical formulation . . . 127
4.4.2 STFEM SENB model . . . 128
4.4.3 STFEM crack propagation result . . . 128
4.5 Phase-field method . . . 130
4.5.1 Historical background and mathematical formulation . . . 130
4.5.2 Phase-field SENB model . . . 131
4.5.3 Phase-field crack propagation result . . . 131
4.6 Lattice element method (LEM) . . . 134
4.6.1 Historical background and relevance to the SENB problem . . . 134
4.6.2 LEM SENB model . . . 137
4.6.3 LEM crack propagation result for the reference SENB case . . . 137
4.6.4 LEM response over geometry variation . . . 140
4.6.5 LEM response over soil-state variation . . . 140
4.6.6 Experimental crack propagation evidence . . . 140
4.7 Comparative validation of the four fracture methods . . . 143
4.7.1 Validation for LS_0 . . . 143
4.7.2 Validation for LS_{15} . . . 144
4.7.3 Validation for LS_{25} . . . 146
4.7.4 Why LEM is selected? . . . 147
4.8 Transition from validated LEM fracture to LEM-based pore-network modelling . . . 148
4.9 LEM-based sequential one-way mechanical-fracture-to-flow coupling model . . . 148
4.9.1 Material parameters . . . 148
4.9.2 Three-dimensional LEM-PNM cylinder construction . . . 149
4.9.3 Hydraulic network equations . . . 150
4.9.4 Connectivity criterion . . . 151
4.10 Triaxial LEM-PNM results . . . 156

4.10.1 Reference LS_0 triaxial crack and aperture evolution . . . 156
4.10.2 Triaxial response of LS_0, LS_{15}, and LS_{25} . . . 157
4.11 UCS LEM-PNM results . . . 163
4.11.1 UCS response of LS_0, LS_{15}, and LS_{25} . . . 163
4.11.2 UCS crack propagation, aperture, and seepage patterns . . . 165
4.12 Comparison of triaxial and UCS hydraulic behaviour . . . 170
4.13 Technical implications . . . 170
4.14 Chapter summary . . . 171

5 Conclusions **173**
5.1 Thesis synthesis . . . 173
5.2 Experimental conclusions . . . 174
5.3 Numerical and coupled modelling conclusions . . . 176
5.4 Fracture based clay barrier design methodology . . . 177
5.5 Original contributions . . . 178
5.6 Limitations . . . 179

Future research scope **181**

References **182**

APPENDICES **201**

Appendix A Experimental Procedures, State Control, Data Reduction, and Quality Assurance **202**
A.1 Purpose and interpretation of the measured quantity . . . 202
A.2 Materials, mixture definitions, and storage . . . 204
A.2.1 Soil families . . . 204
A.2.2 Particle-size distribution and consistency-limit fraction . . . 205
A.2.3 First-order sand-volume and spacing estimate . . . 205
A.3 Conventional characterization and bulk-state calculations . . . 205
A.4 Dry preparation, batching, mixing, and moisture conditioning . . . 206
A.5 Compaction, orientation, and state verification . . . 208
A.6 SENB moulds, geometry, and notch formation . . . 209
A.6.1 Geometry matrix . . . 209
A.6.2 Fabrication drawings organized by SENB geometry . . . 209
A.6.3 Rationale for three-point loading and notch range . . . 216
A.6.4 Notch insert and dimensional control . . . 216

A.7 SENB apparatus, loading frame, and instrumentation . . . 216
A.7.1 Two-sided crack mouth opening displacement (CMOD) measurement and symmetry check . . . 218
A.8 SENB mounting and complete test sequence . . . 218
A.9 Validity and rejection criteria . . . 220
A.10 SENB data reduction and uncertainty . . . 220
A.11 Factorial design and statistical analysis . . . 221
A.12 Unconfined compression tests and elastic inputs . . . 221
A.13 Hydraulic-conductivity procedure . . . 224
A.14 One-dimensional consolidation tests . . . 225
A.15 Experimental limitations and transferability . . . 227

Appendix B Constitutive Assumptions, Numerical Implementation, and Reproducibility 228
B.1 Numerical scope and coupling classification . . . 228
B.2 Common code settings and values used in the analyses . . . 229
B.3 Stress measures and fields actually solved . . . 230
B.4 Model inventory . . . 231
B.5 Chapter 3 Abaqus® SENB contour-integral model . . . 233
B.5.1 Geometry, material idealization, and boundaries . . . 233
B.5.2 Elements, mesh, and contour paths . . . 234
B.5.3 Analysis sequence . . . 235
B.5.4 Benchmark and convergence . . . 235
B.6 Geometric function and effective calibration . . . 236
B.7 Analytical weight function and compliance route . . . 236
B.8 Common two-dimensional SENB comparison . . . 237
B.9 Extended finite element method: implemented analysis steps . . . 238
B.9.1 Driving force and path rule . . . 239
B.9.2 XFEM solution sequence . . . 239
B.10 Space-time finite element method: implemented analysis steps . . . 240
B.10.1 STFEM solution sequence . . . 241
B.11 Phase-field method: implemented analysis steps . . . 243
B.11.1 Phase-field solution sequence . . . 243
B.12 Two-dimensional lattice element method: mesh, failure rule, and analysis steps . . . 245
B.12.1 Voronoi-Delaunay network . . . 245
B.12.2 Two-dimensional LEM solution sequence . . . 245
B.13 Generation of numerical LS_0, LS_{15}, and LS_{25} cases . . . 246
B.14 Three-dimensional lattice-pore-network cylinder and material parameters . . . 247

B.14.1 Three-dimensional bond law 248
B.14.2 Principal phase-level defaults 249
B.15 Three-dimensional mechanical and hydraulic boundary conditions 249
B.16 Pore-network equations, porosity update, and aperture mapping 250
B.17 Connectivity criterion 252
B.18 Complete sequential three-dimensional lattice-PNM analysis 253
B.19 Parameter provenance and calibration 254
B.20 Mesh, lattice, regularization, and random-seed sensitivity 256
B.21 Validation metrics and method selection 257
B.22 Solver controls and output reproducibility 257
B.23 Reproducibility archive 259
B.24 Numerical limitations 259

List of Figures

2.1 Fracture modes . . . 17
2.2 Mode-I specimen configurations . . . 25
2.3 Mode-I and mixed-mode geometries . . . 30

3.1 Specific gravity of the tested soils . . . 57
3.2 Particle-size distributions of the tested soils . . . 58
3.3 Standard Proctor compaction curves . . . 59
3.4 Unconfined compression responses used to obtain elastic inputs . . . 62
3.5 Developed SENB loading system and mould family . . . 65
3.6 Effect of SENB geometry on apparent Mode-I initiation toughness . . . 70
3.7 Normalized notch-ratio response of the SENB experimental design . . . 71
3.8 Representative load and CMOD responses of the four soils . . . 73
3.9 Post-test crack paths for all soils showing notch-controlled Mode I crack propagation and absence of visible diffuse fracture-process-zone growth. . . . 74
3.10 Three-dimensional Abaqus® SENB model used to extract K_I from contour integrals using the laboratory geometry matrix. . . . 76
3.11 Abaqus® verification of the SENB model through (a) mesh convergence against ASTM E399 and (b) geometry-independence checks for compacted-soil specimens. 78
3.12 Numerical, analytical, and compliance-derived $f(a/W)$ functions for individual soils. . . . 82
3.13 Peak load as a function of absolute notch length . . . 85
3.14 Peak load as a function of a/W . . . 86
3.15 Peak load as a function of a/B . . . 87
3.16 Corrected Mode-I initiation toughness as a function of notch length . . . 89
3.17 Corrected Mode-I initiation toughness as a function of a/W . . . 90
3.18 Corrected Mode-I initiation toughness as a function of a/B . . . 91
3.20 Peak load and apparent initiation toughness versus water content and dry density . 96
3.21 Mode-I initiation toughness versus water content . . . 99
3.22 Combined fracture resistance and intact hydraulic conductivity . . . 101

3.23 One-dimensional consolidation responses of the laboratory soils 103
3.24 Additive dosage effects on fracture and compressibility 105
3.25 Empirical K_{Ic}, k, and a_v relationship 109
3.26 Goodness of fit of the empirical K_{Ic}, k, and a_v equation 111
3.27 Preliminary fracture and hydraulic screening chart for clay barriers 112

4.1 SENB modelled using XFEM: (a) triangular mesh and (b) displacement loading and boundary conditions. 125
4.2 Crack propagation using the XFEM framework for the $B = W = 35$ mm, $a/W = 0.45$, LS_0 SENB specimen: (a) one-fourth, (b) two-fourths, (c) three-fourths, and (d) complete crack propagation. 126
4.3 SENB modelled using the space-time finite element framework. 128
4.4 Crack propagation using the space-time finite-element framework for the $B = W = 35$ mm, $a/W = 0.45$, LS_0 SENB specimen: (a) one-fourth, (b) two-fourths, (c) three-fourths, and (d) complete crack propagation. 129
4.5 SENB modelled using the phase-field framework: (a) triangular mesh and (b) displacement loading and boundary conditions. 132
4.6 Crack propagation using the phase-field framework for the $B = W = 35$ mm, $a/W = 0.45$, LS_0 SENB specimen: (a) one-fourth, (b) two-fourths, (c) three-fourths, and (d) complete crack propagation. 133
4.7 SENB modelled using the lattice element method: (a) Voronoi tessellation, (b) Voronoi cells with Delaunay triangulation, and (c) loading and boundary conditions. 136
4.8 Crack propagation using the lattice element method for the $B = W = 35$ mm, $a/W = 0.45$, LS_0 SENB specimen: (a) one-fourth, (b) two-fourths, (c) three-fourths, and (d) complete crack propagation. 138
4.9 Completed LEM crack propagation for $a/W = 0.50$ in LS_0 specimens: (a) $W = 35$ mm, $B = 35$ mm; (b) $W = 35$ mm, $B = 70$ mm; (c) $W = 50$ mm, $B = 50$ mm; (d) $W = 50$ mm, $B = 100$ mm; and (e) $W = 65$ mm, $B = 65$ mm. . . 139
4.10 Completed LEM crack propagation for $a/W = 0.50$, $W = 50$ mm, $B = 50$ mm specimens made of (a) LS_0, (b) LS_{15}, and (c) LS_{25}. 141
4.11 Experimental crack propagation in SENB specimens, used as the physical reference for evaluating the numerical crack paths. 142
4.12 Validation of different numerical methods for crack initiation and propagation in LS_0. 143
4.13 Validation of different numerical methods for crack initiation and propagation in LS_{15}. 145
4.14 Validation of different numerical methods for crack initiation and propagation in LS_{25}. 146

4.15 Generated three-dimensional cylindrical particle/node representation used for the coupled LEM-PNM simulations. 154
4.16 sequential one-way mechanical-fracture-to-flow coupling lattice element construction: (a) nodes representing different soil particles, (b) meshed three-dimensional cylinder, (c) pore network, and (d) pores filled with fluid. 155
4.17 Representative aperture opening for LS_0 under triaxial loading at (a) no loading, (b) crack initiation, (c) crack propagation, and (d) complete failure. [Units = mm] 156
4.18 Representative crack propagation for LS_0 under triaxial loading at (a) no loading, (b) crack initiation, (c) crack propagation, and (d) complete failure. 157
4.19 Representative crack propagation and fluid seepage for LS_0 under triaxial loading at (a) no loading, (b) crack initiation, (c) crack propagation, and (d) complete failure. 158
4.20 Behaviour of the sequential one-way mechanical-fracture-to-flow coupling cylinder under triaxial loading for LS_0, LS_{15}, and LS_{25}: (a) deviatoric stress-axial strain, (b) total porosity-axial strain, (c) hydraulic conductivity and mean crack width, and (d) hydraulic conductivity-axial strain. 159
4.21 Triaxial crack propagation and seepage response for (a) LS_0, (b) LS_{15}, and (c) LS_{25}. 160
4.22 Additional triaxial crack propagation and seepage response for (a) LS_0, (b) LS_{15}, and (c) LS_{25}. 161
4.23 Triaxial aperture opening for (a) LS_0, (b) LS_{15}, and (c) LS_{25}. 162
4.24 Triaxial crack formation and fluid flow for (a) LS_0, (b) LS_{15}, and (c) LS_{25}. 163
4.25 Behaviour of the sequential one-way mechanical-fracture-to-flow coupling cylinder under UCS loading for LS_0, LS_{15}, and LS_{25}: (a) axial stress-axial strain, (b) total porosity-axial strain, (c) hydraulic conductivity-mean crack width, and (d) hydraulic conductivity-axial strain. 164
4.26 UCS crack propagation and seepage response for (a) LS_0, (b) LS_{15}, and (c) LS_{25}. 166
4.27 Additional UCS crack propagation and seepage response for (a) LS_0, (b) LS_{15}, and (c) LS_{25}. 167
4.28 UCS aperture opening for (a) LS_0, (b) LS_{15}, and (c) LS_{25}. 168
4.29 UCS crack formation and fluid flow for (a) LS_0, (b) LS_{15}, and (c) LS_{25}. 169

A.1 Fabrication drawings for SENB Geometry A: W = 35 mm, B = 35 mm, L = 175 mm, and S = 140 mm. 210
A.2 Fabrication drawings for SENB Geometry B: W = 35 mm, B = 70 mm, L = 175 mm, and S = 140 mm. 211
A.3 Fabrication drawings for SENB Geometry C: W = 50 mm, B = 50 mm, L = 250 mm, and S = 200 mm. 212
A.4 Fabrication drawings for SENB Geometry D: W = 50 mm, B = 100 mm, L = 250 mm, and S = 200 mm. 213

A.5 Fabrication drawings for SENB Geometry E: W = 65 mm, B = 65 mm, L = 325 mm, and S = 260 mm. 214
A.6 Fabrication drawings for the attempted Geometry F: W = 65 mm, B = 130 mm, L = 325 mm, and S = 260 mm. This geometry was excluded from the factorial test matrix. 215
A.7 SENB apparatus and mould used for the compacted-soil tests. 217
A.8 Functional arrangement of the SENB loading system. 217
A.9 Functional arrangement of the UCS test used to obtain compressive stress–strain response and the operational elastic inputs. 222
A.10 Functional arrangement of the one-dimensional consolidation test. 225

List of Tables

1.1 Conventional ASTM checks used in clay barrier design. 4

2.1 Literature review logic used to organize Chapter 2. 11
2.2 Literature review questions used to structure the fracture based design synthesis. . 13
2.3 Why strength-based design alone is insufficient for discontinuity-sensitive clay barriers? 14
2.4 Crack controlled mechanisms relevant to clay barriers. 15
2.5 Documented crack controlled consequences requiring a fracture based design layer. 16
2.6 Equation to design meaning for the fracture framework used in this study. 21
2.7 Classical geotechnical models and their limitations for fracture controlled clay systems. 23
2.8 Representative direct Mode-I studies on clayey soils and clay dominant materials. 25
2.9 Experimental Mode-I and mixed-mode fracture studies relevant to clayey soils. . 27
2.10 Strengths and limitations of common soil fracture-test geometries. 31
2.11 Geometry correction frameworks reported for fracture toughness calculation in soil and clay studies. 32
2.12 Minimum reporting checklist for Mode-I fracture testing of clayey soils. 33
2.13 Equation to design meaning for the hydromechanical fracture framework. 36
2.14 Additive families in clay fracture studies and the current state of evidence. 38
2.15 Historical development and role of the numerical fracture methods used in this study. 44
2.16 Comparison of candidate crack propagation methods for clay barrier modelling. . 45
2.17 Numerical studies and modelling approaches relevant to crack initiation and propagation in clayey soils. 46
2.18 Validation pathway from numerical crack comparison to coupled fracture-hydro-mechanical modelling. 48
2.19 Proposed staged fracture-based design workflow for discontinuity-sensitive clay barrier system. 49
2.20 Standardization roadmap for Mode-I fracture characterization of clayey soils. . . 50
2.21 Research gaps in fracture based design of clay barriers. 50

3.1 Experimental design matrix linking soil selection, geometry calibration, SENB testing, and coupled hydraulic compressibility interpretation used to establish a reproducible fracture testing sequence. 55
3.2 Index, compaction, and hydraulic properties of the four soils. 60
3.3 Elastic input properties from UCS testing, used consistently in finite element modelling, analytical derivation, and experimental compliance interpretation of $f(a/W)$. 61
3.4 Instrumentation and control components of the developed SENB apparatus for low load, displacement controlled Mode I testing of compacted clay barrier beams. 64
3.5 SENB geometry matrix used for specimen preparation, Abaqus® contour integral extraction, analytical weight function calculation, and experimental compliance validation. 64
3.6 Blocked factorial DOE results for apparent fracture toughness and peak load, showing geometry significance and crack-ratio sensitivity. 68
3.7 Geometry ranking for K_I^{app} using mean fracture toughness, Tukey grouping, and coefficient of variation (COV) from replicated SENB tests. 69
3.8 Numerical and analytical scaling factors used to calibrate the generalized soil-specific SENB geometry correction function for subsequent K_{Ic} calculations. . . . 77
3.9 weight function coefficients associated with measured Poisson ratios and used to construct the analytical finite-body correction for compacted soil SENB specimens. 80
3.10 Exact integral terms from the non-dimensional bending-stress distribution and five-term edge-crack weight function used in analytical $f(a/W)$ derivation. . . . 80
3.11 Polynomial coefficients defining the analytical soil-specific $f(a/W)$ expression for the investigated crack-ratio range and measured elastic-property domain. . . . 81
3.12 Mean corrected Mode I fracture toughness values for each SENB geometry and crack ratio, calculated using the soil-specific correction function. 95
3.13 Coefficient of variation of corrected K_{Ic} for each geometry, crack ratio, and laboratory soil, identifying specimen C as the most repeatable SENB geometry. . 97
3.14 Hydraulic conductivity values of intact compacted specimens. 100
3.15 Optimum additive dosages and approximate responses read from Figure 3.24, summarizing load, fracture toughness, compressibility, hydraulic response, and barrier suitability. 107

4.1 Summary of the intact constitutive response, fracture initiation or damage criterion, and discontinuity representation adopted in each numerical approach used for the SENB simulations and sequential fracture-to-flow analysis. 122
4.2 Input parameters for sequential one-way mechanical-fracture-to-flow coupling lattice element analysis. 153

A.1 Evidence classification for the experimental programme. 203
A.2 Material identification and records required for reproduction. 204
A.3 Reported conventional properties used to define the experimental states. 206
A.4 SENB geometry matrix. All dimensions are in millimetres. 209
A.5 SENB instrumentation and required calibration information. 217
A.6 State-dependent operational elastic inputs reported in the thesis. 223
A.7 Reported intact saturated hydraulic conductivities. 224
A.8 One-dimensional consolidation test matrix to be confirmed from the original test sheets. 226

B.1 Numerical models and their principal roles. 232
B.2 Boundary conditions used in the Abaqus® 2023 SENB model. 234
B.3 Reported effective calibration multipliers. 236
B.4 Experimental macroscopic inputs available to the two-dimensional SENB models. 238
B.5 Main XFEM settings developed in the code. 241
B.6 Main STFEM settings used in the code. 242
B.7 Main phase-field settings implemented in the code. 244
B.8 Main settings of the two-dimensional LEM code. 247
B.9 Principal default phase and interface values used by the three-dimensional code. . 249
B.10 Mechanical and hydraulic boundary conditions for the three-dimensional analyses. 250
B.11 Source and role of the main numerical inputs. 255
B.12 Principal solver controls defined in the codes. 258

List of Abbreviations

Al_2O_3 Aluminium Oxide

ANOVA Analysis of Variance

ASTM ASTM International

CMOD Crack Mouth Opening Displacement

COV Coefficient of Variation

EPK Edgar Plastic Kaolin

FS Field Soil

LEFM Linear Elastic Fracture Mechanics

LEM Lattice Element Method

MDD Maximum Dry Density

OMC Optimum Moisture Content

PFAS per-and polyfluoroalkyl substances

PNM Pore-Network Model

SCB Semi-Circular Bend

SECB Single Edge Cracked Beam

SENB Single Edge Notched Beam

SiO_2 Silicon dioxide

ZnO-T Zinc Oxide (Tetrapod)

List of Symbols

A Cross-sectional area or system matrix, depending on context

a Notch length or initial crack length

a/B Crack-length-to-thickness ratio

α Non-dimensional crack ratio, commonly a/W

A_n Weight function coefficient

a_v Coefficient of compressibility

a/W Crack-length-to-width ratio

B SENB specimen thickness

b Crack or hydraulic aperture

β Finite-body scaling factor or non-dimensional geometry parameter

b_{ij} Aperture of hydraulic throat connecting pores i and j

b_r Residual aperture

c Cohesion or polynomial coefficient, depending on context

c_0–c_5 Polynomial coefficients for the analytical soil-specific SENB geometry function

χ Hydraulic activation indicator for a cracked throat

C_r Recompression index

d Phase-field damage variable

d_{crit} Critical damage threshold for hydraulic activation

Δp Imposed pressure difference

$\Delta \bar{u}_y$ Imposed vertical displacement increment

E Young's modulus

e Void ratio

ℓ Phase-field regularization length

$\boldsymbol{\varepsilon}$ Strain tensor

E^* Effective elastic modulus used in fracture-energy conversion

η_{b} Aperture transfer coefficient

$f(a/W)$ SENB geometry correction function

FS Field clay-barrier soil

f_{t} Tensile strength

G Energy release rate or specimen-geometry factor, depending on context

Γ_{c} Propagated crack surface

$\gamma_{\mathrm{d,max}}$ Maximum dry unit weight

Γ_{f} Total fracture set

G_{c} Critical fracture energy

G_{f} Fracture energy

g_{ij} Hydraulic conductance of throat connecting pores i and j

G_{s} Specific gravity of soil solids

H History field or Heaviside function, depending on context

I_n Dimensionless bending-stress integral in the weight-function derivation

J J-integral

J_n Dimensionless complementary integral in the weight-function derivation

K Stress intensity factor

k Hydraulic conductivity

κ Intrinsic permeability or curvature depending on context

K_{c} Critical stress intensity factor

k_{eff} Effective hydraulic conductivity

K_{I} Mode-I stress intensity factor

$K_{\mathrm{I}}^{\mathrm{app}}$ Apparent Mode-I stress intensity factor

K_{Ic} Mode-I fracture toughness

K_{II} Mode-II stress intensity factor

K_{IIc} Mode-II fracture toughness

K_{III} Mode-III stress intensity factor

K_{IIIc} Mode-III fracture toughness

k_{r} Residual stiffness factor

L SENB specimen length or hydraulic flow length

L_{ij} Hydraulic throat length between pores i and j

LS_0 Laboratory soil with 100% EPK kaolin clay

LS_{15} Laboratory soil with 85% EPK kaolin clay and 15% Ottawa sand

LS_{25} Laboratory soil with 75% EPK kaolin clay and 25% Ottawa sand

M Bending moment or number of weight-function terms

μ Dynamic viscosity

m_{v} Coefficient of volume compressibility

n Boundary normal, crack normal, or summation index

ν Poisson's ratio

Ω Analysis domain

P Applied load

p Fluid pressure

P_{c} Critical load at fracture initiation

ϕ Friction angle or level-set function depending on context

$P_{\max}$ Maximum load measured during SENB testing

ψ Dilation angle, level-set function, or strain-energy density depending on context

p_{w} Pore water pressure

Q Flow rate

q Flux or softening variable, depending on context

R Residual vector or specimen radius, depending on context

ρ Density

ρ_{d} Dry density

ρ_{w} Density of water

R_{ij} Hydraulic throat radius between pores i and j

S Support span or degree of saturation, depending on context

$\boldsymbol{\sigma}$ Cauchy stress tensor

σ_3 Triaxial confining stress

S_{r} Degree of saturation

S/W Span-to-width ratio

t Time, pseudo-time, or traction depending on context

τ Shear stress

$\mathbf{u}$ Displacement vector

W SENB specimen depth or width used in normalized notation

w Water content

Chapter 1

Motivation and Background

1.1 PFAS: A containment problem

Per- and polyfluoroalkyl substances (PFAS) are man-made fluorinated chemicals employed in various industrial and consumer products due to their resistance to water, oil, heat, stains, and chemical degradation (Buck et al., 2011; Glüge et al., 2020; National Institute of Environmental Health Sciences, 2026; United States Environmental Protection Agency, 2025b). Their persistence renders them valuable in various products, yet it also leads to long-term environmental issues. PFAS can be released during manufacturing, from firefighting foams, coated textiles, food packaging, cookware, personal care items, biosolids, wastewater residuals, and landfill waste. Exposure occurs directly through contact with products containing PFAS, indoor dust, food, and drinking water, or indirectly via environmental transport from contaminated soil, surface water, groundwater, and landfill leachate (Fenton et al., 2021; Health Canada, 2024; Sunderland et al., 2019; United States Environmental Protection Agency, 2025a).

Most commonly investigated PFAS compounds contain an anionic sulfonate or carboxylate head group, while clay-mineral surfaces are generally negatively charged under common environmental conditions. Direct electrostatic adsorption can therefore be limited. Retention may increase through multivalent-cation bridging (Du et al., 2014), hydrophobic interaction of the fluorinated carbon chain with organic matter or surface coatings (Higgins and Luthy, 2006), and association with natural organic matter (Guelfo and Higgins, 2013). Consequently, adsorption-based retardation cannot be assumed solely from clay content, and the physical continuity of the barrier remains important because an open-mode discontinuity can bypass much of the intact clay matrix and reduce the effective contact time available for attenuation.

The geotechnical pathway is indirect but essential. PFAS containing products are disposed of in landfills, where residues enter waste streams (leachate) and interact with infiltrating water. Proper functioning of the leachate collection and barrier system breaks the chain from source to receptor. However, if a crack or fracture develops in the liner, the barrier might lose its low-permeability property. This creates a coupled fracture and transport issue: leachate can travel through the network of connected discontinuities, reach the subgrade or groundwater, and potentially contaminate drinking water sources.

Landfill containment is part of the larger PFAS exposure system. Geotechnical engineering cannot break down PFAS chemicals; that is a treatment issue. Its function is to limit contaminant movement by ensuring barrier integrity. In this role, a clay liner is not just a low-permeability material; it is a discontinuity-sensitive clay barrier whose effectiveness depends on maintaining continuous, intact coverage despite environmental, mechanical, hydraulic, or construction-related stresses.

1.2 Clay barriers as a geostructure

A landfill barrier is a multilayered engineered system that generally consists of a final cover, drainage layer, filtration or separation layer, compacted clay liner, leachate collection layer, compacted foundation, and a natural subgrade. Drainage components are designed to limit hydraulic head, while filters prevent the migration of fines and clogging. Compacted clay liners offer low hydraulic conductivity and act as a mineral barrier when intact, helping to attenuate flow and aligning with geotechnical construction practices. The foundation and subgrade layers provide mechanical support for the system. While the clay liner is part of this system, it remains a vital layer due to its low hydraulic conductivity and need for continuity (Albrecht and Benson, 2001; Daniel and Y.-K. Wu, 1993; Hewitt and Philip, 1999; Julina and Thyagaraj, 2020; J. H. Li et al., 2016; Omidi, Thomas, and Brown, 1996; Rayhani, Yanful, and Fakher, 2007; Tian et al., 2023; Y. Zhou and Rowe, 2005).

Clay barrier performance depends on its microstructure and measured index properties. Factors such as plasticity, clay mineralogy, pore size distribution, fabric, water content, dry density, suction, swelling potential, and fluid compatibility affect hydraulic conductivity and mechanical behaviour. Interactions between clay, water, and contaminants can change particle arrangement, interfacial area, viscosity, and pore connectivity. Adding sand can enhance workability and alter density and stiffness, but might decrease plasticity and affect cracking resistance. Nanomaterials or other modifiers may strengthen bonds or reduce crack growth, but their effects on hydraulic conductivity and consolidation must be assessed, not just fracture toughness

1.3 Conventional clay barrier design checks

The traditional clay barrier design involves a systematic approach: site investigation, material selection, compaction monitoring, hydraulic testing, compatibility evaluation, strength and deformation assessments, and quality assurance during construction. These steps are crucial for identifying the type of barrier material, its placement quality, hydraulic conductivity, strength profile, compressibility, and field compaction. Furthermore, they help detect potential fracture initiation points. Standard tests assess whether the soil behaves as a continuous, intact medium, but a barrier that contains an open-mode discontinuity also requires examining the clay barrier's resistance to crack initiation and subsequent propagation.

The design process shown in Table 1.1 is thorough but does not cover barriers whose functions rely on continuity to ensure hydraulic conductivity. It considers soil type, the placement method via compaction, and measures hydraulic flow, strength, and consolidation response. However, it does not assess fracture toughness (K_{Ic}) or crack propagation resistance. For clay barriers subjected to shrinkage, wetting and drying, leachate chemistry, differential settlement, or hydraulic gradients, a fracture criterion should be incorporated into the standard verification process (Albrecht and Benson, 2001; Daniel and Y.-K. Wu, 1993; Hewitt and Philip, 1999; Julina and Thyagaraj, 2020; J. H. Li et al., 2016; Omidi, Thomas, and Brown, 1996; Rayhani, Yanful, and Fakher, 2007; Rowe, 1998; Tian et al., 2023).

Hydraulic conductivity is the key performance parameter in clay liner design, yet it is highly influenced by cracking. An open-mode discontinuity may occupy a small fraction of the barrier volume yet still dominate the effective hydraulic conductivity by bypassing the intact low-permeability matrix. This underpins the design of clay barriers using fracture mechanics, complementing traditional hydraulic, strength, and compressibility assessments.

1.4 Motivation for fracture based geotechnical design

Clay barriers may remain structurally stable; however, their ability to prevent leachate migration decreases as cracks initiate and propagate. Even if a barrier fulfills soil index, compaction, strength, consolidation, and hydraulic conductivity standards, it can still develop cracks. This is particularly important for PFAS and other persistent contaminants, as their chemical stability requires reliable long-term hydraulic containment.

Fracture based geotechnical design complements traditional methods rather than replaces them, especially when continuity affects performance. Important parameters include Mode-I fracture toughness, crack shape, specimen size effects, hydraulic conductivity, compressibility,

Table 1.1: Conventional ASTM checks used in clay barrier design.

Application	Design stage	ASTM standard	Design information obtained
Landfill clay liner and cover	Site investigation and sampling	ASTM D1586, ASTM D1587, ASTM D5434	Penetration resistance, sampling quality, and field shear strength
	Material selection and classification	ASTM D4318, ASTM D2487, ASTM D854, ASTM D6913/ASTM D7928	Plasticity, classification, specific gravity, and particle-size distribution
	Compaction specification	ASTM D698/ASTM D1557; ASTM D6938, ASTM D5080	OMC, maximum dry unit weight, field density, and percent compaction
	Hydraulic acceptance	ASTM D5084, ASTM D6766, ASTM D6527	Saturated and unsaturated hydraulic conductivity
	Chemical compatibility and swelling	ASTM D5890, ASTM D4972, ASTM D4546	Swell index, pore fluid pH, swell, and collapse tendency
	Interface and stability	ASTM D6243, ASTM D3080, ASTM D4767, ASTM D2850, ASTM D2166	Interface shear, drained shear, CU/UU triaxial strength, and UCS
Dam clay core	Site and foundation investigation	ASTM D1586, ASTM D1587, ASTM D5777, ASTM D2113, ASTM D4719	Subsurface profile, sampling, rock core, and in situ stiffness
	Foundation studies	ASTM D2113, ASTM D4015, ASTM D3080	Foundation material quality, stiffness, damping, and shear strength
	Core material evaluation	ASTM D4318, ASTM D2487, ASTM D698/ASTM D1557, ASTM D5084	Plasticity, classification, compaction state, and hydraulic conductivity
	Compressibility and volume change	ASTM D2435, ASTM D4546	One-dimensional consolidation, swell, and collapse
	Shear strength	ASTM D3080, ASTM D4767, ASTM D2850, ASTM D2166	Drained, consolidated undrained, unconsolidated undrained, and unconfined strength
	Dynamic and seismic response	ASTM D4015, ASTM D5311	Small strain modulus, damping, and cyclic resistance
	Filter, transition zone, and CQA	ASTM D2487, ASTM C136, ASTM D5101, ASTM D6938, ASTM D5080	Gradation, filter compatibility, density, and field compaction
Mine tailings clay core	Geotechnical investigation	ASTM D1586, ASTM D1587, ASTM D2113	Subsurface profile, tube sampling, and rock/core conditions
	Foundation analysis	ASTM D2166, ASTM D3080, ASTM D4767	Undrained strength, drained shear strength, and triaxial strength
	Core material properties	ASTM D4318, ASTM D2487, ASTM D698/ASTM D1557, ASTM D5084	Plasticity, classification, compaction, and hydraulic conductivity
	Seepage analysis	ASTM D5084, ASTM D6527	Saturated and unsaturated hydraulic conductivity
	Slope stability and shear strength	ASTM D3080, ASTM D4767, ASTM D2850	Strength parameters for stability under relevant drainage conditions.
	Filter design	ASTM D2487, ASTM C136	Gradation and filter compatibility

strength, and the ability to model crack initiation and growth. Hydraulic conductivity is vital, while fracture toughness provides additional insight into crack growth resistance. Compressibility and stiffness influence deformation, fabric evolution, and stress redistribution. All these factors must be considered together, particularly when the clay barrier's function relies on remaining intact or uncracked.

Checks on index property, compaction, hydraulic conductivity, and shear strength are generally standardized and widely used. In contrast, Mode-I soil fracture testing, soil-specific geometry factors, fracture-hydraulic-compressibility relationships, validated crack propagation models, and fracture coupled leachate transport are less standardized and more interconnected. The present study aims to address these gaps by developing a laboratory and numerical framework for fracture based assessment of clay barriers.

In this thesis, an open-mode discontinuity means a localized tensile separation that produces opening normal to the discontinuity plane. The term discontinuity is used when discussing field scale separations, preferential pathways, and continuity loss in clay barriers. The term crack is retained where it forms part of established fracture mechanics and laboratory terminology, including crack tip, crack path, crack mouth opening displacement, fracture process zone, pre-existing crack, hydraulic fracture, and crack propagation in single edge notched beam (SENB) specimens and numerical models. The two terms are therefore not used indiscriminately: open-mode discontinuity describes the physical loss of continuity in the barrier, while crack is retained for standard fracture mechanics definitions and test specific quantities. Retention may increase through multivalent-cation bridging, hydrophobic interaction of the fluorinated carbon chain with organic matter or surface coatings, and association with natural organic matter (W. Cai et al., 2022; W. Wang et al., 2022).

1.5 Research hypotheses, objectives and associated tasks

The present study is structured around three main research objectives: experimental development, numerical modelling, and design methodology. Below are the detailed hypotheses, objectives and the specific tasks that guide this work.

Hypothesis 1. **Experimental hypothesis: within the tested material, water-content, dry-density, geometry, and loading domain, compacted clay soils exhibit a measurable state-conditioned apparent Mode-I initiation toughness that can be interpreted together with hydraulic conductivity and compressibility.**

H1a: For geometrically similar SENB specimens within the tested ranges of specimen size, thickness, and notch ratio, application of the calibrated geometry correction factor ($f(a/W)$) will reduce the dependence of the calculated state-conditioned K_{Ic} on geometry relative to the raw peak load. The resulting value is expected to provide a repeatable initiation parameter within the stated test domain rather than a universal state-independent material constant.

H1b: Within the tested soil and compaction states, apparent Mode-I initiation toughness will vary with water content and dry density, while the effect of Ottawa sand addition will be non-monotonic and soil dependent. The response of FS may differ from that of the laboratory mixtures because its gradation, mineralogy, density, and natural fabric differ.

H1c: Selected additive dosages may improve one or more of apparent Mode-I initiation toughness, hydraulic conductivity, and compressibility. An additive will be considered beneficial only when the measured changes in these properties are assessed together.

H1d: Within the tested dataset, K_{Ic}, saturated hydraulic conductivity (k), and coefficient of compressibility (a_{v}) may exhibit an empirical association that is useful for preliminary material screening. The association is not assumed to represent a universal constitutive law or proof that one microstructural mechanism governs all three quantities.

Hypothesis 2. Numerical hypothesis: when applied to the same SENB benchmark, different numerical fracture formulations will provide different levels of agreement with the selected experimental response measures, and a method that provides explicit discontinuity topology and opening can be extended sequentially to a pore-network calculation.

H2a: Under common SENB geometry, material inputs, loading, and nominal discretization, Extended Finite Element Method (XFEM), Space-Time Finite Element Method (STFEM), phase-field fracture, and Lattice Element Method (LEM) will differ in predicted peak load, Crack Mouth Opening Displacement (CMOD), initiation, discontinuity path, fracture work, numerical sensitivity, and computational requirements. Method selection will therefore depend

on the stated comparison criteria and the intended fracture-to-flow application.

H2b: The failed-link graph and displacement jumps obtained from the lattice element method can be passed stepwise into a pore-network model, allowing the resulting equivalent hydraulic conductivity to vary according to the transferred aperture field, the specified throat conductances, and the connectivity between inlet and outlet. This constitutes a one-way numerical prediction of flow from fracture mechanics and does not incorporate any pore-pressure feedback into the mechanical solver, nor does it involve calibration or validation against experimentally measured flow in mechanically fractured samples.

Hypothesis 3. Design methodology hypothesis: adding state-conditioned fracture-resistance screening to conventional clay-barrier checks provides a more complete basis for comparing the tested materials.

H3a: For the tested soils, combined assessment of intact hydraulic conductivity and apparent Mode-I initiation toughness will identify material trade-offs that are not evident from hydraulic conductivity alone. The proposed screening limits are preliminary research thresholds for the investigated dataset and are not reliability-calibrated design or regulatory acceptance criteria.

Objective 1. Experimental objective: develop a laboratory test setup and interpretation framework for Mode-I fracture characterization of clay barriers.

Task 1: Develop a displacement-controlled SENB testing system for compacted soils that includes load measurement, vertical displacement measurement, dual CMOD sensors, roller supports, and moulds designed to produce controlled notch depths during compaction.

Task 2: Develop and cross-check an effective SENB load-to-K_{I} correction for the tested beam, contact, geometry, and material-state domain using Abaqus® contour-integral analysis, analytical weight-function calculations, and experimental compliance measurements.

Task 3: Quantify how SENB specimen size, thickness, notch ratio, and geometry influence the corrected K_{Ic} to enable selecting a consistent test geometry for compacted clayey soils.

Task 4: Quantify the effect of soil composition, clay and sand mixture ratio, water content, dry density, void ratio, and field soil fabric on Mode-I fracture toughness.

Task 5: Evaluate additive (nanomaterials) enhancement strategies by analyzing fracture toughness, hydraulic conductivity, and consolidation to consider material improvement as a combined barrier performance challenge.

Task 6: Develop and propose K_{Ic}-k-a_{v} interrelationships by interpreting fracture toughness, saturated hydraulic conductivity, and coefficient of compressibility for the same clay barrier material compositions.

Objective 2. Numerical objective: compare crack propagation methods and develop a sequential mechanical-fracture-to-flow modelling framework.

Task 7: Formulate, compare, and evaluate the Extended Finite Element Method (XFEM), Space-Time Finite Element Method (STFEM), phase-field method, and Lattice Element Method (LEM) for the same SENB fracture problem using the soil-specific geometry correction factor ($f(a/W)$) developed under the experimental objective and the stated experimental comparison measures.

Task 8: Building on Task 7, select the method that provides the closest combined agreement for the examined SENB cases and an explicit discontinuity graph, then develop a sequential pore-network extension that maps calculated opening to hydraulic conductance and equivalent hydraulic conductivity under the prescribed UCS and triaxial loading conditions.

Objective 3. Design methodology objective: develop a fracture based geotechnical design framework for clay barriers.

Task 9: Combine traditional clay barrier design evaluations with fracture toughness and hydraulic conductivity screening processes.

Chapter 3 addresses Tasks 1-6 and 9. Chapter 4 addresses Tasks 7-8 and provides the modelling basis for coupled hydraulic interpretation. Chapter 5 provides major conclusions and synthesizes Tasks 9 into the final design methodology and future research scope.

Chapter 2

Literature Review

2.1 Scope, review strategy, and synthesis logic

This chapter brings together the key literature needed to link traditional geotechnical analysis with fracture based design of clay barriers. It focuses on clayey soils and clay-rich engineered geomaterials employed as landfill liners, covers, clay cores, cutoffs, bentonite seals, and containment barriers. These materials are selected because their engineering performance depends on factors such as continuity, low hydraulic conductivity, limited compressibility, and resistance to crack propagation. In these systems, a crack is more than just a mechanical flaw; it can also pose a hydraulic risk.

The review is organized around mechanisms rather than a chronological sequence. It begins by highlighting the significance of fracture mechanics alongside tests of strength, compaction, consolidation, and hydraulic conductivity. It then explores crack modes, quasi-brittle fracture, the effect of specimen size, and Mode-I test geometries. The discussion then addresses geometry correction factors and underscores the importance of soil-specific $f(a/W)$. Next, it examines hydromechanical cracking, healing, and hydraulic fracture. The review continues with an analysis of additive (nanomaterials) modification within the coupled K_{Ic}-k-a_{v} space. Lastly, it compares four numerical approaches: the Extended Finite Element Method, the Space-Time Finite Element Method, Phase-field modelling, and lattice element modelling, emphasizing that coupled fracture-hydro-mechanical modelling should follow only after validation of crack propagation techniques against experimental fracture data.

This synthesis is a technical review of literature, not a bibliometric listing, and it directly supports clay barrier design. It includes laboratory Mode-I testing, fracture process zone behaviour,

specimen geometry, desiccation cracking, preferential flow, material enhancements, hydraulic fracture, and numerical crack growth. The literature forms the basis for the experimental, numerical, and design approaches covered in later chapters. The present study objectives and research gaps, detailed in Chapter 1 and summarized at the end of the chapter, are also grounded in this review.

A discontinuity-sensitive clay barrier is a barrier whose mechanical or hydraulic performance depends on the initiation, opening, closure, persistence, or connectivity of localized discontinuities rather than only on the properties of the intact matrix. Suction history means the sequence of wetting, drying, and associated suction states experienced by the soil. Suction redistribution means a spatial or temporal change in suction caused by internal water movement. Hydromechanical state means the combined mechanical condition, expressed through stress and strain, and hydraulic condition, expressed through water content, degree of saturation, pore pressure, or suction. Because suction and pore pressure were not measured in the present experimental programme, the experimental specimens are described more precisely by their measured water-content and dry-density state. Moisture conditioning means sealed storage intended to reduce water-content gradients after mixing and does not imply that uniform suction was verified.

2.2 Fracture mechanics as the missing design layer

Clayey soils are usually assessed using strength, deformation, consolidation, and hydraulic-conductivity measurements, but these quantities do not fully represent loss of barrier continuity. Omidi, Thomas, and Brown (1996) and Rayhani, Yanful, and Fakher (2007) measured increases in hydraulic conductivity following desiccation-induced discontinuity formation, while J. H. Li et al. (2016) documented vertical preferential flow through landfill clay liners and Julina and Thyagaraj (2020) examined the combined effects of wetting-drying cycles and interacting pore fluid.

Strength and fracture address different limit states. Baker (1981) examined the role of tension cracks in slope stability, whereas Sherard (1986) addressed hydraulic fracture in embankment dams. Peron et al. (2009b) and Shin and Santamarina (2011) related desiccation-induced tensile localization to shrinkage, suction, and effective stress. These studies show that a barrier may remain globally stable while losing hydraulic continuity through a localized open-mode discontinuity.

Direct Mode-I testing of compacted clay has progressively identified the variables required for reproducible characterization. J.-J. Wang, J.-G. Zhu, et al. (2007) quantified the effects of water content and dry density on clay fracture toughness, Amarasiri, Costa, and J. K. Kodikara (2011) inferred cohesive fracture properties from compacted-clay beams, and J.-J. Wang, Huang, and J.-F. Hu (2016) examined the influence of normalized notch depth. Alternative semicircular and bentonite test geometries were investigated by J. Wang, Huang, et al. (2020) and Qiao et al. (2023).

Table 2.1: Literature review logic used to organize Chapter 2.

Theme	Key question	Role in the present study
Fracture basis	What does fracture mechanics add beyond strength and hydraulic conductivity tests?	Defines K_{I}, K_{Ic}, G_{f}, J, crack opening, process zone size, and size effect
Mode-I testing	Which specimen geometries and control variables produce reproducible Mode-I cracking in clay?	Justifies the SENB experimental programme and the geometry matrix used in Chapter 3
Geometry correction	Why is a soil specific $f(a/W)$ required instead of directly adopting metallic SENB functions?	Connects measured peak load to corrected K_{Ic} for compacted clay beams
Hydromechanical consequence	How do cracks alter flow, healing, compressibility, and hydraulic fracture risk?	Links fracture resistance to barrier performance and design screening
Material modification	How should fibers, biopolymers, and nanomaterials be judged for clay barriers?	Prevents ranking additives by toughness alone without checking k, strength, and consolidation
Numerical methods	Which method can reproduce crack initiation, propagation, aperture, and hydraulic connectivity?	Frames the comparison of XFEM, space-time FEM, phase-field modelling, and LEM before coupled modelling

The fracture-process zone and structural-size dependence were examined by J. Wang, Lv, et al. (2023), Lv, J. Wang, Huang, et al. (2024), and Huang, X. Wang, et al. (2025), while J. J. Wang et al. (2013) investigated hydraulic recovery after wetting.

In this thesis, the term cohesive soil is used descriptively for a fine-grained soil that can sustain measurable tensile or shear resistance at low applied normal stress because of physicochemical interparticle forces, capillary effects, cementation, or a combination of these mechanisms. The term does not imply that cohesion is a unique intrinsic constant or that all fine-grained soils follow the same constitutive law.

Studies of other quasibrittle geomaterials provide useful scale and geometry comparisons. Sture, Alqasabi, and Ayari (1999) examined size effects in cemented sand, Lenci, Clementi, and

Sadowski (2012) characterized fracture in unfired earth, and Atkinson (1984) reviewed subcritical crack growth in geological materials. ASTM E399 provides the conventional metallic SENB reference geometry and validity framework (ASTM International, 2024); its direct application to compacted clay nevertheless requires evaluation of specimen state, process-zone size, and boundary conditions.

The hydraulic state must also be identified carefully. Terzaghi (1943) established the classical saturated effective-stress framework, Bishop (1959) and D. G. Fredlund and Rahardjo (1993) extended the description to unsaturated conditions, and Biot (1941) and Coussy (2004) developed the poromechanical basis for coupling pressure and deformation. These formulations provide physical context, although suction and pore-pressure feedback were not implemented in the present SENB mechanical calculations.

Desiccation models identify different parts of the drying process. Ayad, Konrad, and Souli'e (1997) and Konrad and Ayad (1997) developed analytical descriptions of cohesive-soil desiccation, while Peron et al. (2009a), Trabelsi, Romero, and Jamei (2012), and Sima, Jiang, and C. B. Zhou (2013) represented shrinkage and discontinuity-network formation using discrete numerical methods. Rahmani et al. (2024) combined digital image correlation and finite-element analysis to characterize shrinkage and fracture in bentonite.

Specific experiments have isolated important geometric and environmental effects. Bradley (1933) and Allen (1982) examined curvature of dried layers, Nahlawi and J. Kodikara (2002) investigated discontinuity formation in thin soil layers, and Berney, Tingle, and Newman (2008) examined curling of compacted clay. Goehring et al. (2015) synthesized desiccation-pattern formation across materials, while Lin et al. (2020) quantified desiccation geometry using image-based measurements.

Temperature, salinity, wetting-drying history, and monitoring method also affect the observed response. C.-S. Tang, Y.-J. Cui, et al. (2007), Shirazi et al. (2010), and Shokri, P. Zhou, and Keshmiri (2015) examined temperature, salinity, and solution effects. C. S. Tang, Y. J. Cui, et al. (2011) and C. S. Tang, C. Zhu, et al. (2019) quantified changes associated with repeated drying and specimen geometry. Poulsen, W. L. Cai, and Garg (2020) examined evaporation from discontinuities, while J.-J. Xu, C.-S. Tang, Q. Cheng, Vahedifard, et al. (2022) used distributed sensing to monitor deformation and discontinuity development. Collectively, these studies show that fracture results must be reported together with material state, environmental boundary conditions, geometry, and measurement method.

The evidence can be organized into the literature review questions listed in Table 2.2. These questions are not objectives of the present study; they are the logic used to interpret the state of knowledge before the experimental, numerical, and design methodology contributions are developed in later chapters.

Table 2.2: Literature review questions used to structure the fracture based design synthesis.

Question	Focus	Relevance to clay barrier design
Q1	Why is strength-based design insufficient for discontinuity-sensitive clay barrier system?	Establishes the need for fracture metrics where continuity, not only strength, controls function
Q2	Which fracture parameters are meaningful in clayey soils?	Separates K_{Ic}, G_{f}, J, crack opening response, and network of connected discontinuities descriptors
Q3	Which laboratory geometries dominate Mode-I testing?	Determines whether the field is converging on a test standard or remains geometry dependent
Q4	How do water content, density, suction, and cracking translate into hydraulic consequence?	Links fracture mechanics to permeability, leakage, and preferential flow
Q5	What do additives and nanomodifiers change?	Distinguishes true fracture improvement from isolated strength or crack area reduction
Q6	How do hydraulic pressure and coupled pore pressure effects broaden the fracture problem?	Clarifies why hydraulic fracture is relevant to liners, cores, and bentonite barriers
Q7	Which numerical tools are credible for initiation and propagation?	Defines the validation requirement for XFEM, STFEM, phase-field, and LEM

2.3 Evidence from crack-controlled geotechnical systems

The issue of fractures in clayey soils extends beyond laboratory notches; it frequently occurs in both engineered and natural systems requiring soil continuity. Desiccation cracks and differential settlement in compacted liners and covers can form preferential flow paths. Similarly, in embankment cores and cut-offs, hydraulic gradients and differential settlement can focus tensile stresses. On slopes and in excavations, tension cracks diminish the effective resisting mass and enhance infiltration. In bentonite buffers and seals, hydration gradients and pressure loads can initiate macrocracks even during swelling. All these scenarios share a common mechanical trait: the primary instability is a localized discontinuity, rather than a distributed yield surface (Baker, 1981; Peron et al., 2009b; Sherard, 1986). Hydraulic fracturing, ice lensing, and desiccation-induced discontinuity formation can all produce localized tensile opening and can all alter the hydraulic continuity of soil. However, their driving mechanisms and boundary conditions differ. These distinctions are developed in Section 2.7.

Table 2.3: Why strength-based design alone is insufficient for discontinuity-sensitive clay barriers?

Issue	Strength based interpretation	Fracture based interpretation
Barrier continuity	Checks average stress state and yield condition	Checks whether a flaw can initiate and propagate into a connected pathway
Thin layer drying	Treats cracking mainly as shrinkage or tensile threshold exceedance	Treats drying as suction driven contraction followed by fracture localization
Specimen size transfer	Often assumes direct property transfer between test size and application	Requires explicit size effect and fracture process zone interpretation
Post crack serviceability	rarely explicit in classical design	Central, because crack aperture, persistence, and connectivity control the barrier function
Hydraulic pressurization	Represents pore-pressure influence through the stress carried by the soil skeleton	Requires a consistent treatment of skeleton stress and, where an open discontinuity is fluid-filled, pressure traction on the discontinuity faces
Numerical modelling	emphasizes local yielding, plasticity, or continuum deformation	Emphasizes initiation, propagation, crack path, aperture, and hydromechanical feedback

Desiccation studies demonstrate that a network of connected discontinuities can increase hydraulic conductivity and bypass the low-permeability clay matrix (Julina and Thyagaraj, 2020; J. H. Li et al., 2016). Bending studies show that thin clay layers can fail through tensile cracking under boundary restraint and curvature (Ameur and Hattab, 2022; Cengiz, Su, and Zwanenburg, 2025; Plé et al., 2012). Hydraulic fracturing studies show that pore water pressure can do mechanical work on crack faces and drive fracture extension in cohesive soils and compacted bentonite (Detournay, 2016; Detournay and A. H. D. Cheng, 1993; K.-P. Li et al., 2025). These mechanisms originate differently but share a common design goal: quantifying crack initiation and propagation is essential if the clay is to serve as an effective barrier.

The broader body of tensile cracking research agrees with this conclusion. Early studies on tensile and bending behaviour demonstrated that crack formation in clay can be directly observed, and that variables such as crack depth, support conditions, and layer thickness influence its response (Al-Hussaini and Townsend, 1973; Sun et al., 2024). Desiccation studies linked evaporation,

Table 2.4: Crack controlled mechanisms relevant to clay barriers.

System	Crack driving mechanism	Consequence	Design implication
Landfill liner or cover	Desiccation, wetting and drying, settlement, construction defects	Preferential leachate flow and increased effective hydraulic conductivity	Hydraulic conductivity must be paired with crack resistance
Clay core or cut-off	Hydraulic gradient, differential deformation, tensile stress concentration	Seepage localization and possible hydraulic fracture	Pore pressure can become a crack driving load
Compacted clay layer under bending	Layer curvature, differential support, restraint, drying gradients	Opening mode tensile cracks and layer separation	Flexural cracking require Mode-I interpretation
Unsaturated clay surface	Evaporation, suction increase, shrinkage restraint	network of connected discontinuities formation and infiltration concentration	Suction and shrinkage must be linked to fracture
Bentonite seal or buffer	Hydration, swelling pressure, confinement, gas or water pressure	Fracture pathways through an otherwise low permeability material	Swelling capacity does not eliminate fracture risk

suction increase, shrinkage restraint, and crack-network formation (J. Kodikara, Barbour, and D. D. Fredlund, 1999; J. Kodikara and Choi, 2006; J. Kodikara, Nahlawi, and Bouazza, 2004). Hydraulic studies demonstrated the serviceability consequence: cracks can increase effective flow, concentrate infiltration, and create vertical preferential pathways through clay liners (Julina and Thyagaraj, 2020; Krisnanto et al., 2014; J. H. Li et al., 2016). The research direction is therefore not simply to measure fracture toughness as a mechanical index. It is to connect crack resistance to the hydraulic and compressibility properties used in clay barrier design.

Table 2.5: Documented crack controlled consequences requiring a fracture based design layer.

Structure or system	Crack driving mechanism	Documented consequence	Why strength based design alone is incomplete?
Compacted clay liners and covers	Desiccation, restrained shrinkage, wetting and drying cycles	Increased hydraulic conductivity, preferential flow, and leakage (Julina and Thyagaraj, 2020; Tian et al., 2023)	Strength checks do not quantify continuity loss or seepage path formation
Clay embankment and slope surfaces	Seasonal shrinkage, crest tension, stress relief	Crack deepening, infiltration concentration, and suction redistribution (Baker, 1981; Dyer, Utili, and Zielinski, 2009; Z. Yu et al., 2021)	Limit equilibrium safety factors do not predict crack opening or post-crack hydraulic feedback
Clay cores and cut-offs	Hydraulic loading, differential settlement, tensile stress concentration	Localized pressurized crack growth and seepage path development (Komak Panah and Yanagisawa, 1989; Sherard, 1986; J.-J. Wang and Liu, 2010; J.-J. Wang, H.-P. Zhang, et al., 2009)	A continuum yield criterion without an explicit pressurized-discontinuity boundary cannot, by itself, predict pressure-driven discontinuity extension
Bentonite buffers and seals	Hydration gradients, confinement change, pressure gradients	Crack initiation, pathway formation, and hydromechanical instability (K.-P. Li et al., 2025; K.-p. Li et al., 2024; Rahmani et al., 2024)	The governing instability is coupled fracture rather than distributed yielding
Laboratory compacted clay specimens	Geometry, notch ratio, specimen size, moisture state	Apparent toughness varies with size and geometry (Huang, X. Wang, et al., 2025; Lv, J. Wang, Huang, et al., 2024; J.-J. Wang, Huang, and J.-F. Hu, 2016; J. Wang, Lv, et al., 2023)	A transferred material strength value is insufficient without fracture scaling

2.4 Fracture mechanics basis for crack controlled clay systems

2.4.1 Crack modes and the priority of Mode I

Fracture mechanics categorizes crack deformation into three main modes: Mode I involves opening perpendicular to the crack plane, Mode II involves in-plane sliding, and Mode III involves out-of-plane tearing. When loading conditions, support friction, interfaces, or pre-existing defects involve multiple modes, it results in mixed-mode fracture processes (Aliha and Haghighatpour, 2022; Erdogan and Sih, 1963; Sih, 1974). For compacted clay barriers, Mode I is the primary reference condition because opening creates an aperture. This aperture forms a hydraulic pathway that enables the low-permeability matrix to act as a preferential flow system when connected.

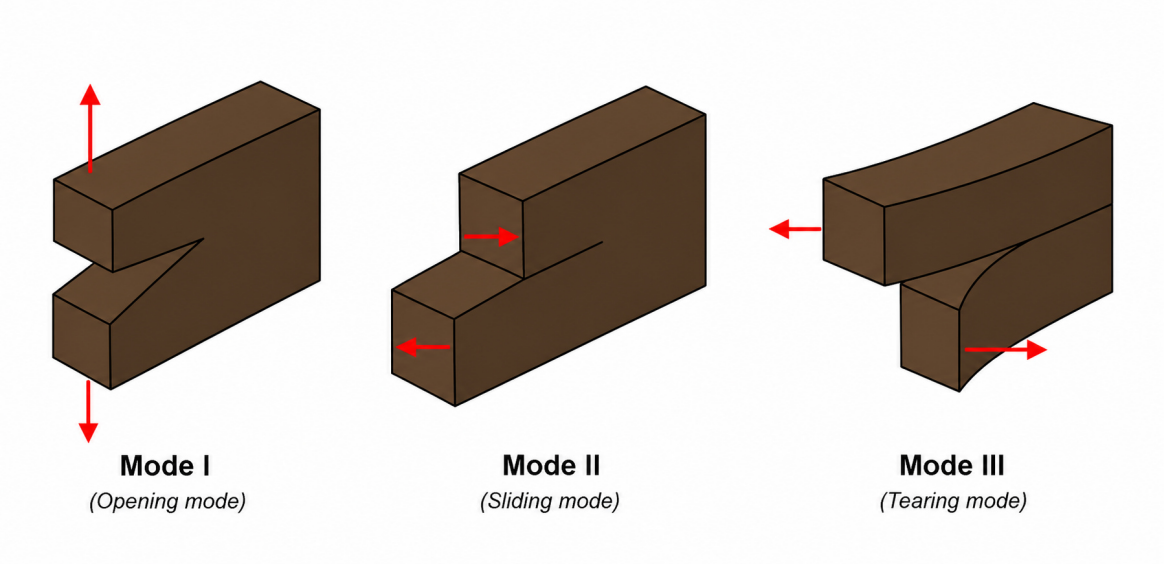


Figure 2.1: Primary modes of crack/fracture creation: opening, sliding, and tearing.

The near-tip stress field in linear elastic fracture mechanics is written as

$$\sigma_{ij}(r,\theta) = \frac{K}{\sqrt{2\pi r}} f_{ij}(\theta) + O(1) \tag{2.1}$$

where K is the stress intensity factor, r and θ are crack tip coordinates, and f_{ij} describes the angular stress distribution (Anderson, 2017; Griffith, 1921; Irwin, 1957). For Mode I,

$$K_I = K_{Ic} \tag{2.2}$$

marks the onset of crack extension under idealized linear-elastic conditions. The energy release rate is

$$G = \frac{K_{\mathrm{I}}^2}{E'} \qquad E' = \begin{cases} E & \text{plane stress} \\ E/(1-\nu^2) & \text{plane strain} \end{cases} \tag{2.3}$$

where E is Young's modulus and ν is Poisson's ratio. Linear Elastic Fracture Mechanics (LEFM) provides a mathematical framework for evaluating structural integrity by quantifying stress fields near localized flaws. This approach remains highly precise under small-scale yielding conditions, where the plastic zone around the flaw is negligible relative to the component's overall size. By comparing the calculated stress intensity factor (K) to the material's critical fracture toughness (K_{Ic}), engineers can reliably predict and prevent catastrophic brittle failures.

The J-integral extends the energy concept to nonlinear or quasi-brittle fracture:

$$J = \int_{\Gamma} \left(W n_{\mathrm{x}} - T_{\mathrm{i}} \frac{\partial u_{\mathrm{i}}}{\partial x} \right) \mathrm{d}s \tag{2.4}$$

where W is strain energy density, T_{i} are tractions, and Γ is a contour around the crack tip (Cherepanov, 1967; J. Rice, P. Paris, and Merkle, 1973; J. R. Rice, 1968). In soils, J-type and energy-based interpretations are important because the material is not a small-scale yielding metal. Moisture state, suction, density, fabric, plastic dissipation, and crack bridging can create a fracture process zone large enough to influence measured toughness (Chandler, 1984; Costa, Htike, et al., 2016; Costa and J. Kodikara, 2012; Costa, J. Kodikara, and Xue, 2013; Hallett, Dexter, and Seville, 1995; Hallett and Newson, 2001; Hallett and Newson, 2005).

A useful way to generalize the clay fracture is to write the total potential energy of a cracked body as

$$\Pi(a) = U(a) - W(a) \tag{2.5}$$

where $U(a)$ is stored strain energy and $W(a)$ is external work. The crack driving energy is

$$G = -\frac{\mathrm{d}\Pi}{\mathrm{d}a} \tag{2.6}$$

For compacted clay barriers, the crack driving contribution is rarely purely mechanical. It may include elastic energy, fluid pressure, shrinkage restraint, thermal gradients, and chemical or salinity effects:

$$G_{\mathrm{tot}} = G_{\mathrm{mech}} + G_{\mathrm{fluid}} + G_{\mathrm{sh}} + G_{\mathrm{th}} + G_{\mathrm{chem}} \qquad G_{\mathrm{tot}} \geq G_{\mathrm{c}}(s, T, c, \rho_{\mathrm{d}}) \tag{2.7}$$

where the resistance is allowed to depend on suction s, temperature T, pore chemistry c, and dry density ρ_{d}. This form is useful for clay barriers because drying, wetting, pore pressure, and

chemical exposure can act together rather than in isolation. For the present study, LEFM is assumed to be applicable due to small sample sizes, small yield surface, and fracture process zone.

At the microstructural scale, compacted clay contains a distribution of pores, weak contacts, shrinkage fissures, and fabric defects. A microflaw of half-length a_{m} may be idealized as

$$K_{\mathrm{I,m}} = Y_{\mathrm{m}}\sigma\sqrt{\pi a_{\mathrm{m}}} \qquad K_{\mathrm{I,m}} \geq K_{\mathrm{Ic,m}} \tag{2.8}$$

where Y_{m} is a microflaw geometry factor. This does not mean that clay acts as a perfect brittle solid. Rather, it explains why crack initiation occurs gradually: various flaws activate under different stress, suction, and density conditions, creating a fracture process zone before a visible macrocrack takes over.

For the beam family that dominates the clay literature, apparent Mode-I fracture toughness is commonly written in SENB or SECB form as

$$K_{\mathrm{Ic}} = \frac{P_{max}S}{BW^{3/2}}\, f(a/W) \tag{2.9}$$

where P_{max} is maximum/peak load at which crack initiates, S is support span, B is thickness, W is specimen width, and $f(a/W)$ is the dimensionless beam geometry function. A commonly used beam correction is

$$f(x) = \frac{3\sqrt{x}\left[1.99 - x(1-x)\left(2.15 - 3.93x + 2.7x^2\right)\right]}{2(1+2x)(1-x)^{3/2}} \qquad x = \frac{a}{W} \tag{2.10}$$

Equation 2.10 is useful, but its direct transfer to compacted clay is not automatically safe because clay has low stiffness, suction corresponding to the stated water content, density, and wetting–drying history, and a fracture process zone that can be large relative to the ligament (ASTM International, 2024).

For the semi-circular bend family,

$$K_{\mathrm{I}} = \frac{P}{BR^{1/2}}\, Y_{\mathrm{I}}\left(\frac{a}{R}, \frac{S}{R}\right) \tag{2.11}$$

where R is specimen radius and Y_{I} is the semicircular geometry function. The clay-specific significance of Eq. 2.11 is not merely that it provides an alternative specimen; it shows that the field remains geometry specific rather than standardized (Huang, X. Wang, et al., 2025; Qiao et al., 2023; J. Wang, Huang, et al., 2020).

A cohesive fracture representation is often more realistic for compacted clay. In its simplest traction-separation form,

$$t(w) = f_{\mathrm{t}}\left(1 - \frac{w}{w_{\mathrm{c}}}\right) \qquad 0 \leq w \leq w_{\mathrm{c}} \tag{2.12}$$

where t is normal traction, w is crack opening displacement, f_t is tensile strength, and w_c is critical crack opening. The fracture energy for this law is

$$G_f = \int_0^{w_c} t(w)\,\mathrm{d}w = \frac{f_t w_c}{2} \tag{2.13}$$

This equation is useful for clay because two soils with similar tensile strengths can differ markedly in crack opening resistance and post-peak response.

A material characteristic length can be written as

$$\ell_{ch} = \frac{E G_f}{f_t^2} \tag{2.14}$$

which measures the relative importance of stiffness, fracture energy, and tensile strength (Hillerborg, Modeer, and Petersson, 1976). When ℓ_{ch} is not negligible relative to ligament size, specimen geometry and structural size influence the measured result. This is why the quasibrittle size effect law

$$\sigma_N = \frac{B_0 f_t}{\sqrt{1 + D/D_0}} \tag{2.15}$$

is important for clay testing, where D is characteristic size and D_0 is a transitional size parameter (Bazant, 1984; Bazant, 2002; Bazant and Planas, 1998). In the SENB specimen, the remaining ligament is $W - a$, which is the intact beam depth between the notch tip and the opposite surface. The characteristic material length, $\ell_{ch} = E G_f / f_t^2$, provides an estimate of the scale over which nonlinear fracture-process-zone behaviour is important relative to the specimen dimensions. The transitional size parameter, D_0, identifies the structural size over which the nominal response changes from a strength-dominated regime to a fracture-mechanics size-effect regime. When the fracture-process-zone length is not small compared with $W - a$, a measured K_{Ic} should be interpreted as an apparent, state-conditioned initiation parameter rather than a size-independent intrinsic constant.

2.5 Classical soil models and the fracture limitation

Mohr–Coulomb and Critical State Soil Mechanics are included as the conventional reference frameworks for the intact soil matrix, not as models of Mode-I discontinuity propagation. Mohr–Coulomb describes stress-dependent shear failure, while Critical State models describe yielding, volumetric change, hardening, and the approach to a critical state under a prescribed

Table 2.6: Equation to design meaning for the fracture framework used in this study.

Equation	Meaning	Design relevance for clayey soils
Eq. 2.1	Near tip stress field	Shows why preexisting flaws matter even before global strength is exhausted
Eq. 2.9	SENB/SECB fracture reduction	Explains why beam tests became the practical Mode-I baseline
Eq. 2.11	Semicircular bend reduction	Demonstrates that geometry-specific calibration remains necessary
Eq. 2.3	Energy release rate	Links stiffness and crack driving force
Eq. 2.4	Nonlinear crack driving integral	Relevant because compacted clay may not satisfy ideal LEFM assumptions
Eq. 2.13	Fracture energy	Captures crack opening resistance and post-peak dissipation
Eq. 2.14	Characteristic material length	Indicates whether the fracture process zone is large relative to specimen size
Eq. 2.15	Structural size effect	Shows why laboratory fracture values are not automatically independent of size-effect

effective-stress path. These frameworks remain necessary for evaluating strength, deformation, and stability of a clay barrier.

The present thesis introduces fracture mechanics because bulk yielding and discontinuity propagation are different questions. A soil may satisfy a global shear-strength or critical-state stability requirement while a pre-existing flaw still extends when the stress-intensity factor or energy-release rate reaches the corresponding fracture resistance. Conversely, fracture mechanics does not replace conventional shear-strength or critical-state analysis of the intact matrix. It provides an additional criterion for initiation and propagation of a localized tensile discontinuity. The two descriptions are therefore complementary rather than competing.

The classical Mohr-Coulomb criterion is

$$\tau_f = c' + \sigma'_n \tan \phi' \tag{2.16}$$

where c' is effective cohesion, σ'_n is normal effective stress, and ϕ' is friction angle. A tensile cutoff may be appended in Rankine form as

$$\sigma'_1 = f_t \tag{2.17}$$

and the Drucker-Prager surface may be written as

$$F = \sqrt{J_2} + \alpha I_1 - k = 0 \tag{2.18}$$

where I_1 is the first stress invariant and J_2 is the second invariant of deviatoric stress. Critical state formulations incorporate volumetric hardening but remain fracture blind. A common Modified Cam Clay yield surface is

$$\frac{q^2}{M^2} + p' \left(p' - p'_c\right) = 0 \tag{2.19}$$

where p' is mean effective stress, q is deviatoric stress, M is the critical state slope, and p'_c is preconsolidation pressure.

These relations lack explicit mention of a crack length a, fracture resistance, or structural size scale. As a result, they cannot independently determine if a preexisting flaw will stop or grow, whether a crack will localize into a conductive path, or if hydraulic loading will provide enough energy on the crack faces to cause unstable extension. The continuum fracture mechanics treatment used in this thesis assumes that stress, strain, and crack driving fields are defined at a scale much larger than the constituent clay particles. This is reasonable for clay-rich compacted specimens when the representative continuum scale is small relative to the specimen and discontinuity dimensions. In coarse granular media, load is transferred through discrete contacts and force chains, and localized deformation commonly occurs through particle rearrangement, rolling, sliding, dilation, and contact breakage. A stress intensity factor may still be used as an effective structural descriptor in a bonded or cemented granular material, but it is not automatically an intrinsic property of an unbonded granular assembly. In a compacted cohesive medium, apparent fracture toughness represents the macroscopic resistance to extending a localized tensile separation and includes energy associated with physicochemical bonding, capillary forces, aggregate separation, particle rearrangement, fabric disruption, and process-zone dissipation. In a predominantly unbonded granular medium, there is no equivalent continuous bonded fracture plane, and the apparent resistance to localization is governed more strongly by frictional sliding, dilation, force-chain reorganization, and particle interlocking. The measured SENB parameter in this thesis therefore represents a state-conditioned macroscopic response of the compacted clay-rich material and does not isolate one unique contact-scale mechanism.

Table 2.7: Classical geotechnical models and their limitations for fracture controlled clay systems.

Model family	Representative form	Fracture related limitation
Mohr-Coulomb	Eq. 2.16	Captures distributed shear failure but contains no crack length, fracture energy, or process zone term
Rankine tension cutoff	Eq. 2.17	Identifies tensile onset only; it does not represent stable or unstable propagation
Drucker-Prager	Eq. 2.18	Convenient numerically, but remains a yield criterion rather than a crack growth law
Modified Cam Clay	Eq. 2.19	Represents volumetric hardening and critical state, but not discontinuity evolution or energy release
Unsaturated critical state extensions	Suction dependent yield surface	Introduce suction effects, yet still treat failure through yielding rather than fracture propagation

2.6 Experimental characterization of Mode-I fracture in clayey soils

2.6.1 SENB/SECB as the historical reference geometry

The significant experimental advancement in the study of clay fracture is the adoption of single edge notched beam (SENB or SECB) configurations tested under three-point bending. The widespread use of this beam design is due to its simplicity: rectangular specimens are easy to prepare and shape, notches can be added with minimal effort, and the loading and support setups are straightforward. Additionally, this geometry aligns well with existing fracture mechanics equations used for other materials. It also facilitates measurements such as crack mouth opening displacement, local displacement, and image based observations more easily than many other setups.

J.-J. Wang, J.-G. Zhu, et al. (2007) provided one of the seminal demonstrations of this approach by reporting fracture toughness and tensile strength of compacted clay as functions of water content and dry density. Amarasiri, Costa, and J. K. Kodikara (2011) used compacted clay beams to infer cohesive properties and fracture energy for Mode-I fracture. J.-J. Wang, Huang, and J.-F. Hu (2016) subsequently examined notch-depth limitations in SECB testing and showed that

the apparent fracture toughness varies with the normalized crack depth. These studies explain why the beam became the historical baseline: it is experimentally feasible, mechanically interpretable, and sufficiently rich to reveal the limitations that standardization must address.

In the analyses completed in this thesis, the Chapter 3 SENB contour-integral models use a homogeneous, isotropic, linear-elastic representation before initiation. The Chapter 4 lattice formulation includes local tensile and shear link-failure criteria and fracture-energy-controlled softening, but it does not implement the complete Modified Cam Clay yield surface, volumetric hardening law, or critical-state evolution. Mohr–Coulomb and Critical State concepts are therefore included to define the conventional soil-mechanics basis and its limitations, not to imply that these constitutive models were used in every numerical simulation.

2.6.2 Alternative geometries and specimen preparation

If the beam were universally satisfactory, experimental convergence would already be clear. Instead, the literature continues to use semicircular bend, notched semicircular bend, notched deep beam, ring, plate, compact tension, disc, and cylinder type specimens. NSCB specimens are attractive because they can be prepared from cylindrical samples and loaded under controlled support spacing (Huang, X. Wang, et al., 2025; Qiao et al., 2023; J. Wang, Huang, et al., 2020). Notched deep beams are useful for size effect analysis (Lv, J. Wang, Huang, et al., 2024). Disc type and plate-bending configurations address different parts of the representativeness problem, particularly thin-layer bending, additive studies, and mixed-mode effects (Aliha and Haghighatpour, 2022; Aliha, Iranmanesh, et al., 2026; Cengiz, Su, and Zwanenburg, 2025).

Beam configurations are attractive because they are compatible with three-point bending, simple loading, and conventional stress intensity reductions. SENB and SECB specimens have therefore become common for cohesive soils and compacted clays (Amarasiri, Costa, and J. K. Kodikara, 2011; J.-J. Wang, Huang, and J.-F. Hu, 2016; J.-J. Wang, J.-G. Zhu, et al., 2007). SCB and NSCB specimens are attractive because semicircular samples can be prepared from cylindrical cores and can be loaded under controlled support spacing (Aliha and Haghighatpour, 2022; J. Wang, Huang, et al., 2020). Ring tests and plate tests provide alternative tensile cracking paths for compacted cohesive soils and thin clay layers (Ameur and Hattab, 2022; Camp, Gourc, and Plé, 2010; Camp, Plé, and Gourc, 2009; Cengiz, Su, and Zwanenburg, 2025; Harison, Hardin, and Mahboub, 1994; Plé et al., 2012). The presence of many specimen families is not merely a matter of preference; it reflects unresolved issues in preparation, boundary conditions, mode purity, and scale transfer.

One key reason why comparing clay fracture results is challenging is that the specimen's state is not just defined by its geometry. Instead, it represents a hydromechanical condition established

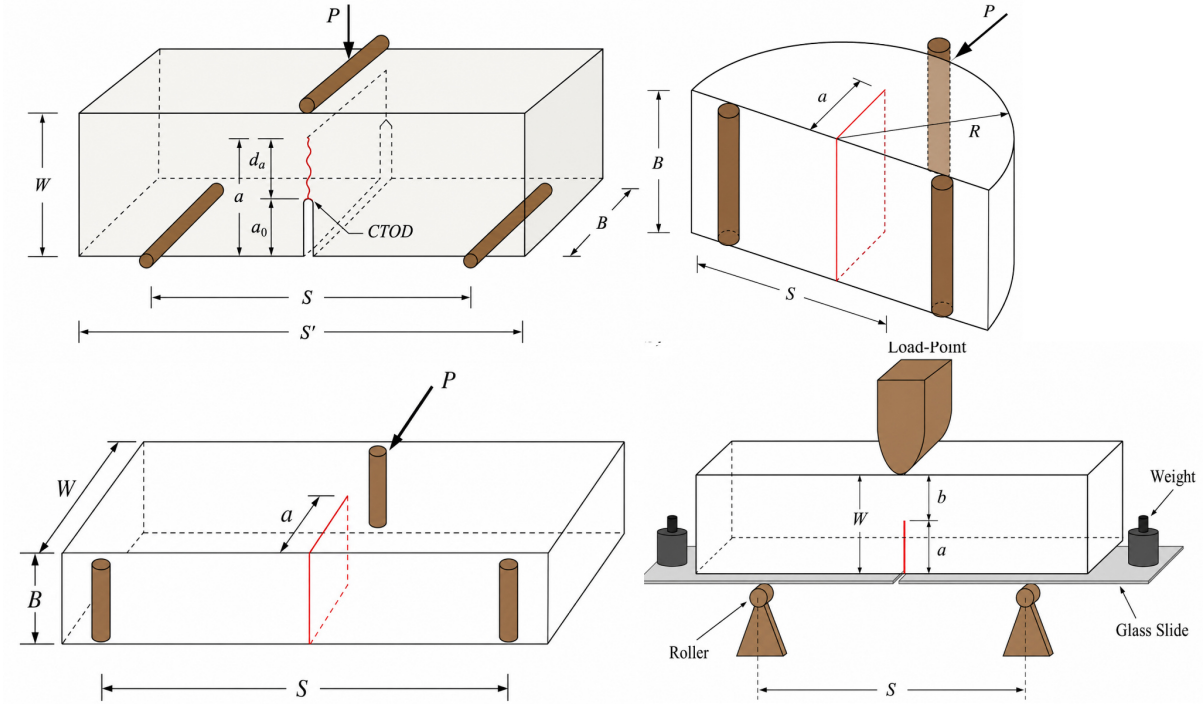


Figure 2.2: Different shapes and configurations of Mode-I fracture toughness test under 3-point bending (J.-J. Xu, C.-S. Tang, Q. Cheng, Q.-l. Xu, et al., 2022).

through a specific process. Factors such as water content, dry density, compaction energy and method, fabric, curing time, notch-making procedure, moisture conditioning and possible suction redistribution, boundary friction, and loading rate all influence the measured response. This highlights a crucial difference between soil fracture testing and metallic fracture testing: the preparation process has a direct impact. In notched deep beam and mixed-mode tests, support friction plays a significant role because it can alter the apparent mode mixity (Lv, J. Wang, Ling, et al., 2026; Trabelsi, Romero, and Jamei, 2018).

Table 2.8: Representative direct Mode-I studies on clayey soils and clay dominant materials.

Study	Material and test geometry	Main variables and outputs	Main implication
Harison, Hardin, and Mahboub (1994)	Compacted cohesive soils; ring test	Fracture response under restraint	Fracture parameters can be obtained outside the beam tradition

Continued on next page

Table 2.8 continued.

Study	Material and test geometry	Main variables and outputs	Main implication
Nishimura and Shimizu (2004)	Cohesive soil; centre-crack cylinder	Initial crack size and specimen diameter	Apparent toughness depends on flaw proportion and specimen size
J.-J. Wang, J.-G. Zhu, et al. (2007)	Compacted clay; SECB/direct tension	Water content, dry density, K_{Ic}, tensile strength	Landmark study linking fracture resistance to geotechnical state variables
Amarasiri, Costa, and J. K. Kodikara (2011)	Compacted clay; SECB with cohesive interpretation	Moisture content, K_{Ic}, G_{f}	Strong case for cohesive rather than pure LEFM interpretation
J.-J. Wang, Huang, and J.-F. Hu (2016)	Red clay; SECB	Notch ratio and apparent K_{Ic}	Shows need for crack depth limits and admissible geometry ranges
J. Wang, Huang, et al. (2020)	Compacted clay; NSCB	Water content, dry density, notch ratio	Viable alternative geometry; confirms absence of a general standard
Qiao et al. (2023)	Compacted bentonite clay; NSCB	Water content, density, process zone effects	Extends Mode-I testing to barrier grade bentonite systems
J. Wang, Lv, et al. (2023)	Compacted clay; DIC-assisted Mode-I test	Fracture process zone length and full field displacement	Quantifies process zone size and supports quasi brittle interpretation
Lv, J. Wang, Huang, et al. (2024)	Compacted clay; notched deep beam	Size effect and crack length ratio	Demonstrates strength to fracture transition with size
Huang, X. Wang, et al. (2025)	Compacted clay; NSCB	Size effect with different initial crack lengths	Confirms size dependence within the semi circular family

Continued on next page

Table 2.8 continued.

Study	Material and test geometry	Main variables and outputs	Main implication
Aliha, Iranmanesh, et al. (2026)	Stabilized clay; disc type Mode I	Additive effects on K_{Ic} and G_c	Shows direct fracture metrics can be coupled to modification studies
Cengiz, Su, and Zwanenburg (2025)	Kaolin plates; pure-bending plate test	Curvature and suction related cracking parameters	Service condition realism motivates new protocols

Note: SECB/SENB = single edge cracked/notched beam; NSCB = notched semi-circular bend; NDB = notched deep beam; DIC = digital image correlation

Table 2.9: Experimental Mode-I and mixed-mode fracture studies relevant to clayey soils.

Study	Mode and material	Specimen or test type	Principal contribution
Chandler (1984)	Mode I; clay mixed with cement	Single edge notched beam	Introduced nonlinear fracture interpretation for a soil-like material
F. H. Lee, Lo, and S. L. Lee (1988)	Mode I; overconsolidated cohesive soil	Compact tension specimen	Demonstrated tensile fracture testing outside the beam tradition
Nishimura and Shimizu (2004)	Mode I; soft pyroclastic ash loam	Centre-crack cylinder	Showed dependence on flaw size and specimen diameter
Harison, Hardin, and Mahboub (1994)	Mode I; residual cohesive soils	Ring test	Established an alternative restrained fracture testing route
J.-J. Wang, J.-G. Zhu, et al. (2007)	Mode I; compacted clay	SECB/direct tension	Linked apparent K_{Ic} and tensile strength to water content and dry density

Continued on next page

Table 2.9 continued.

Study	Mode and material	Specimen or test type	Principal contribution
Amarasiri, Costa, and J. K. Kodikara (2011)	Mode I; Werribee clay	SECB	Provided cohesive interpretation of beam response
J.-J. Wang, Huang, and J.-F. Hu (2016)	Mode I; red clay	SECB	Established crack-to-width ratio sensitivity and crack-to-width limits
J. Wang, Huang, et al. (2020)	Mode I; compacted clay	NSCB	Demonstrated an alternative Mode-I geometry and noted the absence of a standard
Qiao et al. (2023)	Mode I; compacted bentonite clay	NSCB	Extended direct fracture testing to barrier-grade bentonite
J. Wang, Lv, et al. (2023)	Mode I; compacted clay	DIC-assisted fracture test	Quantified fracture process zone length and supported a quasibrittle interpretation
Lv, J. Wang, Huang, et al. (2024)	Mode I; compacted clay	Notched deep beam	Linked specimen size and crack-to-width ratio to the transition from strength control to fracture control
Huang, X. Wang, et al. (2025)	Mode I; compacted clay	NSCB	Confirmed geometry and initial crack sensitivity in compacted clay fracture measurements
Aliha, Iranmanesh, et al. (2026)	Mode I; additive stabilized clay	Disc type geometry	Coupled direct fracture metrics with material modification
Aliha and Haghighatpour (2022)	Mixed Mode I/II; compacted soil material	Asymmetric SCB	Demonstrated relevance of mixed-mode testing for friction sensitive and mixed Mode-I conditions

Continued on next page

Table 2.9 continued.

Study	Mode and material	Specimen or test type	Principal contribution
Huang, X. Li, W. Yu, et al. (2023), Huang, X. Li, T. Zhao, et al. (2026), and Lv, J. Wang, Ling, et al. (2026)	Mixed Mode I/II; compacted clay	NDB with fixed supports	Demonstrated boundary friction sensitivity of apparent fracture response

Note: SECB/SENB = single edge cracked/notched beam; NSCB = notched semicircular bend; NDB = notched deep beam; SCB = semicircular bend; DIC = digital image correlation.

The literature supports two closely related conclusions. First, there is no fixed specimen shape for laboratory fracture characterization of clayey soils. Second, the field still lacks a universally accepted soil-specific geometry correction factor for Mode-I SENB/SECB fracture toughness. Borrowed correction functions and empirical crack-to-width ratio limits remain useful, but they are still geometry-specific and state-specific rather than universally adopted soil standards (Huang, X. Wang, et al., 2025; Lv, J. Wang, Huang, et al., 2024; J.-J. Wang, Huang, and J.-F. Hu, 2016; J. Wang, Huang, et al., 2020; J. Wang, Lv, et al., 2023).

2.7 Hydromechanical coupling, hydraulic conductivity change, and hydraulic fracture

Hydraulic fracturing, ice lensing, and desiccation-induced discontinuity formation all involve coupled interaction between the pore fluid and the soil skeleton, and all may produce localized tensile openings. They should not, however, be treated as the same process.

Hydraulic fracturing is driven by positive fluid pressure acting within a flaw, interface, or weak zone relative to the surrounding confinement and fracture resistance. The pressurized fluid may reduce the stress carried by the soil skeleton and, where it enters an open discontinuity, may also apply traction to the discontinuity faces. Propagation is therefore controlled by fluid pressure, confinement, geometry, and fracture resistance.

Ice lensing is driven by freezing and cryosuction. Water migrates from unfrozen soil toward a freezing front, where segregated ice accumulates and displaces the soil skeleton. The resulting

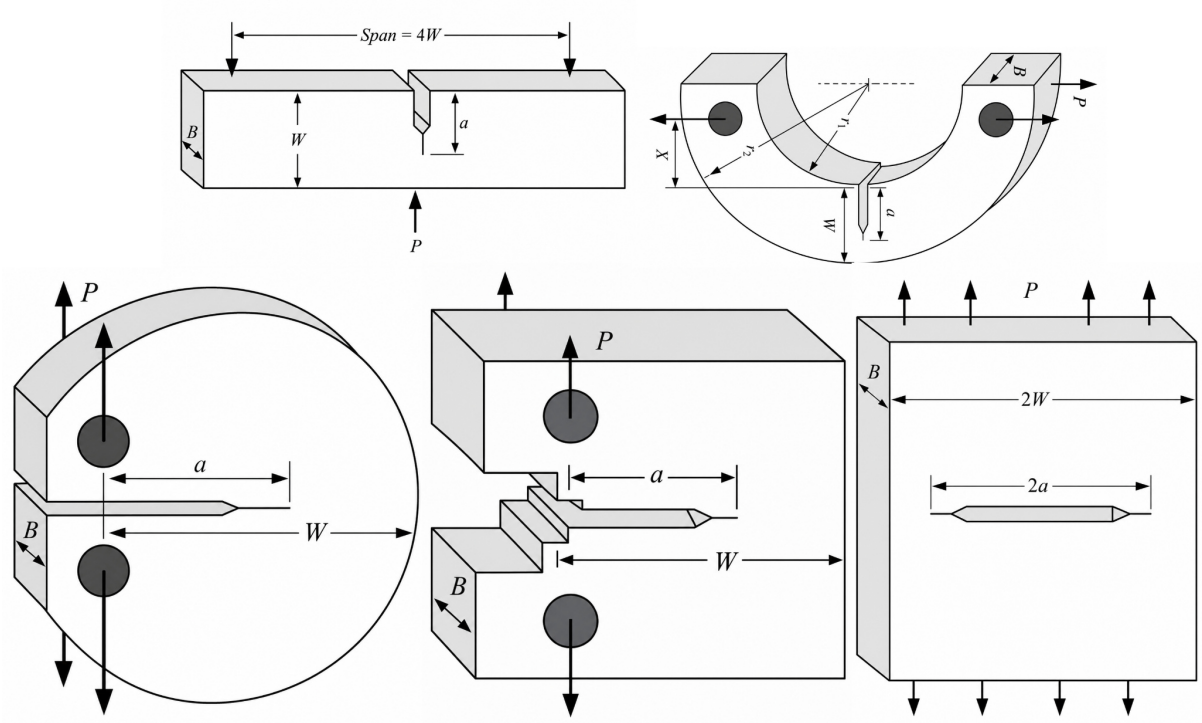


Figure 2.3: Different shapes and configurations of Mode-I and mixed-mode notched geometries (**ASTM1983**; Alqahtani, Starr, and Khan, 2024).

lens may separate or heave the soil, but its growth requires phase change, thermal gradients, and continued water supply. Ice-lens growth is therefore not equivalent to Mode-I propagation of a pre-existing flaw under positive fluid pressure.

Desiccation-induced discontinuity formation is driven by evaporation and drying. Increasing matric suction produces shrinkage of the soil skeleton. If this shrinkage is restrained by the base, adjacent soil, non-uniform drying, or material heterogeneity, tensile stress develops and an open-mode discontinuity may form. Unlike hydraulic fracturing, the driving hydraulic variable is increasing suction rather than positive fluid pressure. Unlike ice lensing, there is no freezing phase change or segregated-ice growth.

The three processes share tensile localization, fluid–solid interaction, and the potential to create preferential pathways. Their stress paths, hydraulic variables, thermal requirements, and propagation mechanisms are nevertheless different and require different constitutive and boundary-condition descriptions. The hydromechanical importance of clay fracture begins with suction. For unsaturated clay,

$$s = u_{\mathrm{a}} - u_{\mathrm{w}} \tag{2.20}$$

Table 2.10: Strengths and limitations of common soil fracture-test geometries.

Geometry	Main advantage	Main limitation	Typical use
SENB/SECB	Simple bending setup, clear notch, and direct compatibility with $f(a/W)$ reductions	Boundary effects, notch quality, and process zone size can bias the calculated K_{Ic}	Compacted clays and cohesive soils
SCB/NSCB	Compatible with cylindrical or semicircular specimens and mixed-mode loading	Curved geometry and support friction require careful reduction	Clays, rocks, and cemented soils
Compact tension	Promotes direct crack opening and stable crack growth	Gripping and specimen preparation are difficult for soft or fragile soils	Stronger or stabilized geomaterials
Ring test	Allows tensile cracking to develop in compacted cohesive rings	Data reduction and stress field are less standardized than beam tests	Compacted cohesive soils under restraint.
Plate/bending tests	More representative of thin clay layers, covers, and restrained bending	Crack path, suction, and boundary restraint are difficult to control independently	Desiccation and liner bending studies

Note: SENB/SECB = single edge notched/cracked beam; SCB/NSCB = semicircular/notched semicircular bend; $f(a/W)$ = SENB geometry correction function.

where u_{a} and u_{w} are pore air and pore water pressures. A convenient saturation measure is the effective degree of saturation,

$$S_{\mathrm{e}} = \frac{\theta - \theta_{\mathrm{r}}}{\theta_{\mathrm{s}} - \theta_{\mathrm{r}}} \tag{2.21}$$

where θ is volumetric water content, θ_{r} is residual volumetric water content, and θ_{s} is saturated volumetric water content. A Bishop-type effective stress expression can be written as

$$\boldsymbol{\sigma}' = (\boldsymbol{\sigma} - u_{\mathrm{a}}\mathbf{I}) + \chi(S_{\mathrm{e}})(u_{\mathrm{a}} - u_{\mathrm{w}})\mathbf{I} \tag{2.22}$$

where χ is a saturation dependent parameter (Bishop, 1959; D. G. Fredlund and Rahardjo, 1993). Equation 2.22 matters because fracture resistance in clay is not state-free; it evolves with suction, density, and water retention.

Desiccation cracking is best interpreted as a suction-contraction process. A convenient

Table 2.11: Geometry correction frameworks reported for fracture toughness calculation in soil and clay studies.

Geometry family	Representative correction or reduction	How fracture toughness is obtained	Key implication for clayey soils
SENB/SECB beam	$K_{\mathrm{I}} = PSf(a/W)/(BW^{3/2})$	Fracture load substituted into beam geometry function	Widely used baseline, but clay results remain sensitive to crack ratio and size
NSCB	$K_{\mathrm{I}} = PY_{\mathrm{I}}/(BR^{1/2})$	Fracture load combined with semicircular geometry factor	Attractive alternative, but not yet universally standardized for clay
Notched deep beam	Geometry correction factor embedded in NDB reduction	Fracture load interpreted with size effect analysis	Useful for identifying strength to fracture transition
Compact tension	Compact specimen energetic or stress intensity reduction	Load and crack geometry converted to G_{c} or K_{Ic}	Less common in soils because specimen preparation is difficult
Ring test	Ring specific energetic evaluation	Crack driving inferred from ring restraint and load response	Useful when nonlinear fracture is emphasized
Cylinder/disc type tests	Geometry specific crack length or diameter reduction	Load and specimen dimensions converted to fracture parameters	Valuable for modifiers and alternative preparation routes

Table 2.12: Minimum reporting checklist for Mode-I fracture testing of clayey soils.

Item to report	Why it is necessary
Clay mineralogy, plasticity index, and grain size distribution	Fracture response is not transferable without mineralogical and consistency context
Initial water content, dry density, void ratio, and compaction route	These are first-order state variables for K_{Ic}, G_{f}, tensile strength, and shrinkage response
Suction or moisture conditioning method	Specimens with identical water content may have different suction histories and crack driving potential
Specimen dimensions, notch ratio, thickness, and span/support geometry	Geometry correction and size effect interpretation require complete dimensional reporting
Notch making procedure and observed notch tip quality	Notch sharpness and disturbance can alter apparent initiation behaviour
Boundary condition details including support friction	Particularly important for NDB, disc, and mixed-mode tests
Loading mode, displacement rate, and control protocol	Rate effects and post-peak stability depend on the loading algorithm
Measurement system	Determines whether local crack evolution, fracture process zone length, and softening can be interpreted credibly
Reduction method used to compute fracture parameters	LEFM, cohesive law, inverse analysis, and J-integral procedures are not directly equivalent
Post-test documentation of crack path and failure mode	Necessary to confirm that the intended fracture mode is achieved

shrinkage measure is

$$\varepsilon_{\mathrm{sh}} = \frac{V_0 - V}{V_0} \tag{2.23}$$

where V_0 and V are initial and current volumes. Hydraulic aperture is not required to calculate the initial tensile localization caused by desiccation. Desiccation-induced discontinuity formation is governed by drying, shrinkage, restraint, and fracture resistance. Hydraulic aperture is introduced only after a discontinuity has formed, because the residual or reopened aperture controls the subsequent serviceability consequence, including preferential flow, infiltration, and equivalent hydraulic conductivity. For a restrained layer, only part of the free shrinkage strain can develop,

and an effective restrained tensile stress may be written as

$$\sigma_{\mathrm{res}}(t) \approx E_{\mathrm{eff}}(s, \rho_{\mathrm{d}})\, \varepsilon_{\mathrm{sh}}^{\mathrm{r}}(t) \tag{2.24}$$

where $\varepsilon_{\mathrm{sh}}^{\mathrm{r}}$ is the restrained component of shrinkage strain and E_{eff} is a state-dependent secant stiffness. A direct fracture-based crack initiation check follows:

$$K_{\mathrm{I}}^{\mathrm{res}} = Y_{\mathrm{I}} \sigma_{\mathrm{res}} \sqrt{\pi a_0} \qquad K_{\mathrm{I}}^{\mathrm{res}} \geq K_{\mathrm{Ic}} \tag{2.25}$$

where a_0 is an initial flaw size. This connects desiccation mechanics to Mode-I fracture rather than treating cracking as a purely descriptive surface phenomenon.

Matrix flow can be described by Darcy's law,

$$\mathbf{q}_{\mathrm{m}} = -k_{\mathrm{m}} \nabla h \tag{2.26}$$

where $\mathbf{q}_{\mathrm{m}}$ is Darcy flux, k_{m} is matrix hydraulic conductivity, and h is hydraulic head. Once a crack opens, the fracture pathway may be approximated by the cubic-law form

$$k_{\mathrm{f}} = \frac{\rho_{\mathrm{w}} g b^2}{12 \mu} \tag{2.27}$$

where ρ_{w} is water density, g is gravitational acceleration, μ is dynamic viscosity, and b is crack aperture (Snow, 1969). If a cracked clay mass is idealized as a matrix plus approximately parallel cracks with characteristic spacing λ, an equivalent hydraulic conductivity can be written as

$$k_{\mathrm{eq}} \approx k_{\mathrm{m}} + \frac{\rho_{\mathrm{w}} g}{12 \mu} \frac{b^3}{\lambda} \tag{2.28}$$

This equation clarifies why small crack volumes can produce large hydraulic penalties: the conductivity contribution scales with aperture cubed.

Because swelling and wetting can partly close cracks, a normalized hydraulic recovery index is useful:

$$H_k = 1 - \frac{k_{\mathrm{healed}} - k_{\mathrm{intact}}}{k_{\mathrm{cracked}} - k_{\mathrm{intact}}} \tag{2.29}$$

A value of $H_k = 0$ implies no hydraulic recovery, and $H_k = 1$ implies recovery to the intact state. The index also makes clear that visual closure is not equivalent to full hydraulic restoration.

For coupled hydraulic loading, a Biot-type effective stress is

$$\boldsymbol{\sigma}' = \boldsymbol{\sigma} - \alpha p \mathbf{I} \tag{2.30}$$

where α is the Biot coefficient and p is pore pressure (Biot, 1941; Coussy, 2004). Terzaghi's effective-stress relation is sufficient for the classical saturated-soil condition in which the solid mineral grains are treated as effectively incompressible and the Biot coefficient is approximately equal to one. Biot's relation is a more general poromechanical form for a compressible porous skeleton in which α may differ from one. It is included here as theoretical background rather than as an implemented constitutive relation. The Chapter 3 SENB experiments and contour-integral simulations did not apply a pore-pressure boundary and were interpreted using a total-stress, linear-elastic formulation. In the Chapter 4 LEM–PNM calculations, the mechanical solution generated discontinuity opening and the hydraulic network subsequently used that opening to calculate pressure and flow. The calculated hydraulic pressure was not returned to the mechanical equilibrium equation through a Biot effective-stress update. Therefore, the present implementation is a sequential one-way mechanical-fracture-to-flow model, rather than a fully two-way Biot-coupled formulation. Fluid pressure can influence discontinuity growth through two related effects. First, pore pressure changes the stress carried by the porous soil skeleton. Second, where fluid occupies an open discontinuity, it may apply traction directly to the discontinuity faces. These effects must be introduced consistently within one poromechanical and fracture boundary-value formulation to avoid double counting the same pressure contribution. A fracture criterion can therefore be written as

$$K_{\mathrm{I}}^{\mathrm{tot}} = K_{\mathrm{I}}^{\mathrm{mech}} + K_{\mathrm{I}}^{p} \qquad K_{\mathrm{I}}^{\mathrm{tot}} \geq K_{\mathrm{Ic}} \tag{2.31}$$

or, in energy form,

$$G_{\mathrm{tot}} = G_{\mathrm{mech}} + G_{\mathrm{fluid}} \geq G_{\mathrm{c}} \tag{2.32}$$

These relations are included as conceptual background for a pressurized discontinuity. Pressure acting on the discontinuity faces was not applied in the Chapter 3 SENB models or in the current one-way LEM–PNM mechanical calculation.

Wetting-induced closure or hydraulic recovery and hydraulic-fracture initiation are distinct processes with different driving mechanisms and constitutive requirements. Closure and hydraulic recovery may involve swelling, reduction of suction gradients, particle rearrangement, residual contact, and reduction of discontinuity aperture. Hydraulic fracture is driven by fluid pressure relative to the surrounding confinement and fracture resistance and may cause a discontinuity to initiate or extend. The two processes may occur during different stages of the service life of the same barrier, but they should not be treated as equivalent processes or as opposite branches of one constitutive mechanism.

Equation 2.29 is retained as a literature-based hydraulic-recovery index. Hydraulic recovery was not measured in the present experimental programme. Similarly, pressure-driven hydraulic-fracture initiation was not simulated in the mechanical calculations. These topics are therefore

Table 2.13: Equation to design meaning for the hydromechanical fracture framework.

Equation	Meaning	Design relevance for clayey soils
Eq. 2.20	Matric suction	Governs shrinkage driving force and state dependence of fracture resistance
Eq. 2.22	Unsaturated effective stress	Connects suction state to stress transfer in drying clay
Eq. 2.23	Volumetric shrinkage strain	Measures the contraction source of desiccation cracking
Eq. 2.24	Restrained tensile stress	Converts shrinkage mismatch into crack driving stress
Eq. 2.25	Desiccation fracture check	Connects restrained shrinkage directly to flaw growth
Eq. 2.27	Crack hydraulic conductivity	Explains why small apertures can dominate flow
Eq. 2.28	Equivalent cracked-medium conductivity	Connects crack aperture and spacing to barrier serviceability
Eq. 2.29	Hydraulic recovery index	Quantifies hydraulic recovery after wetting; not evaluated experimentally in this study
Eq. 2.30-2.32	Conceptual pressure-driven discontinuity extension	Provides conceptual background for pressure-driven extension; not implemented in the present mechanical models

included as relevant extensions of the design problem rather than as processes validated in the present work.

2.8 Material modification for fracture resistant clay barriers

Material modification offers a promising approach to enhance crack resistance, but it should be considered a multi-property challenge. Fibers help bridge cracks, boost post-peak resistance, and spread tensile strain. Bio-polymers can change bond formation, suction behaviour, and crack patterns. Nanomaterials can influence interparticle contacts, pore structure, and possibly affect contaminant interactions. However, an additive that raises fracture toughness but also increases

hydraulic conductivity or compressibility might not improve overall barrier performance.

The literature shows three recurring mechanisms. First, discrete reinforcement such as fibers can transfer tensile load across an opening crack, reduce crack width, and increase energy dissipation (Z. Rizvi et al., 2022; C.-S. Tang, Shi, et al., 2012). Second, cementation or biopolymer bonding can increase apparent stiffness and fracture resistance, but durability, hydration state, and environmental compatibility must be examined (Bai et al., 2025; Barani and Barfar, 2021; B. Zhang, Hallett, and G. Zhang, 2008). Third, nanoparticles and mineral modifiers can influence pore structure and leaching or self-healing processes, but their effects must be measured across fracture, flow, strength, and consolidation (Aliha, Iranmanesh, et al., 2026; Mazaheri et al., 2021; Tao et al., 2023).

The literature on additives should be reviewed with caution. Some materials help hide visible desiccation cracks by enhancing tensile bridging or altering the shrinkage pattern, but they may also impact hydraulic conductivity or compressibility. Fibers can span cracks and distribute strain, yet excessive fiber content can create preferred interfaces or pose challenges during compaction. Biopolymers can bind particles and make the material more ductile, but their long-term performance and reaction to wetting and drying cycles need further validation. Nanomaterials like nano-silica, nano-clay, zinc oxide-T (Tetrapod), and alumina may improve bonding or refine pore structures, but their effects should be evaluated alongside hydraulic conductivity and consolidation tests (Abdi, Parsapajouh, and Arjomand, 2008; Barani and Barfar, 2021; Mazaheri et al., 2021; Miller and Rifai, 2004; Ziegler et al., 1998). For clay barriers, an additive is useful only if it improves crack resistance without compromising low permeability, compactability, strength, and volume-change behaviour.

For the present study, nanomaterial improvement is part of a barrier performance framework. The relevant question is whether Al_2O_3, SiO_2, ZnO-T, Glassfiber or related mineral additives can improve fracture toughness while preserving low hydraulic conductivity and acceptable strength and compressibility. The correct comparison is not additive versus no additive on K_{Ic} alone; it is additive performance in the coupled K_{Ic}-k-a_v space.

2.9 Fracture capable constitutive models and numerical methods

Experimental studies show that crack initiation and growth in clay soils depend on factors like geometry, water content, density, and the size of the fracture process zone. Numerical research explores which modelling approaches can accurately replicate this sequence under boundary conditions relevant to barrier systems. This study examines four common numerical methods for

Table 2.14: Additive families in clay fracture studies and the current state of evidence.

Additive family	Dominant mechanism	Common output metrics	Main unresolved issue
Synthetic or natural fibers	Crack bridging, load redistribution, delayed localization	Crack factor, permeability, deformation, and selected fracture metrics (Abdi, Parsapajouh, and Arjomand, 2008; Z. Rizvi et al., 2022; Ziegler et al., 1998)	Need for common Mode-I benchmarking and clearer post-peak comparison
Biopolymers	Bond enhancement and moisture sensitive matrix stiffening	Load-displacement response, crack morphology, permeability, and selected fracture metrics (Bai et al., 2025; Barani and Barfar, 2021; B. Zhang, Hallett, and G. Zhang, 2008)	Strong promise, but inconsistent geometry and state definitions across studies
Nanomaterials	Densification, aperture reduction, and self-healing enhancement	Crack maps, conductivity, self-healing, and selected fracture metrics (Aliha, Iranmanesh, et al., 2026; Mazaheri et al., 2021; Tao et al., 2023)	Direct fracture toughness evidence under standardized SENB/SECB conditions remains limited
Hybrid systems	Combined bridging and densification	Mixed crack, strength, and permeability metrics (Aliha, Iranmanesh, et al., 2026; Tao et al., 2023)	Mechanistic attribution remains difficult due to the strong variability in protocols

crack propagation: the extended finite element method (XFEM), the space-time finite element method, phase field modelling, and the lattice element method (LEM).

Understanding the historical evolution of numerical fracture methods is crucial because each was designed to overcome specific limitations of classical FEM. Standard displacement-based FEM effectively simulates the continuum before cracking, but once a displacement discontinuity occurs, the crack path must either follow element boundaries, require remeshing, or be depicted as damage. Cohesive zone models incorporate traction-separation laws to model process zones in fractures. XFEM employs enrichment functions that enable sharp cracks to pass through elements. Space-time FEM manages transient, evolving domains within a unified framework. Phase field modelling treats cracks as diffuse damage zones controlled by an energy functional, while lattice approaches simulate fracture through progressive bond failure in a discrete, heterogeneous network. These methods are not interchangeable, and their appropriateness depends on whether the focus is on crack initiation, path, branching, aperture, hydraulic connectivity, computational cost, or calibration to soil properties.

2.9.1 Classical yield models and why crack capable extensions are required

Classical geotechnical models describe distributed yielding, hardening, softening, and stress path dependence. They remain essential for strength and deformation analysis, but they do not include crack length, crack-driving energy, fracture process zone size, or a hydraulic aperture law. The Mohr-Coulomb shear criterion,

$$\tau_f = c' + \sigma'_{\mathrm{n}} \tan \phi' \tag{2.33}$$

identifies a shear-failure stress state through effective cohesion c' and friction angle ϕ'. A tensile cutoff may be appended as

$$\sigma'_1 = f_{\mathrm{t}} \tag{2.34}$$

but this only marks tensile onset; it does not determine whether a flaw arrests or propagates. Critical state models, such as Modified Cam Clay, add volumetric hardening through

$$\frac{q^2}{M^2} + p'(p' - p'_c) = 0 \tag{2.35}$$

where p' is mean effective stress, q is deviatoric stress, M is the critical-state slope, and p'_c is preconsolidation pressure. Unsaturated extensions incorporate suction dependence, but they still model failure through yielding rather than through an evolving discontinuity. Therefore, discontinuity-sensitive clay barrier analysis requires a fracture capable layer on top of conventional constitutive modelling.

The simplest continuum damage representation is

$$\boldsymbol{\sigma} = (1 - D)\mathbf{C}_0 : \boldsymbol{\varepsilon} \tag{2.36}$$

where D is a scalar degradation variable. Because purely local damage can become mesh-dependent, a gradient or nonlocal enhancement is usually required:

$$\bar{\kappa} - \ell_{\mathrm{g}}^2 \nabla^2 \bar{\kappa} = \kappa \tag{2.37}$$

where κ is a local history variable, $\bar{\kappa}$ is its regularized counterpart, and ℓ_{g} is an internal length. Damage-plasticity may be written as

$$\boldsymbol{\sigma} = (1 - D)\mathbf{C}_0 : (\boldsymbol{\varepsilon} - \boldsymbol{\varepsilon}^{\mathrm{p}}) \qquad \dot{\boldsymbol{\varepsilon}}^{\mathrm{p}} = \dot{\lambda} \frac{\partial g}{\partial \boldsymbol{\sigma}} \tag{2.38}$$

where g is the plastic potential and $\dot{\lambda}$ is the plastic multiplier. These regularized continuum models improve objectivity but still require a fracture interpretation to connect softening, crack opening, aperture, and hydraulic response.

Cohesive zone models provide the historical bridge between continuum damage and discrete crack growth. Originating from the Dugdale-Barenblatt cohesive crack concept and later adopted in quasibrittle fracture, they represent the fracture process zone by a traction-separation law (Barenblatt, 1962; Dugdale, 1960). A Mode-I cohesive law may be written as

$$T_{\mathrm{n}} = T_{\mathrm{n}}(\delta_{\mathrm{n}}) \qquad G_{\mathrm{f}} = \int_0^{\delta_{\mathrm{c}}} T_{\mathrm{n}}(\delta_{\mathrm{n}})\, \mathrm{d}\delta_{\mathrm{n}} \tag{2.39}$$

where T_{n} is normal traction and δ_{n} is normal separation. Cohesive laws are useful for compacted clay because the fracture process zone can be large, but the method is most reliable when the crack path or interface is known. For unknown crack paths in clay barriers, additional path selection or remeshing strategies are needed.

2.9.2 Hydro-mechanical field equations required by any predictive crack model

A numerical method for clay barrier fracture must satisfy mechanical equilibrium and hydraulic continuity. A general small strain coupled formulation contains the momentum balance

$$\nabla \cdot \boldsymbol{\sigma} + \mathbf{b} = 0 \tag{2.40}$$

fluid mass balance

$$\dot{\zeta} + \nabla \cdot \mathbf{q} = 0 \tag{2.41}$$

and Darcy-type flow

$$\mathbf{q} = -\frac{k(d, s, b)}{\mu} \nabla p \tag{2.42}$$

where ζ is fluid storage, $\mathbf{q}$ is fluid flux, p is pore pressure, μ is fluid viscosity, and $k(d, s, b)$ is an evolving conductivity affected by damage d, suction s, and crack aperture b. This form makes the coupled problem explicit. A crack model that only reproduces a plausible fracture pattern but does not update hydraulic connectivity is inadequate for barrier design. On the other hand, a hydraulic model that relies on a prescribed crack without confirming crack initiation and growth is not a predictive fracture model.

2.9.3 Extended finite element method (XFEM)

XFEM emerged to overcome the remeshing burden of conventional FEM when cracks propagate through a continuum mesh. The method enriches the displacement approximation with discontinuity and crack-tip functions, following the partition-of-unity concept developed for discontinuities and crack growth (**Moes1999XFEM**; Belytschko and Black, 1999; Moës, Dolbow, and Belytschko, 1999). A generic approximation is

$$\mathbf{u}(\mathbf{x}) = \sum_{i \in I} N_i(\mathbf{x}) \mathbf{u}_i + \sum_{j \in H} N_j(\mathbf{x}) H(\mathbf{x}) \mathbf{a}_j + \sum_{k \in F} N_k(\mathbf{x}) \sum_{\alpha=1}^{4} F_\alpha(\mathbf{x}) \mathbf{b}_k^\alpha \tag{2.43}$$

where N_i are shape functions, $H(\mathbf{x})$ is a jump enrichment, and $F_\alpha(\mathbf{x})$ are crack tip enrichment functions. Historically, this was a major advancement because the crack could pass through elements without conforming to element edges.

For clay barriers, XFEM has three important advantages. First, it maintains a sharp crack representation, which is compatible with LEFM quantities such as $K_{\mathrm{I}}$and K_{Ic}. Second, it avoids repeated remeshing, which is useful when comparing several SENB geometries. Third, it can be implemented in commercial finite element environments, making it attractive for engineering studies. Its limitations are equally important: crack initiation must be prescribed or governed by a separate damage criterion; crack branching and merging are more difficult than in phase-field formulations; and hydraulic aperture must be supplied via an additional crack-flow model. In clayey soils, XFEM therefore gives a strong validation tool for sharp cracks, but not a complete fracture-hydraulic design framework by itself (J.-J. Xu, C.-S. Tang, Q. Cheng, Q.-l. Xu, et al., 2022).

2.9.4 Space-time finite element method (STFEM)

STFEM developed from transient finite element formulations in which space and time are discretized together rather than through a sequence of spatial problems (Hughes and Hulbert, 1988). A space-time slab is written as $Q_n = \Omega \times [t_n, t_{n+1}]$, and a generic weak statement is

$$\int_{Q_n} \delta\varepsilon : \boldsymbol{\sigma}(\mathbf{u}, d)\, \mathrm{d}Q + \int_{Q_n} \rho\, \delta\mathbf{u} \cdot \dot{\mathbf{u}}\, \mathrm{d}Q - \int_{Q_n} \delta\mathbf{u} \cdot \mathbf{b}\, \mathrm{d}Q - \int_{P_n} \delta\mathbf{u} \cdot \bar{\mathbf{t}}\, \mathrm{d}P = 0 \tag{2.44}$$

where P_n denotes the traction boundary in space-time. The historical motivation was not only crack modelling; it was accurate treatment of moving boundaries, evolving domains, and transient transport. This makes the method conceptually attractive for fracture in unsaturated or pressurized clay, where pore-pressure evolution, wetting, drying, and crack growth are time-dependent.

This study highlights the strength of the STFEM in integrating evolving crack geometry, loading history, and hydraulic transients within a unified, time-continuous framework. Its main limitation is practicality, as the formulation demands significant computational resources, making it less suitable for routine geotechnical workflows and not yet well-validated for crack initiation and propagation in clayey soils. Therefore, its comparative role is to determine if the added space-time consistency offers a measurable advantage over conventional enriched or regularized methods, based on SENB fracture data and crack-path observations.

2.9.5 Phase-field modelling

Phase-field fracture developed from the variational interpretation of brittle fracture, where crack growth is obtained by minimizing a total energy functional rather than tracking a sharp crack explicitly (Ambati, Gerasimov, and De Lorenzis, 2015; Bourdin, Francfort, and Marigo, 2008; Francfort and Marigo, 1998). The sharp crack is replaced by a diffused damage variable $d \in [0, 1]$ and a regularization length ℓ:

$$\Pi(\mathbf{u}, d) = \int_\Omega \left[g(d)\psi^+(\varepsilon) + \psi^-(\varepsilon) + G_\mathrm{c} \left(\frac{d^2}{2\ell} + \frac{\ell}{2} |\nabla d|^2 \right) \right] \mathrm{d}\Omega - W_\mathrm{ext} \tag{2.45}$$

where $g(d)$ degrades the tensile part of elastic energy, ψ^+ and ψ^- are tensile and compressive energy components, and G_c is the critical fracture energy.

The main advantage of phase-field modelling is topological freedom. Crack initiation, curving, branching, and coalescence can emerge without a dedicated crack propagation algorithm. This is valuable for desiccation cracking, where multiple cracks nucleate and interact. The main limitation

is calibration. The length scale ℓ, tensile-compressive split, degradation function, and $G_c$must be tied to measurable soil properties; otherwise, the computed crack pattern may be visually convincing but not predictive. For clay barriers, phase-field modelling also needs a defensible translation between diffuse damage and hydraulic aperture. Without that translation, it cannot directly predict crack-controlled hydraulic conductivity (Cajuhi et al., 2024).

2.9.6 Lattice element method (LEM)

Lattice models have a long history in heterogeneous quasibrittle materials because they replace the continuum with a network of bonds or elements that can fail progressively. In this framework, disorder is not added after the solution; it is part of the discretization. This feature is important for compacted clay, where fabric, particle arrangement, moisture distribution, and weak planes are inherently heterogeneous (Grassl and Bolander, 2016; Schlangen and Garboczi, 1997). The discrete equilibrium equation is

$$\mathbf{K}(\mathcal{B})\mathbf{u} = \mathbf{f} \tag{2.46}$$

where $\mathbf{K}$ is assembled from the active bond set $\mathcal{B}$. Bond failure changes the active network and therefore changes stiffness and connectivity. The lattice strain energy may be written as

$$\Pi_{\text{lat}} = \sum_{e=1}^{N_e} \frac{1}{2} k_e \delta_e^2 \qquad \delta_e = \mathbf{n}_e \cdot (\mathbf{u}_j - \mathbf{u}_i) \tag{2.47}$$

where k_e is bond stiffness and δ_e is bond extension. A simple failure criterion is

$$\sigma_e \geq f_{\text{t},e} \tag{2.48}$$

and the local strength can be assigned through a random field, for example

$$f_{\text{t},e} = \bar{f}_{\text{t}}[-\ln(1-\xi_e)]^{1/m} \qquad 0 < \xi_e < 1 \tag{2.49}$$

where m is the Weibull modulus and ξ_e is a uniform random variable.

LEM is especially beneficial when the crack path, branching, and hydraulic connectivity are more critical than a smooth stress field. It models mechanical bond failure using a connected network of connected discontinuities, which can be linked to flow channels or pore-network models. However, it has limitations: bond stiffness and strength require calibration, lattice resolution influences crack roughness, and equivalent continuum properties must be derived for design-scale applications.

Table 2.15: Historical development and role of the numerical fracture methods used in this study.

Method	Historical motivation	Main fracture capability	Main limitation for clay barriers
Cohesive-zone FEM	Dugdale-Barenblatt cohesive cracks and quasibrittle cohesive models (Barenblatt, 1962; Dugdale, 1960; Hillerborg, Modeer, and Petersson, 1976).	Represents fracture process zone softening through a traction-separation law.	Crack path and cohesive law must be known or calibrated
XFEM	Enrichment of FEM to avoid remeshing for cracks crossing elements (Belytschko and Black, 1999; Moës, Dolbow, and Belytschko, 1999).	Represents sharp discontinuities and crack-tip fields within a fixed mesh.	Needs separate initiation, propagation, and hydraulic-aperture rules
STFEM	Unified treatment of transient moving-boundary and evolving-domain problems (Hughes and Hulbert, 1988; Tezduyar, Behr, and Liou, 1992).	Represents crack evolution and time-dependent fields in one space-time slab.	High computational cost and limited clay specific benchmarking
Phase-field	Variational fracture regularized by a diffused crack field (Bourdin, Francfort, and Marigo, 2008; Francfort and Marigo, 1998; Miehe, Hofacker, and Welschinger, 2010).	Captures initiation, branching, and coalescence without explicit tracking.	Length scale, G_c, and hydraulic aperture require calibration
LEM	Discrete representation of heterogeneous quasibrittle materials (Grassl and Bolander, 2016; Schlangen and Garboczi, 1997).	Captures local disorder, bond failure, crack coalescence, and network connectivity.	Requires bond to continuum calibration and scale checks

Note: The four numerical methods evaluated in this study are XFEM, STFEM, phase-field modelling, and LEM; cohesive-zone FEM is included as historical and constitutive background.

Table 2.16: Comparison of candidate crack propagation methods for clay barrier modelling.

Method	Crack topology	Required calibration	Strongest use in this study	Limitation to check before coupled modelling
XFEM	Sharp crack	Initiation criterion, propagation law, crack tip or cohesive parameters	Independent sharp-crack benchmark against SENB response.	Hydraulic aperture and branching are not automatic.
STFEM	Sharp or regularized evolving domain	Time-dependent material response, fracture evolution law, boundary history	Transient benchmark for evolving crack paths.	Computational effort may exceed the benefit for routine design.
Phase-field	Diffuse crack	G_c, ℓ, degradation law, tension-compression split	Topology benchmark for branching or multiple cracks.	Diffuse damage must be converted into a physical aperture.
LEM	Discrete bond network	Bond stiffness, bond strength, randomness, continuum equivalent properties	Crack path, coalescence, and connectivity benchmark.	Calibration and mesh/lattice scale must be controlled.

Note: "Crack topology" describes how easily the method represents changes in crack path, branching, and coalescence.

2.9.7 Method comparison before coupled modelling

The clay barrier problem is not solved by choosing the most sophisticated numerical method. It is solved by choosing the method that best reproduces the measured fracture response while minimizing physically meaningful error, and then extending that method to hydraulic coupling. The validation sequence should therefore compare XFEM, STFEM, phase-field modelling, and

Table 2.17: Numerical studies and modelling approaches relevant to crack initiation and propagation in clayey soils.

Approach	Source	Contribution to cracks in clay modelling
FLAC-type continuum modelling	(J. Kodikara and Choi, 2006; J. Kodikara, Nahlawi, and Bouazza, 2004; Nahlawi and J. Kodikara, 2006)	Simulated curling behaviour during desiccation and highlighted the role of boundary restraint
Finite element modelling	(Pouya et al., 2019)	Treated crack propagation in unsaturated porous bodies and linked deformation to moisture state
Discrete element modelling	(Sima, Jiang, and C. B. Zhou, 2013; Sima, Jiang, and C. B. Zhou, 2014)	Examined layer thickness, base interface, micromechanical parameters, and soil-water characteristic behaviour
Mesh-fragmentation FEM	(Sánchez, Manzoli, and Guimarães, 2014)	Simulated three-dimensional crack patterns and cracking behaviour in drying soils
Distinct lattice spring models	(Y. L. Gui and Z. Y. Zhao, 2015)	Investigated particle size, heterogeneity, and boundary effects on crack initiation and patterning
Discrete element approaches	(Peron et al., 2009a; Peron et al., 2009b)	Predicted crack occurrence time and crack patterns under drying conditions
Cohesive crack methods	(Amarasiri and J. K. Kodikara, 2013)	Related measured fracture properties to desiccation crack evolution in clay
UDEC fracture mechanics	(Y. Gui et al., 2016)	Modelled Mode-I cracking and fracture properties of propagating cracks
Particle discretization FEM	(Hirobe and Oguni, 2017)	Provided seamless deformation-fracture analysis for pattern formation

LEM against the same experimental references: load-CMOD response, peak load, crack path, corrected K_{Ic}, and the soil-specific $f(a/W)$.
Only after this comparison should the best performing method be used for coupled fracture-hydro-mechanical modelling.

The validation target can be written as a multi-output inverse problem,

$$\begin{aligned}\mathcal{E}_{\text{frac}}(\boldsymbol{\theta}) = {} & w_1 \left\| P^{\text{exp}} - P^{\text{num}}(\boldsymbol{\theta}) \right\|_2^2 \\ & + w_2 \left\| \text{CMOD}^{\text{exp}} - \text{CMOD}^{\text{num}}(\boldsymbol{\theta}) \right\|_2^2 \\ & + w_3 \left\| a^{\text{exp}} - a^{\text{num}}(\boldsymbol{\theta}) \right\|_2^2 \\ & + w_4 \left\| K_{\text{Ic}}^{\text{exp}} - K_{\text{Ic}}^{\text{num}}(\boldsymbol{\theta}) \right\|_2^2 \\ \boldsymbol{\theta}^* = {} & \arg\min_{\boldsymbol{\theta}} \mathcal{E}_{\text{frac}}(\boldsymbol{\theta})\end{aligned} \tag{2.50}$$

where $\boldsymbol{\theta}$ is the method-specific parameter vector. If hydraulic data are available, the objective should be extended as

$$\begin{aligned}\mathcal{E}_{\text{CFHM}} = {} & \mathcal{E}_{\text{frac}} \\ & + w_5 \left\| k^{\text{exp}} - k^{\text{num}} \right\|_2^2 \\ & + w_6 \left\| b^{\text{obs}} - b^{\text{num}} \right\|_2^2\end{aligned} \tag{2.51}$$

where $\mathcal{E}_{\text{frac}}$ is the fracture error in Eq. 2.50, k is hydraulic conductivity, and b is crack aperture. This formulation is important because a method can reproduce a crack visually while failing to predict hydraulic connectivity. For barrier design, the accepted method must reproduce both the mechanical crack and its hydraulic consequence.

This study, therefore, treats numerical modelling as a staged decision. First, the soil-specific $f(a/W)$ from Chapter 3 converts SENB peak loads into corrected K_{Ic} values. Second, the four numerical methods are compared against the same corrected experimental fracture response. Third, the method with the strongest agreement in crack path, K_{Ic}, and aperture/connectivity is extended to coupled fracture-hydro-mechanical modelling in Chapter 4.

The central numerical conclusion is that no method is universally superior in the abstract. XFEM is strongest for sharp-crack benchmarks, STFEM is strongest for transient evolving domains, phase-field modelling is strongest for complex topology, and LEM is strongest for heterogeneity and network connectivity. For clay barrier design, the decisive criterion is not the elegance of the formulation but validation against soil-specific experiments and the ability to incorporate the validated crack into a hydraulic model. That is why method comparison is required before coupled fracture-hydro-mechanical modelling.

Table 2.18: Validation pathway from numerical crack comparison to coupled fracture-hydro-mechanical modelling.

Stage	Quantity checked	Why is it required?	Consequence for Chapter 4
1	Geometry and $f(a/W)$	Ensures the laboratory and numerical SENB reductions use the same crack-to-width ratio and span assumptions	Prevents comparison of uncorrected or nonequivalent toughness values
2	Load-CMOD and peak load	Checks global stiffness, compliance, and fracture onset	Screens methods that match peak load but not deformation response
3	Crack path and propagation sequence	Checks whether the crack initiates at the notch and follows the observed trajectory	Removes methods that give plausible strength but incorrect fracture topology
4	Corrected K_{Ic}	Compares numerical fracture resistance with the experimentally reduced value	Identifies the most accurate method for Mode-I clay fracture
5	Aperture, connectivity, and k	Connects mechanical cracking to hydraulic consequence	Provides the basis for coupled fracture-hydro-mechanical barrier modelling

2.10 Hydraulic conductivity, fracture toughness, and compressibility as coupled metrics

A fracture based barrier design cannot rely on a single property. Hydraulic conductivity k quantifies matrix flow under specified conditions. Fracture toughness K_{Ic} quantifies resistance to crack extension under a specified mode and geometry. Coefficient of compressibility a_{v} or related consolidation parameters quantify the change in void ratio with effective stress. These properties are linked through fabric, void ratio, dry density, water content, suction, and microstructure.

A clay with very low hydraulic conductivity may still be unsuitable if it has low fracture toughness. Clay with high fracture toughness may be unsuitable if the sand content or additive dosage increases hydraulic conductivity beyond acceptable limits. A material modification that

reduces compressibility but creates brittle crack paths may also be undesirable. The relevant design space is therefore multiobjective: low k, adequate K_{Ic}, controlled compressibility, acceptable strength, and stable behaviour under wetting, drying, loading, and chemical exposure.

The soil-specific correction factor must therefore be linked to measured elastic parameters, density, water content, and specimen dimensions. A general correction may be useful for screening, but soil-specific coefficients are required for standardization. This is one of the central gaps in the soil fracture literature.

Table 2.19: Proposed staged fracture-based design workflow for discontinuity-sensitive clay barrier system.

Stage	Design task	Practical interpretation
1	Identify the dominant crack driving mechanism	Distinguish desiccation, restrained shrinkage, bending, stress relief, or hydraulic pressurization
2	Characterize the material state	Treat water content, density, suction, and preparation route as part of the design specification
3	Choose a laboratory baseline geometry	Use SENB/SECB as the simplest baseline for comparability, supplemented where needed by NSCB, NDB, or plate bending
4	Check size effect and notch sensitivity	Avoid promoting a value to design status before size and crack-ratio effects are understood
5	Connect fracture to serviceability	Translate crack development into permeability, leakance, preferential flow, or continuity loss
6	Calibrate a numerical model	Select the modelling framework by the crack process of interest, not by software preference
7	Preserve classical checks	Fracture based design supplements, rather than replacing, global stability and deformation checks

2.11 Research gaps

The literature supports the need for fracture based clay barrier design and also shows why the framework must be built carefully. The following gaps exist in the literature.

Table 2.20: Standardization roadmap for Mode-I fracture characterization of clayey soils.

Stage	Priority action	Why is it necessary?
I	Establish benchmark clays and benchmark states	Prevent every study from becoming a unique material specific case
II	Run cross-geometry matrices on the same materials	Quantify comparability among SENB/SECB, NSCB, NDB, and service specific bending protocols
III	Couple fracture testing to hydraulic consequence measurement	Connect fracture metrics to permeability and serviceability rather than to force-displacement alone
IV	Publish open full field benchmark datasets	Enable rigorous cross-validation of numerical crack propagation models
V	Adopt a provisional baseline standard	SENB/SECB remains the strongest candidate baseline because it is simple, historically dominant, and experimentally accessible

Table 2.21: Research gaps in fracture based design of clay barriers.

Gap	Evidence from literature	Required development
Mode-I standardization	Studies use SENB, SCB, ring, plate, and notched geometries with different preparation and reduction methods (Amarasiri, Costa, and J. K. Kodikara, 2011; Harison, Hardin, and Mahboub, 1994; J.-J. Wang, J.-G. Zhu, et al., 2007)	A reproducible Mode-I testing protocol for clay-rich soils
Soil-specific $f(a/W)$	Metallic and brittle material functions are often borrowed, although soil process zones and low stiffness change apparent response	Analytical and numerical derivation calibrated to soil properties
Specimen scaling	Size effect, crack limits, and process-zone effects are documented in compacted clay fracture tests (Huang, X. Wang, et al., 2025; Lv, J. Wang, Huang, et al., 2024; J.-J. Wang, Huang, and J.-F. Hu, 2016; J. Wang, Lv, et al., 2023)	Standard specimen dimensions with minimized boundary effects

Gap	Evidence from literature	Required development
Hydraulic consequence of cracking	Desiccation and hydraulic studies show increased conductivity and preferential flow after cracking (Julina and Thyagaraj, 2020; Omidi, Thomas, and Brown, 1996; Rayhani, Yanful, and Fakher, 2007)	Coupled interpretation of K_{Ic}, k, and compressibility
Material modification	Fibers, biopolymers, and nanomaterials show promise but are often evaluated by isolated properties (Barani and Barfar, 2021; Mazaheri et al., 2021; Z. Rizvi et al., 2022)	Multiproperty assessment using fracture, flow, strength, and consolidation metrics
Numerical validation	Advanced methods exist, but clay specific validation of crack path, aperture, and flow remains limited (C. Hu et al., 2020)	Method comparison against laboratory data and coupled barrier response
Design adoption	Conventional practice standardizes index, compaction, hydraulic, and strength checks, not fracture checks	A fracture based design layer compatible with existing geotechnical procedures

2.12 Summary of literature review

The literature demonstrates that clay barriers can lose their function through cracking before reaching global strength failure. LEFM provides a stress intensity framework, but soils require a quasibrittle, state-dependent interpretation because water content, suction, density, process zone size, and geometry strongly affect measured fracture resistance. Mode I is the baseline mode for clay barriers because crack opening creates hydraulic aperture. SENB testing is a practical foundation, but soil-specific standardization and $f(a/W)$ validation remain unresolved.

Hydromechanical studies show that cracks alter hydraulic conductivity, suction redistribution, preferential flow, and healing. Material modification studies show that fibers, biopolymers, and nanomaterials can improve crack resistance, but the effect must be judged together with hydraulic conductivity, strength, and consolidation. Numerical modelling provides a route from laboratory fracture parameters to barrier scale prediction, but XFEM, STFEM, phase-field modelling, and LEM each require calibration and validation against soil-specific fracture data. These findings

justify the present study framework that links Mode-I testing, geometry correction, material modification, hydraulic conductivity, compressibility, and numerical crack propagation.

Chapter 3

Experimental Investigation for Fracture Based Clay Barrier Design

As established in Chapter 1, the first requirement for a clay barrier is low hydraulic conductivity, which is the conventional basis for compacted clay liners and contaminant-barrier systems (Daniel and Y.-K. Wu, 1993; Malusis and Shackelford, 2002; Rowe, 2005). A compacted clay barrier is selected because its intact matrix can restrict leachate migration, but this condition is meaningful only if the soil matrix remains hydraulically continuous. When a connected tensile crack forms, the controlling transport path shifts from soil matrix flow through small pores to preferential flow through the open discontinuity. The design problem is therefore not only to obtain a low hydraulic conductivity, k, in an intact specimen, but to select and compact a soil that also resists crack initiation under tensile opening. This chapter develops the experimental basis for that fracture based extension of clay barrier design.

The chapter is organized around six connected contributions. First, the soils are selected and characterized using the conventional geotechnical properties required for barrier evaluation. Second, the elastic properties required for fracture calculations are measured from unconfined compression tests. Third, a dedicated displacement controlled single edge notched beam (SENB) apparatus and mould system are developed for low-strength compacted clay specimens. Fourth, a soil-specific SENB geometry correction function, $f(a/W)$, is derived through numerical, analytical, and experimental routes. Fifth, the measured Mode I fracture toughness, K_{Ic}, is interpreted with respect to crack geometry, specimen scale, water content, dry density, and field-soil fabric. Finally, fracture toughness is coupled with hydraulic conductivity and compressibility through the proposed K_{Ic}-k-a_{v} interrelationship for clay barrier screening.

3.1 Experimental programme

The experimental programme is designed to answer a single mechanics question, following the SENB based soil fracture logic developed in previous compacted-clay studies (**Wang2007**; **Amarasiri2011**; **Wang2020**; **Qiao2023**): under what material state and specimen geometry can the Mode I fracture toughness of a compacted clay barrier be measured as a reproducible engineering property? This required more than running SENB tests. It required a sequence in which soil selection, compaction state, elastic characterization, geometry calibration, crack-opening measurement, and hydraulic compressibility interpretation were consistently controlled. Table 3.1 summarizes this design sequence.

Table 3.1 also explains the order of the chapter. The soil property tests are presented first because the material must satisfy the conventional clay barrier requirements before fracture resistance becomes meaningful. The laboratory test setup and representative load-CMOD response are then presented before $f(a/W)$ because the validity of K_{Ic} depends on stable crack initiation and direct crack mouth measurement. The $f(a/W)$ section follows as an independent development: numerical, analytical, and experimental methods are used for the same SENB geometry family. The corrected K_{Ic} results are then interpreted in terms of geometry, water content, dry density, hydraulic conductivity, and compressibility. This sequence prevents a common error in soil fracture testing, namely, using a peak load from an unverified specimen geometry as if it were already a material property.

The factorial structure in Table 3.1 is important because the objective is not simply to report one fracture toughness value for one soil. The programme separates three types of uncertainty that are usually mixed together in soil fracture tests. The first is material-state uncertainty, controlled by water content, dry density, and soil family. The second is geometry uncertainty, controlled through specimen size, thickness, and notch ratio. The third is interpretation uncertainty, which is controlled by deriving $f(a/W)$ from three independent routes. This structure allows a poor result to be traced to its physical origin: hydraulic unsuitability, inadequate crack resistance, unstable specimen geometry, or measurement scatter.

The experimental design also provides an internal validation sequence. Conventional soil tests establish whether the material is a plausible barrier soil. Unconfined Compression Strength (UCS) tests provide the elastic constants required for numerical and analytical fracture solutions. The SENB apparatus then tests whether the selected geometries produce stable crack initiation from the notch. Only after these checks is K_{Ic} interpreted as a material response. This order is essential in compacted soils because apparent fracture toughness can be artificially increased by blunt notches, large fracture process zones, support indentation, or uncontrolled moisture redistribution.

Matric suction was neither directly measured nor independently controlled in the present

Table 3.1: Experimental design matrix linking soil selection, geometry calibration, SENB testing, and coupled hydraulic compressibility interpretation used to establish a reproducible fracture testing sequence.

Control block	Levels or measurements	Purpose in Chapter 3
Soil family	LS_0, LS_{15}, LS_{25}, and FS	Separates clay-rich behaviour, controlled sand addition, and natural field-soil fabric
Conventional barrier state	Specific gravity, gradation, Atterberg limits, compaction curve, and hydraulic conductivity	Confirms whether each soil satisfies the conventional material basis for barrier use
Elastic input	E and ν from UCS testing	Provides consistent inputs for J-integral conversion, Abaqus® contour integrals, and analytical $f(a/W)$ derivation
SENB geometry	Specimens A-E; W = 35, 50, and 65 mm; $B = W$ and $B = 2W$ where feasible; $S = 4W$; $L = 5W$	Tests specimen-size effects and identifies a geometry that minimizes measured K_{Ic} variability
Crack-ratio domain	a/W = 0.45, 0.50, and 0.55	Checks whether corrected K_{Ic} becomes weakly dependent on notch depth within a practical range of large cracks
Fracture instrumentation	10 kN load cell, loading-point displacement gauge, and two CMOD gauges	Captures low peak loads, stable crack opening, and possible eccentricity during Mode I testing
$f(a/W)$ validation	Abaqus® contour integral, weight function derivation, and experimental compliance route	Avoids direct transfer of metallic SENB geometry factors to low stiffness compacted soils
Design interpretation	P_{max}, CMOD, K_{Ic}, k, C_r, m_v, and a_v	Links crack initiation, intact sealing, and compressibility in a single proposed design framework

Note: P_{max} = peak load, CMOD = crack mouth opening displacement, k = hydraulic conductivity, and C_r, m_v, and a_v = compressibility parameters.

experimental programme. Specimens were prepared and compared using gravimetric water content and dry density as the controlled state variables. Consequently, the measured trends include any suction-related contribution associated with the preparation state, but the separate effects of suction, degree of saturation, density, fabric, and previous wetting–drying history cannot be identified from the present data. References to suction in the interpretation of the results are therefore physically plausible interpretations rather than direct suction measurements.

3.2 Soil selection and conventional clay barrier properties

The selected soils represent a controlled progression from a clay-rich laboratory material to a naturally variable field clay. This selection follows the soil fabric basis of clay behaviour and the hydraulic-barrier design requirement that mineralogy, gradation, plasticity, and compacted fabric be interpreted together (Daniel and Y.-K. Wu, 1993; Mitchell and Soga, 2005; Rowe, 2005). The first soil, LS_0, contains 100% EPK kaolin clay and provides a repeatable clay-dominated reference. The second and third soils, LS_{15} and LS_{25}, contain 15% and 25% Ottawa sand by dry mass, respectively, and were selected to evaluate whether sand addition improves crack resistance without destroying hydraulic containment. The fourth soil, FS, is a field-clay barrier soil and therefore exhibits natural gradation, fabric, and mineralogical variability. This sequence allows the fracture response to be interpreted as a function of clay fraction, granular inclusion, compaction state, and field fabric rather than as a single isolated material result.

EPK kaolin was selected because its relatively uniform mineralogy and reproducible compaction behaviour provide a controlled laboratory reference for examining specimen geometry and sand addition. The measured numerical values should not be transferred directly to smectite-rich, bentonitic, or highly active natural clays. Clays with higher specific surface area may develop greater suction, swelling, shrinkage, physicochemical interaction, and rate dependence, while their larger plastic deformation may alter the size of the fracture-process zone and the validity of a linear-elastic initiation interpretation. The testing method may remain applicable, but the material-state conditioning, loading rate, geometry correction, and acceptance thresholds require separate calibration.

Specific gravity, particle-size distribution, Atterberg limits, standard Proctor compaction, and saturated hydraulic conductivity were measured using the relevant ASTM standards. Specific gravity is measured using ASTM D854; grain-size distribution using ASTM D6913 and ASTM D7928; liquid and plastic limits using ASTM D4318; compaction characteristics using ASTM D698; and hydraulic conductivity using ASTM D5084. Figures 3.1-3.3 and Table 3.2 provide the conventional geotechnical basis for the subsequent fracture programme.

The numerical values in Table 3.2 establish the first material design contrast. LS_0 has the lowest measured intact hydraulic conductivity, $k = 0.132 \times 10^{-9}$ m/s, but also the highest OMC, 35.89%, and the lowest maximum dry unit weight, 12.97 kN/m^3. LS_{15} and LS_{25} progressively densify the matrix, increasing maximum dry unit weight to 14.26 and 14.63 kN/m^3 while reducing OMC to 29.57% and 26.84%, respectively. The measured hydraulic conductivity increases to 1.330×10^{-9} and 6.340×10^{-9} m/s for LS_{15} and LS_{25}, respectively. FS is distinct because it combines a high dry unit weight of 17.77 kN/m^3 with a relatively low hydraulic conductivity of 0.531×10^{-9} m/s. For the tested states, FS therefore provides a more favourable measured balance than the laboratory mixtures, although the individual effects of gradation, mineralogy, density, and natural fabric were not isolated.

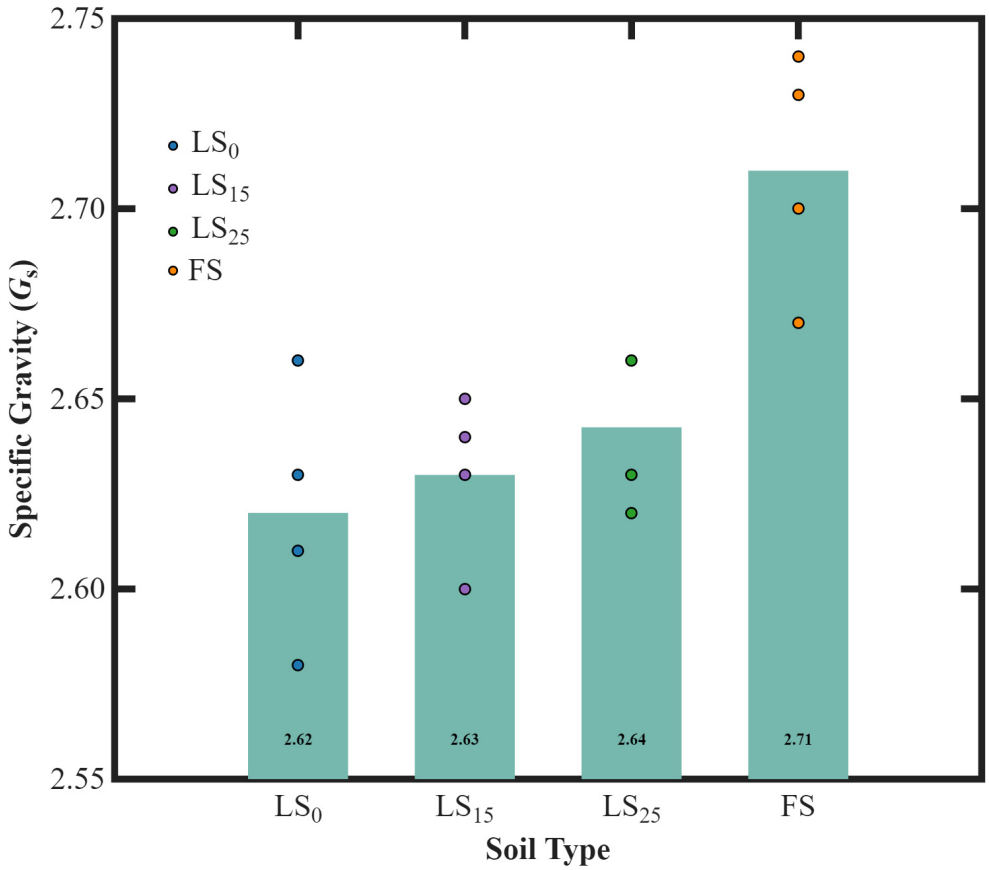


Figure 3.1: Specific gravity, G_s, of the four soils used in the experimental programme measured in accordance with ASTM D854.

Figure 3.1 provides a first indication that the materials do not only differ by plasticity. The laboratory mixtures show a narrow increase in G_s from 2.62 for LS_0 to 2.63 for LS_{15} and 2.64

for LS_{25}, whereas FS reaches 2.71. This small difference is mechanically important because void ratio and degree of saturation are calculated from G_s. The difference in specific gravity affects the calculated void ratio and degree of saturation for a given dry density and water content. Specific gravity alone does not establish a difference in particle coordination, contact continuity, or discontinuity-tip resistance, because these microstructural quantities were not measured directly.

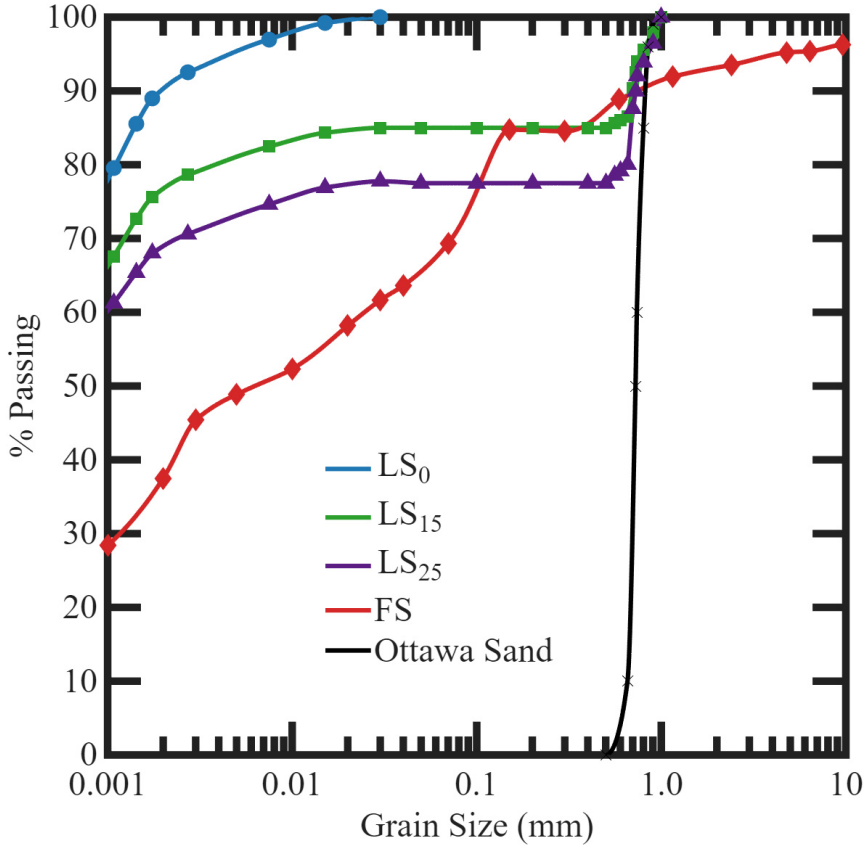


Figure 3.2: Particle-size distributions of LS_0, LS_{15}, LS_{25}, and FS determined using ASTM D6913 and ASTM D7928.

The grain-size distributions in Figure 3.2 show the progressive addition of Ottawa sand from LS_0 to LS_{15} and LS_{25}. At the selected compacted states, the first-order calculation in Appendix A gives estimated bulk sand-volume fractions of approximately 0.081 for LS_{15} and 0.138 for LS_{25}. For an illustrative sand diameter of 0.70 mm, the corresponding estimated centre spacings are approximately 1.30 and 1.09 mm, while the estimated clear surface gaps are approximately 0.60 and 0.39 mm, respectively. These estimates do not demonstrate grain-to-grain percolation or the presence of a continuous load-bearing sand skeleton. The first-order interpretation is therefore that the clay-rich matrix remains the continuous phase governing baseline hydraulic sealing and much

of the bulk matrix response, while the sand acts as dispersed inclusions that alter packing, density, local stiffness, and heterogeneity. This interpretation is not a direct microstructural observation because phase connectivity and particle contacts were not measured using computed tomography or another internal imaging method. FS has a broader natural gradation and a different fabric, but the present measurements do not isolate the contribution of each constituent to its response.

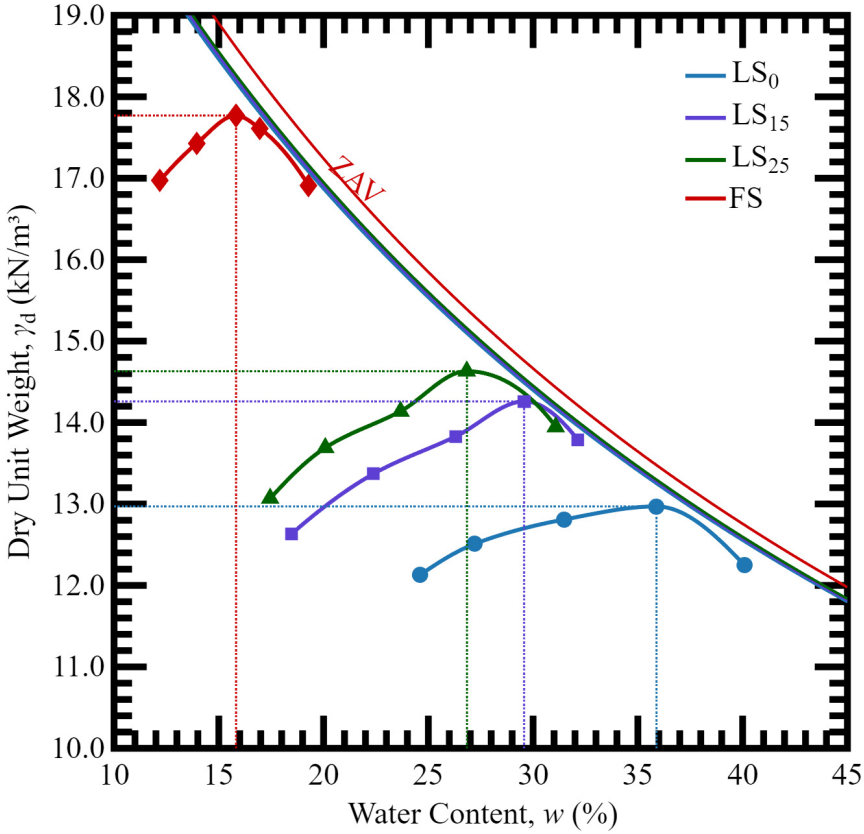


Figure 3.3: Standard Proctor compaction curves obtained in accordance with ASTM D698 and used to define the target water content and dry density states for the SENB, unconfined compression, hydraulic conductivity, and one-dimensional consolidation specimens.

Figure 3.3 shows the compaction state used in the fracture tests. The peak of the Proctor curve moves from $w_{\mathrm{OMC}} = 35.89\%$ for LS_0 to 29.57% for LS_{15} and 26.84% for LS_{25}, while FS has a much lower OMC of 15.82%. The corresponding maximum dry unit weights increase from 12.97 to 17.77 kN/m^3 across the same sequence. This trend is favourable for mechanical interlock, but it is not sufficient for barrier design because the hydraulic conductivity of LS_{25} still rises to 6.340×10^{-9} m/s.

Table 3.2 shows why a design decision based on a single property is unsafe. based on

Table 3.2: Index, compaction, and hydraulic properties of the four soils.

Property	LS_0	LS_{15}	LS_{25}	FS	Standard
Specific gravity, G_s	2.62	2.63	2.64	2.71	ASTM D854
Liquid limit (%)	68	68	68	34	
Plastic limit (%)	39	39	39	16	ASTM D4318
Plasticity index (%)	29	29	29	18	
OMC (%)	35.89	29.57	26.84	15.82	ASTM D698
$\gamma_{d,max}$ (kN/m^3)	12.97	14.26	14.63	17.77	
k (10^{-9} m/s)	0.132	1.330	6.340	0.531	ASTM D5084

Note: OMC = optimum moisture content, $\gamma_{d,max}$ = maximum dry unit weight, k = saturated hydraulic conductivity

hydraulic conductivity, LS_0 and FS are favourable because their intact k values are below 1.0×10^{-9} m/s. LS_{15} has the highest measured modulus among the laboratory mixtures, but its hydraulic conductivity is already slightly above the preliminary screening limit. This measured response is associated with the tested composition and compaction state and does not by itself prove that sand addition improved packing or formed a continuous load-bearing skeleton. LS_{25} is the most distinct example of a mixture that may look desirable from a density perspective while being poor from a containment perspective. The table, therefore, motivates the coupled interpretation adopted in this chapter: clay barrier soils must be assessed simultaneously with respect to hydraulic conductivity, fracture toughness, and compressibility.

3.3 Elastic characterization for fracture calculations

The SENB fracture calculation requires elastic properties because LEFM converts global loading into a local crack-tip intensity through the elastic stress field (**Anderson2005**; Broek, 1982; Gdoutos, 2005). The stress intensity factor is extracted numerically from the J-integral, converted through the appropriate elastic modulus, and checked analytically using weight functions. Therefore, the unconfined compression tests in this chapter are not merely strength tests; they provide the elastic input that links continuum stress-strain response to crack-tip intensity. UCS testing is carried out using ASTM D2166, and the elastic modulus is evaluated from representative tangent/secant slopes in the pre-peak range. Poisson's ratio is obtained from the corresponding lateral-to-axial strain ratio. The reported Young's modulus and Poisson's ratio are operational pre-peak properties for the stated water-content and dry-density conditions. Because matric suction was not measured,

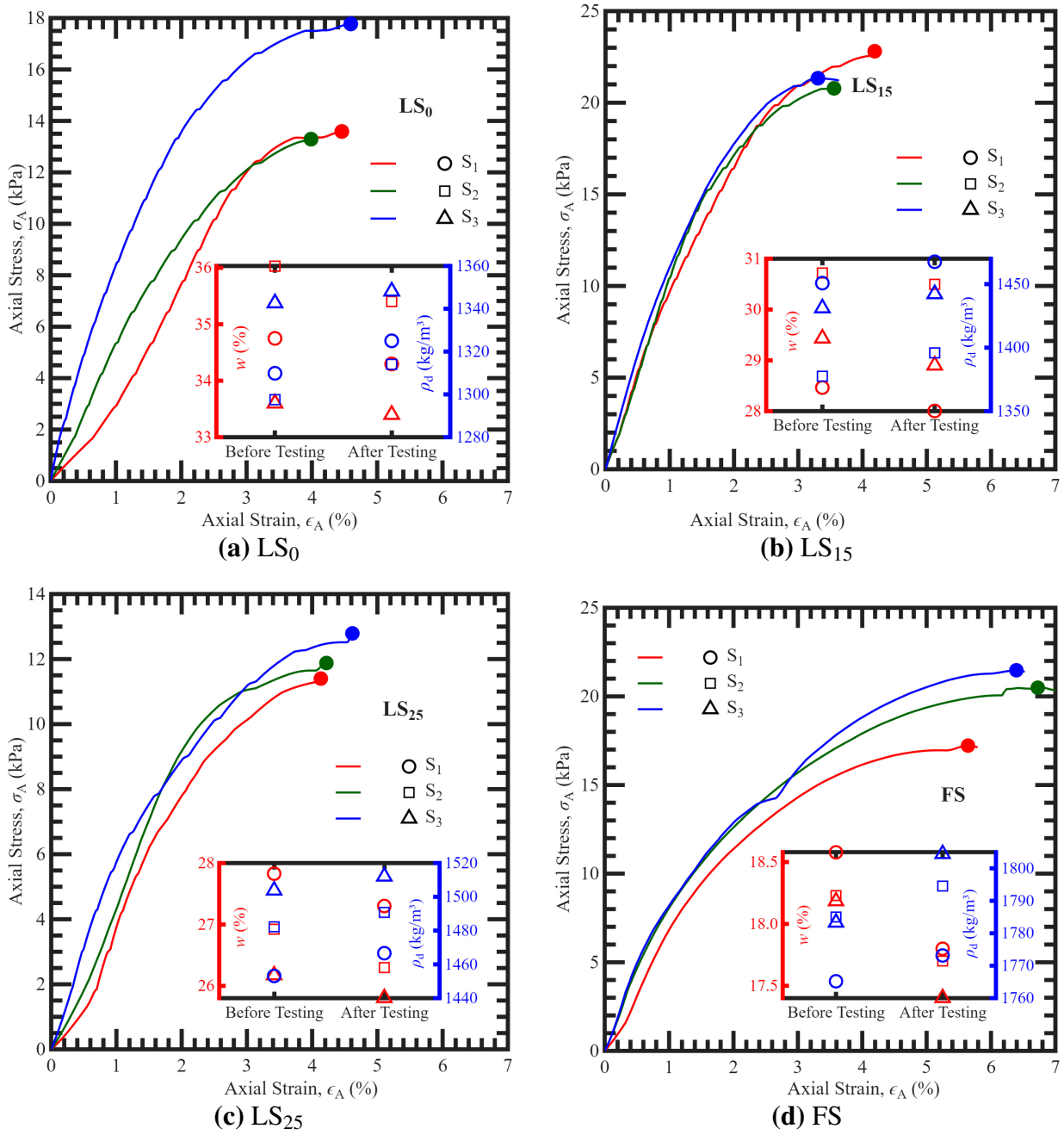
these values should not be interpreted as suction-independent elastic constants.

Table 3.3: Elastic input properties from UCS testing, used consistently in finite element modelling, analytical derivation, and experimental compliance interpretation of $f(a/W)$.

Soil	State	ρ_d (kg/m^3)	w (%)	ν	E (kPa)
LS_0	1	1315	31.58	0.322	651.6
	2	1335	33.58	0.318	445.7
	3	1355	35.58	0.315	370.9
LS_{15}	1	1425	26.58	0.270	968.1
	2	1450	28.58	""	910.5
	3	1475	30.58	""	849.4
LS_{25}	1	1476	23.83	0.240	465.7
	2	1496	25.83	""	425.4
	3	1516	27.83	0.239	358.9
FS	1	1787	17.35	0.199	667.8
	2	1797	17.55	0.197	608.3
	3	1807	17.75	""	519.6

Note: ρ_d = dry density, w = water content, ν = Poisson ratio, and E = Young's modulus used in fracture calculations.

Figure 3.4 and Table 3.3 show that the elastic response is not controlled by density alone. LS_{15} has the largest laboratory soil modulus over the wet states, decreasing from E = 968.1 to 849.4 kPa as water content increases from 26.58% to 30.58%. LS_0 decreases from 651.6 to 370.9 kPa, and LS_{25} decreases from 465.7 to 358.9 kPa despite its higher dry density. FS ranges from 519.6 to 667.8 kPa with the lowest Poisson ratio, 0.197-0.199. LS_{15} showed the highest measured modulus among the laboratory mixtures, whereas LS_{25} showed a lower modulus despite its higher dry density. The results demonstrate that the elastic response is not controlled by dry density or sand content alone. The individual contributions of particle arrangement, sand spacing, clay continuity, suction, and contact scale stiffness were not measured and therefore cannot be separated from the present UCS results. They also justify deriving a soil-specific $f(a/W)$ because a low modulus compacted beam cannot be assumed to amplify stress intensity in exactly the same way as a high modulus metallic SENB specimen.



(a) LS_0 **(b)** LS_{15} **(c)** LS_{25} **(d)** FS

Figure 3.4: Unconfined compression responses of 50 mm diameter and 100 mm height, compacted specimens tested under strain-controlled axial compression in general accordance with ASTM D2166/D2166M.

3.4 Development of the SENB laboratory test setup

A central contribution of this chapter is the development of a fracture toughness testing setup for compacted soils, because standard SENB concepts must be adapted carefully before being applied to weak and moisture sensitive geomaterials (**Anderson2005**; **Wang2007**; **Amarasiri2011**; ASTM International, 2024). The apparatus is not treated as a generic three-point bending device because the testing requirements for clayey soils differ substantially from those for metals, concrete, and intact rock. Clay specimens develop low peak loads, are sensitive to moisture disturbance, and can be damaged by demoulding, notch cutting, support indentation, and handling. A soil fracture setup must therefore resolve small loads, maintain displacement control, measure crack mouth opening directly, and produce repeatable notches without post-compaction machining.

Table 3.4 makes clear why the apparatus is part of the research outcome. A high capacity fracture machine would be mechanically safe, but it would not provide adequate resolution for compacted clay peak loads. A routine geotechnical loading frame can measure axial deformation, but it is not designed to capture two-sided crack mouth opening. The dual CMOD system is particularly important because a compacted clay beam can rotate slightly on the rollers; if only one side were measured, this rotation could be interpreted incorrectly as crack opening. Measuring both sides provides a direct check on Mode I symmetry.

The selection of the load cell is especially important for the soils in question. The expected peak loads of compacted clay beams are far below those encountered in rock, concrete, or metal fracture tests. A load cell with excessive capacity would reduce resolution near the peak and obscure the small load drops associated with crack initiation. The selected 10 kN load cell with 0.1 N readability provides sufficient mechanical capacity while retaining the resolution required to identify $P_{\max}$ precisely. Because K_{Ic} is directly proportional to $P_{\max}$, any uncertainty in the peak load propagates directly into the reported fracture toughness.

The displacement measurements serve two different purposes. The vertical gauge records the imposed displacement and confirms quasistatic loading, whereas the two CMOD gauges measure the local crack opening response that actually governs fracture interpretation. This separation is necessary because global platen displacement includes support compliance, small seating effects, and beam rotation. CMOD is a local fracture variable, so it provides a more reliable indication of crack initiation and post-peak crack opening. The two-sided CMOD arrangement also allows eccentric loading to be detected; unequal readings would indicate rotation or asymmetric contact rather than pure Mode I opening.

Table 3.4: Instrumentation and control components of the developed SENB apparatus for low load, displacement controlled Mode I testing of compacted clay barrier beams.

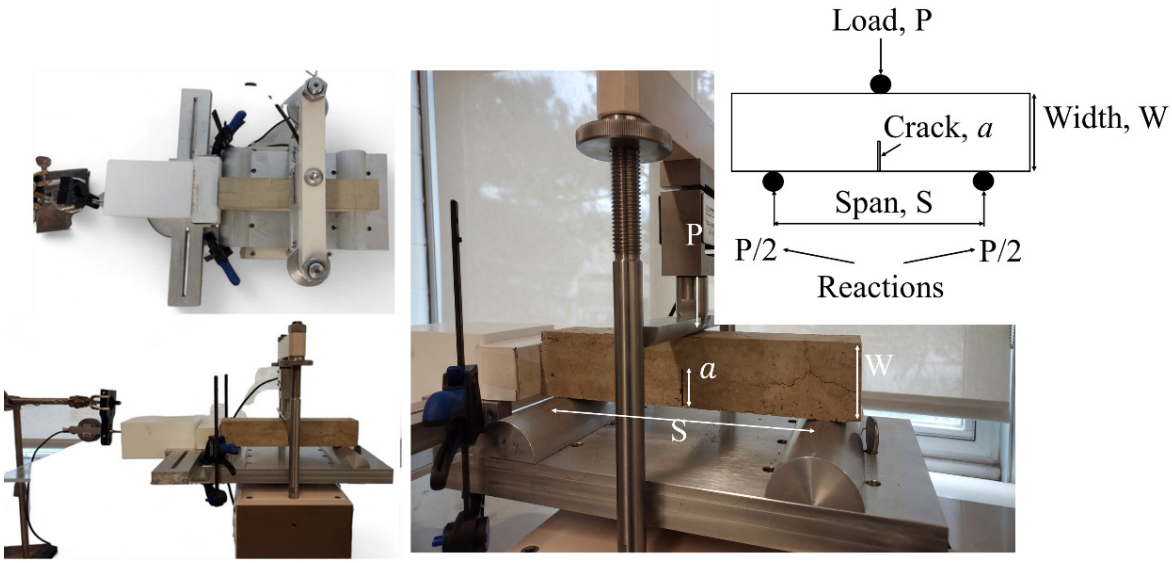
Component	Specification	Role in the fracture test
Load cell	10 kN capacity with 0.1 N readability	Measures the low peak loads of clay beams without sacrificing resolution near crack initiation.
Vertical displacement gauge	15 mm range with 0.001 mm readability	Records loading point displacement and verifies displacement controlled loading.
Two CMOD gauges	Sylvac displacement gauges, 15 mm range and 0.001 mm readability	Measure crack mouth opening on both faces and identify specimen rotation or eccentric contact.
Loading system	Quasistatic displacement controlled loading	Promotes stable crack initiation and avoids dynamic snap-through before $P_{\max}$ is reached.
Mould family	Geometrically scaled A-E moulds with notch forming inserts	Produces repeatable beams and preformed cracks without cutting or disturbing the compacted clay fabric.

Note: CMOD = crack mouth opening displacement; the two CMOD gauges were used to check symmetric Mode I crack opening.

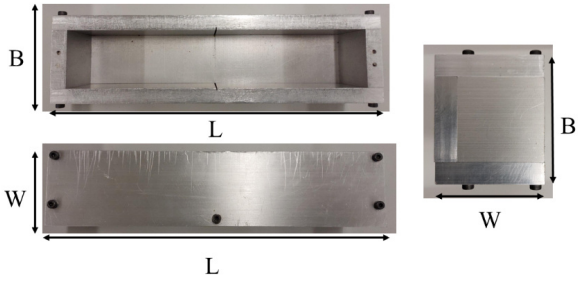
Table 3.5: SENB geometry matrix used for specimen preparation, Abaqus® contour integral extraction, analytical weight function calculation, and experimental compliance validation.

Spec.	W	B	L	S	$a_{0.45}$	$a_{0.50}$	$a_{0.55}$
A	35	35	175	140	15.75	17.50	19.25
B	""	70	""	""	""	""	""
C	50	50	250	200	22.50	25.00	27.50
D	""	100	""	""	""	""	""
E	65	65	325	260	29.25	32.50	35.75

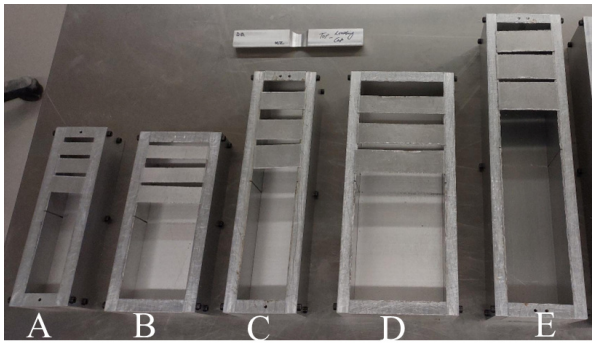
Note: all dimensions are in mm; W = specimen depth, B = thickness, L = length, S = span, and $a_{0.45} = 0.45W$, $a_{0.50} = 0.50W$, and $a_{0.55} = 0.55W$ are notch depths.



(a) Loading frame and instrumentation



(b) Notch forming mould cross-section



(c) Fabricated SENB mould family

Figure 3.5: Developed single-edge-notched-beam testing system and mould family comprising the displacement-controlled loading frame with built-in actuator, fabricated mould families A to E, with the beam supported on two 50.8 mm diameter aluminium rollers at $S/W = 4$, loaded at midspan with the notch facing downward, and tested at a constant displacement rate of $0.006\ \mathrm{mm\,s^{-1}}$

Figure 3.5 and Table 3.5 together define the developed SENB testing system. The lower supports impose the $S = 4W$ span used in finite element and analytical calculations, while the loading nose applies a mid-span force that opens the preformed notch in Mode I. The mould cross-section shows the most important preparation feature: the crack is predefined during compaction. This avoids notch smearing and reduces the risk of producing a rounded or damaged

notch tip. For clayey soils, this is not a minor practical detail. If the notch is disturbed, the measured peak load reflects local preparation damage rather than the crack resistance of the compacted soil. The mould family, therefore, forms the physical basis for repeatable fracture toughness testing.

The final SENB experimental program consisted of a balanced 5×3 factorial design with three independent replications, where specimen geometry and notch ratio were the controlled design factors. All specimens were prepared and tested near OMC and MDD, with $S/W = 4$, $L/W = 5$, a fixed loading rate, a fixed load-cell configuration, randomized test order, and valid crack propagation from the notch tip in all included tests. A larger rectangular geometry ($W = 65$ mm, $B = 130$ mm) is attempted but excluded from the factorial analysis because self-weight made valid testing impractical.

Table 3.5 is therefore more than a mould schedule. It is the common dimensional basis for the numerical, analytical, and experimental derivation of $f(a/W)$. The same W, B, L, S, and a/W values were used to construct the Abaqus® SENB models, evaluate the weight function solution, and prepare the physical beams. The chosen dimensions also respect practical geotechnical sampling constraints. Soil specimens commonly used in UCS, triaxial, hydraulic conductivity, and consolidation testing have diameters of 35-100 mm; therefore, the SENB widths of 35, 50, and 65 mm were selected to remain compatible with standard soil sampling and trimming practices. The span-to-width ratio $S/W = 4$ is retained because it produces a bending-dominated response while limiting the influence of self-weight. The total length $L = 5W$ provides sufficient overhang beyond the rollers so that the supports do not control the crack-tip field.

The excluded $W = 65$ mm, $B = 130$ mm geometry is informative rather than a failure of the programme. It shows that soil fracture testing cannot replicate metallic SENB scaling without accounting for self-weight, handling damage, and demoulding stability. A very thick, compacted clay beam may satisfy geometric similarity on paper, but the specimen can disturb itself under its own weight before a controlled fracture test begins. Excluding this geometry, therefore, strengthens, rather than weakens, the final recommendation because it distinguishes mathematically possible geometries from physically valid soil specimens.

3.4.1 Design of experiments for SENB

The geometry part of the SENB programme is treated as a formal design-of-experiments problem rather than as a sequence of isolated trial specimens. The purpose is to determine whether a compacted clay beam could be tested in a geometry that gives a stable, repeatable, and geometry-normalized Mode I response. The factor called "geometry" therefore represents the five feasible mould families A-E in Table 3.5. It is not interpreted as independent variation of W, B, and L

because these dimensions were deliberately linked through $S = 4W$ and $L = 5W$ to preserve SENB similarity.

The complete factorial matrix used two controlled factors: specimen geometry and initial crack-to-width ratio. The geometry had five levels: A-E. The notch ratio is set to three levels: $a/W = 0.45$, 0.50, and 0.55. Three independently prepared and tested specimens were used for each geometry-notch combination. For each laboratory soil with a complete matrix, this gives $5 \times 3 \times 3 = 45$ valid SENB tests. The individual beam, not the load-CMOD data point, is the experimental unit. This distinction is important because the load-CMOD points within a single test are repeated observations of the same cracking event, whereas three separately compacted beams provide true replication.

All specimens included in the factorial analysis were prepared close to the OMC-MDD condition, tested using the same load cell, CMOD instrumentation, loading rate, support arrangement, and notch-forming procedure, and accepted only when the crack propagated from the preformed notch tip. The test order is randomized to reduce time-order bias associated with specimen preparation, moisture redistribution, or operator sequence. The larger $W = 65$ mm, $B = 130$ mm rectangular specimen is considered as a sixth geometry but is excluded from statistical analysis because self-weight and handling disturbances rendered valid SENB testing impractical. This exclusion is a mechanics based feasibility decision and reinforces the need to design soil fracture specimens for both LEFM similarity and physical stability.

The primary response for geometry selection is the apparent Mode-I stress intensity factor ($K_{\mathrm{I}}^{\mathrm{app}}$), calculated from the peak load using the SENB normalization and the soil-specific geometry correction function. Peak load, $P_{\max}$, is retained as a supporting response because it verifies load cell resolution and shows whether a crack-to-width ratio change produces the expected ligament effect. The comparison is made using a blocked two-way factorial model,

$$Y_{ijk} = \mu + G_i + A_j + (GA)_{ij} + B_k + \varepsilon_{ijk} \tag{3.1}$$

where G_i is the fixed effect of SENB geometry, A_j is the fixed effect of notch ratio, $(GA)_{ij}$ is their interaction, B_k is the replicate block, and ε_{ijk} is the residual error. The block term accounts for small but unavoidable differences among independently compacted replicate sets. Since compacted clay fracture is sensitive to moisture, fabric, and crack notch, blocking is not merely a statistical luxury; it is the correct way to separate preparation scatter from genuine geometric effects (Montgomery, 2012).

Table 3.6 gives two important results. First, geometry is significant for both $K_{\mathrm{I}}^{\mathrm{app}}$ and $P_{\max}$ in all three complete soil matrices. This means the selected mould family affects the measured fracture response and cannot be treated as a trivial laboratory detail. Second, the notch ratio is significant for $P_{\max}$ but not for $K_{\mathrm{I}}^{\mathrm{app}}$ over $a/W = 0.45$-0.55. Mechanically, this is the expected outcome if the

Table 3.6: Blocked factorial DOE results for apparent fracture toughness and peak load, showing geometry significance and crack-ratio sensitivity.

Soil	Response	p_G	$p_{a/W}$	$p_{G\times a/W}$	p_{block}	p_L	p_Q
LS_0	K_I^{app}	< 0.001	0.710	0.564	< 0.001	0.488	0.659
	P_{max}	< 0.001	< 0.001	0.622	< 0.001	< 0.001	0.777
LS_{15}	K_I^{app}	< 0.001	0.237	0.845	< 0.001	0.099	0.734
	P_{max}	< 0.001	< 0.001	0.660	< 0.001	< 0.001	0.997
LS_{25}	K_I^{app}	< 0.001	0.245	0.991	< 0.001	0.097	0.948
	P_{max}	< 0.001	< 0.001	0.924	< 0.001	< 0.001	0.697

Note: G = specimen geometry, a/W = notch ratio, $G \times a/W$ = interaction, block = replication block, and L and Q = linear and quadratic crack-ratio contrasts.

SENB correction is working properly. A deeper notch reduces ligament length and therefore lowers the raw peak load; after applying the geometry normalization, the corrected fracture toughness should become much less sensitive to the notch ratio. The insignificant interaction terms for K_I^{app} also show that the a/W effect does not change strongly from one geometry to another within the tested domain.

The linear and quadratic contrasts provide a sharper interpretation of the notch-ratio response. For P_{max}, the linear contrast is significant in all soils, confirming that peak load decreases monotonically as a/W increases. The quadratic contrast is not significant, so the intermediate notch ratio $a/W = 0.50$ does not behave as an anomalous point. For K_I^{app}, neither contrast is significant, indicating that the corrected fracture toughness remains stable across the three notch ratios and can be used to select the geometry. This is the statistical expression of the fracture mechanics correction: crack length changes the raw load, but the corrected crack initiation parameter is approximately invariant over the selected a/W range.

Table 3.7 shows why specimen selection cannot be based on the highest mean fracture toughness alone. Geometry A gives the highest apparent toughness for the three laboratory soil matrices, but its scatter is substantial in LS_0 and LS_{15}. Geometry E is consistently unfavourable because it gives the lowest toughness in all three soils and high variability, which is consistent with the practical difficulty of scaling compacted soil beams to larger sizes. Geometry C does not always give the highest mean value, but it provides a balance between mechanical representativeness, manageable specimen mass, low handling disturbance, and good repeatability. For LS_0 and LS_{15}, specimen C has COV values near 12.0% or lower in the pooled ranking, and the more detailed COV analysis shows values as low as 1.0% and 0.5% at $a/W = 0.50$. This is why the $W = B = 50$ mm, $L = 250$ mm configuration is adopted as the representative geometry for subsequent material

Table 3.7: Geometry ranking for K_I^{app} using mean fracture toughness, Tukey grouping, and coefficient of variation (COV) from replicated SENB tests.

Soil	A 35×35	B 35×70	C 50×50	D 50×100	E 65×65
LS_0	0.980 A; 26.6%	0.782 B; 12.0%	0.866 A; 11.9%	0.803 B; 28.0%	0.574 C; 33.6%
LS_{15}	1.274 A; 23.1%	0.821 C; 17.0%	1.002 B; 12.2%	0.772 C; 21.3%	0.737 C; 15.5%
LS_{25}	1.294 A; 20.4%	0.882 B; 23.4%	0.569 C; 32.1%	0.476 C; 17.3%	0.403 D; 36.6%

Note: Values are mean K_I^{app} in $kPam^{0.5}$; letters indicate Tukey groups within each soil; percentages are COV.

comparison.

Figure 3.6 visualizes the same conclusion as Table 3.7. The geometric effect is not random scatter around a single universal value. Geometry A yields large apparent toughness values because the smaller beam and ligament arrangement mobilizes a higher normalized response, whereas Geometry E yields the lowest values and broad scatter. Specimen C is important because it occupies a mechanically useful middle ground: it is large enough to avoid the most severe small-specimen bias, but small enough to compact, demould, notch, align, and test without self-weight disturbance. This middle-scale behaviour is exactly what is needed for a standard soil SENB specimen. A standard geometry should not be selected because it gives the maximum apparent toughness; it should be selected because it gives a reproducible toughness that can be compared across soils, water contents, and improvement strategies.

Figure 3.7 shows why $a/W = 0.45$-0.55 is an appropriate validation window for compacted-clay SENB testing. The normalized K_I^{app} response remains close to the reference value, decreasing only from 100% at $a/W = 0.45$ to about 98% at $a/W = 0.50$ and about 94% at $a/W = 0.55$. This small reduction indicates that the corrected crack-tip parameter is not dominated by notch depth. By contrast, P_{max} decreases from 100% to about 84-85% and then to about 68-69% over the same interval, which is expected because the remaining ligament shortens and the stress-intensity amplification increases with deeper notches. The separation between nearly stable K_I^{app} and strongly decreasing P_{max} is the central DOE result: peak load is a geometry-sensitive measurement, whereas the corrected fracture toughness is a more defensible material response. The error bars also show that the scatter in K_I^{app} is small relative to the load reduction, so the three notch ratios function as a robustness check for $f(a/W)$ rather than as three separate material states.

The DOE therefore provides the statistical bridge between the physical apparatus and the

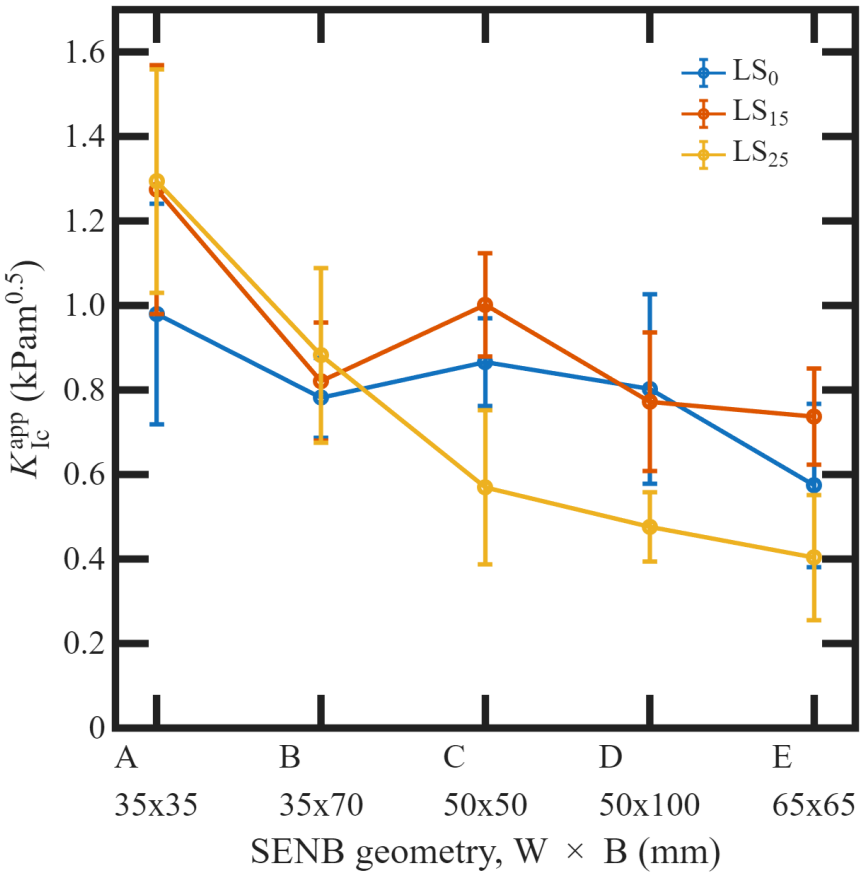


Figure 3.6: Effect of SENB geometry on the apparent Mode-I initiation toughness of LS_0, LS_{15}, and LS_{25} specimens prepared near their respective OMC and MDD states.

toughness results. Figure 3.5 demonstrates that the test can be built and instrumented; Table 3.5 defines the feasible specimen space; Tables 3.6 and 3.7 show that the specimen space has a measurable but interpretable effect; and Figures 3.6 and 3.7 show why specimen C and the selected notch-ratio range are defensible. The interpretation of K_{Ic} is therefore not an isolated calculation from peak load. It is the result of a controlled-geometry study, a verified loading system, and a replicated experimental design.

Specimens were compacted in layers to target the desired water-density state and sealed to prevent moisture redistribution prior to testing. During the test, the beam is placed on the rollers with the notch at midspan and oriented normal to the tensile face. The loading rate is selected to maintain quasi-static crack opening. Load, loading-point displacement, and the two CMOD measurements were recorded continuously. The peak load P_{max} is used as the crack-initiation load, while the CMOD response is used to check the stability and symmetry of opening. The fracture

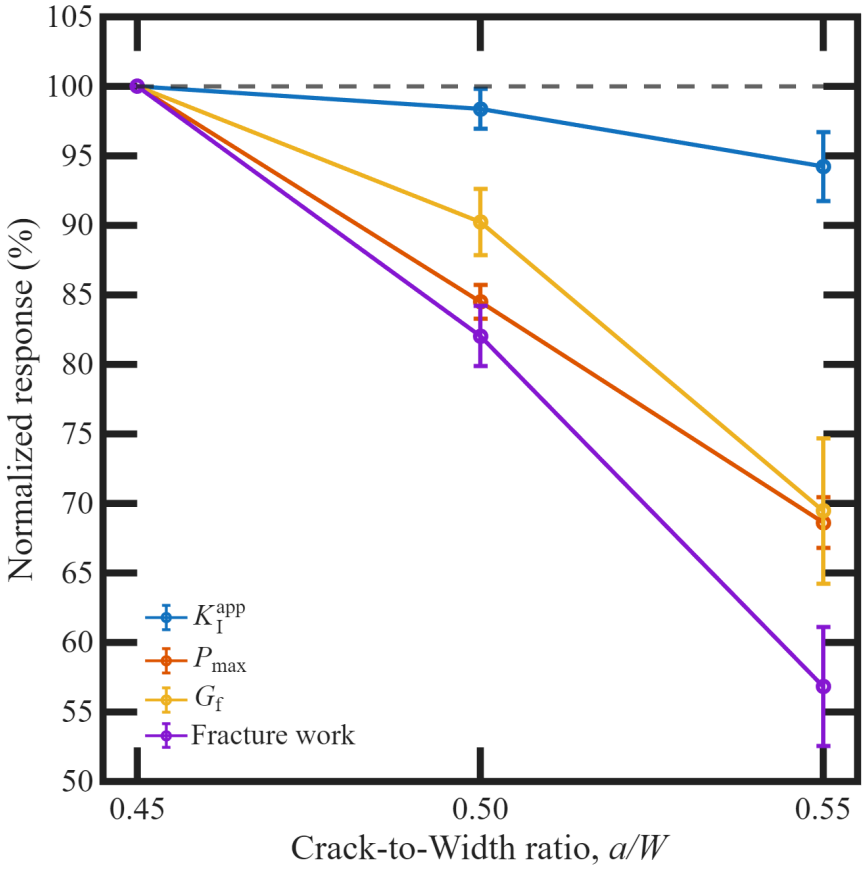


Figure 3.7: Normalized apparent Mode-I initiation toughness and peak load over $a/W = 0.45$, 0.50, and 0.55 using the $a/W = 0.45$ response as the 100% reference, with values pooled from the complete LS_0, LS_{15}, and LS_{25} SENB matrices.

toughness is then calculated only after applying the soil-specific $f(a/W)$ developed in Section 3.6.

3.5 Baseline load-CMOD response and crack morphology

The load-CMOD response must be examined before the geometry correction factor is used because P_{max} is meaningful as a crack-initiation load only when the pre-peak response remains dominantly elastic and the notch controls the crack path (**Anderson2005**; **Wang2007**; **Wang2023**). The SENB calculation assumes that the crack-initiation load is reached after a dominantly elastic loading branch and that the crack opens from the notch rather than from support crushing, eccentric bending, or distributed ductile yielding. These checks are especially important for compacted

soils, where the response can be affected by moisture, suction, local fabric, and specimen handling.

Figure 3.8 shows that the developed test setup produces interpretable crack opening responses. For the representative $W = B = 50$ mm, $L = 250$ mm, $a/W = 0.45$ geometry, the peak load increases with lower water content and higher dry density in each soil: LS_0 rises from about 2.5 to 3.1 N as ρ_d increases from 1314 to 1354 kg/m^3; LS_{15} rises from about 2.8 to 3.6 N as w decreases from 29.7% to 26.1%; LS_{25} rises from about 1.6 to 2.5 N; and FS rises from about 5.2 to 6.5 N. The field soil, therefore, carries roughly twice the peak load of LS_0 at a similar SENB geometry, which is a direct manifestation of its denser natural fabric. The post-peak branches also differ: FS and LS_{15} retain load to CMOD values close to 4 mm, whereas LS_0 and LS_{25} generally lose load over shorter opening intervals. This combination of a linear pre-peak branch and controlled post-peak softening confirms that the apparatus captures crack initiation and subsequent ligament degradation rather than only a brittle snap-through event.

The load-CMOD curves also justify why P_{max} is used as a crack-initiation quantity but not as the final design parameter. P_{max} depends on beam size, span, thickness, and notch length. Two beams made from the same soil can have different peak loads simply because their remaining ligaments differ. Therefore, P_{max} is necessary for calculating K_{Ic}, but it cannot be compared directly across geometries without applying $f(a/W)$.

The plotted values also show that P_{max} and K_{Ic} cannot be interpreted from water content alone. Under the tested water-content and dry-density conditions, LS_{15} had a higher peak load than LS_0, whereas LS_{25} did not show a further increase with additional sand. The measured response is therefore non-monotonic with sand content. The present results do not demonstrate that LS_{15} developed a continuous load-bearing sand skeleton, that clay continuity was lost in LS_{25}, or that either mixture contained a more connected pore structure. They show that changing the sand content altered the combined compaction, elastic, fracture, and hydraulic responses. The resulting design trade-off should therefore be interpreted from the measured properties rather than from an assumed contact-scale mechanism.

This interpretation is directly relevant to clay barrier design. In service, a liner or core will not fail solely because a load exceeds its compressive strength; it fails when a tensile opening localizes into a connected pathway. The load-CMOD response captures this transition more directly than a conventional unconfined compression test. It identifies the rate at which the crack mouth opens after the peak and whether the compacted fabric can continue to resist separation after crack initiation.

Figure 3.9 provides the visual check that complements Figure 3.8. The crack path starts at the notch tip and follows the tensile ligament, confirming that the moulded notch controlled the crack initiation point. The visible post-test paths were not identical among the soils. Some specimens had relatively direct paths, while some sand-containing and field-soil specimens showed greater

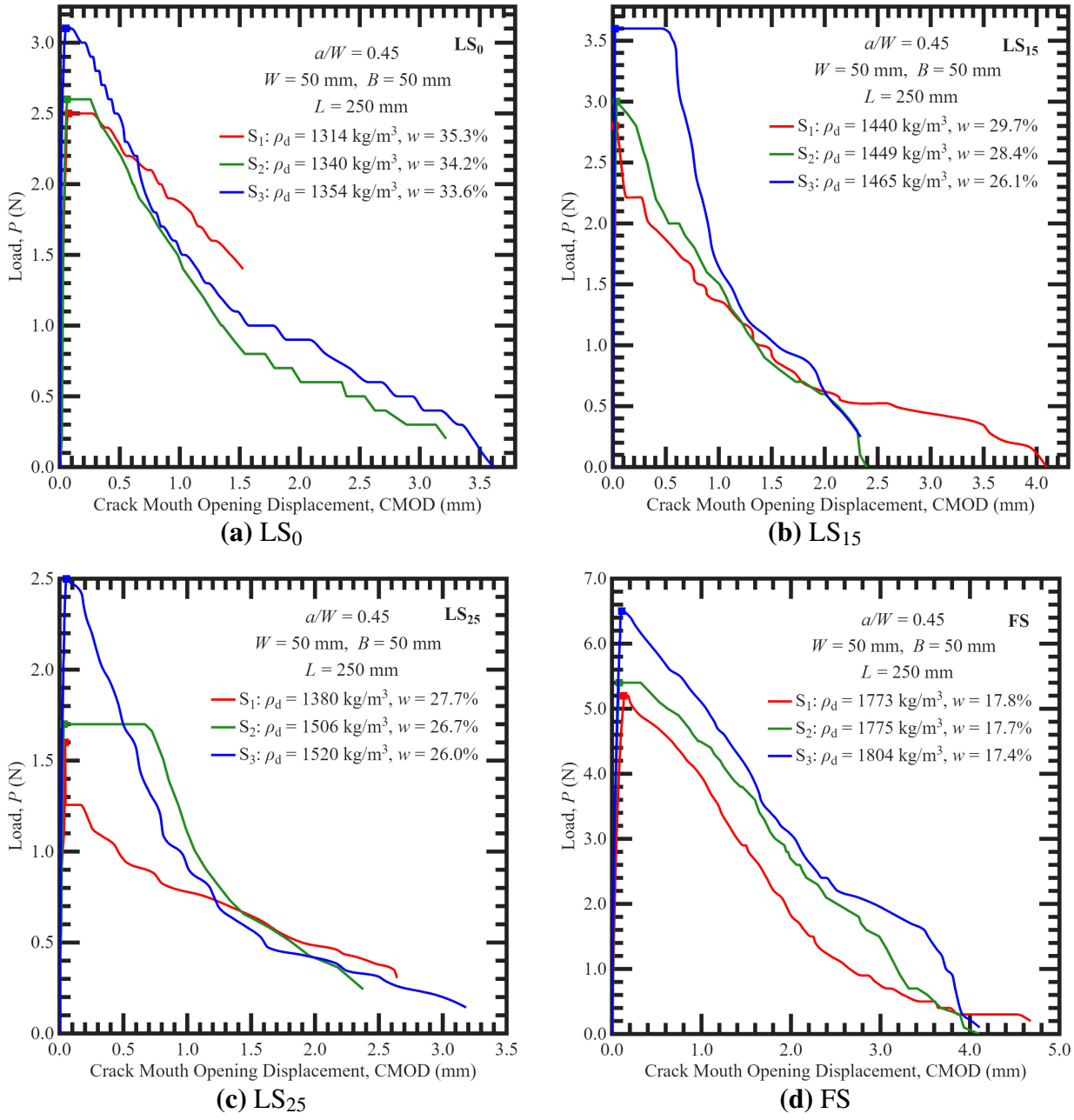


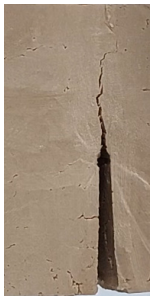
Figure 3.8: Representative load and crack-mouth-opening-displacement responses obtained using Geometry C with $W = B = 50$ mm, $L = 250$ mm, $S = 200$ mm, and $a/W = 0.45$, where CMOD was calculated as the average of measurements on the two specimen faces .



(a) LS_0



(b) LS_{15}



(c) LS_{25}



(d) FS

Figure 3.9: Post-test crack paths for all soils showing notch-controlled Mode I crack propagation and absence of visible diffuse fracture-process-zone growth.

final surface tortuosity. The photographs document these differences but do not identify the internal mechanism that caused them. The post-test photographs document the visible path but do not identify the contact-scale mechanism that produced the deviation. Particle deflection, aggregate structure, moisture distribution, and local fabric are possible contributors that require direct microstructural or full-field measurement. The present photographs do not establish why FS showed higher apparent Mode-I initiation resistance or different scatter because its internal fabric, local moisture distribution, and fracture-process-zone development were not measured directly.

The absence of a broad visible damage band should be interpreted carefully. Microscale damage is still expected ahead of the notch tip, particularly in compacted clays where interparticle debonding, suction change, and local rearrangement may accompany discontinuity advance, but these processes were not measured in the present tests. The key point is that the visible damaged region is not spread over the full ligament. The dominant crack remains localized and notch-controlled, as required for an initiation-fracture toughness interpretation. If the specimen had failed through widespread ligament crushing or distributed ductile deformation, the peak load would not represent a meaningful Mode I crack-initiation event.

3.6 Development of the SENB geometry correction function $f(a/W)$

3.6.1 Governing LEFM form

The local Mode I crack-tip stress field in LEFM is

$$\sigma_{ij}(r,\theta) = \frac{K_{\mathrm{I}}}{\sqrt{2\pi r}} F_{ij}^{\mathrm{I}}(\theta) + O(r^0) \tag{3.2}$$

where r and θ are local polar coordinates at the crack tip, and F_{ij}^{I} are universal angular functions (**Anderson2005**; Irwin, 1957; Williams, 1957). The singular term is universal, but the relation between external load and K_{I} depends on finite-body geometry. For a three-point SENB specimen,

$$K_{\mathrm{I}} = \frac{P_{\max} S}{B W^{3/2}} f(a/W) \tag{3.3}$$

where S is the span, B is the specimen thickness, W is the specimen width/depth, and a is the notch length. The purpose of the present $f(a/W)$ development is not to change LEFM; it is to calibrate the finite-body amplification factor for low-stiffness compacted soils.

The validity of Eq. (3.3) requires three checks. First, the load-CMOD response must be predominantly linear up to crack initiation, which is observed in Figure 3.8. Second, the crack must initiate from the notch and propagate in Mode I, which is confirmed in Figure 3.9. Third, the geometry function must be verified for the specimen family and elastic range used in the experiments. This third requirement is addressed using numerical, analytical, and experimental routes.

3.6.2 Numerical development using Abaqus® contour integrals

The numerical route used three-dimensional Abaqus® models of the SENB geometry, following the contour integral basis of fracture mechanics and the need to verify finite-body correction functions before applying them outside their calibration domain (ASTM-E1820, 2021; J. R. Rice, 1968; Tada, P. C. Paris, and Irwin, 1973). The specimens were modelled as homogeneous, isotropic, linearly elastic bodies using the elastic properties in Table 3.3. The loading nose and supports were represented to reproduce the three-point bending condition, the span is maintained at $S = 4W$, and the specimen length is maintained at $L = 5W$. The crack is defined explicitly from the preformed notch tip toward the top surface. The stress intensity factor is extracted using contour integrals

around the crack tip, and $f(a/W)$ is obtained by normalizing the resulting K_I using Eq. (3.3). The Chapter 3 Abaqus® analysis was a stationary-discontinuity contour integral calculation rather than a propagation simulation. The SENB beam was represented as a homogeneous, isotropic, linear elastic body using the measured values of E and ν in Table 3.3. The notch and crack front were predefined. No elastoplastic law, suction-dependent law, damage model, tensile-failure criterion, or crack-growth law was used in this stage. The purpose of the analysis was solely to calculate J, K_I, and the corresponding SENB load-to-K_I correction.

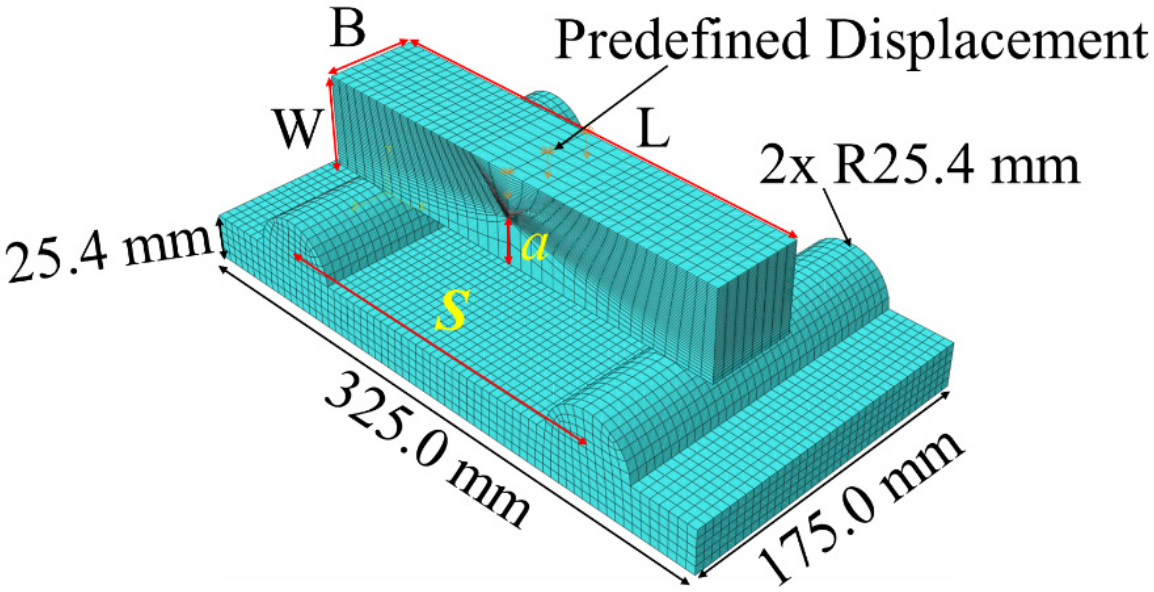


Figure 3.10: Three-dimensional Abaqus® SENB model used to extract K_I from contour integrals using the laboratory geometry matrix.

Figure 3.10 illustrates the numerical model used to convert the physical SENB problem into a crack-tip intensity calculation. Each model used the specimen dimensions and notch ratios listed in Table 3.5, so that the Abaqus® contour integral route and the laboratory SENB route were defined by the same geometry family. The contour integral method is selected because it evaluates the energy release around the crack tip and is less sensitive to local stress noise than direct stress extrapolation. The crack-tip mesh is refined sufficiently to reproduce the near-tip singularity, and multiple contours were checked for path consistency. This is important for clay specimens because their elastic moduli are low; global deformation can be large even when the crack-tip response remains within the LEFM initiation regime.

The model therefore separates two effects that are easily confused experimentally. The first is global compliance of the beam, which depends on E, ν, span, thickness, and contact

conditions. The second is crack-tip amplification, expressed by K_{I}. The geometry correction factor must account for the finite-body conversion between these two responses without absorbing material-state effects that belong in $P_{\max}$ and the measured elastic constants. This is why the same Table 3.5 dimensions are used in the FEM models, analytical integration, and laboratory beams.

Figure 3.11 gives the validation ladder for the numerical route. The aluminium benchmark is necessary because, without it, any deviation between the soil-specific function and ASTM E399 could be dismissed as a modelling error. Once the mesh reproduces a known high-modulus metallic solution, the same framework can be applied to the soil beams. The geometry-independence plot then shows that the normalized correction factor is governed primarily by a/W, not by the absolute values of W and B, provided geometric similarity is maintained. This result supports the use of a single functional form for the soil family and confirms that the SENB specimens operate within the expected LEFM scaling regime.

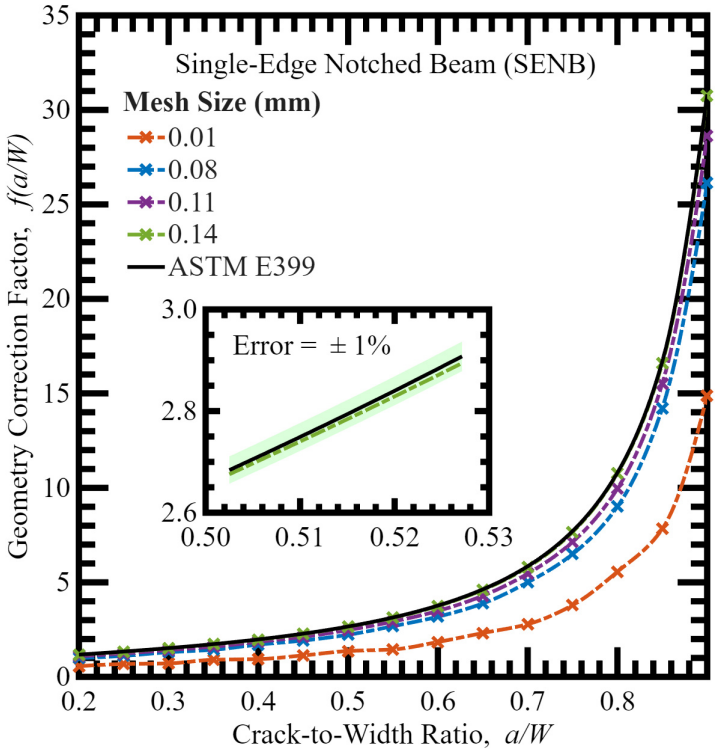
The geometry-independence result also clarifies the role of specimen size. Size still affects measured peak load, crack stability, and experimental scatter, but it should not change the normalized finite-body correction when similarity is preserved. In other words, W and B affect the practical quality of the test, while a/W controls the theoretical amplification factor. This distinction is the basis for selecting specimen C statistically while still using a generalized $f(a/W)$ function. Soil-specific $f(a/W)$ is given as:

$$f\left(\frac{a}{W}\right) = \beta\sqrt{\frac{a}{W}}\,\frac{1.99 - \frac{a}{W}\left(1-\frac{a}{W}\right)\left[2.095 - 3.805\frac{a}{W} + 2.635\left(\frac{a}{W}\right)^2\right]}{2\left(1+2.015\frac{a}{W}\right)\left(1-\frac{a}{W}\right)^{3/2}} \tag{3.4}$$

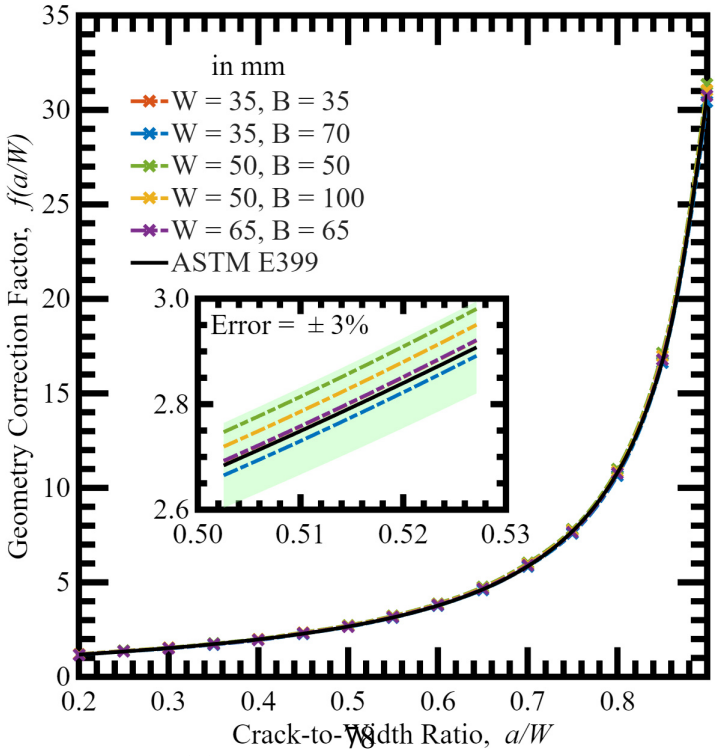
Table 3.8: Numerical and analytical scaling factors used to calibrate the generalized soil-specific SENB geometry correction function for subsequent K_{Ic} calculations.

Soil	ν range	Numerical β	Analytical β
LS_0	0.315-0.322	1.320	1.190
LS_{15}	0.270	0.880	1.030
LS_{25}	0.239-0.240	1.375	1.140
FS	0.197-0.199	1.111	1.162
General	approximately 0.250	1.1715	1.141

Note: ν = Poisson ratio and β = finite-body scaling factor used in the soil-specific SENB correction function.



(a) Mesh convergence



(b) Geometry independence

Figure 3.11: Abaqus® verification of the SENB model through (a) mesh convergence against ASTM E399 and (b) geometry-independence checks for compacted-soil specimens.

Table 3.8 summarizes the numerical and analytical scaling factors. The factors are not interpreted as new fracture properties; they are finite-body calibration constants for the SENB function. The generalized numerical value of 1.1715 is used for the main K_{Ic} calculation because it provides a practical single expression for clayey soils while remaining anchored to the numerical contour integral solution. The comparison with analytical values shows that the two independent derivation routes produce similar calibration magnitudes.

3.6.3 Analytical weight function derivation

The analytical route starts from the weight function expression for a linear elastic cracked body,

$$K_I = \int_0^a \sigma(y) m(a, y)\, dy \tag{3.5}$$

where $\sigma(y)$ is the bending stress acting along the prospective crack plane and $m(a, y)$ is the edge-crack weight function (Fett and Munz, 1997; Sih, P. C. Paris, and Irwin, 1965; X. R. Wu and Carlsson, 1991). For a three-point SENB specimen, the uncracked beam stress along the tensile face can be written using Euler-Bernoulli bending as

$$\sigma(y) = \frac{M(W/2 - y)}{I} \qquad M = \frac{PS}{4} \qquad I = \frac{BW^3}{12} \tag{3.6}$$

Substitution of Eq. (3.6) into Eq. (3.5), followed by non-dimensionalization with $\alpha = a/W$, gives the SENB finite-body structure

$$f_s(\alpha) = \beta \left(c_0 + c_1\alpha + c_2\alpha^2 + c_3\alpha^3 + c_4\alpha^4 + c_5\alpha^5 \right) \qquad \alpha = \frac{a}{W} \tag{3.7}$$

This preserves the classical SENB polynomial form but recalibrates the coefficients for the measured soil elastic response rather than imposing metallic coefficients (Gross and Srawley, 1965; Kaya and Erdogan, 1987; Tada, P. C. Paris, and Irwin, 1973).

The coefficients in Table 3.9 enter the weight function, not the universal crack-tip field. This distinction is important. LEFM says that the singular stress field has a universal form near the crack tip; it does not say that every finite-body load-to-K_I conversion calibrated for a metal beam can be transferred unchanged to a compacted clay beam. The analytical derivation retains the LEFM singularity and modifies only the finite-body amplification.

Table 3.10 is the analytical core of the derivation. It shows that the final expression for $f(a/W)$ follows from beam stress, crack weight functions, and exact integration. The numerical Abaqus® route is therefore not the only basis for the geometry factor. The analytical route

Table 3.9: weight function coefficients associated with measured Poisson ratios and used to construct the analytical finite-body correction for compacted soil SENB specimens.

Soil	ν	A_1	A_2	A_3	A_4	A_5
LS_0	0.315-0.322	0.452	3.216	-5.812	23.18	-15.92
LS_{15}	0.270	0.623	4.522	-8.974	35.84	-25.17
LS_{25}	0.239-0.240	0.399	2.847	-5.125	20.50	-14.03
FS	0.197-0.199	0.534	3.785	-7.512	30.05	-21.14

Note: A_1-A_5 are weight function coefficients associated with the measured Poisson-ratio range of each soil.

Table 3.10: Exact integral terms from the non-dimensional bending-stress distribution and five-term edge-crack weight function used in analytical $f(a/W)$ derivation.

n	$I_n = \int_0^1 \eta^{n-1}\, d\eta$	Exact value	$J_n = \int_0^1 \eta^{n-1}(1-\eta)\, d\eta$	Exact value
1	$1/1$	1	$1/(1\cdot 2)$	$1/2$
2	$1/2$	$1/2$	$1/(2\cdot 3)$	$1/6$
3	$1/3$	$1/3$	$1/(3\cdot 4)$	$1/12$
4	$1/4$	$1/4$	$1/(4\cdot 5)$	$1/20$
5	$1/5$	$1/5$	$1/(5\cdot 6)$	$1/30$

Note: I_n and J_n are exact non-dimensional integrals used in the analytical weight function derivation of $f(a/W)$.

independently enforces the correct bending-stress distribution and crack-tip singularity, while the fitted coefficients adjust the finite-body response within the soil-compliance range.

Table 3.11 completes the analytical expression. The higher-order terms are needed because $f(a/W)$ is not linear in crack ratio. As a/W increases, the remaining ligament shortens, the finite-body amplification increases, and the load required to achieve a given K_I decreases. A valid $f(a/W)$ must capture this nonlinear amplification; otherwise, the calculated K_{Ic} would artificially depend on notch depth.

Table 3.11: Polynomial coefficients defining the analytical soil-specific $f(a/W)$ expression for the investigated crack-ratio range and measured elastic-property domain.

Soil	ν	c_0	c_1	c_2	c_3	c_4	c_5
LS_0	0.315-0.322	2.284	6.452	-39.28	112.4	-134.2	59.12
LS_{15}	0.270	2.124	5.892	-35.84	102.7	-122.8	54.02
LS_{25}	0.239-0.240	2.341	6.612	-40.28	115.4	-137.9	60.72
FS	0.197-0.199	2.198	6.124	-37.24	106.8	-127.6	56.18

Note: c_0-c_5 are polynomial coefficients in the analytical soil-specific $f(a/W)$ expression.

3.6.4 Experimental compliance

The third route used the measured load-CMOD response to estimate compliance. For a cracked elastic body, the energy release rate can be expressed in terms of compliance as

$$G = \frac{P^2}{2B}\frac{dC}{da} \tag{3.8}$$

where C is the measured compliance. Under LEFM, G is related to K_I through the relevant elastic modulus. This provides an experimental route to back-calculate $f(a/W)$. Because differentiation of compliance data can amplify measurement noise, the compliance values were smoothed across the three notch ratios before differentiation. This route is not used because it is easier than the numerical route; rather, it is used to test whether the numerical and analytical functions are consistent with the measured crack-opening behaviour.

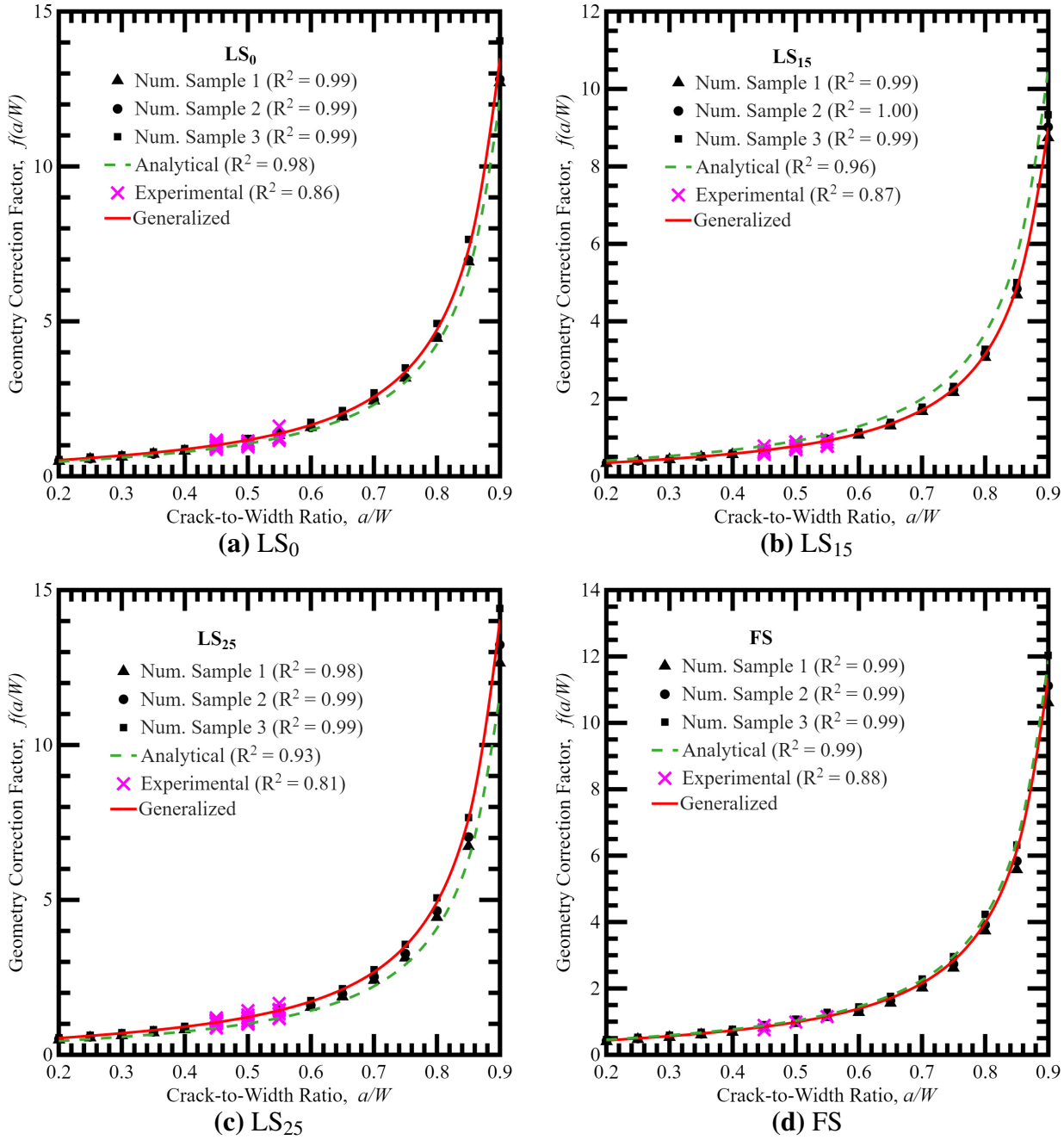
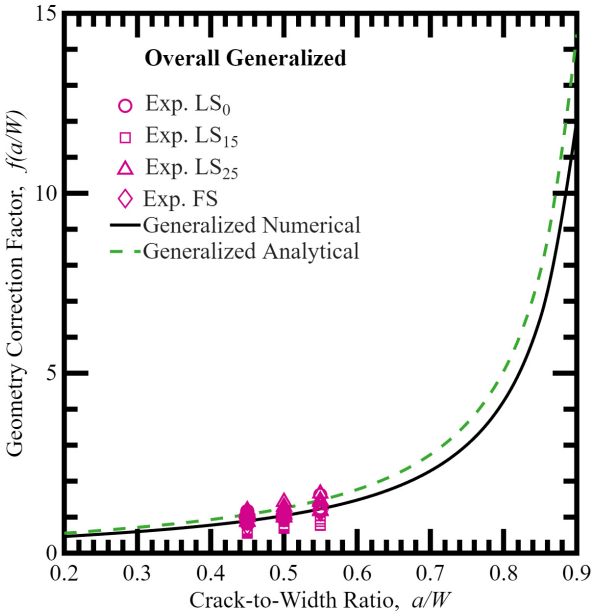


Figure 3.12: Numerical, analytical, and compliance-derived $f(a/W)$ functions for individual soils.



(e) Generalized function

Figure 3.12: Numerical, analytical, and compliance-derived $f(a/W)$ functions for individual soils and the generalized soil-specific SENB correction adopted in this chapter.

Figure 3.12e provides the generalized function used in the subsequent calculations. The generalized expression is a practical compromise. It avoids the need for a different equation for each clay barrier material while still correcting the major limitation of directly transferring a metallic SENB factor to compacted soils. The function is recommended for the test domain investigated here: geometrically scaled SENB beams, $S = 4W$, $L = 5W$, and $a/W = 0.45$-0.55. Outside this domain, the same sequence of numerical, analytical, and experimental validation should be repeated.

3.7 Mode I Fracture Toughness Results

3.7.1 Maximum load as a geometry-dependent response

The maximum load is the first measurable fracture response obtained from the SENB test, but classical fracture mechanics distinguishes this specimen load from the material crack-resistance parameter (**Anderson2005**; Tada, P. C. Paris, and Irwin, 1973). It is useful because it identifies

the onset of unstable crack opening for a given specimen, but it is not a material parameter by itself. Figures 3.13-3.15 show how strongly P_{max} depends on crack geometry.

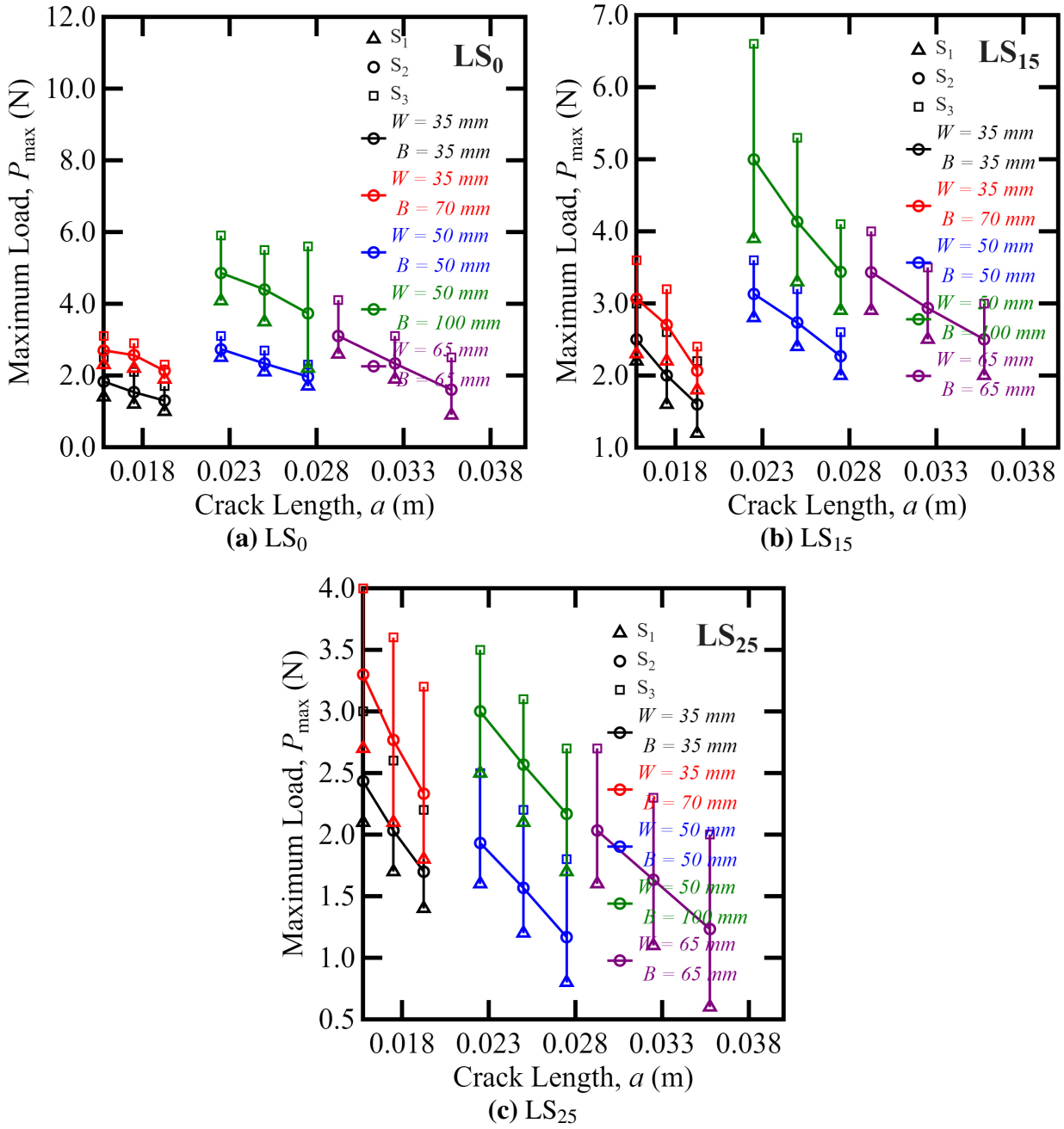
Figures 3.13, 3.14, and 3.15 show the expected SENB behaviour with measurable magnitude. For LS_0, the largest raw peak loads occur in smaller and intermediate specimens and are typically within about 2-6 N, while deeper notches reduce the load toward the lower end of this range. LS_{15} reaches the largest laboratory-soil peak loads, locally approaching 6-7 N in the plotted geometry combinations. LS_{25} generally remains lower, about 1-4 N, despite higher dry density, confirming that excessive sand addition does not automatically increase crack-initiation load. A longer initial crack reduces the remaining ligament and raises the crack-tip intensity for the same external load, so the specimen reaches instability at lower P_{max}. These values justify the fracture-mechanics conversion: peak load is strongly affected by geometry and cannot be used directly to rank soils.

Figure 3.13 emphasizes the physical effect of ligament length. As the preformed notch becomes deeper, the uncracked ligament becomes shorter, and the tensile stress field concentrates more rapidly near the notch tip. The beam then requires less external force to reach the crack-initiation condition. Figure 3.14 shows that this effect persists after normalizing crack length by specimen depth, confirming that the trend is not merely a dimensional artifact. Figure 3.15 adds the thickness dimension: for a given crack length, thickness controls constraint and load redistribution across the crack front.

The important design implication is that P_{max} should not be used directly to rank soils. A larger beam can show a higher peak load because it has more ligament area, not because the soil is intrinsically tougher. Conversely, a small specimen can exhibit a lower load while still yielding a comparable K_{Ic} after correction. The role of P_{max} is therefore to supply the crack-initiation load for the SENB equation, not to replace fracture toughness.

A second point follows from comparing Figures 3.13-3.15. The three plots show the same mechanics through three different normalizations: absolute crack length emphasizes remaining ligament, a/W emphasizes the finite-body SENB correction, and a/B emphasizes crack-front constraint through specimen thickness. The downward trend in P_{max} is strongest when the data are read against absolute crack length and a/W, because both directly reduce the ligament subjected to bending tension. The a/B response is more scattered because thickness also changes stress redistribution through the beam cross-section. This is why the raw load data are useful diagnostically but not sufficient for design. They demonstrate that the apparatus is sensitive enough to resolve crack-geometry effects, but they also show why $f(a/W)$ is essential before comparing soil types or compaction states.

The relative ordering of the laboratory soils provides a measured material comparison rather than direct evidence of a particular microstructural mechanism. LS_{15} gives the highest peak-load response among the laboratory mixtures, whereas LS_{25} gives lower peak loads despite its higher



(a) LS_0 **(b)** LS_{15} **(c)** LS_{25}

Figure 3.13: Maximum SENB load, P_{max}, plotted against absolute notch length for LS_0, LS_{15}, and LS_{25}, with the dataset including geometries A to E, $S/W = 4$, $L/W = 5$, $a/W = 0.45$, 0.50, and 0.55, three independently prepared state blocks S_1, S_2, and S_3 for each geometry and notch-ratio condition, loading at 0.006 mm s^{-1}.

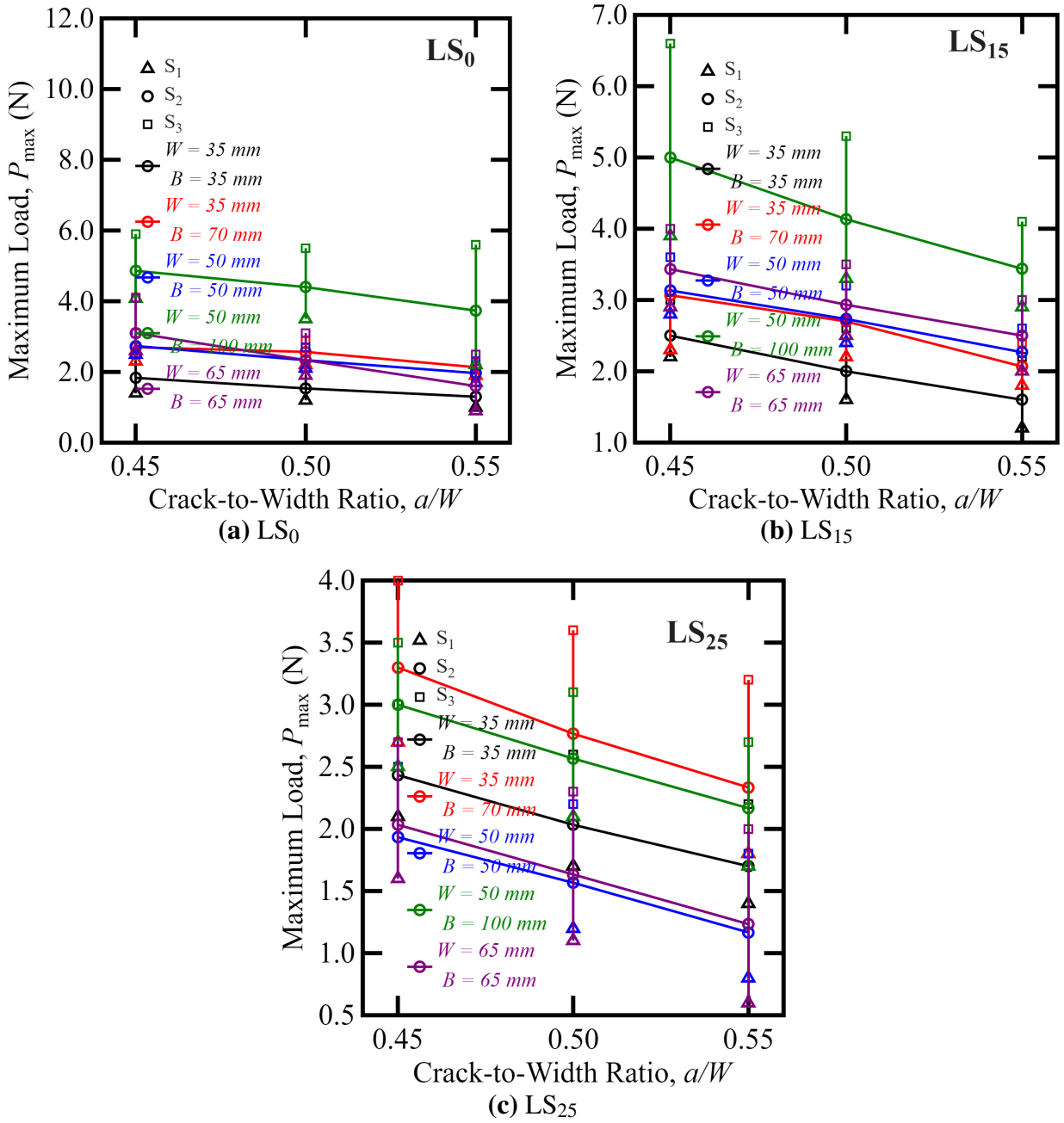


Figure 3.14: Maximum SENB load, P_{max}, plotted against the normalized notch ratio a/W for LS_0, LS_{15}, and LS_{25}, with geometries A to E tested at $a/W = 0.45$, 0.50, and 0.55, $S/W = 4$, $L/W = 5$, a constant displacement rate of 0.006 mm s^{-1}, and symbols S_1, S_2, and S_3 identifying the three independently prepared experimental blocks used for each geometry and notch-ratio condition

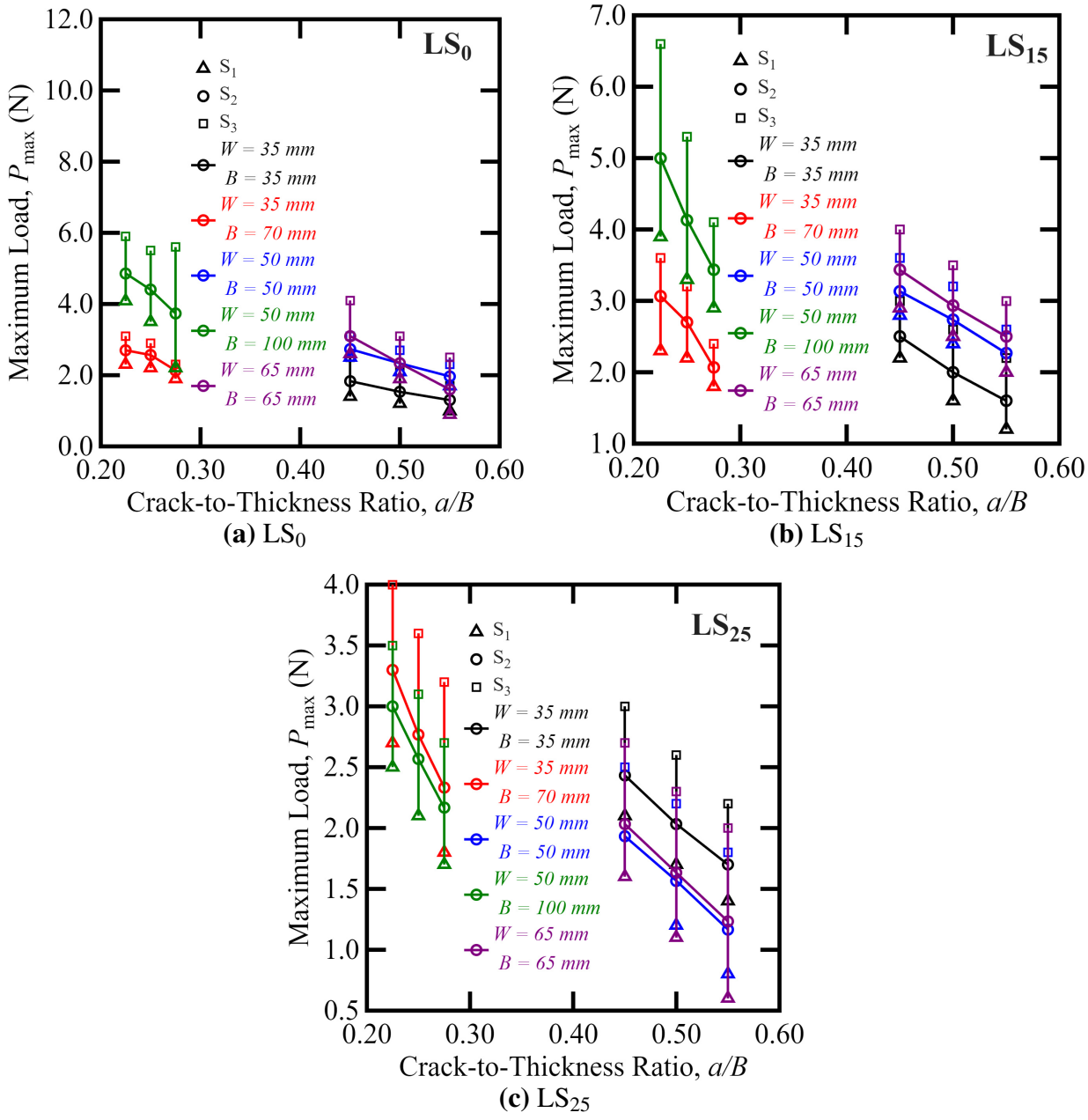


Figure 3.15: Maximum SENB load, P_{max}, plotted against the notch-length-to-thickness ratio a/B for LS_0, LS_{15}, and LS_{25}, with the comparison including geometries A to E, $W = 35$, 50, and 65 mm, $B = W$ or $B = 2W$ where feasible, $S/W = 4$, $L/W = 5$, $a/W = 0.45$, 0.50, and 0.55, three independently prepared experimental blocks, and displacement-controlled loading at 0.006 mm s^{-1}

dry density. This result confirms that the effect of sand addition is non-monotonic within the tested states. It does not establish improved force-chain continuity in LS_{15}, reduced cohesive bridging in LS_{25}, or loss of clay continuity. LS_0 remains hydraulically favourable but is more compliant and water-sensitive. Figures 3.13 to 3.15 therefore support the conclusion that mechanical response, hydraulic sealing, and compressibility must be assessed together rather than optimized independently.

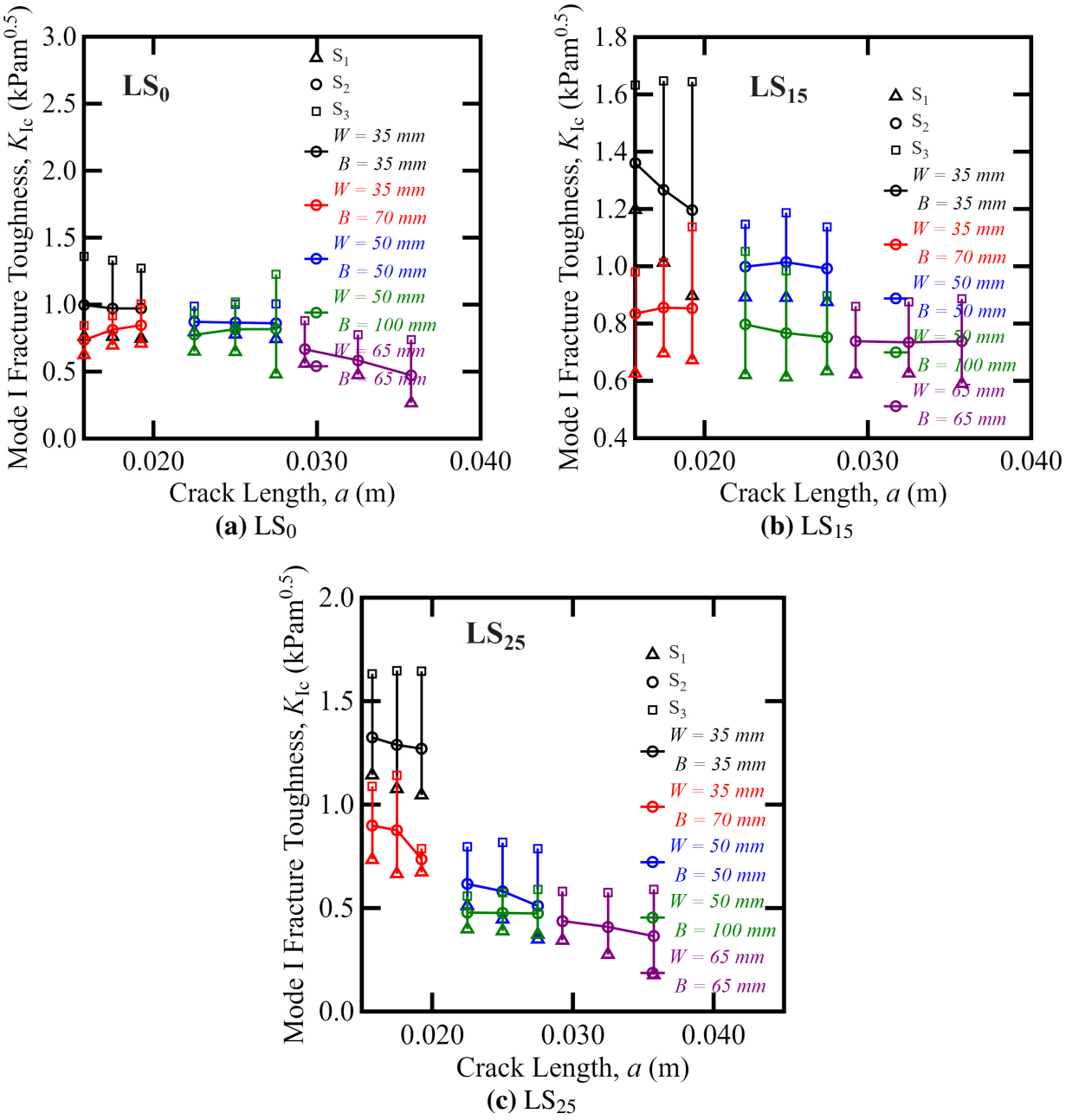
3.7.2 Corrected Mode I fracture toughness and geometry robustness

After applying $f(a/W)$, the fracture response should become less dependent on crack length and specimen geometry. This is the central check on whether the SENB framework measures a material property. Figures 3.16-3.18 present the corrected K_{Ic} values against the same geometric variables used for P_{max}.

Figures 3.16, 3.17, and 3.18 demonstrate the effect of the geometry correction. The same specimens that show large P_{max} differences collapse into narrower fracture toughness bands after applying $f(a/W)$. In Table 3.12, specimen C gives K_{Ic} values of 0.86-0.87 kPam$^{0.5}$ for LS_0, 0.99-1.01 kPam$^{0.5}$ for LS_{15}, 0.51-0.62 kPam$^{0.5}$ for LS_{25}, and 1.70-1.83 kPam$^{0.5}$ for FS. These values show that the corrected response is no longer governed mainly by notch ratio within the tested domain. The corrected values distinguish the tested material states: FS has the highest apparent Mode-I initiation toughness, LS_{15} has the highest value among the laboratory mixtures, and LS_{25} has the lowest value for specimen C. The measurements do not establish loss of clay continuity as the cause of the LS_{25} response.

The remaining scatter may reflect material-state variability, notch preparation, measurement uncertainty, or local heterogeneity; the present dataset does not separate these contributions. The raw load decreases with notch depth, but specimen C remains nearly constant over $a/W = 0.45$-0.55: the maximum change is only about 0.01 kPam$^{0.5}$ for LS_0, 0.02 kPam$^{0.5}$ for LS_{15}, and 0.21 kPam$^{0.5}$ for FS. The larger drop for LS_{25} from 0.62 to 0.51 kPam$^{0.5}$ is not a failure of $f(a/W)$. The larger variation observed for LS_{25} is treated as material-state and local-fabric variability within the sand-containing mixture. The present measurements do not isolate the separate effects of clay continuity, sand-grain spacing, suction, local density, and notch-scale heterogeneity. The remaining scatter is therefore mechanically meaningful rather than an unresolved finite-geometry error.

Figures 3.16-3.18 also separate apparent size effects from material behaviour. If the soil-specific $f(a/W)$ were inadequate, K_{Ic} would continue to decrease systematically with a, a/W, or a/B in the same way as P_{max}. Instead, the corrected values occupy narrow bands for each soil and specimen family, particularly for specimen C. This indicates that the SENB equation removes the



(a) LS_0 **(b)** LS_{15} **(c)** LS_{25}

Figure 3.16: Corrected state-conditioned Mode-I initiation toughness plotted against absolute notch length for LS_0, LS_{15}, and LS_{25}, with values calculated from the measured P_{max} using the adopted SENB correction function and with the dataset including geometries A to E, $S/W = 4$, $L/W = 5$, $a/W = 0.45$, 0.50, and 0.55, three independently prepared experimental blocks for each geometry and notch ratio condition, and loading at 0.006 mm s^{-1}

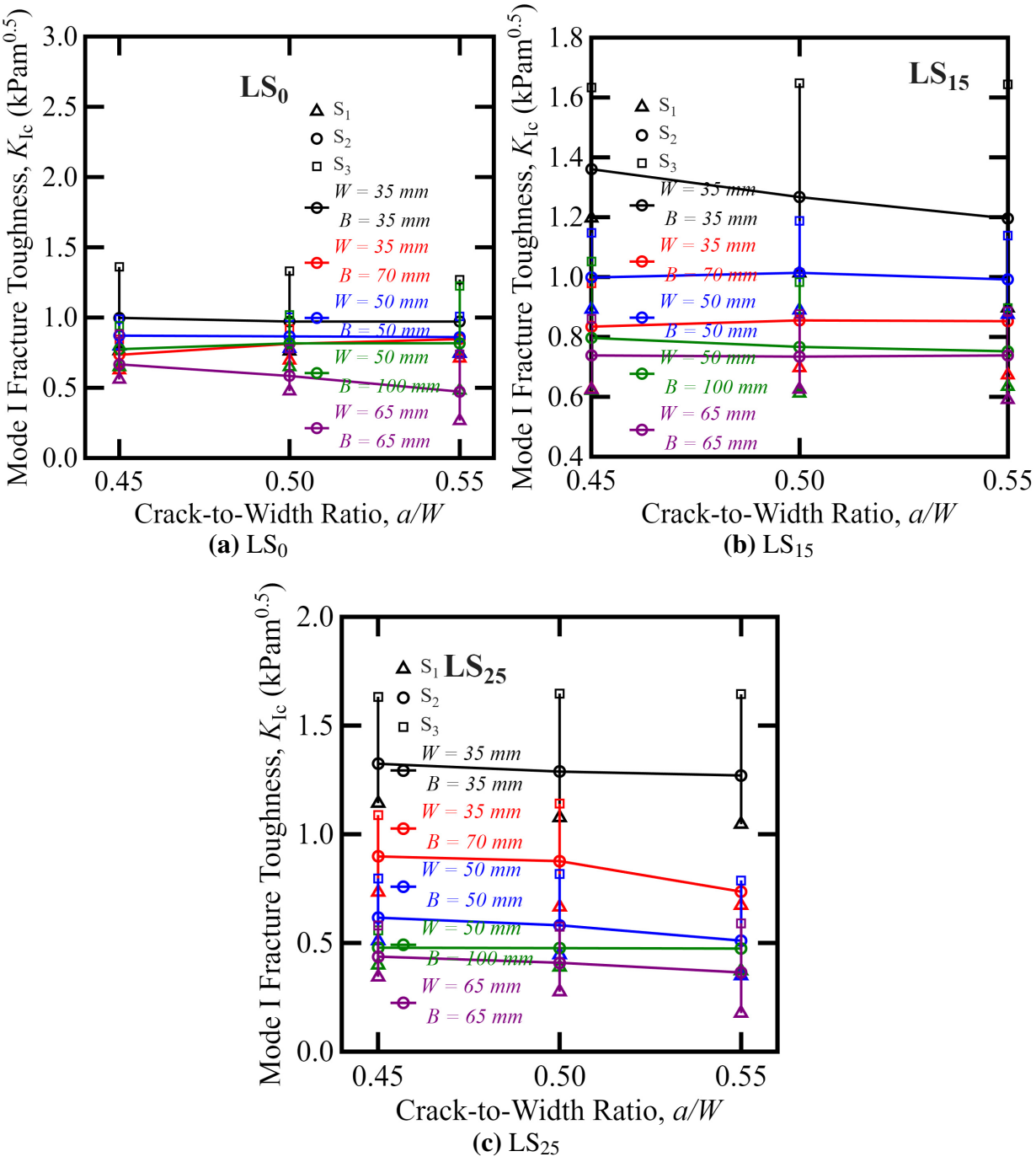


Figure 3.17: Corrected state-conditioned Mode-I initiation toughness plotted against a/W for LS_0, LS_{15}, and LS_{25}, with geometries A to E tested at $a/W = 0.45$, 0.50, and 0.55, $S/W = 4$, $L/W = 5$, a constant displacement rate of 0.006 mm s^{-1}, and symbols S_1, S_2, and S_3 denoting the three independently prepared experimental blocks

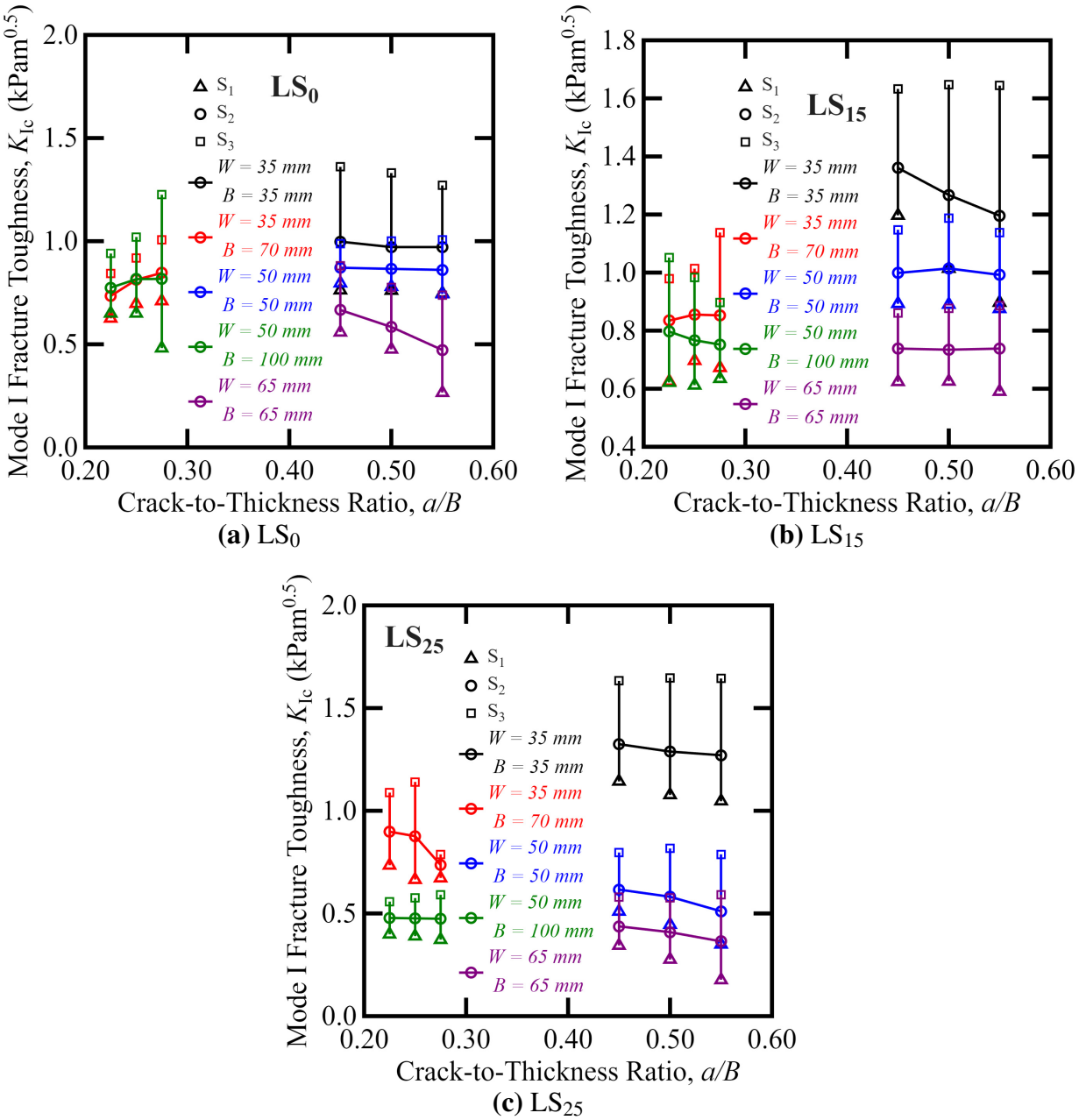


Figure 3.18: Corrected state-conditioned Mode-I initiation toughness plotted against a/B for LS_0, LS_{15}, and LS_{25}, with the comparison including geometries A to E, $B = W$ and $B = 2W$ where feasible, $S/W = 4$, $L/W = 5$, $a/W = 0.45$, 0.50, and 0.55, three independently prepared experimental blocks for each geometry and notch ratio condition, and loading at 0.006 mm s^{-1}

primary finite-body amplification, while the residual differences reflect soil fabric, notch quality, and local crack-path tortuosity. The design framework is that the selected geometry does not merely produce a convenient number; it produces a fracture parameter that can be compared with hydraulic conductivity and compressibility.

The laboratory-mixture ranking is important. LS_{15} gives representative K_{Ic} values near 1.0 kPam$^{0.5}$, which are higher than those of LS_0 and LS_{25} for specimen C. The non-monotonic variation with sand content is a measured result associated with the combined effects of composition, water content, dry density, and preparation state. It does not prove enhanced particle interlock at 15% sand, disruption of the clay matrix at 25% sand, or a change in cohesive bridging. FS gives substantially higher values, approximately 1.70 to 1.83 kPam$^{0.5}$, but the present tests do not separate the individual effects of its dry density, gradation, mineralogy, and natural fabric. FS is therefore retained as a field-reference material without treating its response as evidence of one specific microstructural mechanism.

Figure 3.19 is used to select the representative specimen geometry from a repeatability perspective rather than from peak response alone. For LS_0, specimen C gives COV values of 3.5%, 1.0%, and 1.0% at $a/W = 0.45$, 0.50, and 0.55, respectively. For LS_{15}, the same geometry gives 1.1%, 0.5%, and 2.3%, which is the strongest evidence that the 50 mm $\times$ 50 mm section suppresses notch-ratio sensitivity. The LS_{25} response is less uniform at shallow crack ratios, with specimen C reaching 18.5% and 15.7% at $a/W = 0.45$ and 0.50, but it drops to 1.8% at $a/W = 0.55$. The present dataset does not identify the cause of this larger variability because local sand distribution, dry-density variation, notch quality, suction, and internal fabric were not measured at the crack tip. The COV values are therefore used as descriptive measures of repeatability rather than as proof of a sand-controlled mechanism. The field soil also shows additional scatter at the shallower notch ratios, but the cause of that scatter was not isolated. The full-width grouped layout of Figure 3.19 makes this comparison clear: specimen C is not chosen because it maximizes K_{Ic}; it is chosen because it provides the best balance of repeatability, manageable self-weight, crack-front stability, and specimen preparation reliability.

Table 3.12 brings the corrected fracture toughness values into a single comparison. Specimen C is the decisive row because it is the recommended geometry. Its fracture toughness values are almost invariant with crack ratio for LS_0 (0.87, 0.87, and 0.86 kPam$^{0.5}$) and LS_{15} (1.00, 1.01, and 0.99 kPam$^{0.5}$). FS is substantially tougher, decreasing only from 1.83 to 1.70 kPam$^{0.5}$ as a/W increases from 0.45 to 0.55. By contrast, LS_{25} gives only 0.62, 0.58, and 0.51 kPam$^{0.5}$. The table therefore identifies two different optima: LS_{15} is the best laboratory mixture in mechanical fracture toughness, whereas FS gives the strongest field-soil crack resistance. LS_{25} is not optimum because its higher density is offset by poor hydraulic response and lower corrected fracture toughness.

Table 3.13 supports the same conclusion statistically. Specimen C gives very low variability

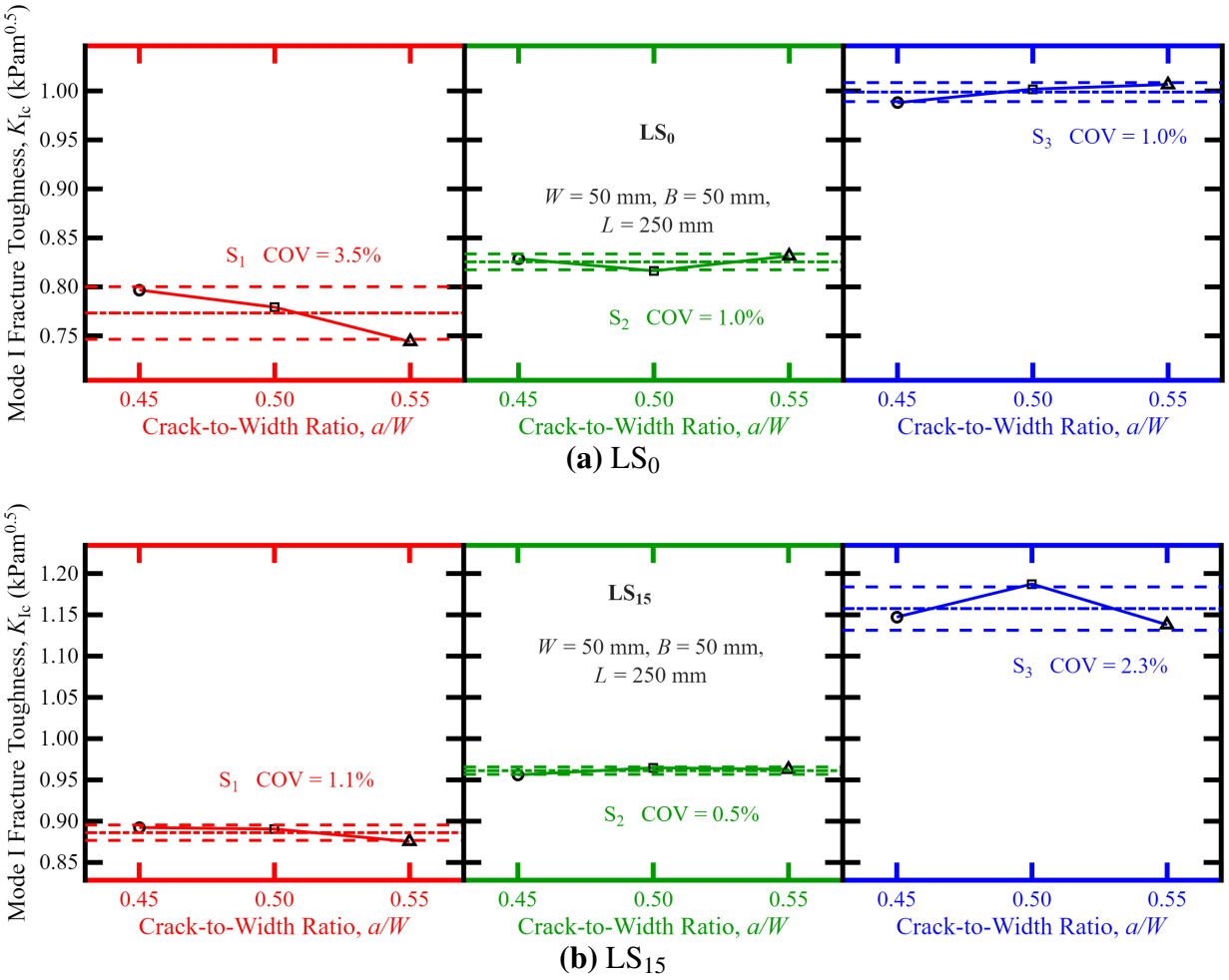
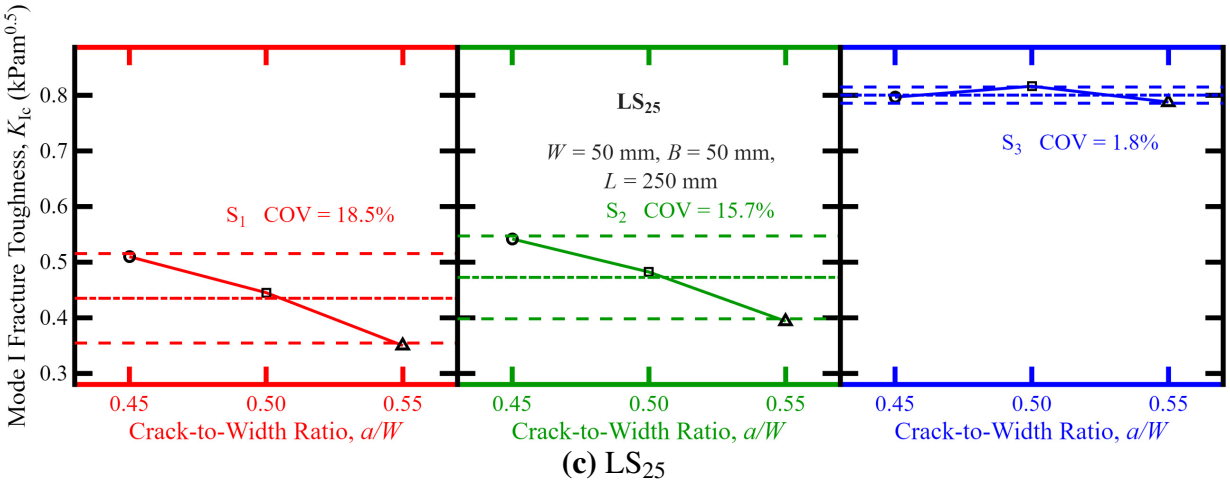
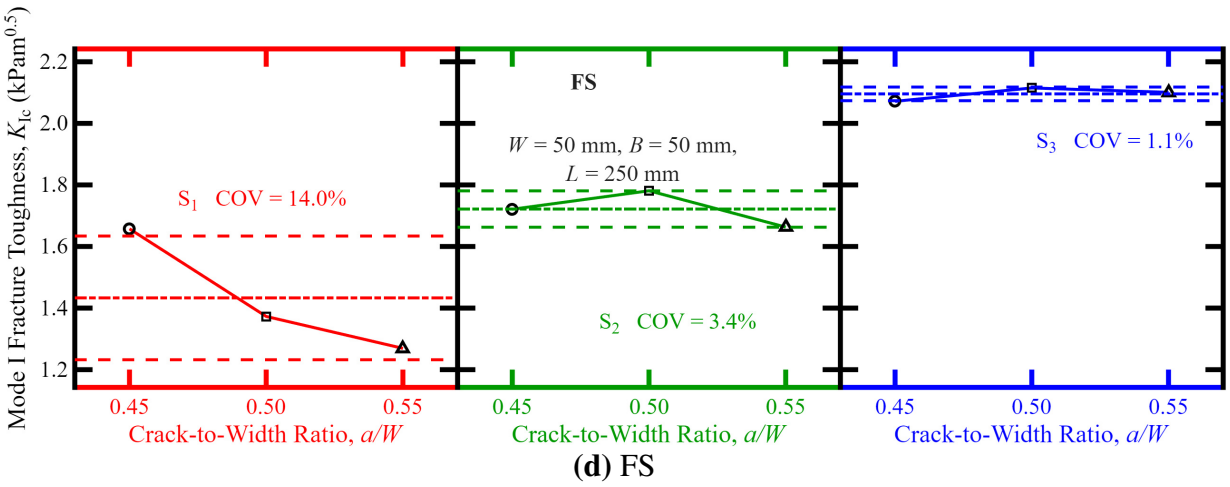


Figure 3.19: Notch-ratio variation of corrected Mode-I initiation toughness for Geometry C in (a) LS_0 and (b) LS_{15}, with S_1, S_2, and S_3 representing the three independently prepared water-content and dry-density blocks and the displayed coefficient of variation calculated from the three values obtained at $a/W = 0.45$, 0.50, and 0.55 within each block

for LS_0 and LS_{15}, and it reduces geometry-driven scatter over the practical crack-ratio domain. For LS_{25}, variability is larger at the shallower notches. The present measurements do not determine whether this variation arose from local sand distribution, density variation, notch quality, suction, or another source of specimen heterogeneity. However, even in that material, the variability decreases at higher notch ratios. This shows that specimen C provided relatively low variability in many of the tested cells, while specimen geometry did not eliminate all specimen-state variability. Material preparation and state control remain essential.



(c) LS_{25}



(d) FS

Figure 3.19: Continuation of Figure 3.19, showing (c) LS_{25} and (d) FS under the same Geometry C, loading, and notch-ratio conditions

The coefficient of variation analysis is especially valuable because it treats repeatability as a mechanics outcome rather than a cosmetic statistic. A geometry with low COV indicates that small changes in notch ratio do not dominate the measured fracture toughness. Specimen C satisfies this condition for most soils while remaining practical to fabricate, compact, demould, and test. This makes the 50 mm $\times$ 50 mm geometry a suitable representative SENB configuration for subsequent comparisons with clay barriers, including interpretations of hydraulic conductivity and compressibility.

Table 3.12: Mean corrected Mode I fracture toughness values for each SENB geometry and crack ratio, calculated using the soil-specific correction function.

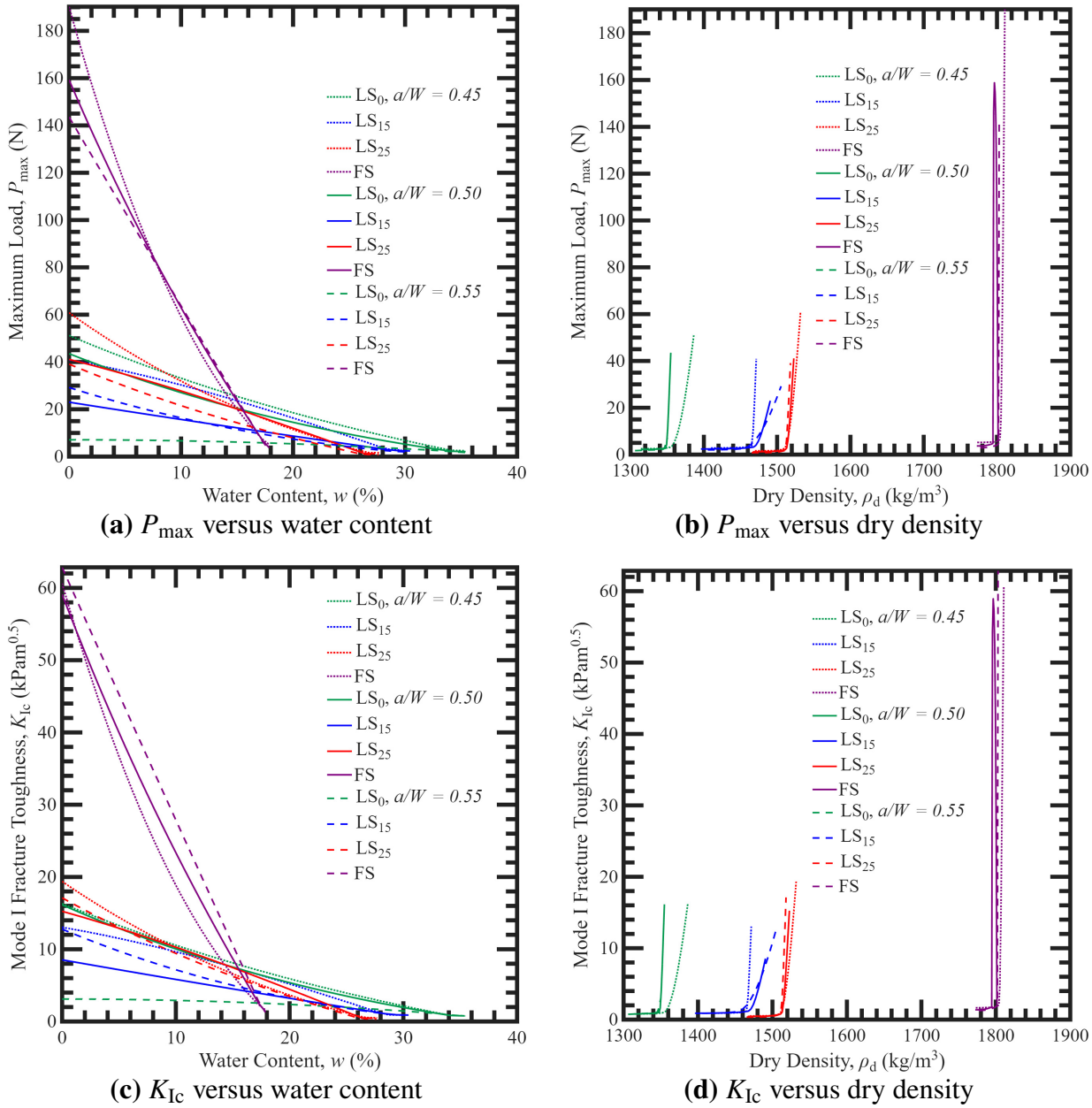
Specimen	a/W	LS_0	LS_{15}	LS_{25}	FS
			K_{Ic} (kPam$^{0.5}$)		
	0.45	1.00	1.36	1.32	-
A	0.50	0.97	1.27	1.29	-
	0.55	0.97	1.20	1.27	-
	0.45	0.73	0.84	0.90	-
B	0.50	0.81	0.86	0.88	-
	0.55	0.80	0.77	0.87	-
	0.45	0.87	1.00	0.62	1.83
C	0.50	0.87	1.01	0.58	1.77
	0.55	0.86	0.99	0.51	1.70
	0.45	0.77	0.80	0.48	-
D	0.50	0.82	0.76	0.48	-
	0.55	0.82	0.75	0.47	-
	0.45	0.67	0.74	0.44	-
E	0.50	0.59	0.74	0.41	-
	0.55	0.47	0.74	0.36	-

Note: A-E are the SENB geometries in Table 3.5; a/W = crack-to-width ratio.

3.7.3 Water content, dry density, and soil fabric

The geometry-corrected fracture results indicate that water content and dry density are the dominant material-state variables. Figure 3.20 compares P_{max} and K_{Ic} against w and ρ_d for the representative specimen family.

The experimental programme directly measured load, crack mouth opening displacement, specimen water content, dry density, and specimen dimensions. Fracture parameters were calculated from these measurements. Matric suction, local degree of saturation, contact coordination, contact friction, contact-scale stiffness, particle rearrangement, and local pore-pressure changes were not measured. These variables were also not represented explicitly in the linear-elastic Chapter 3 numerical model. Therefore, microscopic explanations concerning suction, contact lubrication, coordination number, particle bridging, and contact softening are treated as possible interpretations consistent with the measured trends, rather than as mechanisms confirmed by the



(a) P_{max} versus water content

(b) P_{max} versus dry density

(c) K_{Ic} versus water content

(d) K_{Ic} versus dry density

Figure 3.20: Measured variation of peak load and apparent Mode-I initiation toughness with water content and dry density for LS_0, LS_{15}, LS_{25}, and FS, with the SENB results obtained from the representative $W = B = 50$ mm, $L = 250$ mm, and $S = 200$ mm specimen family over $0.45 \leq a/W \leq 0.55$ using displacement-controlled loading at 0.006 mm s^{-1}, and with matric suction, local degree of saturation, contact coordination, contact friction, and contact-scale stiffness not measured.

Table 3.13: Coefficient of variation of corrected K_{Ic} for each geometry, crack ratio, and laboratory soil, identifying specimen C as the most repeatable SENB geometry.

LS_0					
a/W	A	B	C	D	E
0.45	18.1	26.7	3.5	26.4	34.9
0.50	14.3	16.4	1.0	13.2	14.9
0.55	3.5	4.5	1.0	10.9	9.3
LS_{15}					
a/W	A	B	C	D	E
0.45	14.6	15.4	1.1	11.8	23.2
0.50	9.0	9.3	0.5	10.4	12.7
0.55	4.5	6.2	2.3	7.9	2.5
LS_{25}					
a/W	A	B	C	D	E
0.45	14.5	35.5	18.5	23.5	31.6
0.50	13.4	17.7	15.7	12.1	9.1
0.55	3.5	4.7	1.8	2.9	2.3

Note: COV is the coefficient of variation of corrected K_{Ic} across replicate measurements; A-E are SENB geometries.

present experiments.

Figure 3.20 therefore shows measured water-content and density dependence, not a direct measurement of suction dependence. Figure 3.20 documents the measured association of water content and dry density with peak load and apparent Mode-I initiation toughness. The figure does not, by itself, confirm a specific hydromechanical mechanism because matric suction, degree of saturation, contact coordination, contact friction, and contact-scale stiffness were not measured. These variables were also not represented explicitly in the homogeneous linear-elastic Chapter 3 model. In the oven-dried state, the field soil reaches the largest peak-load range, approximately 140-190 N depending on a/W, whereas LS_{25} reaches about 40-60 N and the clay-rich laboratory mixtures are lower. At near-OMC water contents, the same response collapses to the low-Newton range shown in Figure 3.8. The corresponding fracture toughness values in Figure 3.20 and

Figure 3.21 fall from dry-state values of roughly 60 kPam$^{0.5}$ for FS, 17 kPam$^{0.5}$ for LS_{25}, and about 11-12 kPam$^{0.5}$ for LS_0 and LS_{15} to near-OMC values below about 2 kPam$^{0.5}$. The large reduction from the oven-dry condition to the near-OMC condition is a measured state-dependent trend. Suction loss is a physically plausible contributor, but the present tests do not separate it from simultaneous changes in degree of saturation, density, fabric, and moisture history.

The competition between water content and dry density explains why the response is not purely monotonic with respect to a single compaction variable. Within several soil series, higher dry density was associated with greater peak load and apparent initiation resistance, while higher water content was associated with lower values. Contact coordination and contact lubrication were not measured, so these mechanisms cannot be stated as confirmed explanations. For barrier design, the important outcome is that the best compaction state is not the driest state in the plot. Oven-dried specimens yield very high P_{max} and K_{Ic}, but they are not representative of compacted clay barrier placement. The practically relevant comparison is around OMC and MDD, where FS retains about 1.7-1.8 kPam$^{0.5}$, LS_{15} about 1.0 kPam$^{0.5}$, LS_0 about 0.86-0.87 kPam$^{0.5}$, and LS_{25} about 0.5-0.6 kPam$^{0.5}$. These near-OMC values are the design-relevant fracture toughness values used later in the chapter.

Figure 3.20 should therefore be read as a state-variable map. The P_{max}-w and K_{Ic}-w panels show that increasing water content degrades both load capacity and crack-tip resistance, but the degradation is not identical for all soils. FS retained a higher apparent initiation resistance at the tested wet-state conditions. Its broader gradation, higher dry density, mineralogy, and natural fabric may contribute to this response, but the present tests do not identify the relative contribution of each factor. The P_{max}-ρ_d and K_{Ic}-ρ_d panels show that the measured relationship between density and initiation resistance differed among the soils, showing that density alone is not sufficient to predict the response. This is why LS_{25} does not outperform LS_{15} despite its higher density. The comparison shows that dry density alone is insufficient to predict apparent Mode-I initiation toughness because the measured values also vary with composition, water content, and preparation state. The present tests do not establish that sand addition disrupted the clay matrix.

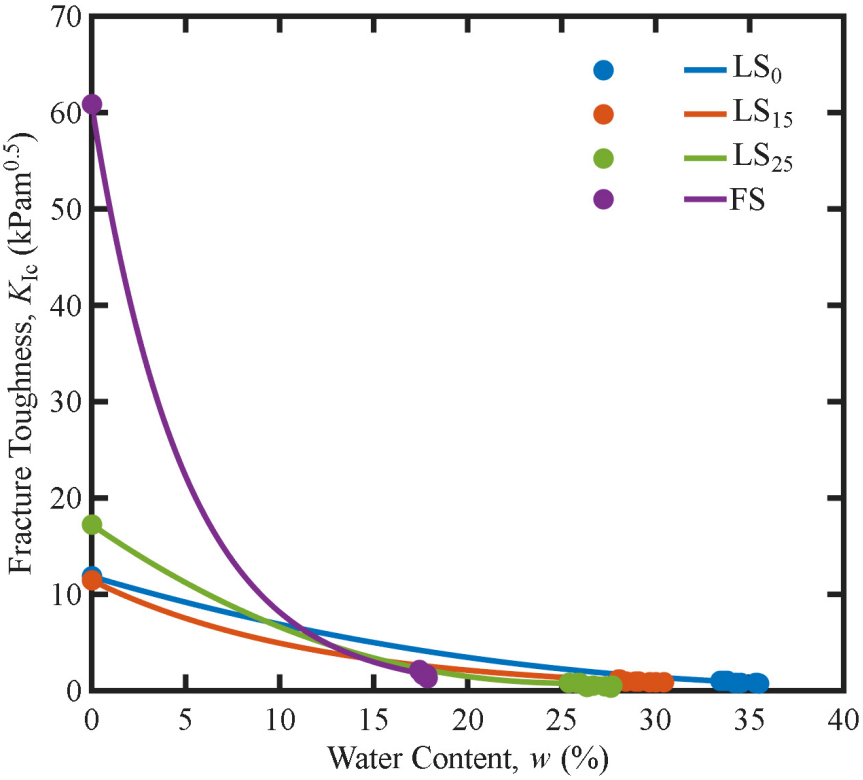


Figure 3.21: State-conditioned apparent Mode-I initiation toughness plotted against gravimetric water content for LS_0, LS_{15}, LS_{25}, and FS, with results obtained using the representative $W = B = 50$ mm, $L = 250$ mm, and $S = 200$ mm SENB family over $0.45 \leq a/W \leq 0.55$ at a loading rate of 0.006 mm s^{-1}, and with the dataset spanning oven-dry to near-OMC conditions while matric suction was neither measured nor independently controlled.

Figure 3.21 isolates the moisture effect on K_{Ic}. The measured reduction is steepest over the lower water-content range. This trend is consistent with a substantial change in the unsaturated state, but the contribution of matric suction was not quantified because suction was not measured. FS falls from about 61 kPam$^{0.5}$ in the dry condition to about 1.7-2.1 kPam$^{0.5}$ near w = 17-18%. LS_{25} falls from about 17 kPam$^{0.5}$ to approximately 0.5-0.8 kPam$^{0.5}$, while LS_0 and LS_{15} converge toward about 0.8-1.2 kPam$^{0.5}$ near their OMC ranges. The field soil therefore retains the highest wet-state fracture toughness, but LS_0 remains the best laboratory soil hydraulically. This separation between mechanical and hydraulic ranking motivates the interrelationship developed later in the chapter.

For a containment barrier, the moisture trend has two consequences. First, fracture resistance measured at a laboratory water content cannot be transferred directly to field wetting or drying

conditions. Second, a material optimized only for low hydraulic conductivity may not maximize crack resistance. A clay-rich matrix may seal well, but if it opens a connected crack under tensile loading, the low intact hydraulic conductivity no longer represents the service condition. The fracture toughness-water content relationship, therefore, becomes a direct design input rather than a secondary material observation.

Figure 3.21 also shows why the chapter focuses on near-OMC values when proposing design screening. Dry-state K_{Ic} values are useful for understanding the upper bound of suction-controlled resistance, but a field liner or clay core is constructed close to a compaction target rather than in an oven-dried state. At this placement-relevant state, FS and LS_{15} are mechanically favourable, while LS_0 remains acceptable and LS_{25} falls below the proposed fracture toughness threshold. The curve shapes therefore distinguish material mechanisms: the dry-to-wet reduction is strongly associated with water content; suction is one possible contributor that requires direct measurement, while fabric and gradation determine the amount of fracture toughness remaining after wetting. This is the basis for linking K_{Ic} to hydraulic conductivity and a_v instead of reporting a single fracture toughness value.

Table 3.14: Hydraulic conductivity values of intact compacted specimens.

Soil	Hydraulic conductivity, k (10^{-9} m/s)
LS_0	0.132
LS_{15}	1.330
LS_{25}	6.340
FS	0.531

Note: k = saturated hydraulic conductivity measured on intact compacted specimens; values are reported in 10^{-9} m/s.

Table 3.14 must be read together with the fracture toughness results. LS_0 has the best laboratory sealing response, 0.132×10^{-9} m/s, but its representative K_{Ic} is only about 0.86-0.87 kPam$^{0.5}$. LS_{25} has the poorest hydraulic response, 6.340×10^{-9} m/s, and also the lowest representative fracture toughness, about 0.51-0.62 kPam$^{0.5}$. FS is favourable because it satisfies the hydraulic criterion with $k = 0.531 \times 10^{-9}$ m/s and gives high wet-state fracture toughness of about 1.70-1.83 kPam$^{0.5}$. LS_{15} is mechanically attractive but hydraulically marginal because $k = 1.330 \times 10^{-9}$ m/s.

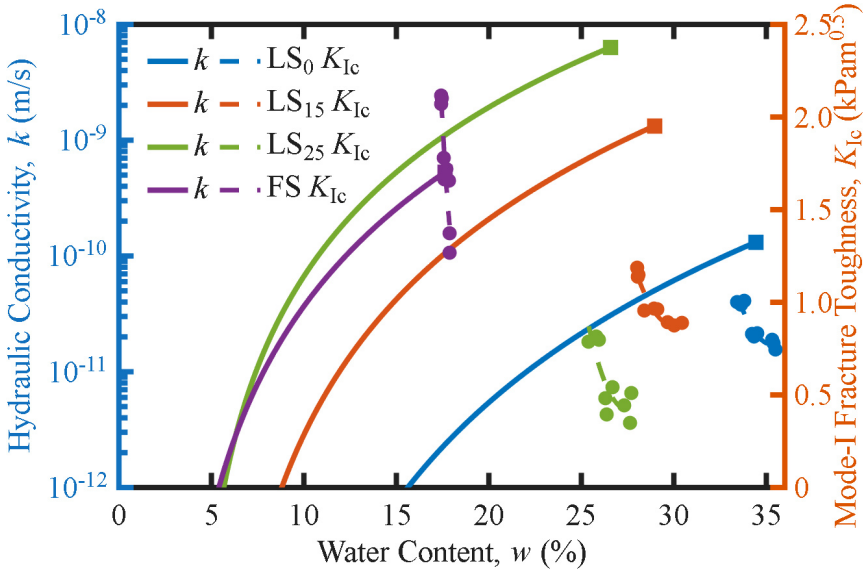


Figure 3.22: Combined apparent Mode-I initiation toughness and intact saturated hydraulic conductivity as functions of water content for LS_0, LS_{15}, LS_{25}, and FS, with fracture values obtained from the representative $W = B = 50$ mm, $L = 250$ mm, and $S = 200$ mm SENB specimens over $0.45 \leq a/W \leq 0.55$ at 0.006 mm s^{-1}, and hydraulic-conductivity values measured on separate intact saturated specimens in accordance with ASTM D5084.

Figure 3.22 is the first direct bridge between fracture mechanics and barrier hydraulics. On the hydraulic axis, LS_0 and FS sit below 10^{-9} m/s, whereas LS_{15} and LS_{25} lie above this conventional barrier threshold. On the fracture toughness axis, however, FS retains the highest near-OMC crack resistance, LS_{15} is next, LS_0 is acceptable, and LS_{25} is weakest. The figure, therefore, prevents a misleading conclusion. LS_{15} cannot be selected only because it has a higher K_{Ic} than LS_0, and LS_0 cannot be selected only because it has the lowest intact k. A clay barrier is acceptable only if it simultaneously resists seepage and crack initiation.

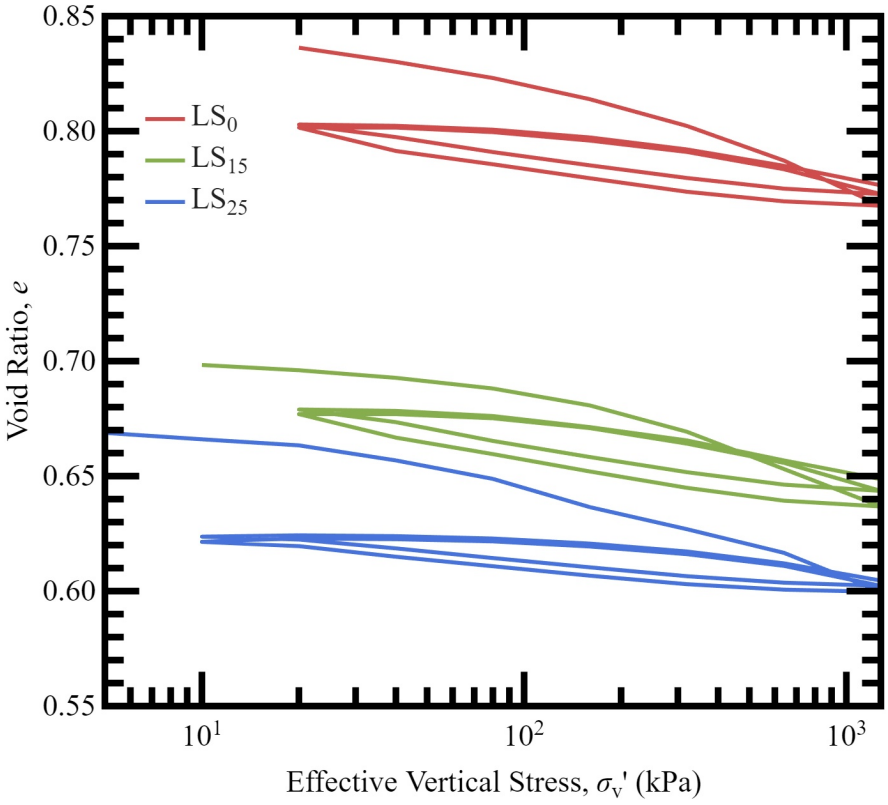
The coupled plot clarifies the measured trade-off among the laboratory mixtures. LS_{15} has a higher apparent Mode-I initiation toughness than LS_0, but its intact hydraulic conductivity is slightly above the preliminary screening limit. LS_{25} has a higher intact hydraulic conductivity and a lower apparent initiation toughness than LS_{15}. These results do not prove increased particle interlock, loss of clay continuity, or crack bridging. FS combines a broad natural gradation with relatively low hydraulic conductivity and higher apparent initiation toughness under the tested conditions, but the relative contributions of gradation, mineralogy, density, and natural fabric were not isolated. Site-specific verification therefore remains necessary.

3.8 Compressibility and nanomaterial improvement metrics

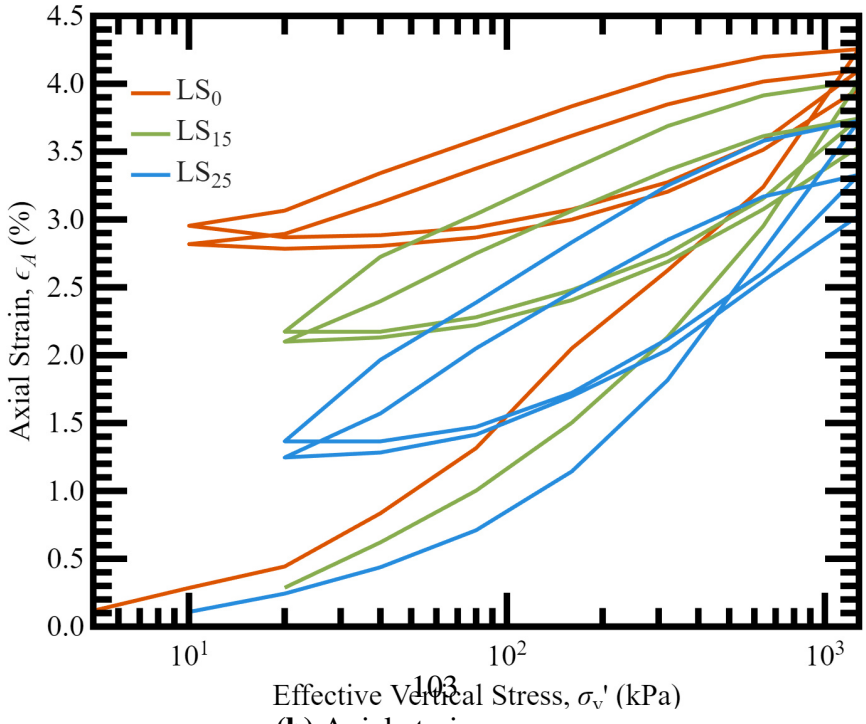
Compressibility is included because crack resistance and hydraulic conductivity are both affected by pore structure, volume-change tendency, and the evolution of compacted fabric under stress (Daniel and Y.-K. Wu, 1993; Mitchell and Soga, 2005; Rowe, 2005). One-dimensional consolidation tests were conducted in accordance with ASTM D2435. The specimens were taken from the same soil family used in the fracture programme so that compressibility could be interpreted consistently with K_{Ic} and k.

Figure 3.23 shows that compressibility is not a secondary property in clay barrier design. The void-ratio curves start near the measured compacted states and decrease with effective vertical stress, while the strain curves reach approximately 3-4.3% by the highest applied stress. LS_0 indicates the largest compressive deformation band, reflecting its clay-rich, water-sensitive fabric. LS_{15} occupies an intermediate range, and LS_{25} shows lower strain in several states but with the hydraulic penalty already identified in Table 3.14. The consolidation response, therefore, provides the third design axis: a material can have acceptable k and K_{Ic} yet still be vulnerable if loading induces fabric rearrangement, pore-network evolution, or tensile stress concentration during settlement.

The consolidation response also affects the interpretation of fracture resistance over time. Compression can close pore space and reduce flow locally, but it can also generate fabric anisotropy and stress redistribution around interfaces. A low a_v is favourable only when it is achieved without increasing k or reducing K_{Ic}. This is why the K_{Ic}-k-a_v relationship is needed: it prevents the design interpretation from treating compressibility as an isolated oedometer parameter. In service, compressibility controls how the compacted fabric evolves after construction, while K_{Ic} controls whether tensile zones open into connected cracks and k controls whether those cracks bypass the intact matrix.



(a) Void-ratio response



(b) Axial-strain response

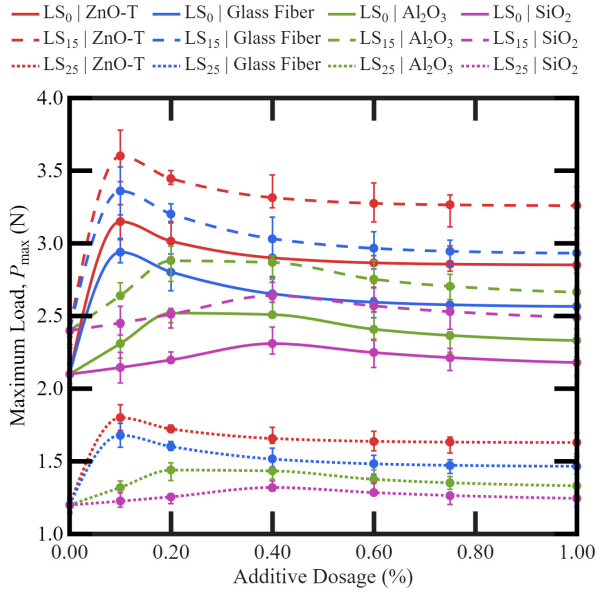
Figure 3.23: One-dimensional consolidation responses of LS_0, LS_{15}, and LS_{25} specimens tested in accordance with ASTM D2435/D2435M, showing void ratio and axial strain against effective vertical stress for specimens approximately 49.92 mm in diameter and 19.25 mm in initial height, laterally confined in rigid rings with drainage through porous stones, with three independently prepared specimens tested for each soil and the vertical stress increased incrementally.

The nanomaterial part of the chapter is treated as a screening-level improvement strategy. The purpose is to examine whether additives can improve fracture toughness, hydraulic conductivity, strength, and consolidation metrics without relying on PFAS-containing components or conventional geomembrane assumptions. The measured responses are summarized in Figure 3.24. The low-dosage optimum is an experimental observation based on the measured load and derived fracture response. Particle agglomeration, contact refinement, fibre bridging, and modification of the clay-particle network are possible explanations for the non-monotonic trend. These mechanisms were not independently measured using microscopy, particle-dispersion analysis, or local strain measurements and are therefore not presented as confirmed mechanisms.

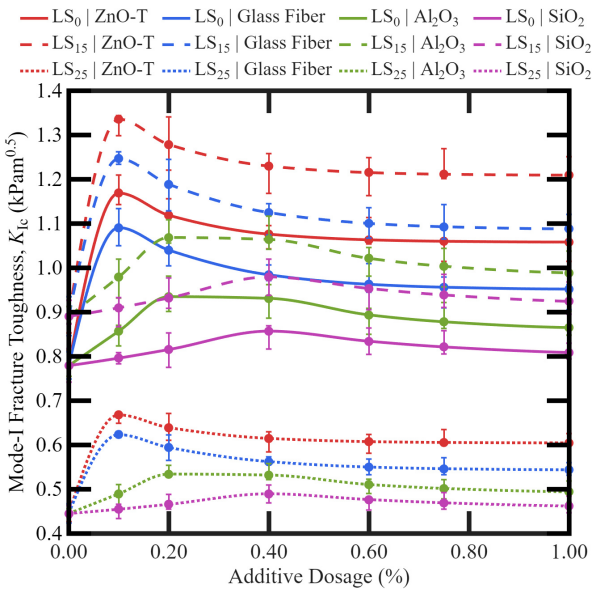
Figure 3.24 shows a non-monotonic dosage response. For the tested soils, the largest measured increase in peak load and apparent Mode-I initiation toughness occurred at a relatively low additive dosage, after which the response either decreased or levelled off. ZnO-T and glass fibre produced the largest measured mechanical changes, while the aluminium-oxide and silica additions showed broader and smaller response ranges. The low-dosage optima are experimental observations. Particle agglomeration, contact modification, fibre bridging, and changes in the compacted pore structure are possible explanations, but these mechanisms were not measured independently using microscopy, dispersion analysis, local strain measurements, or internal imaging and are therefore not presented as confirmed mechanisms.

The compressibility plots provide the second part of the decision. ZnO-T at 0.10% gives the lowest or near-lowest compressibility indices in Figure 3.24. For LS_0, the approximate values are $C_r = 0.80 \times 10^{-2}$, $m_v = 0.40 \times 10^{-2}$ m^2/MN, and $a_v = 0.74 \times 10^{-2}$ m^2/MN. For LS_{15}, the same dosage gives approximately $C_r = 0.42 \times 10^{-2}$, $m_v = 0.40 \times 10^{-2}$ m^2/MN, and $a_v = 0.66 \times 10^{-2}$ m^2/MN. For LS_{25}, the values are approximately $C_r = 0.97 \times 10^{-2}$, $m_v = 0.42 \times 10^{-2}$ m^2/MN, and $a_v = 0.71 \times 10^{-2}$ m^2/MN. After 0.10%, the compressibility indices increase progressively. This reversal is significant because it shows that excessive dosage can stiffen the response at crack initiation while degrading the compacted fabric under one-dimensional loading.

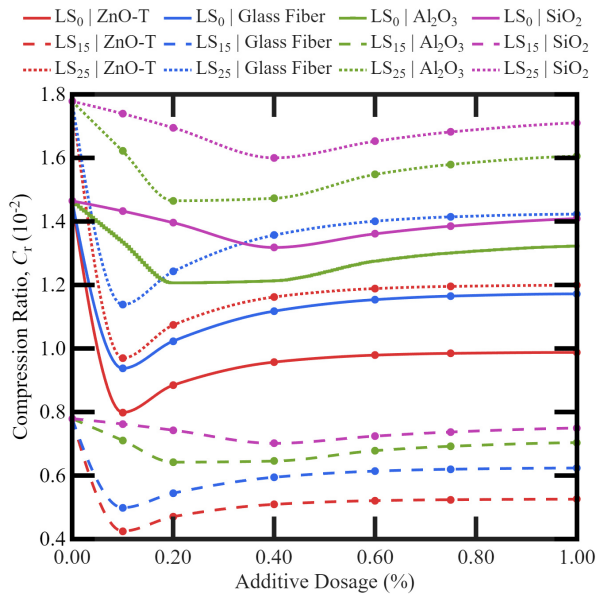
The coefficient of compressibility and hydraulic conductivity subplots in Figure 3.24e prevent a purely mechanical interpretation. For LS_0, hydraulic conductivity remains close to the baseline, approximately 0.13-0.15 $\times 10^{-9}$ m/s, across the additives. Therefore, 0.10% ZnO-T improves fracture toughness while keeping the material inside the hydraulic screening limit. For LS_{15}, the best mechanical dosage still leaves k near 1.4-1.5 $\times 10^{-9}$ m/s, which is slightly above the proposed barrier threshold. For LS_{25}, hydraulic conductivity remains much higher, roughly 6.5-7.4 $\times 10^{-9}$ m/s, regardless of the additive. Thus, the optimum dosage is not determined by maximum K_{Ic} alone. It is determined by the simultaneous behaviour of P_{max}, K_{Ic}, C_r, m_v, a_v, and k.



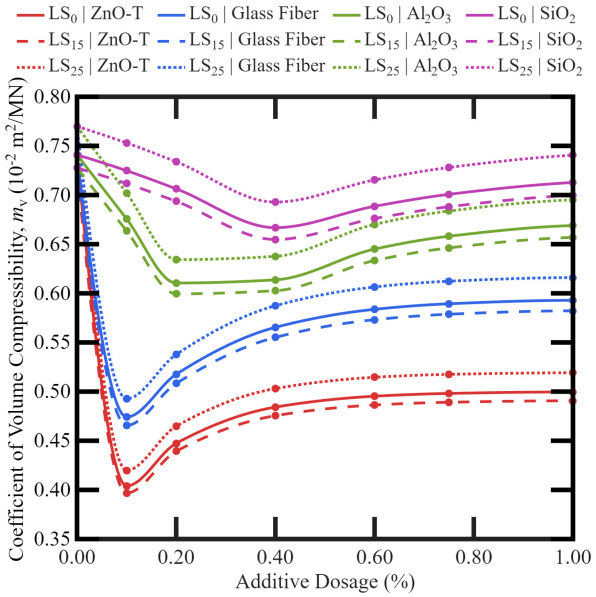
(a) Peak load



(b) Mode I fracture toughness

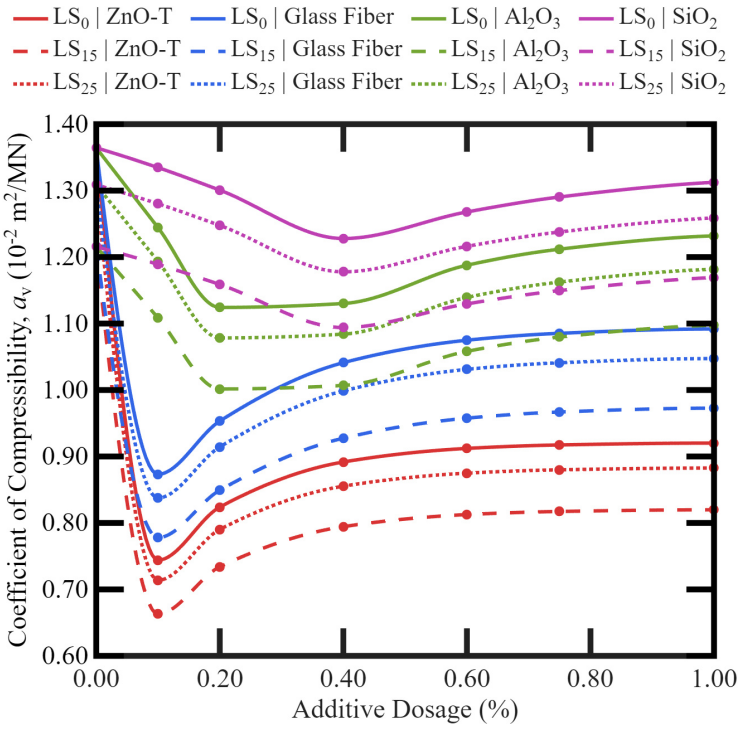


(c) Compression ratio

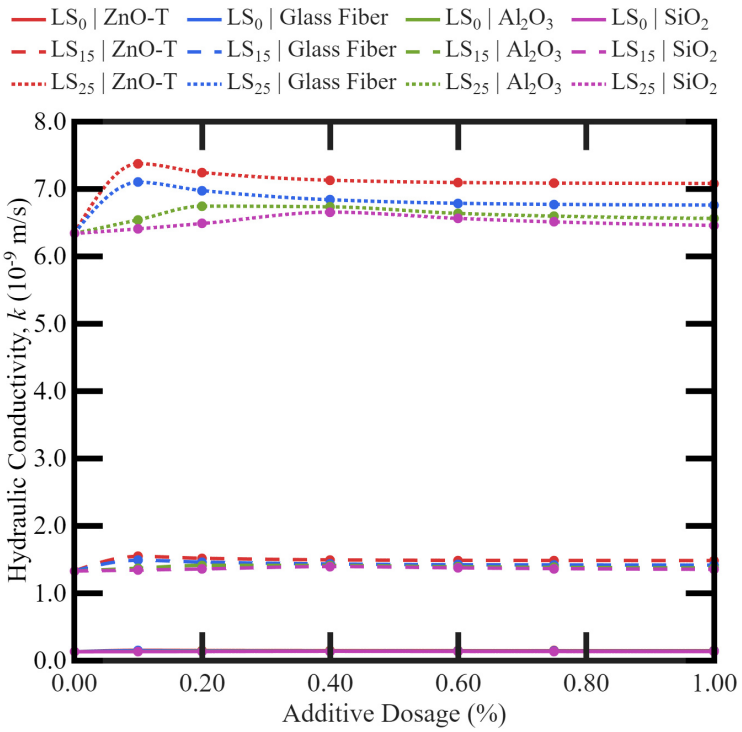


(d) Coefficient of volume compressibility

Figure 3.24: Dosage-dependent response of LS_0, LS_{15}, and LS_{25} treated with ZnO-T, glass fibre, Al_2O_3, and SiO_2, with dosage expressed as a percentage of oven-dry soil mass and the plotted quantities comprising SENB peak load, apparent Mode-I initiation toughness, compression ratio, and coefficient of volume compressibility, where the SENB quantities were obtained using the representative specimen preparation, notch-forming, three-point loading, dual-CMOD measurement, and 0.006 mm s^{-1} displacement rate used for the untreated soils and the consolidation quantities were obtained from separately prepared dosage-specific specimens tested in accordance with ASTM D2435/D2435M



(e) Coefficient of compressibility



(f) Hydraulic conductivity

Figure 3.24: Continuation of Figure 3.24

Table 3.15: Optimum additive dosages and approximate responses read from Figure 3.24, summarizing load, fracture toughness, compressibility, hydraulic response, and barrier suitability.

Soil	Additive	Dosage	Mechanical response	Compressibility and hydraulic response
LS_0	ZnO-T	0.10%	$P_{max} \approx 3.15$ N; $K_{Ic} \approx 1.17$ kPam$^{0.5}$	$C_r \approx 0.80$; $m_v \approx 0.40$; $a_v \approx 0.74$; $k \approx 0.14$. Best coupled response.
	Glass fiber	0.10%	$P_{max} \approx 2.95$ N; $K_{Ic} \approx 1.09$ kPam$^{0.5}$	$C_r \approx 0.93$; $m_v \approx 0.47$; $a_v \approx 0.87$; $k \approx 0.14$. Secondary mechanical option.
	Al_2O_3	0.20-0.40%	$P_{max} \approx 2.50$ N; $K_{Ic} \approx 0.93$ kPam$^{0.5}$	$C_r \approx 1.20$; $m_v \approx 0.61$; $a_v \approx 1.12$; $k \approx 0.13$. Lower fracture toughness gain.
	SiO_2	0.40%	$P_{max} \approx 2.30$ N; $K_{Ic} \approx 0.85$ kPam$^{0.5}$	$C_r \approx 1.31$; $m_v \approx 0.67$; $a_v \approx 1.23$; $k \approx 0.13$. Limited benefit.
LS_{15}	ZnO-T	0.10%	$P_{max} \approx 3.60$ N; $K_{Ic} \approx 1.34$ kPam$^{0.5}$	$C_r \approx 0.42$; $m_v \approx 0.40$; $a_v \approx 0.66$; $k \approx 1.50$. Mechanically strongest, hydraulically marginal.
	Glass fiber	0.10%	$P_{max} \approx 3.35$ N; $K_{Ic} \approx 1.25$ kPam$^{0.5}$	$C_r \approx 0.49$; $m_v \approx 0.46$; $a_v \approx 0.77$; $k \approx 1.45$. Good fracture toughness, marginal k.
	Al_2O_3	0.20%	$P_{max} \approx 2.88$ N; $K_{Ic} \approx 1.07$ kPam$^{0.5}$	$C_r \approx 0.64$; $m_v \approx 0.60$; $a_v \approx 1.00$; $k \approx 1.35$. Moderate coupled response.
	SiO_2	0.40%	$P_{max} \approx 2.62$ N; $K_{Ic} \approx 0.98$ kPam$^{0.5}$	$C_r \approx 0.70$; $m_v \approx 0.65$; $a_v \approx 1.09$; $k \approx 1.35$. Lower mechanical gain.
LS_{25}	ZnO-T	0.10%	$P_{max} \approx 1.80$ N; $K_{Ic} \approx 0.67$ kPam$^{0.5}$	$C_r \approx 0.97$; $m_v \approx 0.42$; $a_v \approx 0.71$; $k \approx 7.4$. Hydraulically unsuitable.

Table 3.15: Optimum additive dosages and approximate responses, continued.

Soil	Additive	Dosage	Mechanical response	Compressibility and hydraulic response
	Glass fiber	0.10%	$P_{max} \approx 1.67$ N; $K_{Ic} \approx 0.62$ kPam$^{0.5}$	$C_r \approx 1.13$; $m_v \approx 0.49$; $a_v \approx 0.83$; $k \approx 7.1$. Hydraulically unsuitable.
	Al_2O_3	0.20%	$P_{max} \approx 1.42$ N; $K_{Ic} \approx 0.53$ kPam$^{0.5}$	$C_r \approx 1.46$; $m_v \approx 0.63$; $a_v \approx 1.08$; $k \approx 6.8$. Low fracture toughness and high k.
	SiO_2	0.40%	$P_{max} \approx 1.30$ N; $K_{Ic} \approx 0.49$ kPam$^{0.5}$	$C_r \approx 1.60$; $m_v \approx 0.69$; $a_v \approx 1.17$; $k \approx 6.6$. Not suitable for clay liner screening.

Note: P_{max} = peak load; K_{Ic} = Mode I fracture toughness; C_r = compression ratio; m_v = coefficient of volume compressibility; a_v = coefficient of compressibility; k = hydraulic conductivity. C_r is reported in 10^{-2}; m_v and a_v are reported in 10^{-2} m^2/MN; k is reported in 10^{-9} m/s.

Table 3.15 converts Figure 3.24 into a coupled design decision. The same dosage that maximizes fracture toughness must also preserve low hydraulic conductivity and reduce compressibility. The table, therefore, separates a mechanically favourable additive from a barrier favourable additive. ZnO-T at 0.10% is the optimum for LS_0 because it increases P_{max} and K_{Ic}, reduces C_r, m_v, and a_v, and keeps k below 1.0×10^{-9} m/s. In contrast, ZnO-T at the same dosage improves LS_{15} mechanically but does not bring its k below the screening line; for LS_{25}, even the best mechanical response remains below the fracture toughness threshold and far above the hydraulic threshold. This is the central interpretation of the nanomaterial results: an additive cannot be selected from a single peak in the plots; it must be selected from the coupled response of all six measured quantities.

3.9 Proposed K_{Ic}-k-a_v interrelationship for clay barrier design

The experimental results support the proposed interrelationships among fracture toughness, hydraulic conductivity, and coefficient of compressibility. The need for this coupling follows directly from the fact that compacted barriers fail by combined hydraulic, mechanical, and

fabric-evolution processes rather than by permeability alone (**AlbrechtBenson2001**; Rowe, 2005; C. S. Tang, Shi, et al., 2011). These quantities describe three coupled aspects of barrier behaviour. K_{Ic} measures resistance to crack initiation; k measures intact hydraulic sealing capacity; and a_v measures compressibility and fabric susceptibility to rearrangement under stress. A useful clay barrier must perform well in all three dimensions.

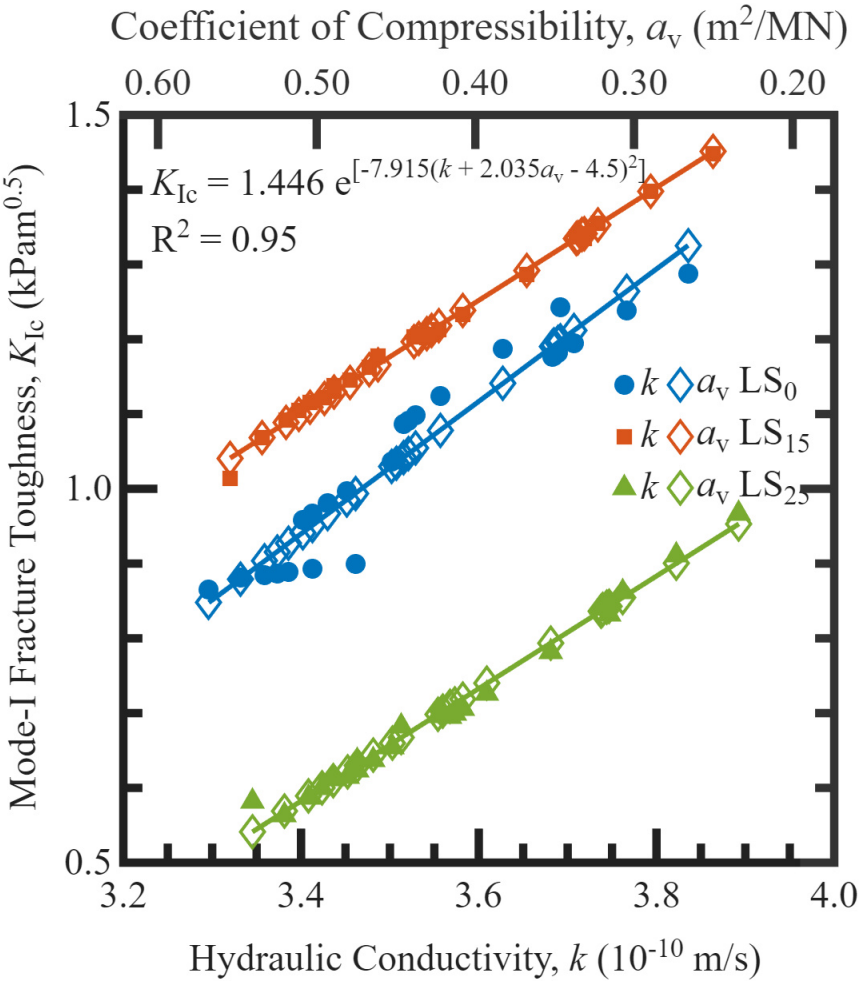


Figure 3.25: Empirical relationship among apparent Mode-I initiation toughness K_{Ic}, intact saturated hydraulic conductivity k, and coefficient of compressibility a_v for the tested LS_0, LS_{15}, and LS_{25} material states, with values compiled from separate but compositionally matched SENB, ASTM D5084 hydraulic-conductivity, and ASTM D2435/D2435M consolidation specimens including the dosage-specific states shown in Figure 3.24, and with the fitted surface describing the association within the calibration dataset rather than an independently validated constitutive law

Figure 3.25 is an important result of the chapter because it places K_{Ic}, k, and a_v on the same material-state map. The plotted laboratory hydraulic conductivity range is approximately 3.3-3.9 $\times 10^{-10}$ m/s, while a_v decreases from about 0.60 to 0.20 m^2/MN along the upper axis. Within this space, K_{Ic} increases from about 0.55 to 0.95 $kPam^{0.5}$ for LS_{25}, from about 0.80 to 1.25 $kPam^{0.5}$ for LS_0, and from about 1.0 to 1.45 $kPam^{0.5}$ for LS_{15}. The fitted expression, $K_{Ic} = 1.446 \exp[-7.915(k + 2.035a_v - 4.5)^2]$, gives $R^2 = 0.95$, showing that the relationship is not a loose qualitative trend. It is a quantitative coupling among crack resistance, pore-flow potential, and compressibility.

The fitted relationship shows a statistical association among the measured or derived values of fracture resistance, hydraulic conductivity, and compressibility for the tested dataset.The fitted relationship shows a statistical association among the measured or derived values of fracture resistance, hydraulic conductivity, and compressibility within the tested dataset. It does not demonstrate that one microstructural mechanism governs all three quantities. Water content, density, pore structure, mineralogy, composition, and preparation method may affect the three responses in different proportions. The separation among the plotted soil bands remains useful for screening because LS_{15} has the highest fitted fracture-toughness band but not the best hydraulic-barrier status, LS_{25} has the lowest fitted fracture-toughness band and comparatively high intact hydraulic conductivity, and LS_0 provides the most favourable hydraulic response among the laboratory mixtures.

Figure 3.25 combines three quantities that are relevant to geotechnical design: apparent Mode-I initiation toughness, intact hydraulic conductivity, and coefficient of compressibility. The figure provides an empirical material-state map for the calibration dataset. It does not prove that the same pore structure or particle-contact network controls all three responses, nor does it establish a continuous sand skeleton, crack-bridging mechanism, or loss of clay continuity.

This interrelationship also creates a practical basis for comparing laboratory and field soils. Instead of asking whether one K_{Ic} value is larger than another, the designer can ask whether the measured fracture toughness is consistent with the hydraulic and compressibility state. That consistency matters because the barrier does not experience fracture, seepage, and compression as independent phenomena in service. Differential settlement, wetting-drying, and leachate pressure can act simultaneously, so a set of design parameters must be interpreted as a coupled state.

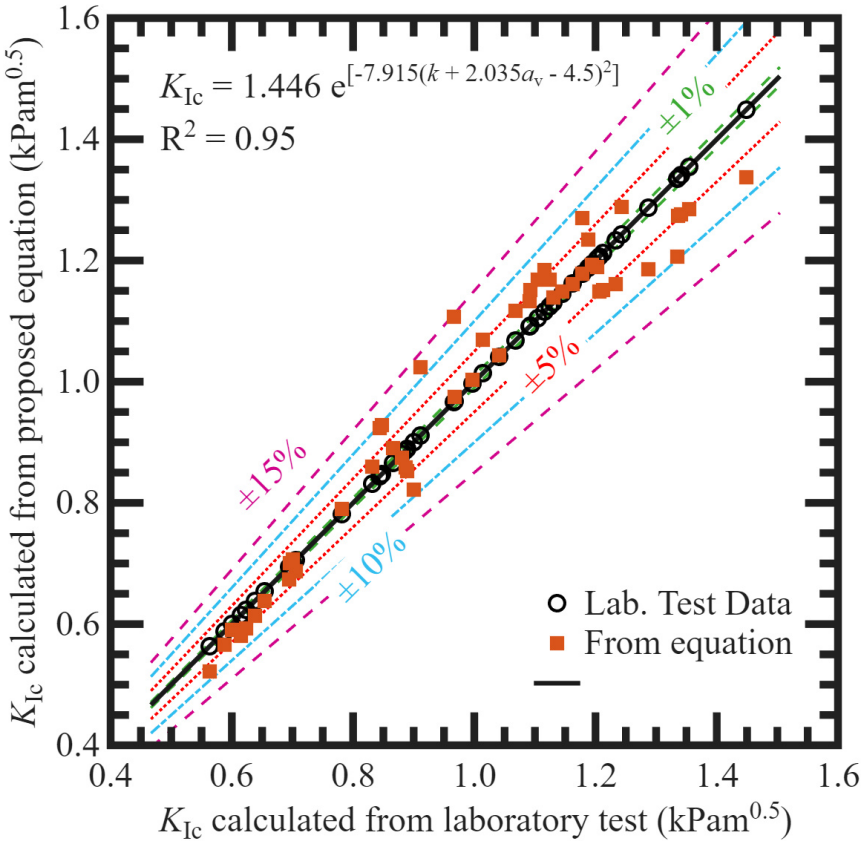


Figure 3.26: Measured versus predicted apparent Mode-I initiation toughness for the empirical K_{Ic}, k, and a_v equation, showing the equality line and the ±5%, ±10%, and ±15% agreement bands, with the measured and predicted values based on the same LS_0, LS_{15}, and LS_{25} dataset used to estimate the equation coefficients and therefore representing a goodness-of-fit assessment rather than validation against an independent or withheld dataset

Figure 3.26 provides the empirical association within the calibration dataset for the proposed interrelationship. The measured laboratory values cover roughly 0.55-1.45 kPam$^{0.5}$, and most predicted values fall close to the equality line. The ±5% band captures the central portion of the data, while the ±10% and ±15% bands contain the remaining scatter. This agreement is meaningful because the predicted K_{Ic} is computed from k and a_v, rather than fitted independently for each point. The result indicates that fracture resistance is connected to hydraulic and compressibility parameters measured on the same material family. A point outside the close bands would therefore indicate either an unusual material fabric or a testing issue such as notch disturbance, moisture non-uniformity, eccentric loading, or local field-soil heterogeneity.

The comparison between measured and predicted values is also useful because it provides a quantitative measure of experimental repeatability. A design dataset in which most points lie within ±10% of the equality line can be treated as internally consistent for proposed screening. A result outside ±15% should not be discarded automatically, but it should be interrogated before use in design. In this sense, Figure 3.26 is both a regression validation and a laboratory quality control diagram: it defines when a measured fracture toughness value is compatible with the hydraulic and compressibility state of the same compacted material.

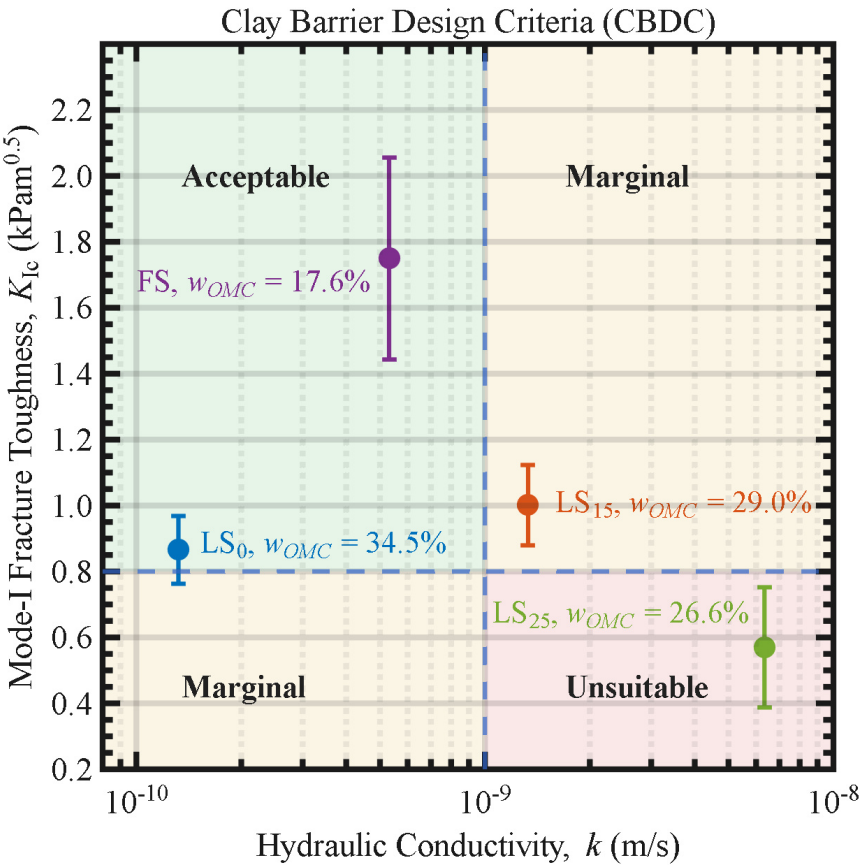


Figure 3.27: Preliminary material-screening chart combining representative near-OMC apparent Mode-I initiation toughness and intact saturated hydraulic conductivity for LS_0, LS_{15}, LS_{25}, and FS, with fracture values obtained from Geometry C SENB specimens having $W = B = 50$ mm, $L = 250$ mm, and $S = 200$ mm over $0.45 \leq a/W \leq 0.55$ at a loading rate of 0.006 mm s^{-1}, hydraulic-conductivity values measured on separate intact saturated specimens in accordance with ASTM D5084, and the boundaries $k \leq 1.0 \times 10^{-9}$ m s^{-1} and $K_{Ic} \geq 0.8$ kPa$\sqrt{\text{m}}$ identified as preliminary research-screening limits rather than ASTM or regulatory acceptance criteria

Figure 3.27 translates the laboratory programme into a proposed screening framework using $k \leq 1.0 \times 10^{-9}$ m/s and $K_{Ic} \geq 0.8$ kPam$^{0.5}$. LS_0 plots in the acceptable region with $k = 0.132 \times 10^{-9}$ m/s and K_{Ic} close to 0.86 kPam$^{0.5}$ at $w_{OMC} \approx 34.5\%$. FS is the strongest point in the acceptable region, with $k = 0.531 \times 10^{-9}$ m/s and wet-state K_{Ic} approximately 1.7-1.8 kPam$^{0.5}$ at $w_{OMC} \approx 17.6\%$. LS_{15} has favourable crack resistance, about 1.0 kPam$^{0.5}$, but $k = 1.330 \times 10^{-9}$ m/s places it in the marginal hydraulic region. LS_{25} is unsuitable because $k = 6.340 \times 10^{-9}$ m/s and K_{Ic} is only about 0.57 kPam$^{0.5}$.

The significance of Figure 3.27 is that it changes the clay barrier acceptance logic from single property screening to coupled performance screening. Conventional design asks whether k is low enough; the fracture based framework asks whether the material will also resist the crack that could bypass the intact matrix. This is why LS_{15} is not automatically accepted despite good K_{Ic}, and why LS_0 remains attractive despite not having the highest fracture toughness. The figure, therefore, provides a rational bridge between laboratory SENB testing and design practice: a soil must seal when intact and must also resist the tensile crack that would undermine that sealing assumption.

The screening chart is therefore simple in appearance but conceptually important. It shifts clay barrier acceptance from an intact-matrix permeability check to a coupled check of crack resistance and sealing. The lower-right region represents soils that may seal poorly even if they are mechanically resistant. The upper-left region represents soils that seal well but may crack too easily. The acceptable region requires both. This is the essential design message of Chapter 3: a low value of k is necessary, but it is not sufficient unless the material also has enough K_{Ic} to resist the formation of the crack that would bypass the intact matrix.

3.10 Chapter summary

This chapter developed and applied a comprehensive experimental framework to measure the Mode I fracture toughness of compacted clay barrier soils and to interpret it alongside hydraulic conductivity and compressibility. The results support the following conclusions.

First, conventional soil tests indicate that material selection cannot be based solely on density or hydraulic conductivity. LS_0 provides the best laboratory sealing response with $k = 0.132 \times 10^{-9}$ m/s; LS_{15} provides the best laboratory-mixture fracture toughness near 1.0 kPam$^{0.5}$ but has $k = 1.330 \times 10^{-9}$ m/s; LS_{25} is hydraulically unfavourable with $k = 6.340 \times 10^{-9}$ m/s and low fracture toughness; and FS combines $k = 0.531 \times 10^{-9}$ m/s with the highest wet-state fracture toughness, about 1.7-1.8 kPam$^{0.5}$.

Second, the developed SENB laboratory setup is a central contribution of the chapter. The system provides low-load resolution, displacement control, dual CMOD measurement, and moulded notches, all of which are necessary for testing weak, moisture-sensitive clay beams. The load-CMOD curves and crack photographs show stable crack initiation from the notch and support an LEFM-based interpretation of fracture toughness.

Third, the SENB geometry correction function $f(a/W)$ is developed through numerical, analytical, and experimental methods. The Abaqus® contour integral model is verified against the ASTM metallic benchmark. The analytical derivation used a weight-function formulation with exact integration terms, and the experimental compliance route verified the function against the measured crack-opening response. This three-route validation provides a defensible soil-specific correction factor.

Fourth, raw peak load is strongly geometry dependent, but corrected K_{Ic} is much less sensitive to crack length over $a/W = 0.45$-0.55. The coefficient of variation analysis identifies the $W = B = 50$ mm SENB specimen as the most reliable geometry, with COV values as low as 1.0% for LS_0 and 0.5% for LS_{15} at $a/W = 0.50$.

Fifth, fracture resistance is governed by the water-content and density state. Higher dry density was generally associated with greater apparent Mode-I initiation resistance, while higher water content was associated with lower resistance within each soil series. Because suction and contact-scale properties were not measured, their separate contributions could not be resolved. The near OMC fracture toughness values are the relevant design values: approximately 0.86-0.87 $\mathrm{kPam}^{0.5}$ for LS_0, 0.99-1.01 $\mathrm{kPam}^{0.5}$ for LS_{15}, 0.51-0.62 $\mathrm{kPam}^{0.5}$ for LS_{25}, and 1.70-1.83 $\mathrm{kPam}^{0.5}$ for FS.

Finally, the proposed K_{Ic}-k-a_{v} interrelationship and screening chart provide a direct means to incorporate fracture resistance into clay barrier design. The proposed screening limits, $k \leq 1.0\times10^{-9}$ m/s and $K_{\mathrm{Ic}} \geq 0.8$ $\mathrm{kPam}^{0.5}$, classify LS_0 and FS as acceptable, LS_{15} as hydraulically marginal, and LS_{25} as unsuitable for the investigated barrier criterion. The framework supplies the experimental foundation for the numerical crack propagation and coupled fracture-hydromechanical analyses developed in the following chapters.

Chapter 4

Advanced Numerical and sequential mechanical-fracture and pore-network flow model

Chapter 3 established the experimental basis for fracture based clay barrier design through the developed SENB setup, the adopted geometry correction function $f(a/W)$, the measured apparent Mode-I initiation toughness, and the proposed K_{Ic}-k-a_{v} screening map. The developed $f(a/W)$ is carried forward as the common reduction used to compare the experimental and simulated SENB responses. The first part of this chapter compares four numerical fracture formulations using the selected experimental initiation, toughness, and visible-path measures. The method that provided the closest combined agreement for the examined cases and an explicit discontinuity graph was then used for the pore-network extension. The resulting LEM-PNM calculation is a sequential one-way fracture-to-flow prediction and is not an independently validated two-way hydromechanical model.

4.1 Technical logic of the chapter

The central purpose of this chapter is to compare the four fracture formulations under the same SENB geometry, material inputs, loading sequence, and evaluation criteria before selecting a method for the present fracture-to-flow workflow. XFEM, STFEM, phase-field fracture, and LEM were therefore evaluated using the same two-dimensional SENB cases. LEM was selected because it provided the closest combined agreement with the examined experimental fracture-toughness

trends and visible crack paths and because it directly supplied a failed-link graph and displacement jumps for hydraulic mapping. This selection is specific to the implementations, parameters, discretizations, and cases examined in this study and is not a universal ranking of the four methods. The PNM was subsequently developed as a sequential hydraulic extension of the selected LEM output.

This ordering is important. A hydraulic calculation based on an inaccurate representation of the crack may produce visually plausible seepage figures while remaining mechanically incorrect. For example, an imposed pore-network update can increase conductivity in damaged regions, but the resulting increase is not meaningful unless the mechanical solver has generated a realistic crack path and a connected aperture field. Conversely, a fracture method can match a peak load or an apparent fracture toughness while still producing a crack path that is too smooth, too mesh constrained, too diffuse, or not hydraulically connected. The validation part of this chapter, therefore, treats crack propagation itself as the primary evidence. The subsequent hydraulic section uses LEM because it provided an explicit failed-link graph and displacement jumps and gave the closest combined agreement for the SENB cases examined in this study.

The mechanical comparison uses the SENB test because this geometry provides a well-controlled Mode-I-dominated crack path from a predefined notch. The crack is forced to initiate at a known location but remains free to select its propagation path through the ligament. In the numerical study, XFEM, STFEM, and phase-field simulations were performed on triangular finite-element meshes, whereas LEM used a Poisson random lattice generated through Voronoi tessellation and Delaunay triangulation. A nominal discretization length of 1 mm was adopted for the production calculations. Its adequacy was assessed from the mesh-dependency results reported in Appendix B using peak load, initiation step, CMOD, fracture work, and discontinuity path; matching the numerical spacing to the nominal notch width was not used as the convergence criterion. The loading is displacement-controlled, as in the experimental setup, with a vertical displacement increment of

$$\Delta \bar{u}_y = 0.001 \text{ mm} \tag{4.1}$$

per accepted step. The specimen dimensions, notch ratio a/W, and ratio a/B were varied according to the present study specimen matrix.

The second part of the chapter moves from two-dimensional SENB validation to three-dimensional sequential one-way mechanical-fracture-to-flow coupling simulations. In that part, three soil states, denoted LS_0, LS_{15}, and LS_{25}, are analysed under two loading conditions. The first is an unconfined compression loading case with pore pressure $p_w = 100$ kPa. The second is a triaxial loading case with confining pressure $\sigma_3 = 100$ kPa and pore pressure $p_w = 100$ kPa. The displacement increment remains 0.001 mm per step, and the spatial discretization remains 1 mm. The objective of the PNM part is to determine how crack initiation, crack coalescence, aperture

opening, and hydraulic connectivity alter the equivalent hydraulic conductivity.

4.2 SENB formulation common to all four fracture solvers

4.2.1 Geometry, boundary conditions, and recorded quantities

Let $\Omega \subset \mathbb{R}^2$ denote the SENB domain. The initial notch is denoted by Γ_0, the propagated crack by Γ_c, and the total fracture set by

$$\Gamma_f = \Gamma_0 \cup \Gamma_c \tag{4.2}$$

The main dimensionless geometry parameters are

$$\alpha = \frac{a}{W} \qquad \beta = \frac{a}{B} \tag{4.3}$$

where a is the notch length, W is the specimen width, and B is the specimen thickness. The support span is denoted by S. For an SENB specimen, the imposed vertical displacement is applied at the loading point, while the lower supports provide the bending reaction. In numerical models, this yields a quasistatic incremental boundary-value problem rather than a force-controlled instability problem.

The continuum statement before the crack advance is

$$\operatorname{div} \boldsymbol{\sigma} = \mathbf{0} \qquad \text{in } \Omega \setminus \Gamma_f \tag{4.4}$$

$$\mathbf{u} = \bar{\mathbf{u}} \qquad \text{on } \Gamma_u \tag{4.5}$$

$$\boldsymbol{\sigma}\mathbf{n} = \bar{\mathbf{t}} \qquad \text{on } \Gamma_t \tag{4.6}$$

$$\boldsymbol{\sigma}\mathbf{n}_c = \mathbf{t}_c \qquad \text{on } \Gamma_c \tag{4.7}$$

Here $\mathbf{u}$ is displacement, $\boldsymbol{\sigma}$ is the Cauchy stress tensor, $\mathbf{n}$ is the boundary normal, Γ_u is the displacement controlled boundary, and $\mathbf{t}_c$ is the cohesive or residual traction acting on the crack faces. For a traction-free crack, $\mathbf{t}_c = \mathbf{0}$. The weak form used by the continuum-based formulations is

$$\int_{\Omega \setminus \Gamma_f} \boldsymbol{\varepsilon}(\delta\mathbf{u}) : \boldsymbol{\sigma}(\mathbf{u}) \, \mathrm{d}\Omega - \int_{\Gamma_t} \delta\mathbf{u} \cdot \bar{\mathbf{t}} \, \mathrm{d}\Gamma - \int_{\Gamma_c} [\![\delta\mathbf{u}]\!] \cdot \mathbf{t}_c \, \mathrm{d}\Gamma = 0 \tag{4.8}$$

where $[\![\cdot]\!]$ is the displacement jump across the crack. For the lattice model, the same physical equilibrium is enforced through nodal force balance over a connected set of beam-like lattice links rather than over continuum elements.

At loading step n, the imposed displacement is updated by

$$\bar{u}_y^{n+1} = \bar{u}_y^n + 0.001 \text{ mm} \tag{4.9}$$

The reaction force P^n, crack-mouth opening displacement (CMOD), active crack set, crack extension, and failure status of elements or links are recorded at each accepted step. CMOD is evaluated at the notch mouth as

$$\text{CMOD}^n = \left(\mathbf{u}_R^n - \mathbf{u}_L^n\right) \cdot \mathbf{e}_x \tag{4.10}$$

where $\mathbf{u}_R^n$ and $\mathbf{u}_L^n$ are displacements at the right and left notch mouth points. CMOD is used because it detects crack opening earlier than global load alone and because it is sensitive to post-initiation softening.

The Mode-I fracture toughness used for comparison is obtained from the SENB relation

$$K_{\text{I}} = \frac{PS}{BW^{3/2}} f(a/W) \tag{4.11}$$

where $f(a/W)$ is the soil-specific SENB geometry correction function developed in Chapter 3. The same function is used in this chapter for experimental and numerical fracture toughness comparisons; therefore, the differences among XFEM, space-time FEM, phase-field fracture, and LEM are attributed to crack initiation, crack tracking, damage localization, and crack path representation rather than to changes in the geometry reduction equation. The direct metallic ASTM polynomial is not used as the controlling reduction for the clay barrier calculations because Chapter 3 showed that compacted soils require a recalibrated finite body amplification factor.

At the maximum (peak) load $P_{\max}$, the Mode-I fracture toughness used for validation is

$$K_{\text{Ic}} = \frac{P_{\max} S}{BW^{3/2}} f(a/W) \tag{4.12}$$

The common SENB comparison uses a homogeneous, isotropic, linear-elastic idealization before discontinuity initiation. The resulting K_{I} values are interpreted as apparent, state-conditioned initiation measures within the tested domain; the analysis does not establish metallic material behaviour or a negligible fracture-process zone. Nevertheless, K_{Ic} remains the correct common comparison metric after applying the developed soil-specific $f(a/W)$, because it reduces the measured or simulated peak load to a crack tip parameter over the same SENB geometry family. The theoretical basis follows the Griffith-Irwin fracture framework, the J-integral energy formulation, and quasibrittle size-effect extensions (Bazant and Planas, 1998; Griffith, 1921; Irwin, 1957; J. R. Rice, 1968; Tada, P. C. Paris, and Irwin, 1973).

4.2.2 Constitutive and fracture models used

The four numerical approaches used the same SENB geometry, boundary conditions, loading sequence, and calibrated macroscopic linear-elastic pre-fracture response. They differed, however, in the manner in which discontinuity initiation, material degradation, and subsequent propagation were represented.

In the XFEM model, the intact matrix was represented by homogeneous isotropic linear elasticity. The displacement approximation was enriched using a Heaviside function across the discontinuity and asymptotic crack-tip functions in the vicinity of the tip. In the final integrated implementation, crack or damage activation was stress based. The code evaluated the maximum principal tensile stress, denoted by σ_1, and activated the corresponding crack-growth region when

$$\mathcal{A}_{n+1}^{\mathrm{XFEM}} = \{\mathbf{x} \in \Omega : \sigma_1(\mathbf{x}) \geq f_t\}, \tag{4.13}$$

where f_t is the prescribed tensile strength. Once activated, the damage or enrichment state was updated irreversibly. The crack-direction update did not employ a mixed-mode maximum-circumferential-stress, maximum-energy-release-rate, or local-symmetry angle calculation. Because the analysed SENB configuration was symmetric and Mode-I dominated, crack tracking was constrained to the notch-connected central ligament. The implemented propagation direction was therefore a zero-kink continuation along the initial notch and specimen symmetry axis,

$$\theta_c = 0. \tag{4.14}$$

This prescribed direction rule is appropriate for the symmetric SENB benchmark considered here, but it should not be interpreted as a general mixed-mode crack-direction criterion.

In the STFEM model, the intact matrix was also represented by homogeneous isotropic linear elasticity. The imposed displacement history was divided into quasi-static space-time slabs, and the displacement and fracture variables were interpolated in both the spatial and pseudo-time coordinates. Within each slab, fracture evolution was represented using a rate-regularized AT2-type scalar damage formulation. The damage field evolved continuously within the slab, whereas a discrete crack-advance event was identified at the end of the slab from the high-damage region.

The preliminary slab-end crack set was defined as

$$\widetilde{\Gamma}_{c,n+1}^{\mathrm{ST}} = \left\{\mathbf{x} \in \Omega : d_{n+1}(\mathbf{x}) \geq d_{\mathrm{cr}}^{\mathrm{ST}}\right\}, \qquad d_{\mathrm{cr}}^{\mathrm{ST}} = 0.94, \tag{4.15}$$

where $d = 0$ denotes intact material and $d = 1$ denotes fully degraded material. Only the component of $\widetilde{\Gamma}_{c,n+1}^{\mathrm{ST}}$ that remained connected to the initial notch and extended ahead of the

previously identified tip was accepted as a crack increment. A lower iso-level, $d_{\text{tip}}^{\text{ST}} = 0.88$, was used only for numerical localization and tracking of the crack tip; it was not the fracture acceptance threshold. After an accepted increment, the damage history, crack-tip position, and degraded stiffness were transferred to the next slab. Pseudo-time therefore represented the ordered loading history and not physical dynamic time.

In the phase-field model, the intact response was homogeneous isotropic linear elasticity with a tensile/compressive strain-energy split. Fracture was represented by the scalar phase-field variable d, with $d = 0$ for intact material and $d = 1$ for fully fractured material. The adopted AT2 formulation used the degradation function

$$g(d) = (1 - d)^2 + k_r, \qquad 0 < k_r \ll 1, \tag{4.16}$$

where k_r is a small residual-stiffness parameter introduced to avoid singularity of the global stiffness matrix. Fracture evolution was controlled by the critical fracture energy G_c, the regularization length ℓ, and the tensile part of the elastic strain-energy density. Damage irreversibility was enforced through the history field

$$\mathcal{H}(\mathbf{x}, t) = \max_{0 \le s \le t} \psi_e^+ \left(\boldsymbol{\varepsilon}(\mathbf{x}, s)\right), \tag{4.17}$$

where ψ_e^+ is the tensile contribution to the elastic strain-energy density. Unlike XFEM, the phase-field model did not require an explicit crack-direction rule because the discontinuity emerged as a diffuse damage band from the regularized energy minimization problem.

In the LEM model, the material domain was represented by Timoshenko-type lattice links constructed from the random Voronoi–Delaunay network. The link stiffnesses were calibrated to recover the prescribed macroscopic linear-elastic response before fracture. For each link e, Mode-I opening failure was activated when

$$\sigma_{n,e} \ge f_{t,e}, \tag{4.18}$$

where $\sigma_{n,e}$ is the link normal stress and $f_{t,e}$ is its tensile strength. The corresponding shear-failure condition was

$$|\tau_e| \ge c_e + \sigma_{n,e} \tan \phi_e, \tag{4.19}$$

where τ_e, c_e, and ϕ_e are the link shear stress, cohesion, and friction angle, respectively. Following initiation, the link response followed a fracture-energy-controlled softening law rather than

instantaneous brittle deletion. Progressive failure of the notch-connected links generated the discrete discontinuity path and its associated opening.

In the sequential LEM–PNM analysis, the failed-link set and the corresponding link openings obtained from the mechanical calculation were transferred to the pore-network model. The calculated openings were converted into hydraulic apertures and local conductances before solving the network-flow problem. This was a one-way sequential fracture-to-flow transfer. Pore pressure calculated by the network model was not returned to the mechanical equilibrium equations.

None of the four SENB fracture models included a suction-dependent constitutive relationship, transient pore-pressure migration during the mechanical calculation, or a pore-pressure feedback term in the mechanical equilibrium equation. Consequently, the simulations represented mechanically driven fracture under the prescribed laboratory boundary conditions and should not be interpreted as sequential one-way mechanical-fracture-to-flow coupling unsaturated hydromechanical analyses.

4.2.3 Validation criteria

The comparison is based on four criteria. The first criterion is crack initiation location: a valid method must initiate the crack at the notch tip rather than from a support, boundary artifact, or artificial mesh singularity. The second is crack path realism: the crack should propagate through the ligament in a manner consistent with experimental crack propagation. The third is quantitative fracture response: the predicted K_{Ic} values must follow the experimental trends as a function of a/W, geometry family, and soil state. The fourth is suitability for coupled fracture flow modelling: the selected solver must provide crack aperture, crack connectivity, and a graph like representation from which a hydraulic network can be constructed without arbitrary post-processing. The fourth criterion is not a secondary programming convenience. It is a physical requirement. Hydraulic conductivity in a fractured geomaterial is controlled by connected transmissive pathways. A solver that gives a smooth damage contour or an enriched discontinuity can be converted to a hydraulic aperture field, but the conversion requires extra assumptions regarding crack connectivity, aperture localization, and isolated damage regions.

Table 4.1: Summary of the intact constitutive response, fracture initiation or damage criterion, and discontinuity representation adopted in each numerical approach used for the SENB simulations and sequential fracture-to-flow analysis.

Method	Intact constitutive response	Initiation or damage criterion	Fracture representation
Abaqus® contour-integral FEM	Homogeneous isotropic linear elasticity	Initiation not simulated; the notch and crack were stationary and predefined	Contour-integral evaluation of J and extraction of K_I for the stationary crack
XFEM	Homogeneous isotropic linear elasticity	Maximum principal tensile stress, $\sigma_1 \geq f_t$; zero-kink propagation along the notch-connected symmetry ligament	Sharp discontinuity represented by Heaviside and crack-tip enrichment functions
STFEM	Homogeneous isotropic linear elasticity in quasi-static space-time slabs	Rate-regularized AT2 damage evolution; slab-end crack set accepted when the notch-connected region reached $d \geq 0.94$	Thresholded diffuse damage band evolved and transferred between successive pseudo-time slabs
Phase field	Isotropic linear elasticity with a tensile/compressive strain-energy split	AT2 energy-based damage governed by G_c, ℓ, k_r, and the irreversible history field $\mathcal{H}$	Diffuse phase-field discontinuity without explicit crack tracking or a prescribed propagation direction
LEM	Timoshenko-type beam-link elasticity calibrated to the macroscopic elastic response	$\sigma_{n,e} \geq f_{t,e}$ and the Mohr–Coulomb-type condition $\lvert\tau_e\rvert \geq c_e + \sigma_{n,e} \tan \phi_e$	Discrete failed-link path with fracture-energy-controlled post-peak softening
LEM–PNM	LEM mechanical-fracture model followed by pore-network flow	LEM link-failure criteria and the resulting failed-link opening	One-way sequential transfer of mechanical aperture to network conductance; no pore-pressure feedback

4.3 Extended finite element method (XFEM)

4.3.1 Historical background and mathematical formulation

XFEM is developed to represent discontinuities independently of the finite element mesh. Its theoretical foundation is the partition-of-unity enrichment of the standard finite element approximation. The crack is permitted to cut through elements, while additional degrees of freedom represent displacement jumps and crack tip asymptotic fields (**BelytschkoBlack1999**; Moës, Dolbow, and Belytschko, 1999; Sukumar et al., 2000). Subsequent developments introduced cohesive crack growth, level-set crack tracking, and generalized enrichment strategies for more complicated discontinuity problems (Fries and Belytschko, 2010; Moës and Belytschko, 2002). In the present study, XFEM is used as a high-quality benchmark because it can propagate a crack from the SENB notch without remeshing.

The enriched displacement field is written as

$$\mathbf{u}^h(\mathbf{x}) = \sum_{i \in I} N_i(\mathbf{x}) \mathbf{u}_i + \sum_{j \in I_H} N_j(\mathbf{x}) H(\mathbf{x}) \mathbf{a}_j + \sum_{k \in I_T} N_k(\mathbf{x}) \sum_{m=1}^{4} F_m(\mathbf{x}) \mathbf{b}_{km} \tag{4.20}$$

Here I is the set of all nodes, I_H is the set of nodes enriched by the Heaviside jump function H, and I_T is the set of crack tip enriched nodes. The standard displacements are $\mathbf{u}_i$, the discontinuity enrichment degrees of freedom are $\mathbf{a}_j$, and the tip enrichment degrees of freedom are $\mathbf{b}_{km}$. For isotropic linear elasticity, the near-tip enrichment functions are commonly taken as

$$\{F_m\}_{m=1}^{4} = \left\{ \sqrt{r}\sin\frac{\theta}{2}, \sqrt{r}\cos\frac{\theta}{2}, \sqrt{r}\sin\frac{\theta}{2}\sin\theta, \sqrt{r}\cos\frac{\theta}{2}\sin\theta \right\} \tag{4.21}$$

where (r, θ) are local crack tip polar coordinates. The crack surface is described using level sets,

$$\Gamma_c = \{ \mathbf{x} : \phi(\mathbf{x}) = 0,\ \psi(\mathbf{x}) \le 0 \} \tag{4.22}$$

where ϕ is the signed distance to the crack and ψ locates the crack tip along the crack direction.

The discrete residual is

$$\mathbf{R}_{\mathrm{XFEM}}(\mathbf{d}) = \int_{\Omega \setminus \Gamma_c} \mathbf{B}_{\mathrm{XFEM}}^{T} \boldsymbol{\sigma} \, \mathrm{d}\Omega + \int_{\Gamma_c} \mathbf{N}_{\Gamma}^{T} \mathbf{t}_c \, \mathrm{d}\Gamma - \mathbf{f}_{\mathrm{ext}} = \mathbf{0} \tag{4.23}$$

The tangent matrix is

$$\mathbf{K}_{\mathrm{XFEM}} = \int_{\Omega \setminus \Gamma_c} \mathbf{B}_{\mathrm{XFEM}}^{T} \mathbf{D} \mathbf{B}_{\mathrm{XFEM}} \, \mathrm{d}\Omega + \int_{\Gamma_c} \mathbf{N}_{\Gamma}^{T} \frac{\partial \mathbf{t}_c}{\partial \, [\![\mathbf{u}]\!]} \mathbf{N}_{\Gamma} \, \mathrm{d}\Gamma \tag{4.24}$$

Cut elements require special quadrature, because the enrichment introduces discontinuous fields within an element. In the SENB simulations, this makes the crack representation geometrically flexible, but it also places considerable weight on crack tracking and on the rule used to update the crack direction.

4.3.2 XFEM SENB model and interpretation

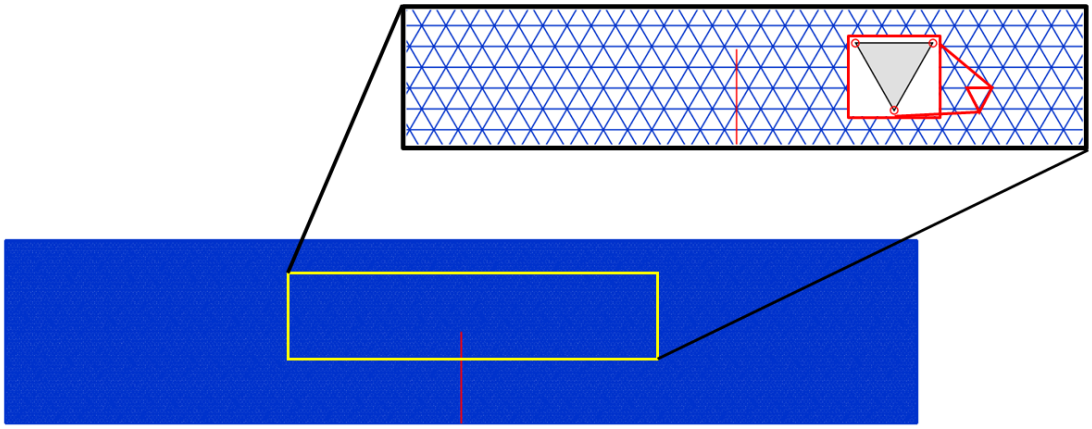
Figure 4.1 shows the two components that matter for judging the XFEM implementation. Part (a) shows the triangular finite element mesh and the predefined notch. Part (b) shows the support and loading condition used to reproduce the SENB experiment. The crack is not forced to coincide with element boundaries; instead, the mesh is used to approximate the displacement field while the level-set description carries the crack. This is a major advantage of XFEM over the conventional finite element method, as the crack can propagate from the notch without remeshing.

The limitation is equally important. In a quasibrittle soil specimen, the crack path is not only a mathematical discontinuity. It results from mesoscale heterogeneity, local tensile rupture, shear perturbations near the process zone, and the progressive coalescence of microcracks. XFEM can represent a sharp crack, but the crack path itself must be updated by a tracking rule. As a result, the method tends to produce a smooth crack trajectory unless the heterogeneity and crack direction algorithm are sufficiently rich. This is why XFEM is a useful benchmark, but it is not necessarily the best physical description of the experimentally observed crack surface in this study.

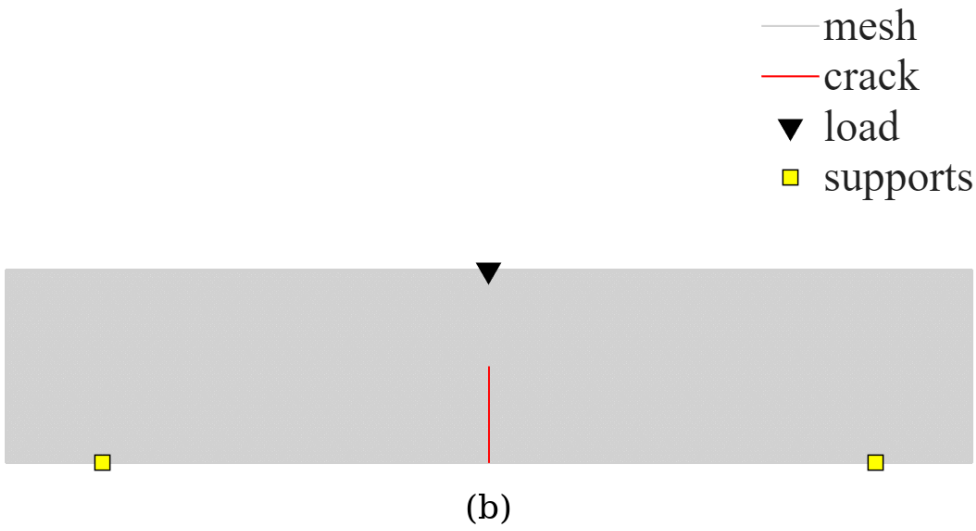
4.3.3 XFEM crack propagation result

Figure 4.2 shows that XFEM initiates the crack at the notch tip and advances it through the ligament. The four snapshots demonstrate a coherent Mode-I dominated crack. From a numerical fracture viewpoint, this is a successful calculation: the crack does not become unstable at the supports, does not require remeshing, and remains connected from the notch to the final fracture state. However, the same figure also reveals the primary shortcoming of this study. The crack is comparatively linear. It does not reproduce the experimentally observed irregularity of the fracture path, as observed with LEM. Smoothness is not merely aesthetic; it affects hydraulic extension because a smooth tracked crack yields a single idealized aperture surface, whereas the experimental crack exhibits local roughness, distributed microcracking, and variable connectivity.

In the later validation plots, XFEM also shows a systematic tendency to deviate from the experimental K_{Ic} trends for the soils considered in the present study and the geometry combinations. In some cases, it underpredicts the fracture toughness; in others, particularly for LS_0, it produces a



(a)



(b)

Figure 4.1: SENB modelled using XFEM: (a) triangular mesh and (b) displacement loading and boundary conditions.

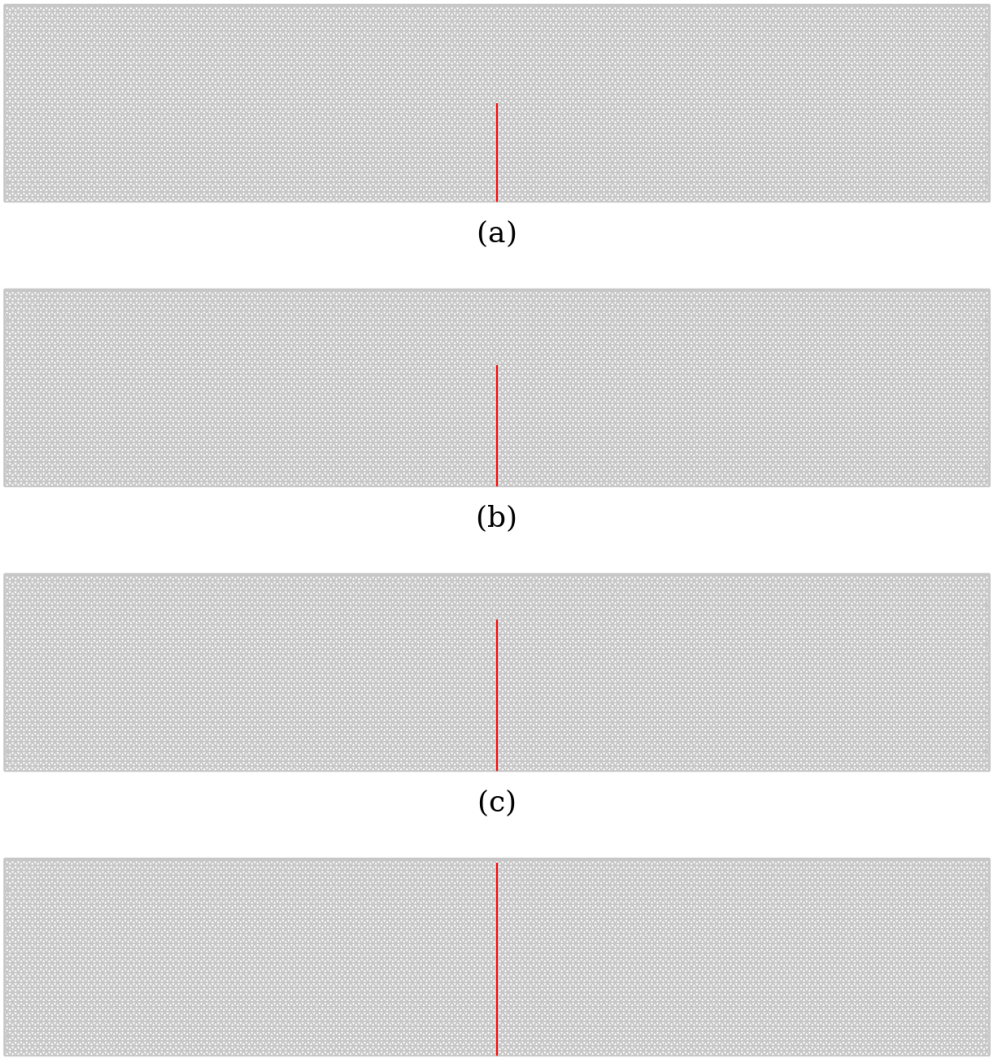


Figure 4.2: Crack propagation using the XFEM framework for the $B = W = 35$ mm, $a/W = 0.45$, LS_0 SENB specimen: (a) one-fourth, (b) two-fourths, (c) three-fourths, and (d) complete crack propagation.

non-smooth response over a/W with a marked jump near $a/W = 0.50$. This indicates that the method is sensitive to the crack tracking and enrichment configuration. XFEM, therefore, remains valuable for confirming that a sharp crack finite element approach can solve the SENB problem, but it is not selected as the basis for the coupled hydraulic model.

4.4 Space-time finite element method (STFEM)

4.4.1 Historical background and mathematical formulation

Space-time finite element methods formulate the unknown field over a combined spatial-temporal domain. Rather than solving a sequence of unrelated spatial problems, the method solves over time slabs $Q_n = \Omega \times [t_n, t_{n+1}]$. Space-time formulations have a long history in transient structural mechanics, electrodynamics, stabilized finite element methods, and moving-boundary problems (**HughesHulbert1988**; Tezduyar, 1992; Tezduyar, 2001). In this study, the "time" coordinate is used as a pseudo-time or load-history parameter because the SENB simulations are displacement-controlled and quasistatic. The method is therefore useful for organizing crack evolution as an event sequence over loading slabs.

The space-time weak form can be written as

$$\int_{t_n}^{t_{n+1}} \left[\int_{\Omega} \boldsymbol{\varepsilon}(\delta \mathbf{u}) : \boldsymbol{\sigma}(\mathbf{u}) \, \mathrm{d}\Omega - \int_{\Gamma_t} \delta \mathbf{u} \cdot \bar{\mathbf{t}} \, \mathrm{d}\Gamma \right] \mathrm{d}t + \mathcal{J}_n = 0 \tag{4.25}$$

where $\mathcal{J}_n$ contains the inter-slab continuity or jump terms. With a space-time interpolation,

$$\mathbf{u}^h(\mathbf{x}, t) = \sum_{a=1}^{n_s} \sum_{b=1}^{n_t} N_a(\mathbf{x}) M_b(t) \mathbf{u}_{ab} \tag{4.26}$$

where N_a are spatial shape functions and M_b are temporal shape functions. If inertia is retained, the dynamic residual over a slab is

$$\mathbf{R}_{\mathrm{ST}} = \int_{t_n}^{t_{n+1}} \left[\mathbf{M}\ddot{\mathbf{d}}(t) + \mathbf{f}_{\mathrm{int}}(\mathbf{d}(t)) - \mathbf{f}_{\mathrm{ext}}(t) \right] \mathrm{d}t + \mathbf{R}_{\mathrm{jump}} = \mathbf{0} \tag{4.27}$$

For the quasistatic SENB problem, the inertia term is suppressed or is numerically negligible, leaving a load-history controlled fracture calculation. Crack advance is accepted when a fracture criterion is satisfied at the end of a slab, after which the crack geometry and stiffness are updated for the next slab.

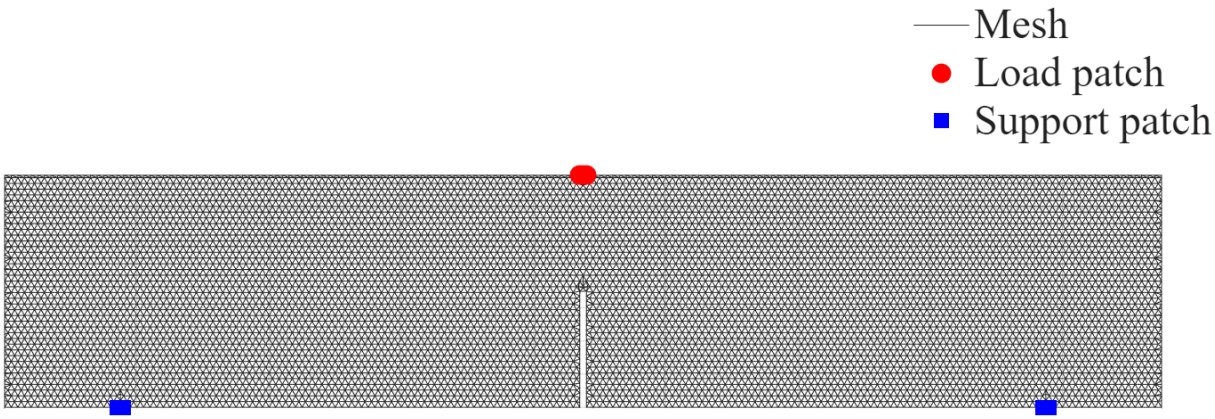


Figure 4.3: SENB modelled using the space-time finite element framework.

4.4.2 STFEM SENB model

Figure 4.3 presents the SENB model used for the STFEM calculation. The geometry and boundary conditions are kept consistent with the XFEM and phase-field cases. The advantage of the formulation is that the crack event is not treated as an isolated static bifurcation; instead, the progression from one loading step to the next is embedded in the slab structure. This gives a clean numerical framework for recording intermediate crack propagation and for managing history-dependent quantities.

For the present SENB validation, however, the critical issue is not only whether the solver remains stable over the loading history. The key question is whether the crack path and the resulting K_{Ic} trends are consistent with the experimental observations. The triangular mesh and event-driven crack representation still require a rule for crack localization. Therefore, STFEM improves temporal organization, but it does not eliminate the spatial challenge of representing an experimentally rough crack in heterogeneous soil.

4.4.3 STFEM crack propagation result

Figure 4.4 shows a sequential crack-growth pattern from the notch tip. The crack remains continuous, and the stages are easy to interpret. The result confirms that the STFEM implementation can advance the crack through the SENB ligament under the prescribed displacement increments. The method is therefore successful as a numerical framework for crack propagation.

In LS_0, the STFEM values tend to overpredict or remain above the experimental K_{Ic} trend for several geometry groups. In LS_{15} and LS_{25}, the response becomes more scattered: in some geometries, STFEM underpredicts the experiment, whereas in others it exhibits a pronounced peak

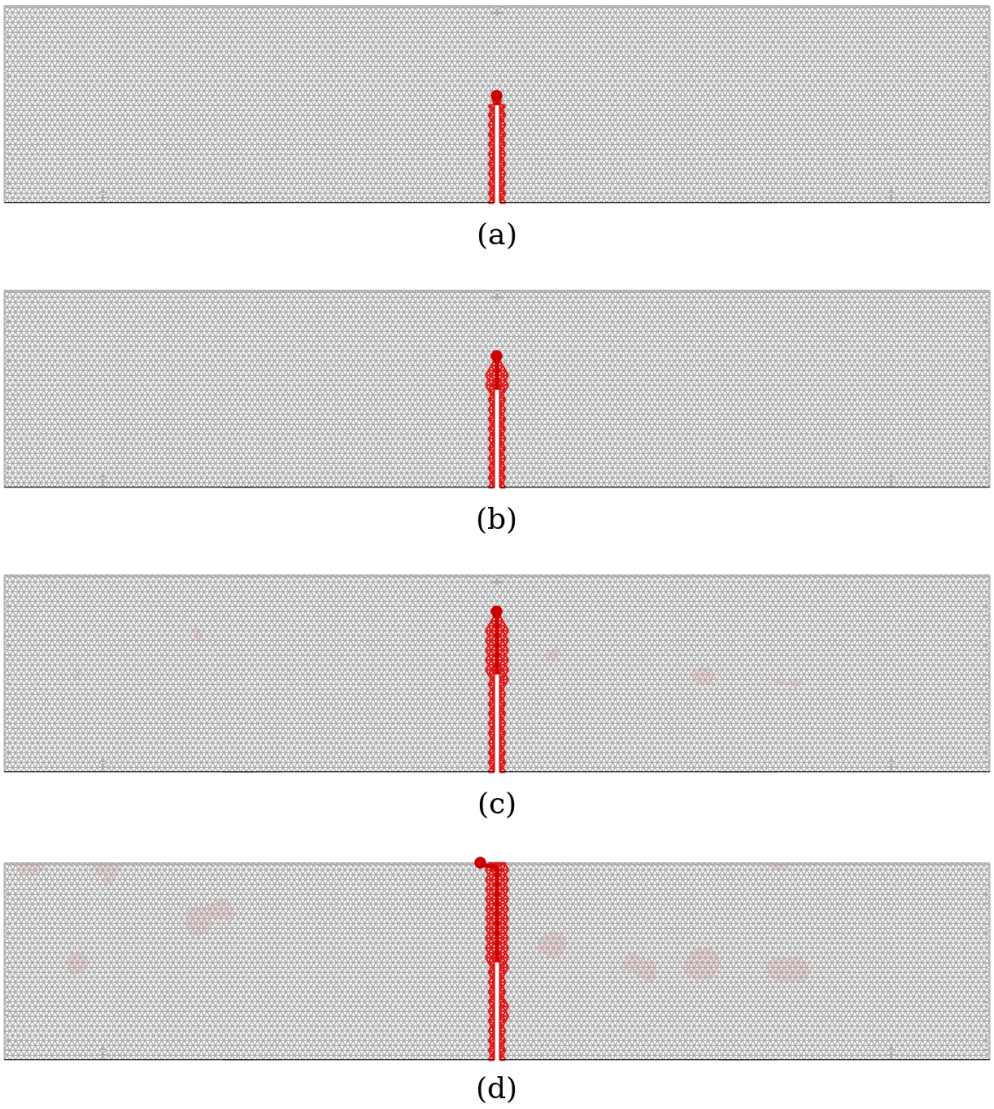


Figure 4.4: Crack propagation using the space-time finite-element framework for the $B = W = 35$ mm, $a/W = 0.45$, LS_0 SENB specimen: (a) one-fourth, (b) two-fourths, (c) three-fourths, and (d) complete crack propagation.

near $a/W = 0.50$. This indicates that the temporal slab formulation does not, by itself, correct the sensitivity of the crack-path prediction to spatial discretization, crack-direction updating, and material heterogeneity. STFEM is consequently treated as a valuable comparison method, but not as the production method for the hydraulic conductivity model.

4.5 Phase-field method

4.5.1 Historical background and mathematical formulation

Phase-field fracture models replace a sharp crack with a regularized scalar damage field. The method is rooted in the variational formulation of brittle fracture proposed by Francfort and Marigo and later regularized for numerical computation by Bourdin et al. (Bourdin, Francfort, and Marigo, 2008; Bourdin, Francfort, and Marigo, 2000; Francfort and Marigo, 1998). Modern phase-field formulations have become widely used because they avoid explicit crack tracking and can represent crack initiation, branching, and coalescence within a single variational framework (Ambati, Gerasimov, and De Lorenzis, 2015; Borden et al., 2012; Miehe, Hofacker, and Welschinger, 2010).

Let $d \in [0, 1]$ be the phase-field damage variable, where $d = 0$ denotes intact material and $d = 1$ denotes fully broken material. The regularized energy functional is

$$\Pi(\mathbf{u}, d) = \int_\Omega \left[g(d)\psi_e^+(\boldsymbol{\varepsilon}) + \psi_e^-(\boldsymbol{\varepsilon}) \right] \mathrm{d}\Omega + G_\mathrm{c} \int_\Omega \gamma_\ell(d, \nabla d)\mathrm{d}\Omega - W_\mathrm{ext} \tag{4.28}$$

where G_c is the critical fracture energy, ℓ is the regularization length, and $g(d)$ is the degradation function. A common choice is

$$g(d) = (1 - d)^2 + k_\mathrm{r}, \qquad 0 < k_\mathrm{r} \ll 1 \tag{4.29}$$

where k_r is a residual stiffness used to avoid singular stiffness matrices. The crack density functional is commonly written as

$$\gamma_\ell(d, \nabla d) = \frac{d^2}{2\ell} + \frac{\ell}{2}|\nabla d|^2 \tag{4.30}$$

The tensile part of the strain energy drives damage, whereas the compressive part remains intact or is only weakly degraded, preventing insubstantial damage growth in compression. The strong forms associated with the staggered solution are

$$\operatorname{div} \boldsymbol{\sigma} = \mathbf{0} \tag{4.31}$$

$$G_\mathrm{c} \left(\frac{d}{\ell} - \ell \Delta d \right) - 2(1 - d)\mathcal{H} = 0 \tag{4.32}$$

where $\mathcal{H}$ is the history field enforcing irreversibility:

$$\mathcal{H}(\mathbf{x}, t) = \max_{s \in [0,t]} \psi_e^+(\boldsymbol{\varepsilon}(\mathbf{x}, s)) \tag{4.33}$$

The displacement and phase-field equations are solved iteratively until both residuals are below tolerance. The approximate crack set is extracted as a contour satisfying $d \geq d_c$, where d_c is typically near 0.8.

4.5.2 Phase-field SENB model

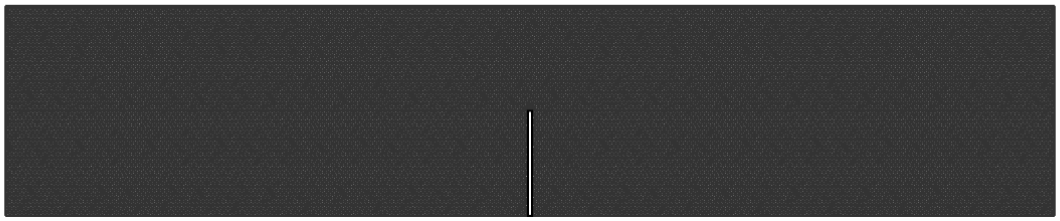
Figure 4.5 shows the phase-field SENB model. The triangular mesh is used to approximate both displacement and damage fields. A key advantage is that the method does not require an explicit crack tracking algorithm. Crack growth is characterized by the localization of the scalar phase field. For complex crack branching, this is attractive because branching can occur without changing mesh topology.

The limitation is the regularization length. The crack is not a line; it is a band of width controlled by ℓ and the mesh size. In a SENB specimen with a predefined 1 mm crack width and a 1 mm mesh size, the phase-field length scale must be chosen carefully. If ℓ is too large, the crack is over-diffuse and the fracture energy is spread over a broad process zone. If ℓ is too small relative to the mesh, the damage field becomes under-resolved and loses numerical robustness. This length-scale sensitivity is central to interpreting the phase-field results.

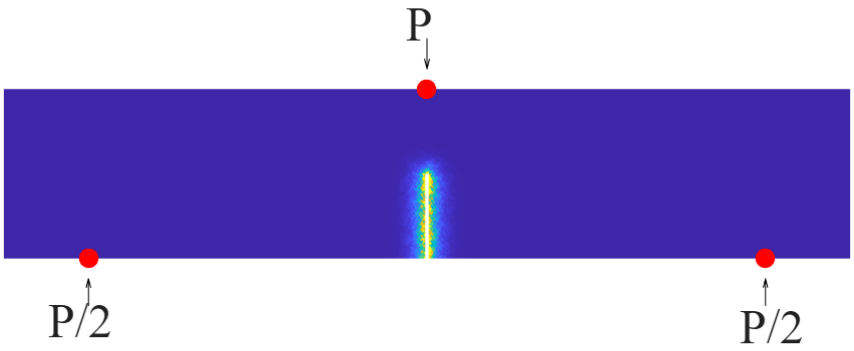
4.5.3 Phase-field crack propagation result

Figure 4.6 shows crack evolution as a progressive damage band. The method captures initiation at the notch and subsequent propagation through the ligament. The phase-field crack is inherently smeared. This means that the crack path must be extracted by a damage threshold before it can be compared with experimental photographs or converted into a hydraulic aperture network.

The validation curves later in the chapter show a material-dependent bias. For LS_{15} and LS_{25}, the phase field tends to overpredict K_{Ic} in several geometries, particularly where the experimental response is lower and more geometry sensitive. This is consistent with excessive regularization or with a damage-band energy that does not localize into the same rough fracture path seen in the experiment. The method is rigorous and powerful, but for the present study, it is less suitable because the final objective is not only to obtain a damage field, but also to obtain a crack graph, an aperture field, and hydraulic connectivity.



(a)



(b)

Figure 4.5: SENB modelled using the phase-field framework: (a) triangular mesh and (b) displacement loading and boundary conditions.

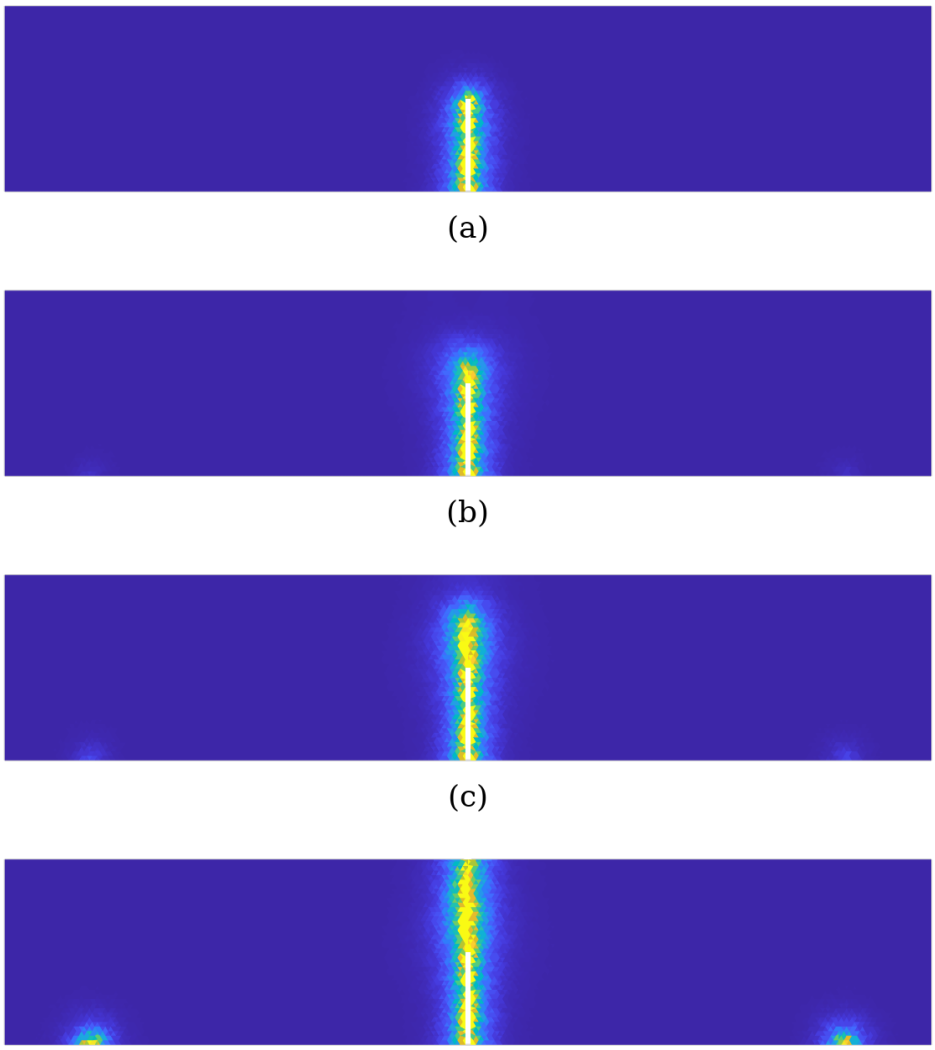


Figure 4.6: Crack propagation using the phase-field framework for the $B = W = 35$ mm, $a/W = 0.45$, LS_0 SENB specimen: (a) one-fourth, (b) two-fourths, (c) three-fourths, and (d) complete crack propagation.

4.6 Lattice element method (LEM)

4.6.1 Historical background and relevance to the SENB problem

The lattice element method represents a continuum or a granular assembly as a network of one-dimensional mechanical links. The idea traces back to the framework method of Hrennikoff and the discrete structural models of Kawai (Hrennikoff, 1941; Kawai, 1978). Later developments used random lattices to model fracture in concrete, rock, and quasibrittle heterogeneous media (Bolander and Saito, 1998; Grassl and Jirásek, 2010; Schlangen and Mier, 1992). Lattice models are particularly attractive for geomaterials because crack propagation is represented by progressive failure of links rather than by an externally imposed crack tracking algorithm. This gives the method an intrinsic ability to model crack initiation, tortuous propagation, crack branching, and coalescence (Nikolić, Ibrahimbegović, and Miščević, 2015; Nikolić, Karavelić, et al., 2018; Z. H. Rizvi, Nikolić, and Wuttke, 2019).

In this study, the LEM mesh is a Poisson random lattice. A set of seed points $\mathcal{P} = \{\mathbf{x}_i\}_{i=1}^{N}$ is generated in the domain. The Voronoi cell associated with seed point $\mathbf{x}_i$ is

$$V_i = \{\mathbf{x} \in \Omega : \|\mathbf{x} - \mathbf{x}_i\| \leq \|\mathbf{x} - \mathbf{x}_j\|,\ j \neq i\} \tag{4.34}$$

The Delaunay triangulation is the dual graph of this tessellation. A lattice link is created between two neighbouring seed points when their Voronoi cells share an edge. The resulting network is statistically isotropic when the seed points are distributed by a homogeneous Poisson process. This is important for the SENB problem because the crack should not be forced to propagate along a regular mesh direction.

Each lattice link is treated as a beam-like cohesive element. In a local coordinate system, a Timoshenko-type element has the strain vector

$$\boldsymbol{\varepsilon}_e(x) = \begin{bmatrix} \varepsilon(x) \\ \gamma(x) \\ \kappa(x) \end{bmatrix} = \begin{bmatrix} \frac{\mathrm{d}u}{\mathrm{d}x} \\ \frac{\mathrm{d}v}{\mathrm{d}x} - \theta \\ \frac{\mathrm{d}\theta}{\mathrm{d}x} \end{bmatrix} \tag{4.35}$$

where u and v are axial and transverse displacements and θ is rotation. The elastic relation is

$$\mathbf{s}_e = \mathbf{D}_e \boldsymbol{\varepsilon}_e, \qquad \mathbf{s}_e = \begin{bmatrix} N & V & M \end{bmatrix}^T \tag{4.36}$$

where N, V, and M are axial force, shear force, and bending moment. The cross-sectional width of a link is obtained from the common Voronoi edge, which transfers the geometry of the random tessellation into the element stiffness.

To represent localized failure, an embedded displacement jump can be introduced in the lattice element. The displacement field is decomposed as

$$\mathbf{u}(x) = \bar{\mathbf{u}}(x) + \boldsymbol{\alpha} H_{x_c}(x) \tag{4.37}$$

where $\boldsymbol{\alpha} = [\alpha_u, \alpha_v, 0]^T$ contains axial and shear displacement jumps and H_{x_c} is a Heaviside function located at the discontinuity point x_c. The corresponding strain field is

$$\boldsymbol{\varepsilon} = \mathbf{B}\mathbf{d} + \mathbf{G}\boldsymbol{\alpha} + \boldsymbol{\alpha}\delta_{x_c} \tag{4.38}$$

where δ_{x_c} is the Dirac distribution. This formulation assigns an explicit crack opening variable to the lattice link. That crack opening later becomes the key transfer variable to the hydraulic pore network.

Failure is checked by tensile and shear criteria. A simple form is

$$\sigma_{\mathrm{n}} \geq f_{\mathrm{t}} \qquad \text{for Mode I opening} \tag{4.39}$$

$$|\tau| \geq c + \sigma_{\mathrm{n}} \tan\phi \qquad \text{for Mode II sliding} \tag{4.40}$$

After the threshold is reached, the link softens according to a fracture energy controlled law. In exponential form,

$$q(\xi) = \sigma_{\mathrm{u}} \left[1 - \exp\left(-\frac{\xi \sigma_{\mathrm{u}}}{G_{\mathrm{f}}} \right) \right] \tag{4.41}$$

where q is the softening variable, ξ is the internal displacement like variable, σ_{u} is the ultimate stress, and G_{f} is fracture energy. The element residuals are assembled into the global equilibrium problem,

$$\mathbf{R}_{\mathrm{LEM}}(\mathbf{d}, \boldsymbol{\alpha}) = \sum_{e=1}^{N_e} \left(\mathbf{f}^e_{\mathrm{int}} - \mathbf{f}^e_{\mathrm{ext}} \right) = \mathbf{0} \tag{4.42}$$

with local discontinuity residual

$$\mathbf{h}^e = \int_0^{\ell_e} \mathbf{G}^T \mathbf{s}_e \, \mathrm{d}x + \mathbf{t}_c = \mathbf{0} \tag{4.43}$$

The explicit link failure state, displacement jump, and graph connectivity are the decisive advantages of LEM for this study.

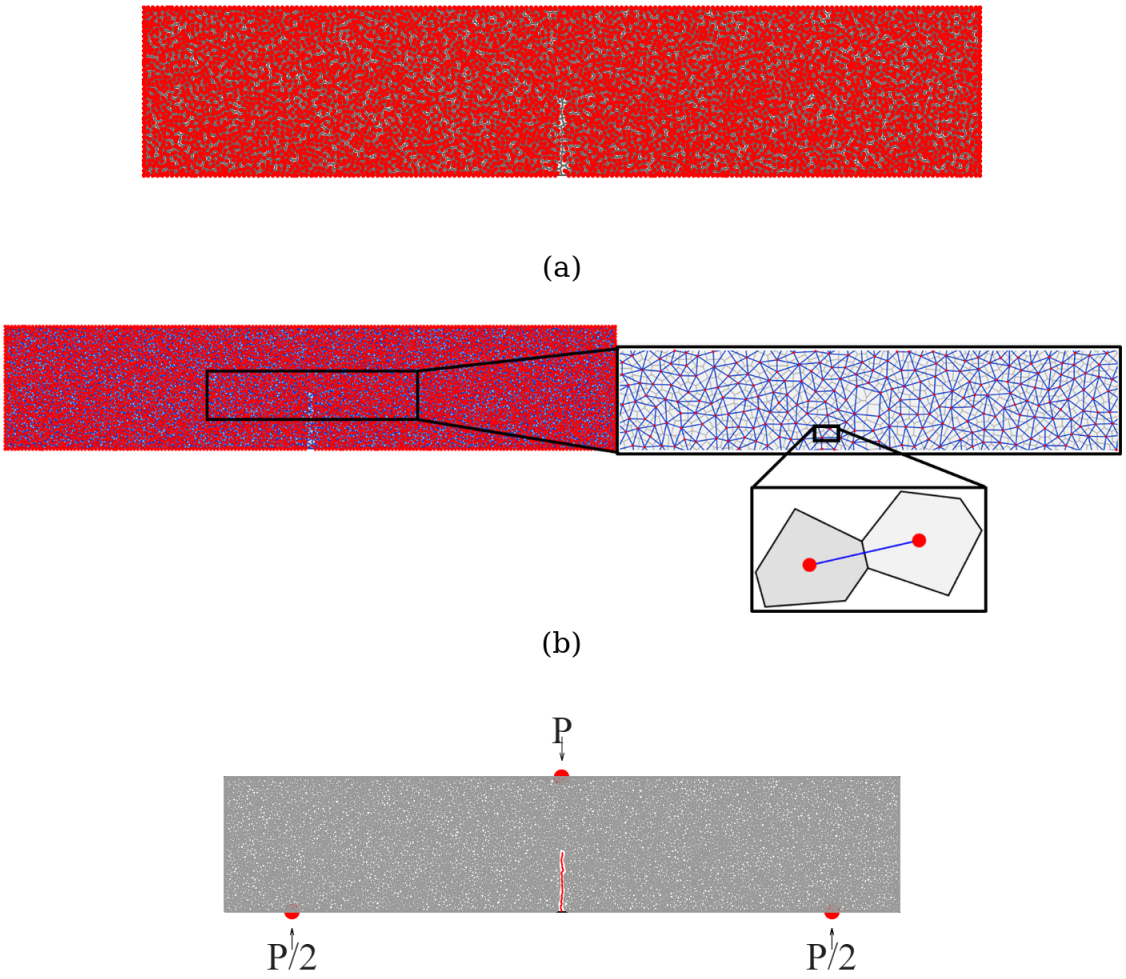


Figure 4.7: SENB modelled using the lattice element method: (a) Voronoi tessellation, (b) Voronoi cells with Delaunay triangulation, and (c) loading and boundary conditions.

4.6.2 LEM SENB model

Figure 4.7 shows the physical meaning of the LEM discretization. Part (a) gives the Voronoi tessellation, which represents the spatial partition of the material. Part (b) superimposes the Delaunay triangulation, which is the mechanical lattice network. Part (c) applies the same SENB loading and support conditions used for the other methods. This figure is more than a mesh illustration. It shows why the LEM crack is not constrained to a regular triangular mesh and why the method can reproduce local crack roughness. A crack forms as a sequence of failed links, and its final trajectory is determined by local strength, stiffness, fracture energy, and neighbourhood connectivity.

Because the lattice is random but statistically isotropic, the model does not create an artificial preferred crack direction. At the same time, the crack path is not artificially smooth. It can deviate locally, branch over short distances, and reconnect, exactly as expected in quasibrittle geomaterials. This is a significant distinction from continuum finite element approaches. In XFEM, the crack is sharp but tracked; in phase field, the crack is not tracked but is smeared; in LEM, the crack is sharp at the link scale and self-organized by failure of the network.

4.6.3 LEM crack propagation result for the reference SENB case

Figure 4.8 shows the LEM crack propagation stages for the reference $B = W = 35\,\text{mm}$, $a/W = 0.45$, LS_0 specimen. The crack initiates at the notch tip, propagates upward through the ligament, and develops a locally irregular path rather than a perfectly straight line. This is the first piece of evidence supporting LEM. The experimental cracks shown later are not ideal mathematical lines. They are rough fracture traces generated by local microstructural resistance. LEM naturally reproduces that character because each link represents a possible local fracture segment.

The sequence in Figure 4.8 also demonstrates stable crack evolution under the same 0.001 mm displacement increment used in the experiment. The crack does not jump unrealistically to the boundary at an early stage. It grows gradually, while the fracture process zone develops around the advancing crack front. This staged evolution is important because the later hydraulic model depends on the timing of crack initiation, crack coalescence, and final percolation. A solver that predicts only the final crack but not the intermediate crack opening would not be sufficient for conductivity evolution.

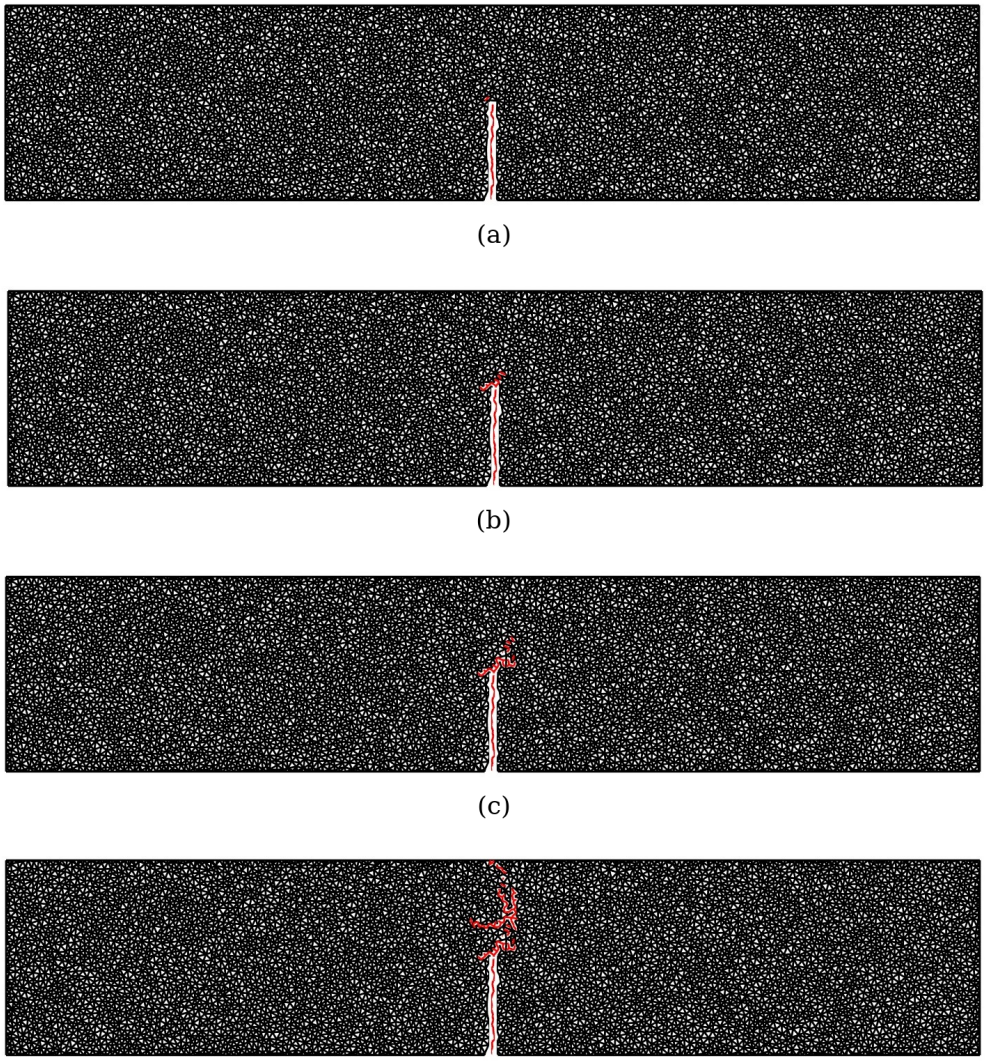


Figure 4.8: Crack propagation using the lattice element method for the $B = W = 35$ mm, $a/W = 0.45$, LS_0 SENB specimen: (a) one-fourth, (b) two-fourths, (c) three-fourths, and (d) complete crack propagation.

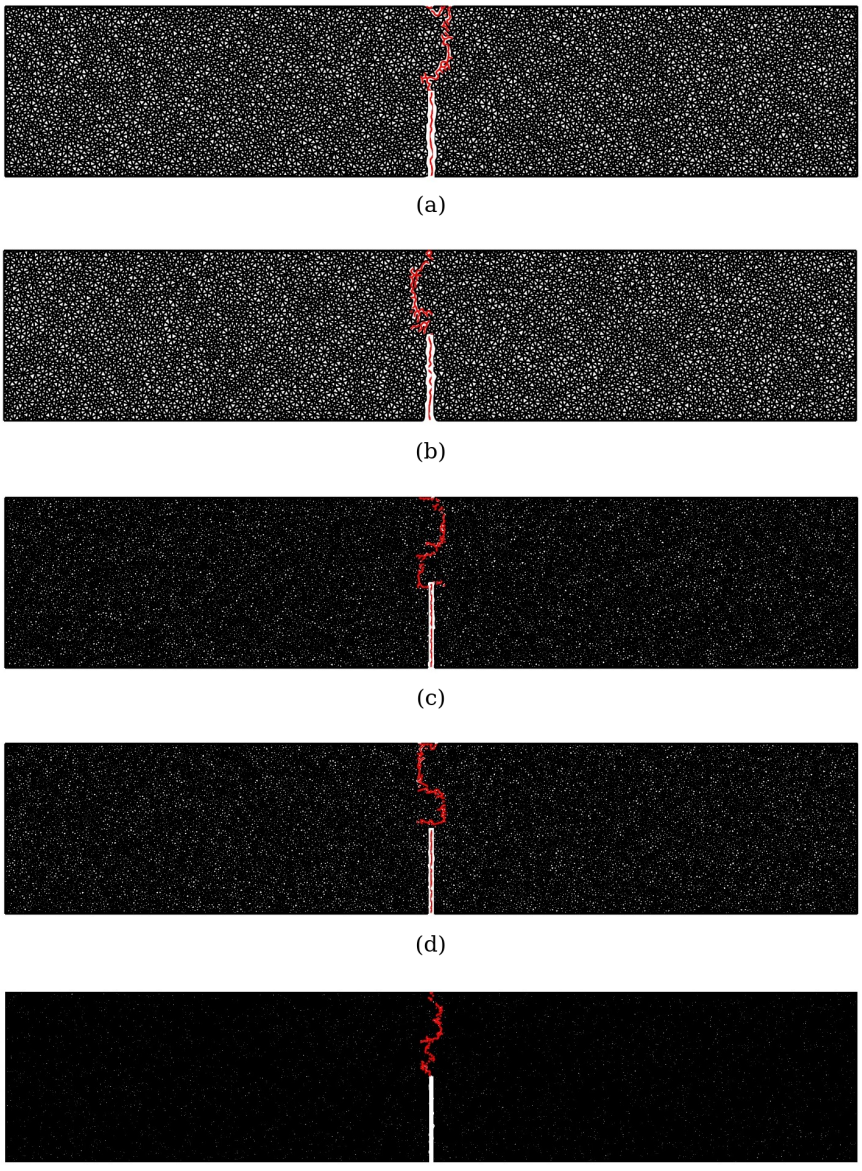


Figure 4.9: Completed LEM crack propagation for $a/W = 0.50$ in LS_0 specimens: (a) $W = 35$ mm, $B = 35$ mm; (b) $W = 35$ mm, $B = 70$ mm; (c) $W = 50$ mm, $B = 50$ mm; (d) $W = 50$ mm, $B = 100$ mm; and (e) $W = 65$ mm, $B = 65$ mm.

4.6.4 LEM response over geometry variation

Figure 4.9 is a central validation figure because it tests whether LEM is robust across specimen geometry. The five figures correspond to geometry A-E. The crack remains notch-driven in all cases, confirming that the model does not produce spurious boundary cracking. At the same time, the final crack trajectory varies slightly across geometries. This variation is physically appropriate. Increasing W, changing B, or altering a/B changes the ligament size, stress gradient, fracture process zone confinement, and effective energy release available to the advancing crack. A credible method should reproduce this sensitivity without losing the fundamental upward propagation pattern.

The LEM results in Figure 4.9 show this behaviour precisely. The crack path is consistently Mode-I dominated, but it is not an identical straight line across all specimens. This is important when validating against the K_{Ic} plots. If a method gives nearly the same ideal crack path for all geometry families, it may still reproduce one scalar value but fail to capture the geometry dependence of crack growth. The LEM geometry series demonstrates that the lattice can represent both the global SENB constraint and the local heterogeneity driven path selection.

4.6.5 LEM response over soil-state variation

Figure 4.10 compares the final LEM crack pattern for LS_0, LS_{15}, and LS_{25} at fixed geometry. The figure shows that the crack remains controlled by the notch and the overall bending field, whereas the local trajectory varies with soil state. This is technically important because the soil state changes stiffness, strength, cohesion/friction response, and fracture energy. The fracture pattern should therefore not be identical for all three materials.

The LEM framework accommodates this naturally. The material parameters are assigned to the lattice links, and the crack propagates through the links that satisfy the local failure criterion. As a result, the method does not require prescribing a crack path or forcing a smooth crack surface. Instead, the crack advances through the weakest compatible sequence of links under the evolving stress field. This mechanism is consistent with the experimental interpretation of quasibrittle fracture in heterogeneous soils.

4.6.6 Experimental crack propagation evidence

Figure 4.11 provides the physical reference for the comparison. The experimental crack originates at the notch and propagates through the ligament, but its path is neither perfectly straight nor

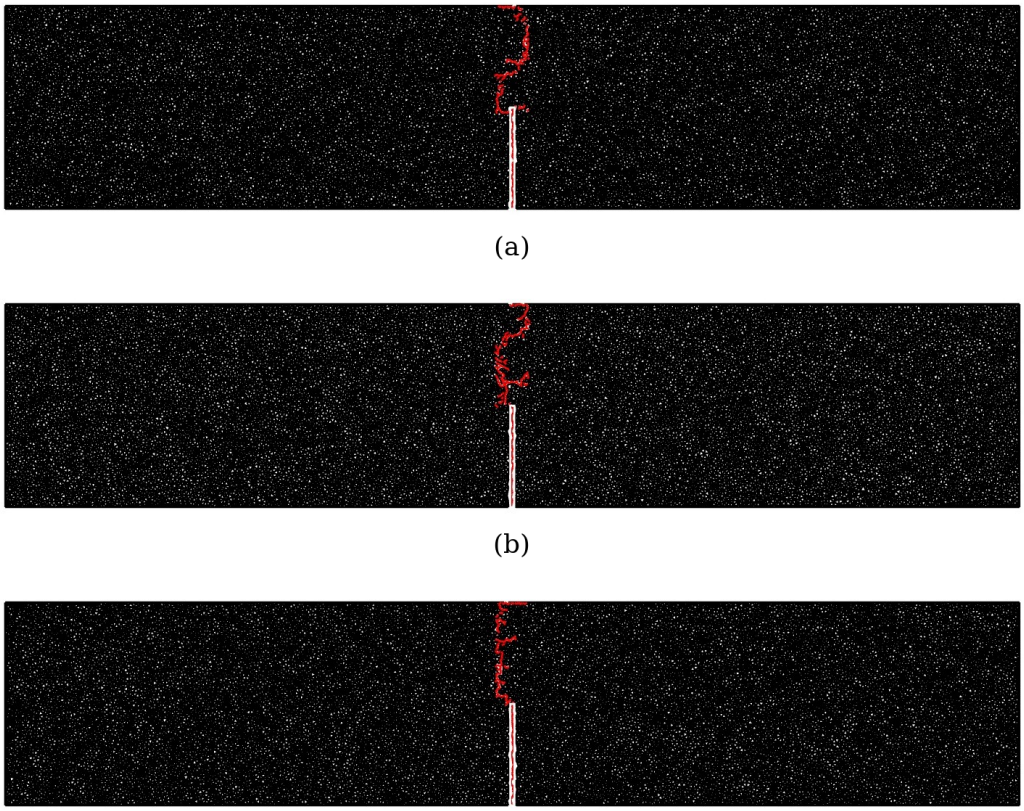


Figure 4.10: Completed LEM crack propagation for $a/W = 0.50$, $W = 50$ mm, $B = 50$ mm specimens made of (a) LS_0, (b) LS_{15}, and (c) LS_{25}.

perfectly smooth. The crack surface exhibits local roughness and small deviations, typical of quasibrittle geomaterials. This figure explains why a method can be mathematically elegant yet less suitable for this study: if it produces a crack that is too idealized, it will not represent the surface geometry that later controls aperture and flow.

Comparing Figures 4.2, 4.4, 4.6, and 4.8 against Figure 4.11, LEM gives the closest qualitative representation of the experimental fracture character. XFEM and STFEM produce connected cracks, but with smoother or more algorithmically controlled paths. Phase field produces a continuous damage band rather than a discrete crack trace. LEM produces a connected crack path with local tortuosity while maintaining the correct global propagation direction. This is the main qualitative reason LEM is selected before the PNM is introduced.

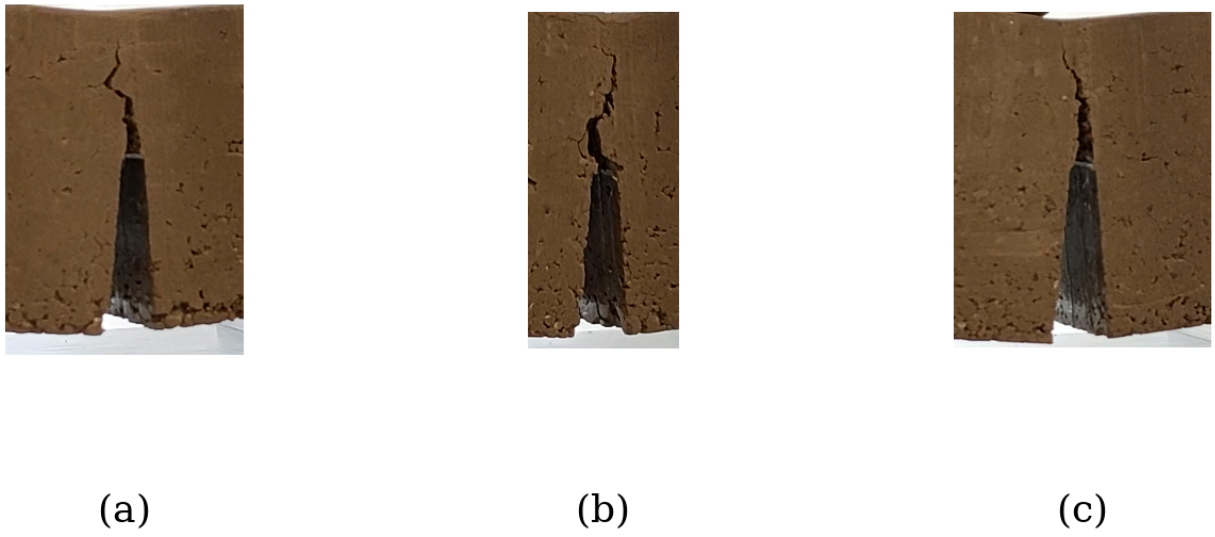


Figure 4.11: Experimental crack propagation in SENB specimens, used as the physical reference for evaluating the numerical crack paths.

4.7 Comparative validation of the four fracture methods

4.7.1 Validation for LS_0

Figure 4.12 compares the experimental and numerical fracture toughness values for LS_0 across the five geometry families. The main observation is that the LEM curve nearly overlaps the experimental trend in all geometries. This is the strongest quantitative validation of the method for the baseline soil state. The agreement is not limited to a single geometry. In geometries A, B, C, D, and E, LEM remains close to the experimental data over $a/W = 0.45$, 0.50, and 0.55. This shows that the LEM calibration is not merely fitting one point; it captures the geometry-dependent

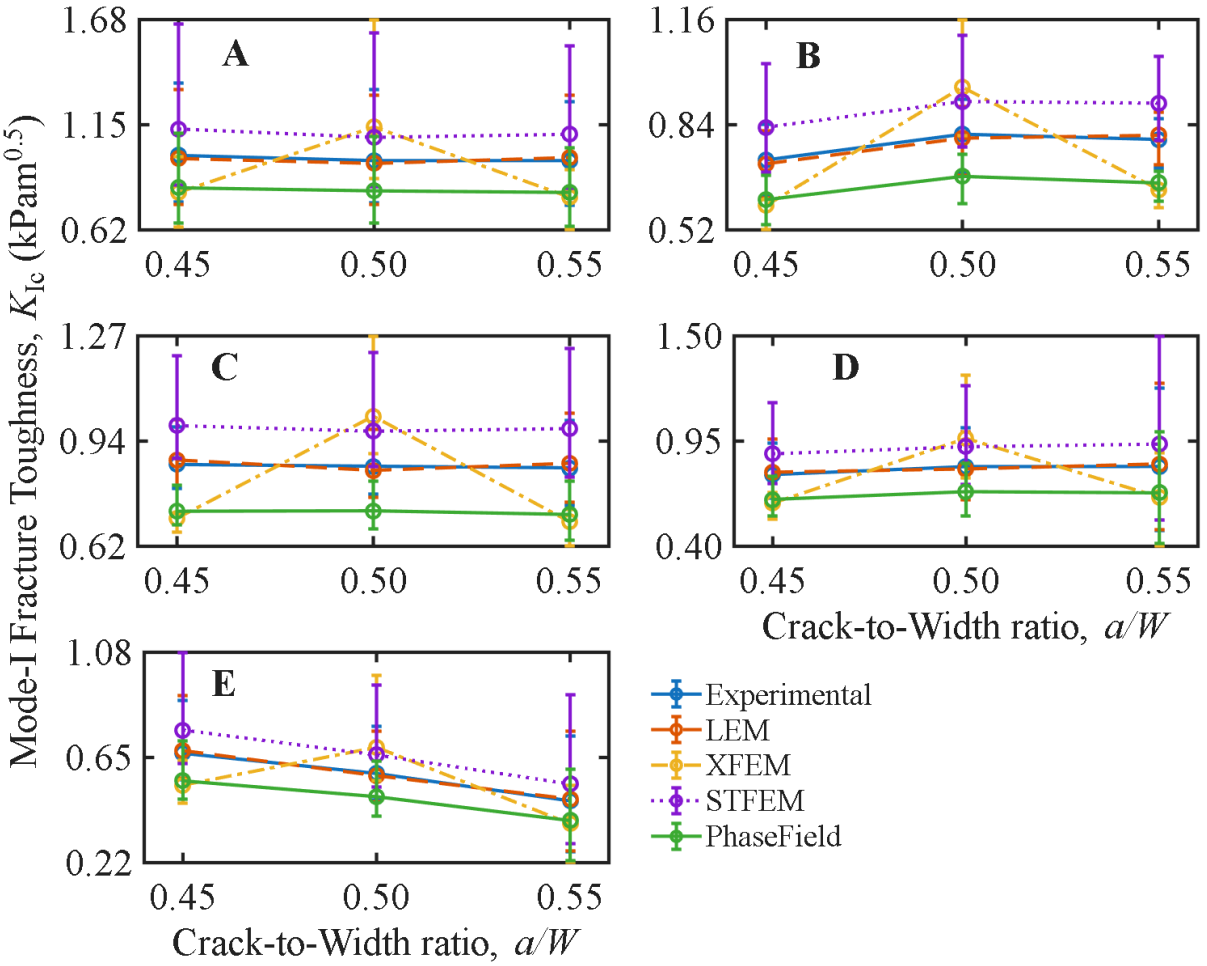


Figure 4.12: Validation of different numerical methods for crack initiation and propagation in LS_0.

fracture response.

XFEM performs reasonably in some LS_0 cases but shows a noticeable non-monotonic response, especially near $a/W = 0.50$. The pronounced increase at this notch ratio indicates sensitivity to crack tracking and local enrichment behaviour. Such sensitivity is not necessarily an error in XFEM, but it is undesirable for a study framework intended to couple crack evolution to hydraulic conductivity. A spurious or algorithm-sensitive jump in K_{Ic} can cause a corresponding nonphysical shift in crack opening and seepage evolution.

STFEM in Figure 4.12 generally lies above the experiment or shows wider scatter, especially in geometries A-C. This indicates that the method can propagate the crack but tends to over-stabilize the fracture response for this material state. Phase field, in contrast, tends to underpredict K_{Ic} for several geometry families. This is consistent with a diffusive crack band that reduces the effective fracture resistance when the length scale and mesh resolution do not exactly match the experimental process zone size.

The LS_0 validation therefore supports two conclusions. First, all four methods can generate a crack from the SENB notch, but not all reproduce the experimental trend in fracture toughness. Second, LEM provides the most consistent agreement across geometry, which is precisely the behaviour required before extending the method to hydraulic modelling.

4.7.2 Validation for LS_{15}

Figure 4.13 shows the same comparison for LS_{15}. This figure is particularly important because the relative performance of the methods becomes clearer than in LS_0. LEM remains close to the experimental data in all five geometry families. The agreement is especially evident in geometry B-E, where the orange LEM curve tracks the blue experimental curve with only a small separation over all a/W values. This again indicates that LEM captures both crack initiation and the geometry-dependent fracture resistance.

XFEM underpredicts K_{Ic} for most LS_{15} cases. The underprediction is not a minor local deviation; it is systematic across geometry A, B, C, D, and E. This suggests that, for this material state, the sharp-crack XFEM representation either advances the crack too easily or fails to capture the energy dissipation in the quasibrittle process zone. For hydraulic coupling, such underprediction would be problematic because it would lead to early crack opening and increased hydraulic conductivity.

The phase field shows the opposite bias. It overpredicts fracture toughness in several cases, particularly in geometry A-C, where the green curve lies clearly above the experimental trend. This suggests that the regularized damage band is too resistant or too diffuse for this soil state.

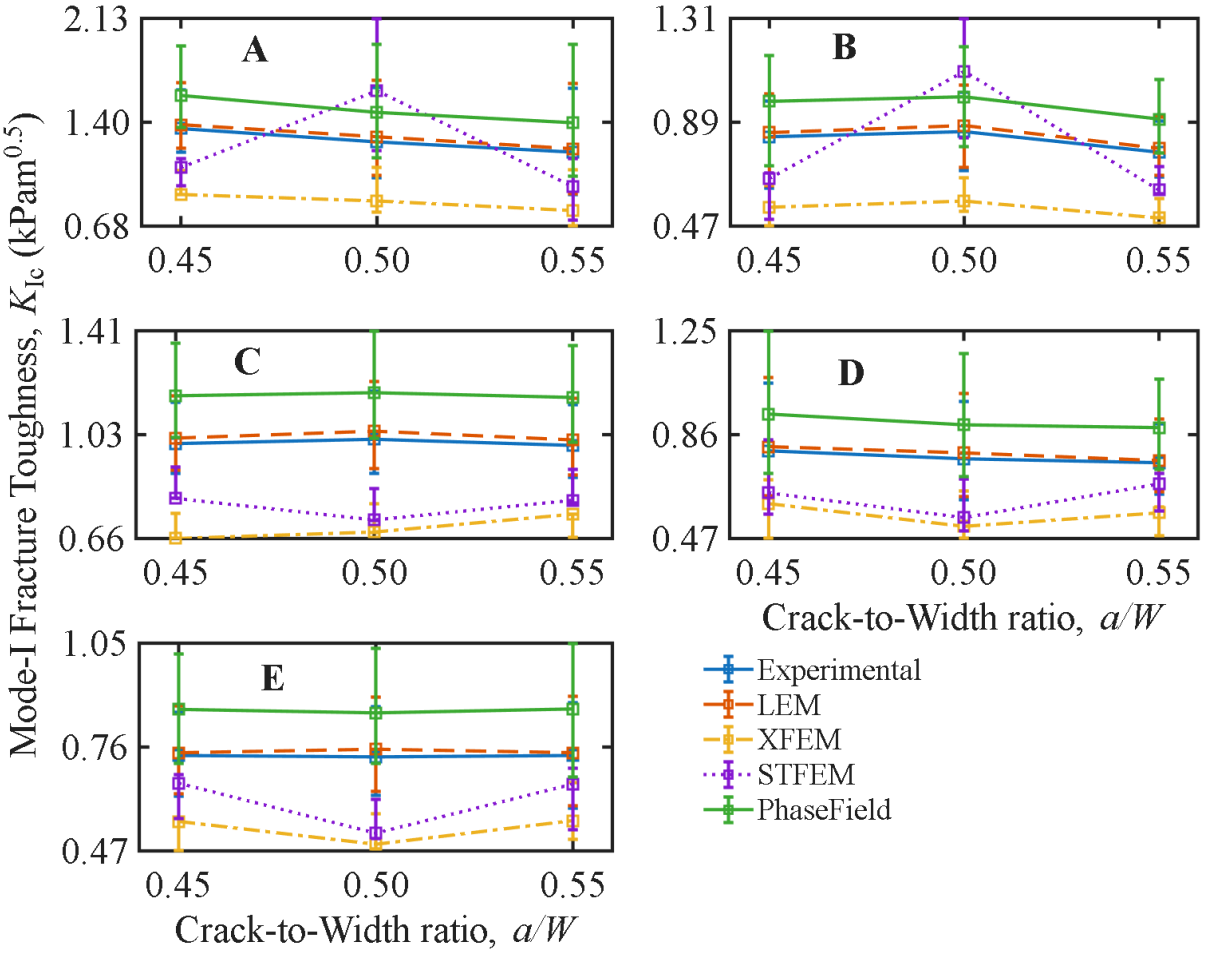


Figure 4.13: Validation of different numerical methods for crack initiation and propagation in LS_{15}.

STFEM exhibits variable behaviour: it may approach the experimental value in isolated cases, but it does not exhibit a consistent trend across geometries. In geometries A and B, a pronounced peak occurs near $a/W = 0.50$, while in geometries C-E, the STFEM response is lower and more irregular.

The LS_{15} validation is therefore a strong argument in favour of LEM. It is the only method in this set that simultaneously preserves crack-path realism and tracks the experimental K_{Ic} trend over the specimen matrix. That combination is essential because hydraulic conductivity later depends on both the mechanical load level at which cracks form and the geometry of the connected crack path.

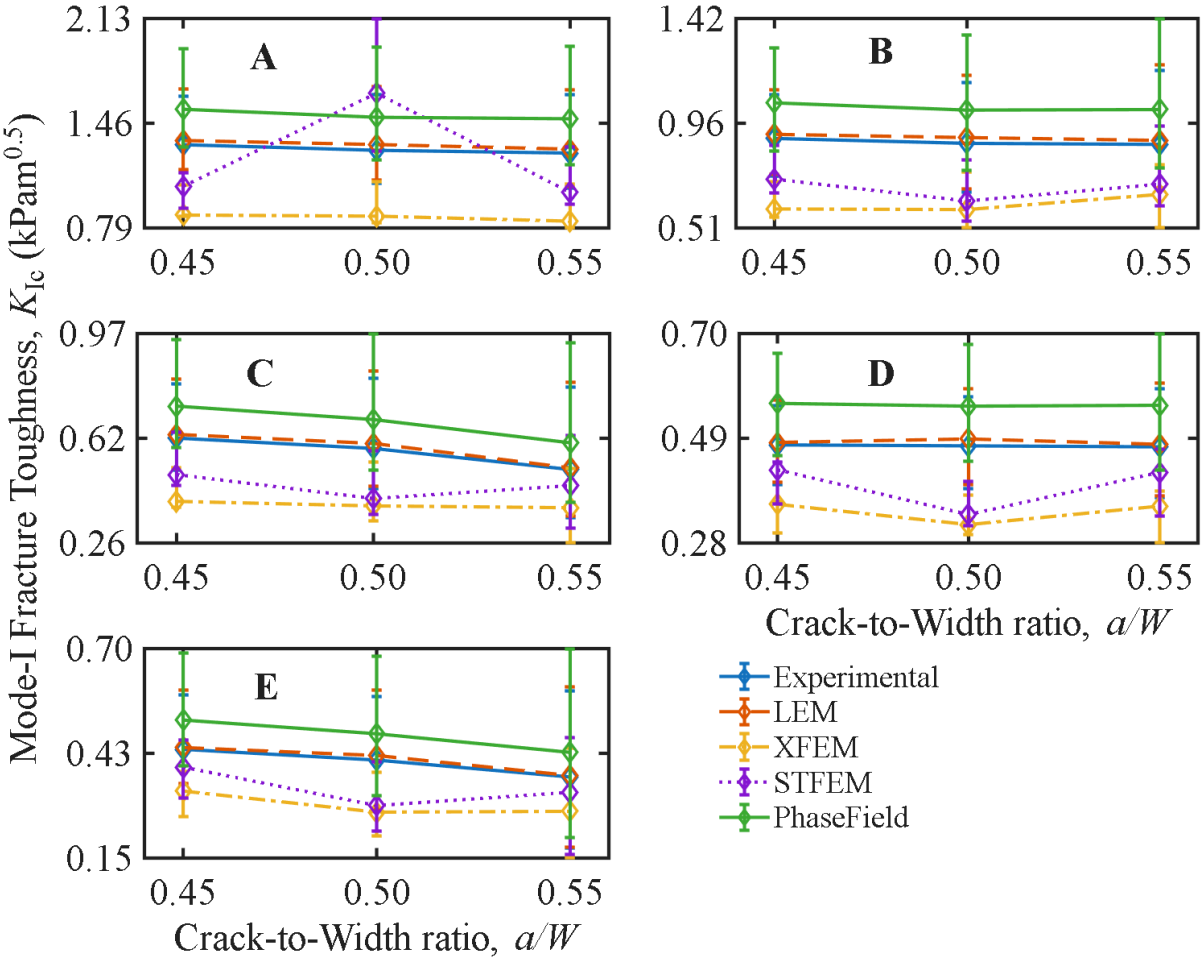


Figure 4.14: Validation of different numerical methods for crack initiation and propagation in LS_{25}.

4.7.3 Validation for LS_{25}

Figure 4.14 confirms the pattern observed in the earlier validation sets. LEM is again closest to the experimental trend across the geometry families. In geometry B-E, the LEM and experimental curves are nearly coincident over the tested a/W range. In geometry A, the LEM curve remains close to the experimental data, whereas the other methods exhibit larger deviations. This consistency across LS_0, LS_{15}, and LS_{25} establishes LEM as the most reliable fracture solver for this study.

XFEM and STFEM both tend to underpredict K_{Ic} in several LS_{25} cases. This underprediction is evident in geometries A-E, particularly for XFEM, where the yellow curve consistently lies

below the experimental data. A method that underpredicts fracture toughness would tend to predict premature crack propagation. In a coupled hydraulic simulation, this would shift the onset of permeability increase to an earlier loading step than observed in the physical system.

Phase field generally overpredicts the LS_{25} fracture toughness, particularly in geometries A-C. This overprediction implies that the diffusive crack band delays localization or spreads the fracture energy over a wider region than the experiment supports. Such a response would delay the formation of a connected hydraulic crack and underestimate the early evolution of conductivity. Thus, phase field and XFEM/STFEM produce opposite types of errors in this dataset: phase field can be overly resistant, whereas XFEM/STFEM can be overly permissive. LEM avoids both systematic extremes.

4.7.4 Why LEM is selected?

The evidence from Figures 4.11-4.14 supports a clear technical decision. LEM is selected as the production method for fracture propagation and as the basis for PNM coupling. This decision is based on four observations.

First, LEM provides the closest visual agreement with the experimental crack paths. It initiates at the notch, propagates through the ligament, and retains local roughness. The method does not require a prescribed crack path, and it does not smear the crack into a broad damage zone. Second, LEM gives the most consistent quantitative agreement with the experimental K_{Ic} values across LS_0, LS_{15}, and LS_{25}. The agreement persists across the five geometry families and the three notch ratios. Third, LEM represents the crack as a failed-link graph. This gives direct access to crack connectivity, crack opening, and fracture sequence. Fourth, this graph representation is exactly what is required for a pore-network hydraulic extension.

The comparison also clarifies why the other methods are not selected for the hydraulic part. XFEM is mathematically sharp and efficient for tracked cracks, but the crack path and aperture graph require additional reconstruction. STFEM organizes crack evolution over loading slabs, but it does not overcome the spatial crack path limitations seen in the validation plots. Phase field avoids crack tracking, but its diffuse damage variable must be thresholded and converted into a crack graph before hydraulic conductivity can be computed. These conversions introduce uncertainty precisely where hydraulic connectivity is most sensitive. LEM avoids this issue by making the fracture state discrete and graph-based from the start.

4.8 Transition from validated LEM fracture to LEM-based pore-network modelling

The pore-network model is introduced only after LEM has been established. The reason is physical rather than procedural. Hydraulic conductivity in a cracked soil specimen is not controlled simply by how many elements are damaged. It is controlled by whether cracks and pores form a connected, transmissive path, by the aperture size, and by the pressure gradient's intersection with that path. A damage field that is not connected from inlet to outlet should not generate a large global conductivity increase. Conversely, a single connected crack with sufficient aperture can dominate the hydraulic response even if the total damaged volume is small.

LEM supplies the mechanical information required for this calculation. At each displacement step, the solver provides the failed-link set

$$\mathcal{E}_f^n = \{e : d_e^n \geq d_{\text{crit}} \text{ or link } e \text{ has activated displacement jump}\} \tag{4.44}$$

where d_e^n is a link damage variable or equivalent failure indicator. It also provides the normal opening of each failed or softened link,

$$b_e^n = b_r + \max\left(0, [[\mathbf{u}]]_e^n \cdot \mathbf{n}_e\right) \tag{4.45}$$

where b_{r} is residual aperture and $\mathbf{n}_e$ is the local crack normal. The crack graph is

$$\mathcal{G}_c^n = \left(\mathcal{V}_c^n, \mathcal{E}_f^n\right) \tag{4.46}$$

where $\mathcal{V}_c^n$ contains the nodes touched by failed links. The PNM uses this graph to update pore connectivity and throat conductance. This is the key methodological transition: LEM determines where cracks exist and how open they are; the PNM determines how those cracks change pressure, seepage, and equivalent conductivity.

4.9 LEM-based sequential one-way mechanical-fracture-to-flow coupling model

4.9.1 Material parameters

Table 4.2 gives the phase-level input parameters for the coupled LEM-PNM analysis. The mechanical contrast between clay and sand is large: the sand phase has a Young's modulus of

120 MPa compared with 25 MPa for clay, whereas the clay phase carries cohesion and tensile strength that are absent or negligible in the sand phase. This contrast produces a heterogeneous mechanical network in which stiffness, strength, and fracture energy vary from link to link depending on the local material assignment. Such heterogeneity is precisely why a lattice representation is appropriate. The crack path is not prescribed; it emerges from the competition between local stiffness, strength, fracture energy, and stress redistribution.

The assigned hydraulic contrast is also large. The model assigns $k = 1.0 \times 10^{-10}$ m/s to clay and $k = 1.0 \times 10^{-5}$ m/s to sand. In the numerical model, this prescribed contrast makes the calculated flow sensitive to the spatial arrangement of sand-assigned throats and mechanically opened links. The larger assigned value of α_b increases the local conductance of sand-assigned throats. These values are phase-level model inputs and do not demonstrate that the experimental mixtures contained a continuous hydraulic or load-bearing granular skeleton. The equivalent specimen conductivity is obtained from the network pressure solution rather than from a weighted average of the two assigned phase values.

The residual stiffness factor k_{r} plays a stabilizing role in the mechanical solve after link softening, while the residual aperture b_{r} plays a similar physical role in the hydraulic solve by avoiding complete numerical closure of all micro-flow paths. These residual terms should not be interpreted as arbitrary curve-fitting parameters. They represent unresolved microcrack roughness, residual contact, and remaining pore-space connectivity at the chosen 1 mm discretization scale.

4.9.2 Three-dimensional LEM-PNM cylinder construction

Figure 4.15 shows the three-dimensional cylindrical specimen used in the coupled hydraulic simulations. The specimen is discretized by a random distribution of nodes within the cylinder. The length scale shown in the figure is consistent with the adopted three-dimensional discretization and the experimental-scale loading program. Unlike the two-dimensional SENB validation, the hydraulic analysis requires a three-dimensional connected pore/crack network because seepage and crack connectivity are spatial, not planar, phenomena.

The random node distribution is not a cosmetic feature. It allows the model to represent heterogeneous local connectivity while avoiding a preferred lattice direction. This is important in both UCS and triaxial compression. Under compression, crack formation and aperture opening are not expected to follow a single grid-aligned plane. A regular lattice could artificially bias the fracture and the resulting flow path. The random lattice reduces this bias and permits more realistic crack coalescence.

Figure 4.16 illustrates the four representations used by the coupled model. fig (a) shows the material/node representation. fig (b) shows the meshed cylinder with mechanical connectivity. fig

(c) isolates the pore network, and fig (d) shows the fluid-filled pore network. This decomposition is technically important because the mechanical and hydraulic graphs are related but not identical. The mechanical lattice carries force, deformation, and damage. The pore network carries pressure and flow. The coupling occurs when mechanical link failure modifies the aperture and conductance of hydraulic throats.

This construction follows the same physical philosophy as pore-lattice modelling in which pores and throats represent mesoscale void connectivity rather than a homogenized continuum (Blunt, 2001; Blunt et al., 2002; Fatt, 1956; Jivkov et al., 2013; Raoof and Hassanizadeh, 2010; Z. H. Rizvi, 2019; Valvatne and Blunt, 2004; Van Marcke et al., 2010). The key advance here is that the pore network is updated by the validated LEM fracture state.

4.9.3 Hydraulic network equations

The pore network is represented by a graph

$$\mathcal{G}_p = (\mathcal{V}_p, \mathcal{E}_p) \tag{4.47}$$

where $\mathcal{V}_p$ is the pore-node set and $\mathcal{E}_p$ is the throat set. For a throat connecting pores i and j, the laminar Poiseuille conductance of a cylindrical throat is

$$g_{ij}^{m} = \frac{\pi R_{ij}^{4}}{8\mu L_{ij}} \tag{4.48}$$

where R_{ij} is throat radius, L_{ij} is throat length, and μ is dynamic viscosity. For a fracture-like throat with aperture b_{ij} and effective width w_{ij}, the cubic-law conductance is

$$g_{ij}^{f} = \frac{b_{ij}^{3} w_{ij}}{12\mu L_{ij}} \tag{4.49}$$

The total throat conductance is updated as

$$g_{ij}^{n} = g_{ij}^{m,n} + \chi_{ij}^{n} g_{ij}^{f,n} \tag{4.50}$$

where $\chi_{ij}^{n} = 1$ if the mechanical fracture state activates a hydraulic fracture connection at step n and $\chi_{ij}^{n} = 0$ otherwise. The aperture is obtained from the LEM displacement jump by

$$b_{ij}^{n} = b_{\mathrm{r}} + \eta_b \max\left(0, [[\mathbf{u}]]_{ij}^{n} \cdot \mathbf{n}_{ij}\right) \tag{4.51}$$

where η_b is an aperture-transfer coefficient. The cubic dependence in Eq. (4.49) means that a small increase in connected aperture can produce a large increase in conductance. This is why crack connectivity and aperture localization matter more than the total volume of damaged material (Snow, 1969; Witherspoon et al., 1980; Zimmerman and Bodvarsson, 1996).

Mass conservation at each internal pore node gives

$$\sum_{j \in \mathcal{N}(i)} g_{ij}(p_i - p_j) = 0, \qquad i \in \mathcal{V}_{\text{int}} \tag{4.52}$$

where $\mathcal{N}(i)$ is the set of pores connected to pore i. In matrix form,

$$\mathbf{A}_h \mathbf{p} = \mathbf{q} \tag{4.53}$$

with

$$A_{ii} = \sum_{j \in \mathcal{N}(i)} g_{ij}, \qquad A_{ij} = -g_{ij} \quad (i \neq j) \tag{4.54}$$

Dirichlet pressure conditions are imposed on inlet and outlet pore sets, while no-flow boundaries are treated by omitting external flux across the impermeable surfaces.

The total flow rate through an outlet boundary is

$$Q = \sum_{i \in \Gamma_{\text{out}}} \sum_{j \in \mathcal{N}(i)} g_{ij}(p_j - p_i) \tag{4.55}$$

The intrinsic permeability κ is calculated from Darcy's law,

$$\kappa = \frac{Q \mu L}{A \Delta p} \tag{4.56}$$

where L is the flow length, A is the cross-sectional area, and Δp is the imposed pressure difference. Hydraulic conductivity is then

$$K = \frac{\rho_w g}{\mu} \kappa \tag{4.57}$$

The figures in this chapter report hydraulic conductivity K in m/s.

4.9.4 Connectivity criterion

A technically sound fracture-flow model must include a connectivity criterion. Let $\mathcal{V}_{\text{in}}$ be the inlet pore set and $\mathcal{V}_{\text{out}}$ the outlet pore set. At each loading step, the connected hydraulic subgraph is evaluated as

$$\mathcal{G}^n_{\text{hyd}} = \{(i,j) \in \mathcal{E}_p : g^n_{ij} > g_{\min}\} \tag{4.58}$$

A percolating path exists if

$$\exists\, \mathcal{P}^n : \quad \mathcal{V}_{\text{in}} \rightarrow \mathcal{V}_{\text{out}} \quad \text{through } \mathcal{G}^n_{\text{hyd}} \tag{4.59}$$

If no such path exists, isolated crack apertures may increase local conductance but should not cause a large jump in global conductivity. This is the main correction that prevents the model from confusing damage with hydraulic conductivity. The increase in conductivity is therefore governed by three requirements: mechanical opening, hydraulic conductance, and inlet-outlet connectivity.

Table 4.2: Input parameters for sequential one-way mechanical-fracture-to-flow coupling lattice element analysis.

Property	Unit	Clay	Sand
Young's modulus, E	MPa	25	120
Poisson's ratio, ν	-	0.35	0.25
Tensile strength, f_{t}	kPa	20	0
Cohesion, c	kPa	50	0
Friction angle, ϕ	degree	22	36
Void ratio, e	-	0.85	0.55
Tensile fracture energy, G_{f}^{I}	J/m^2	5	1
Shear fracture energy, G_{f}^{II}	J/m^2	20	8
Residual stiffness factor, k_{r}	-	0.05	0.03
Dilation angle, ψ	degree	0	8
Base throat scale, α_b	-	0.80	1.20
Hydraulic conductivity, k	m/s	1.0×10^{-10}	1.0×10^{-5}

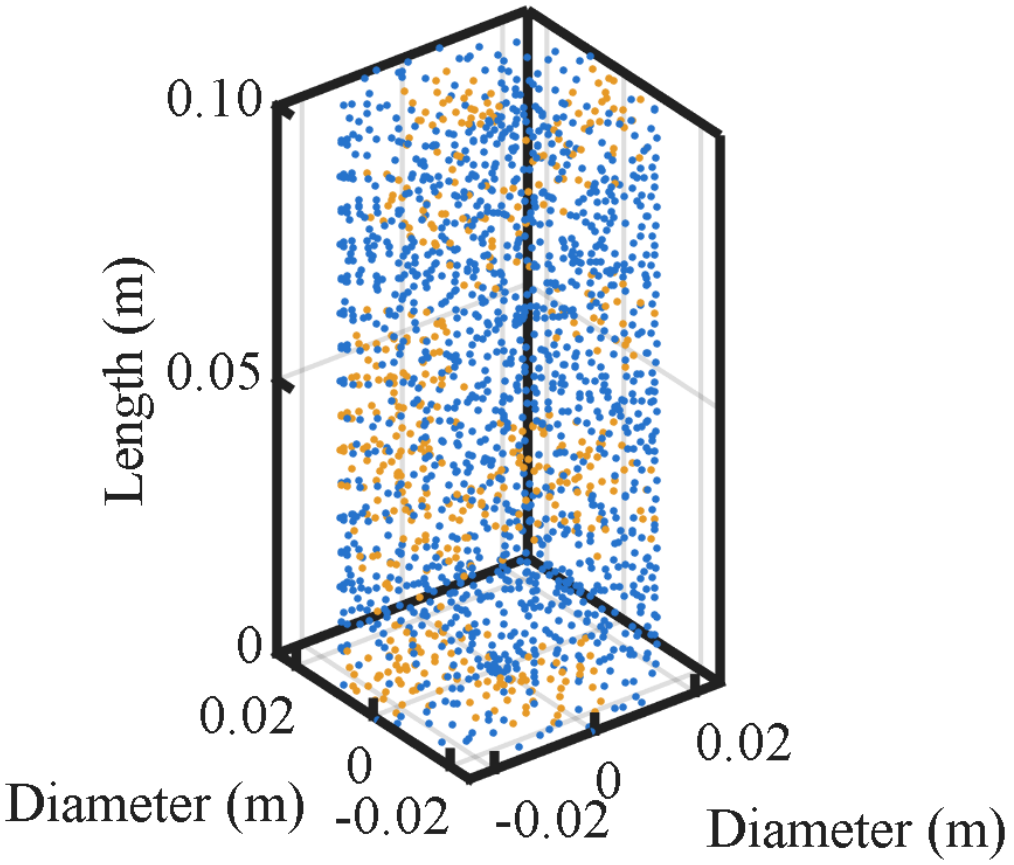
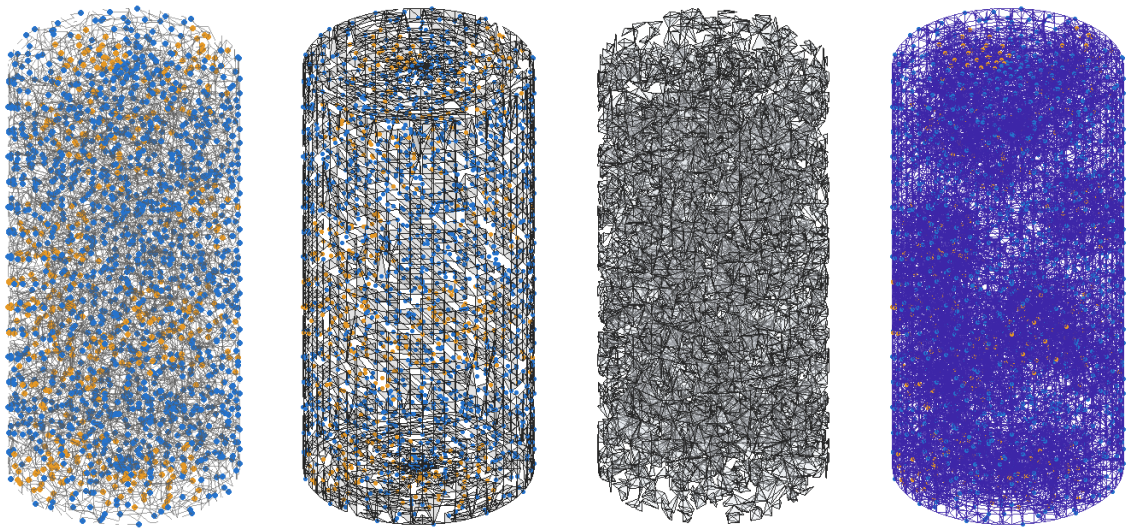


Figure 4.15: Generated three-dimensional cylindrical particle/node representation used for the coupled LEM-PNM simulations.



(a) (b) (c) (d)

Figure 4.16: sequential one-way mechanical-fracture-to-flow coupling lattice element construction: (a) nodes representing different soil particles, (b) meshed three-dimensional cylinder, (c) pore network, and (d) pores filled with fluid.

4.10 Triaxial LEM-PNM results

4.10.1 Reference LS_0 triaxial crack and aperture evolution

Figure 4.17 shows the aperture evolution for LS_0 under triaxial loading. At the no-loading stage, the aperture field is essentially governed by the initial pore network and residual apertures. At crack initiation, only a limited number of localized openings appear. These openings should not be interpreted as an increase in specimen-scale permeability unless they are connected to a hydraulic path. During crack propagation, the aperture field becomes more organized and begins to define a preferential flow zone. At complete failure, the aperture is concentrated along a dominant, connected fracture band, which serves as the principal hydraulic pathway.

The figure illustrates why the aperture must be calculated from mechanical deformation rather than assigned solely on the basis of damage. A damaged link with a small normal opening contributes little to flow because Eq. (4.49) scales as b^3. Conversely, a connected region of moderate aperture can strongly increase hydraulic conductivity. The triaxial confinement influences this process by restraining lateral opening and encouraging a more mechanically constrained fracture path.

Figure 4.18 shows the corresponding crack evolution. The crack initiation stage contains

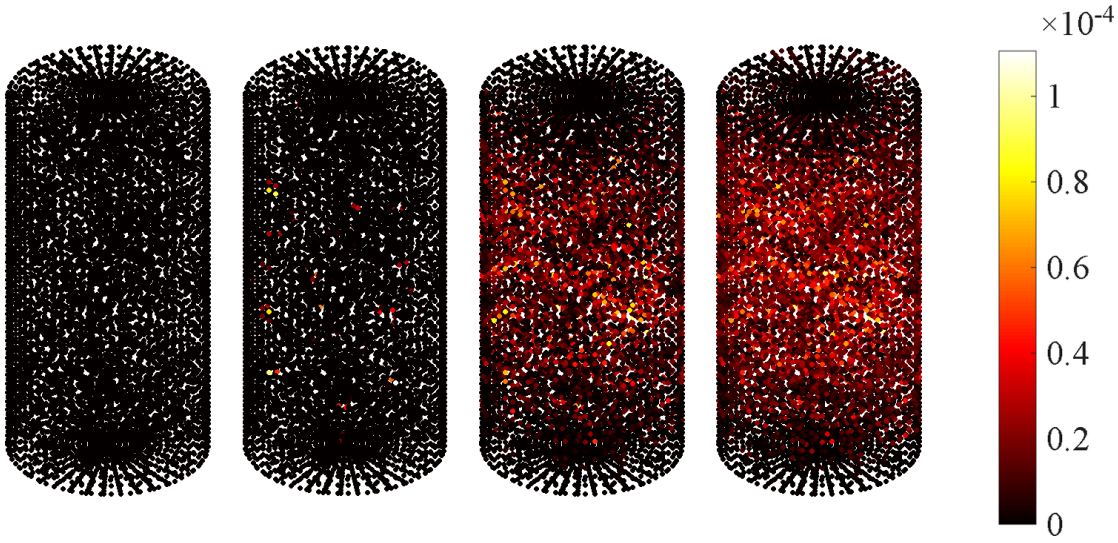
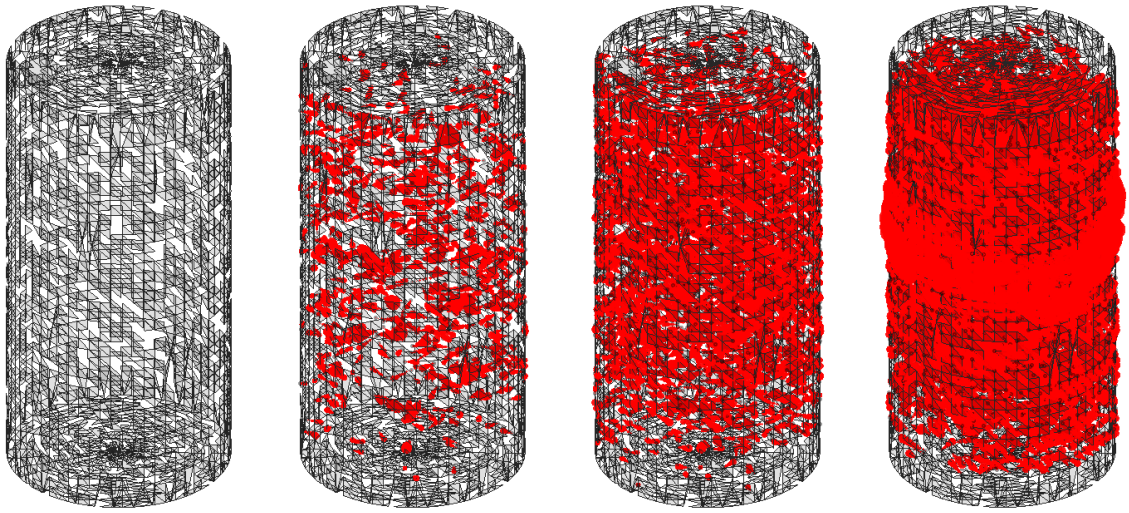


Figure 4.17: Representative aperture opening for LS_0 under triaxial loading at (a) no loading, (b) crack initiation, (c) crack propagation, and (d) complete failure. [Units = mm]



(a) (b) (c) (d)

Figure 4.18: Representative crack propagation for LS_0 under triaxial loading at (a) no loading, (b) crack initiation, (c) crack propagation, and (d) complete failure.

localized failure rather than a fully developed macroscopic crack. The propagation stage shows coalescence of local failed links into a connected fracture structure. At complete failure, the crack network forms a dominant failure surface. The mechanical sequence is consistent with quasibrittle compression: distributed local failures appear first, followed by localization and eventual formation of a specimen-scale fracture band.

Figure 4.19 couples the mechanical crack field to fluid seepage. The important observation is that seepage does not become dominant at the first appearance of a crack. It becomes significant when the crack network coalesces, creating a connected hydraulic pathway. This validates the use of the connectivity criterion in Eq. (4.59). The figure therefore supports the central modelling assumption of the PNM section: the pressure solution must be performed on the evolving network, and equivalent conductivity must emerge from that network.

4.10.2 Triaxial response of LS_0, LS_{15}, and LS_{25}

Figure 4.20 is the main quantitative result for triaxial loading. fig (a) shows the deviatoric stress response. The curves increase nearly monotonically up to the peak, followed by a sharp post-peak stress drop. This drop corresponds to localization and loss of load-carrying capacity as the fracture

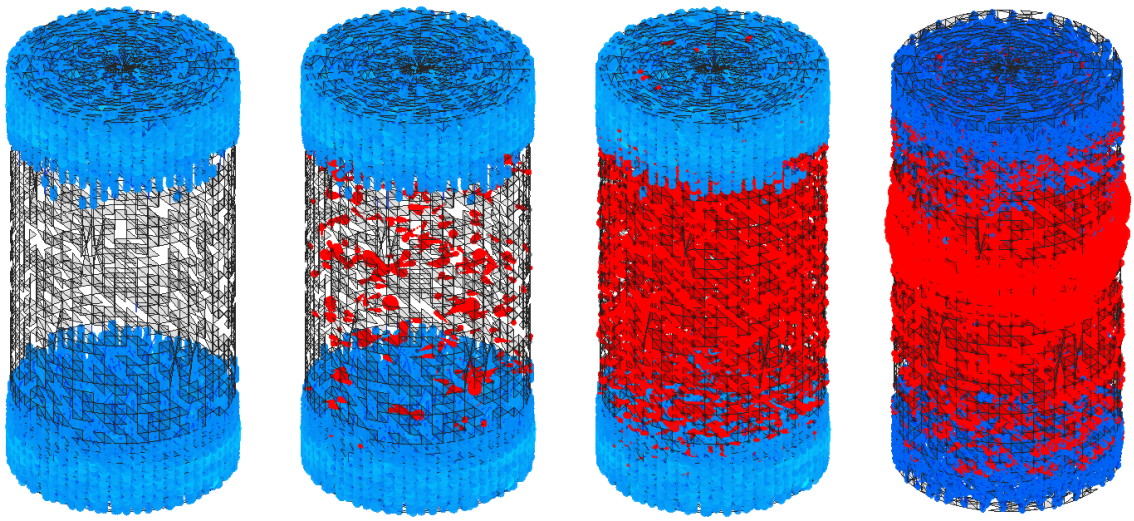


Figure 4.19: Representative crack propagation and fluid seepage for LS_0 under triaxial loading at (a) no loading, (b) crack initiation, (c) crack propagation, and (d) complete failure.

network coalesces. LS_0 reaches the highest peak stress and fails at a larger strain than LS_{15} and LS_{25} in the plotted response. LS_{25} reaches a high stress at a smaller strain, indicating a stiffer and more brittle response. The relative shape of the curves is consistent with the idea that increasing material contrast and lower ductility promote earlier localization.

fig (b) shows total porosity versus axial strain. The porosity changes are small before crack localization, as expected, because elastic compression and the formation of small microcracks do not immediately produce a large volume of connected voids. Near the onset of localization, each curve shows a more distinct increase. This is particularly visible in LS_0 near its failure region and in LS_{15} and LS_{25} near their localization strains. The porosity curves, therefore, confirm that fracture-induced void evolution is a post-initiation phenomenon rather than a uniform process from the first loading step.

fig (c) plots hydraulic conductivity against mean crack width. This is the most direct verification of the aperture-conductivity relation. The response is strongly nonlinear. Conductivity remains low for small mean crack widths, then increases rapidly once the mean aperture is sufficiently large and connected. The nonlinearity is consistent with the cubic-law conductance in Eq. (4.49). LS_0 begins to show a rapid increase at a smaller crack width, while LS_{25} reaches the largest conductivity at a larger crack width. This indicates that early aperture activation and final connected aperture

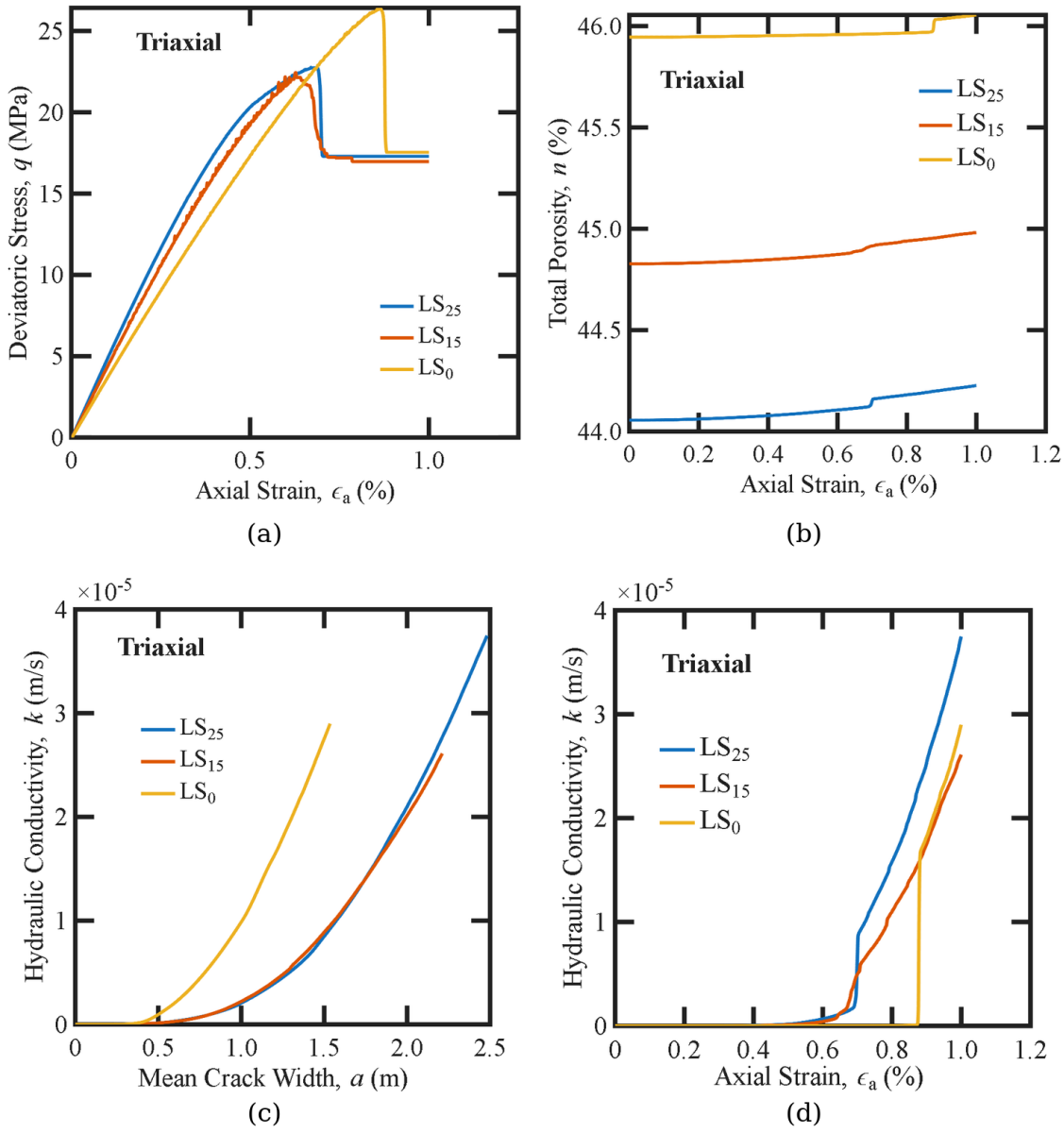


Figure 4.20: Behaviour of the sequential one-way mechanical-fracture-to-flow coupling cylinder under triaxial loading for LS_0, LS_{15}, and LS_{25}: (a) deviatoric stress-axial strain, (b) total porosity-axial strain, (c) hydraulic conductivity and mean crack width, and (d) hydraulic conductivity-axial strain.

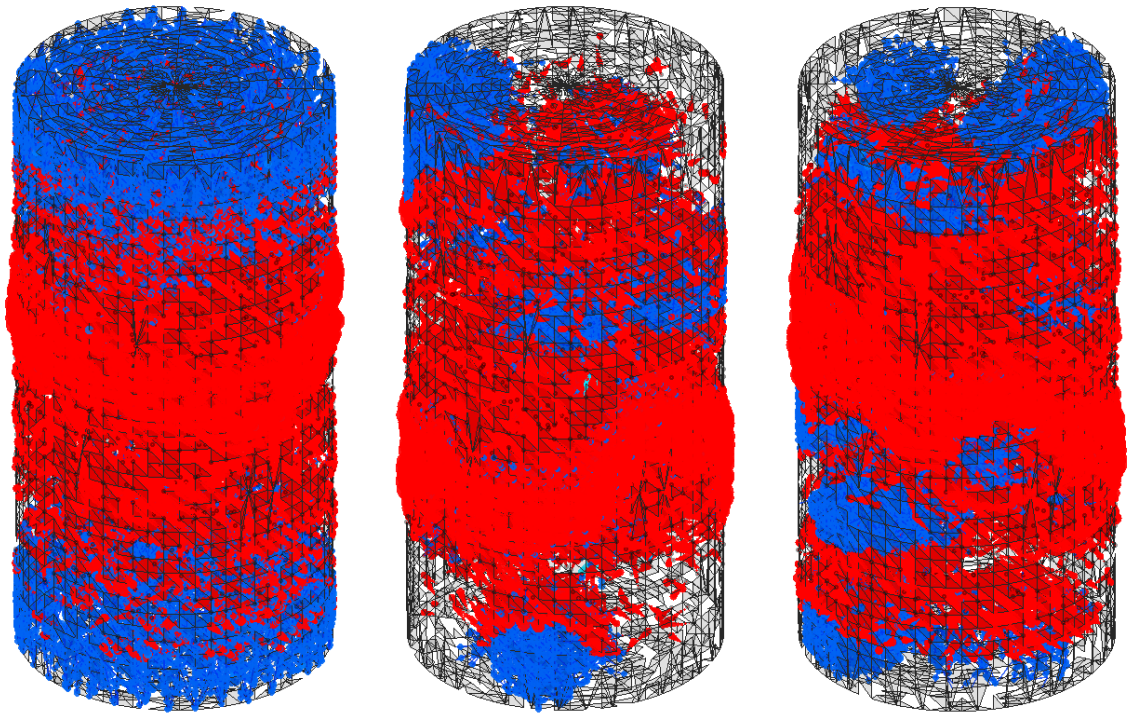


Figure 4.21: Triaxial crack propagation and seepage response for (a) LS_0, (b) LS_{15}, and (c) LS_{25}.

capacity are not the same quantity. A material can begin to conduct earlier, but another can achieve a higher final conductivity if its final connected crack is wider or more continuous.

fig (d) plots hydraulic conductivity against axial strain. The curves remain almost flat during the pre-peak and early damage stages, then rise sharply near fracture localization. The delayed increase in calculated hydraulic conductivity is consistent with the connectivity rule implemented in the LEM–PNM formulation. It is a response of the numerical model and should not be interpreted as independent experimental validation of the fracture-flow mechanism. It shows that conductivity is not being artificially increased as a simple function of strain or damage. Instead, the network remains hydraulically limited until a connected crack path forms. The sudden increase after localization is precisely what should occur when a fracture creates a preferential drainage path.

Figures 4.21 and 4.22 show how the hydraulic path changes with soil state under triaxial loading. The images demonstrate that seepage follows the mechanically generated crack network rather than a uniform vertical pressure gradient. This is a critical result. If the hydraulic problem

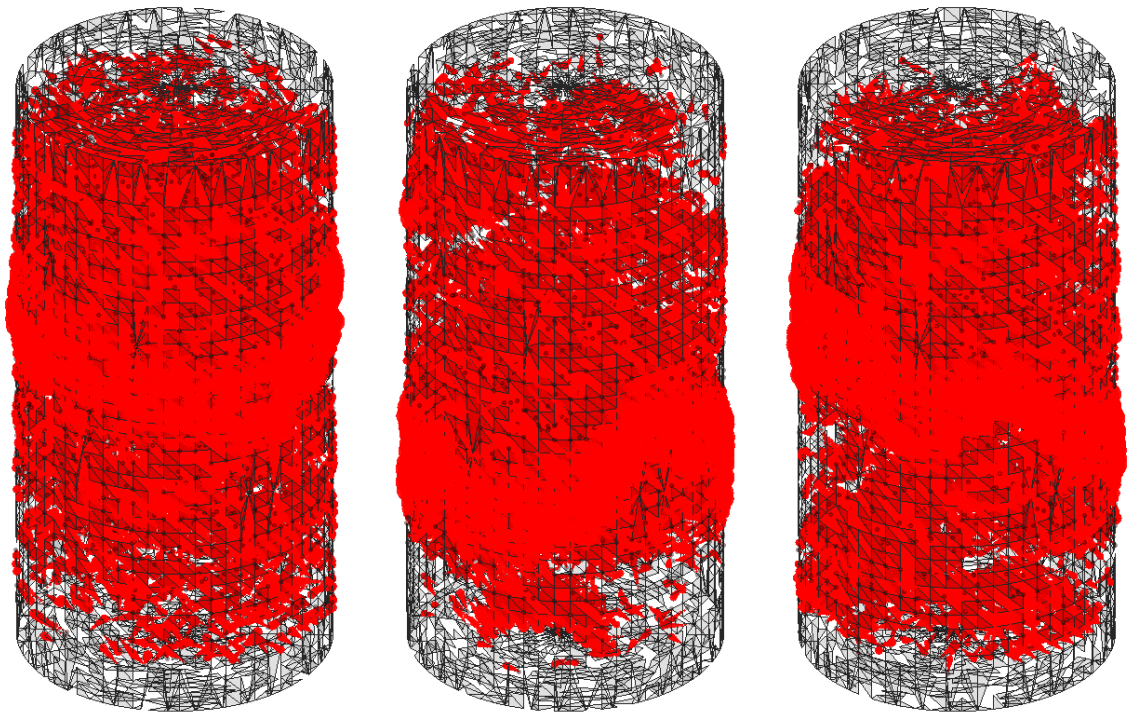


Figure 4.22: Additional triaxial crack propagation and seepage response for (a) LS_0, (b) LS_{15}, and (c) LS_{25}.

were solved as a homogeneous continuum, the pressure gradient would remain smooth, and the flow field would not reveal the fracture controlled channelling. In the LEM-PNM model, the flow concentrates where crack opening and pore connectivity provide lower hydraulic resistance.

The comparison across LS_0, LS_{15}, and LS_{25} shows that the same confining pressure and pore pressure do not produce identical seepage structures. The crack geometry and aperture distribution are material-dependent, and the flow field follows that material-dependent fracture topology. This supports the use of a coupled graph-based model rather than a scalar permeability update law.

Figure 4.23 isolates the aperture field. The aperture maps help explain the hydraulic conductivity curves in Figure 4.20. Conductivity is not proportional to the number of cracked links. It depends on the connected throats with sufficiently large apertures. A few wide, connected apertures can dominate flow because of the cubic relation, while many small or isolated apertures contribute little to the global conductivity. The aperture maps, therefore, provide a mechanical explanation for the increase in nonlinear conductivity.

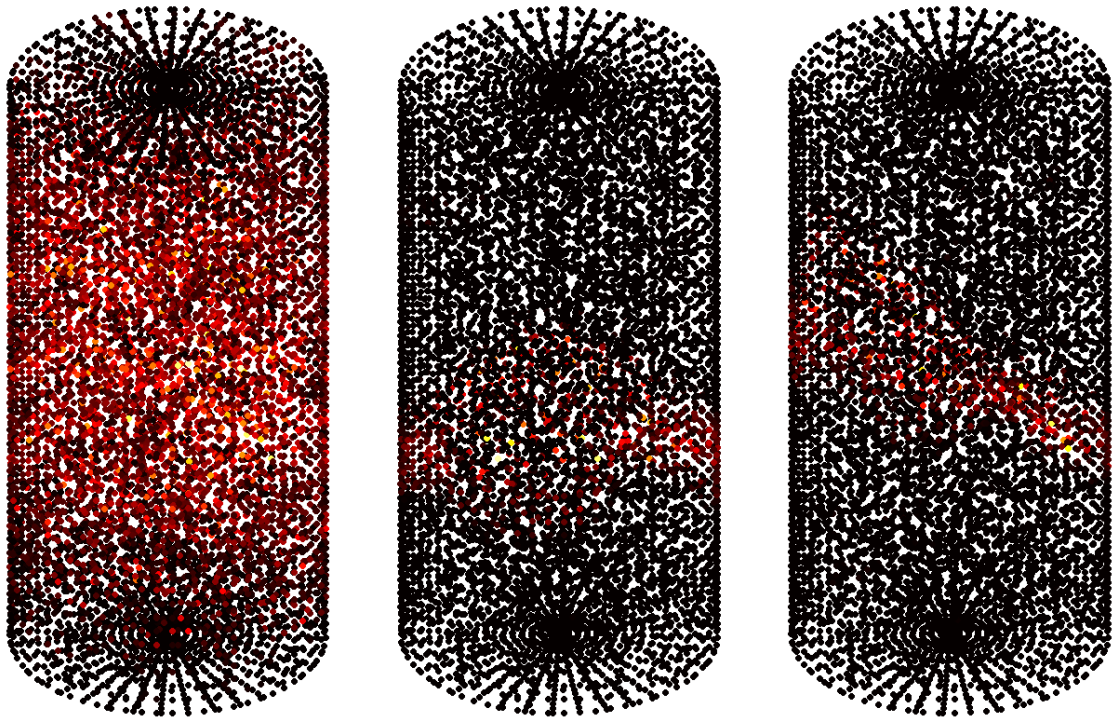


Figure 4.23: Triaxial aperture opening for (a) LS_0, (b) LS_{15}, and (c) LS_{25}.

Figure 4.24 presents the final coupled crack-flow state. The figure confirms that the dominant flow paths coincide with the connected crack network. This provides a visual validation of the pressure-solve approach: the hydraulic response is not imposed after the mechanical calculation; it is obtained by solving Eq. (4.53) on the updated pore/throat graph.

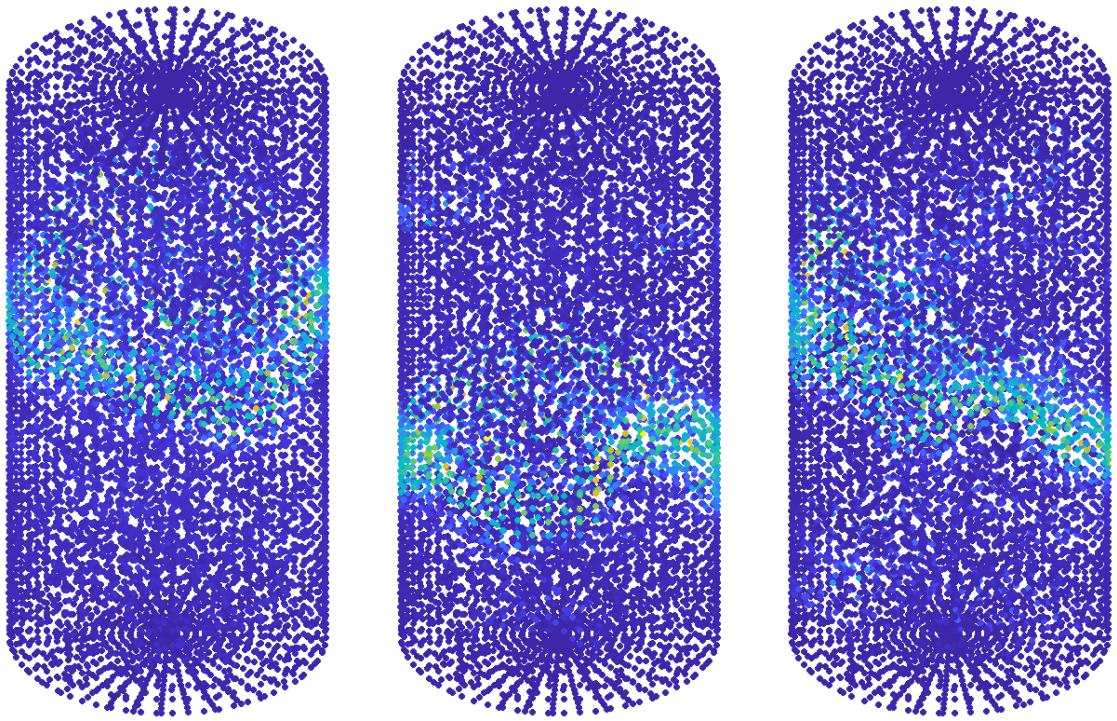


Figure 4.24: Triaxial crack formation and fluid flow for (a) LS_0, (b) LS_{15}, and (c) LS_{25}.

4.11 UCS LEM-PNM results

4.11.1 UCS response of LS_0, LS_{15}, and LS_{25}

Figure 4.25 gives the corresponding UCS results. fig (a) shows the axial stress-axial strain response. The curves again rise to a peak, followed by an abrupt post-peak drop, indicating brittle-to-quasibrittle localization. The failure stress and failure strain differ among LS_0, LS_{15}, and LS_{25}. As in the triaxial case, LS_{25} reaches a high stress at a smaller strain, whereas LS_0 continues to a larger strain before the post-peak drop. The response is consistent with material-dependent stiffness and fracture resistance. fig (b) shows the porosity evolution. The increase in porosity remains small until fracture localization, after which it becomes more pronounced. This mirrors the calculated triaxial response. In the implemented model, the porosity measure is updated from the mechanical opening and network state rather than prescribed independently; this numerical behaviour was not validated using internal porosity measurements. fig (c) shows hydraulic

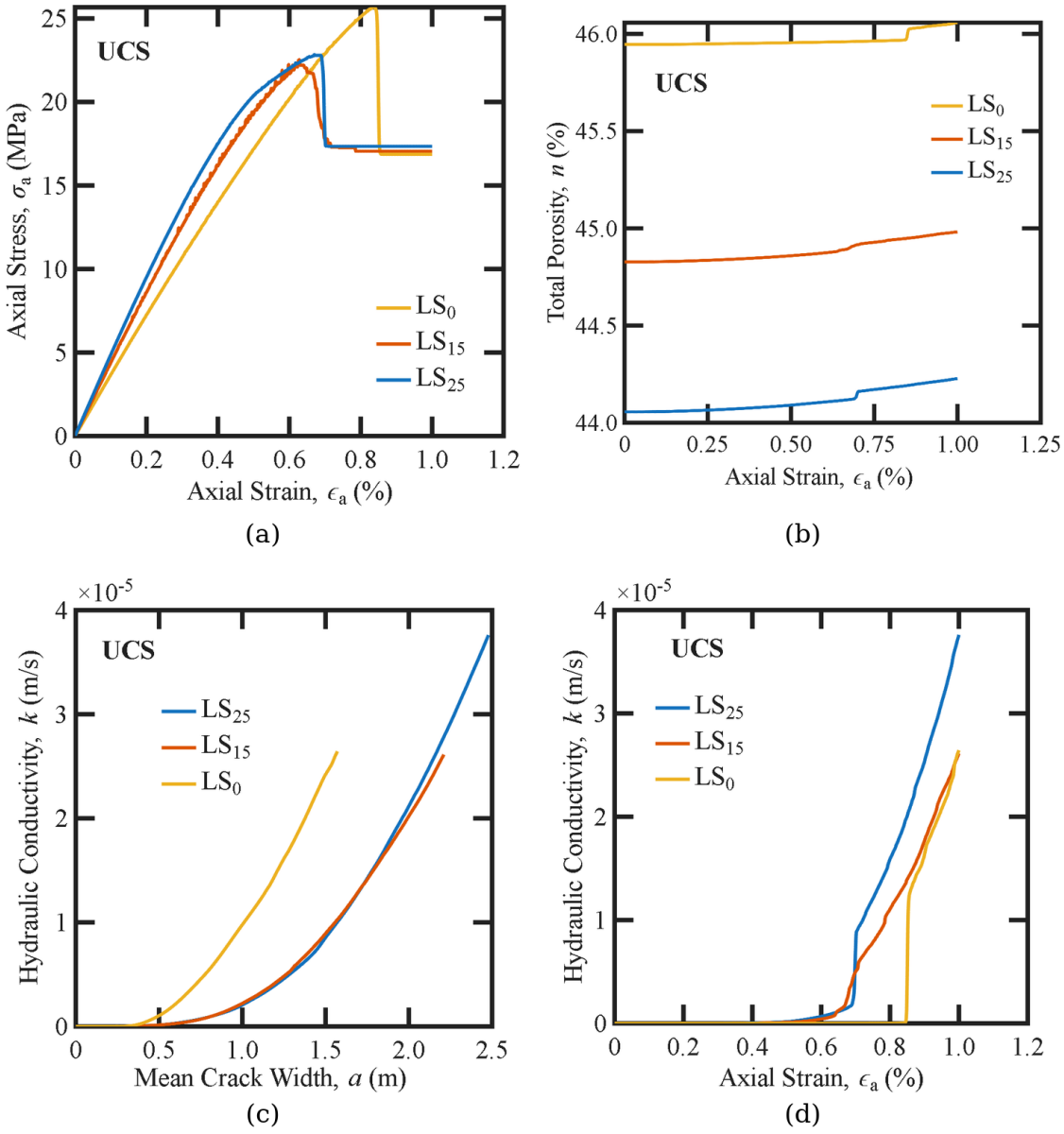


Figure 4.25: Behaviour of the sequential one-way mechanical-fracture-to-flow coupling cylinder under UCS loading for LS_0, LS_{15}, and LS_{25}: (a) axial stress-axial strain, (b) total porosity-axial strain, (c) hydraulic conductivity-mean crack width, and (d) hydraulic conductivity-axial strain.

conductivity versus mean crack width. The same nonlinear relation appears under UCS as under triaxial loading. Conductivity remains low at small crack widths and increases rapidly after connected apertures form. The curve shape is again consistent with Eq. (4.49). The differences among LS_0, LS_{15}, and LS_{25} reflect both the material-dependent crack width and the connectivity of the final crack network. fig (d) shows hydraulic conductivity versus axial strain. The most important feature is the delayed onset of the increase in conductivity. The hydraulic conductivity does not rise significantly at the beginning of loading, even though mechanical deformation is already occurring. It increases only when cracking becomes sufficiently connected. This behaviour is consistent with the implemented graph-based pressure solution, which updates throat conductance from mapped opening and connectivity rather than from a uniform empirical damage-permeability multiplier.

4.11.2 UCS crack propagation, aperture, and seepage patterns

Figures 4.26 and 4.27 show that the UCS flow field is again governed by the crack network. The difference between UCS and triaxial loading is that UCS does not apply confining pressure. Without confinement, crack opening can become more pronounced once localization starts. This produces a rapid hydraulic response once a connected fracture path forms. The figures show that the seepage field is not uniformly distributed through the cylinder; it is concentrated along the crack-controlled connected network.

The three soil states show different fracture-flow structures. The differences are not explained by a single scalar porosity value. They result from the combined influence of mechanical fracture path, aperture opening, local throat conductance, and graph connectivity. This is why the PNM must remain coupled to the LEM fracture state at every loading step.

Figure 4.28 shows aperture opening under UCS. Compared with the triaxial aperture fields, the UCS aperture patterns are less confined. This is expected because the lateral confining stress is absent. The figure supports the hydraulic conductivity curves: once the aperture field aligns with the hydraulic boundary direction, conductivity increases rapidly. The aperture maps also show why mean crack width alone is insufficient. Two specimens can have comparable mean crack width but different global conductivity if one contains a better-connected aperture path.

Figure 4.29 presents the final coupled crack-flow state under UCS. The fluid pathway is aligned with the mechanically formed crack system, confirming that hydraulic conductivity arises from the pore/fracture network. In a homogeneous continuum model, the final flow field cannot represent the local channelization observed here. The LEM-PNM model captures this by directly transferring the failed-link topology and link openings into the hydraulic graph.

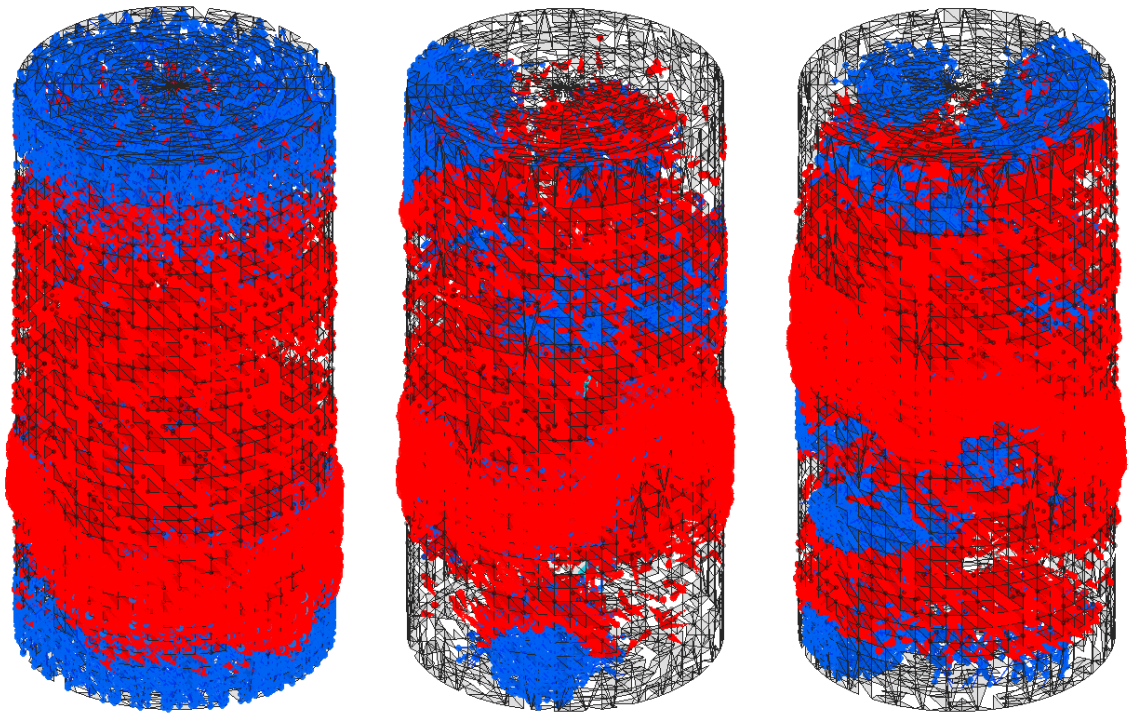


Figure 4.26: UCS crack propagation and seepage response for (a) LS_0, (b) LS_{15}, and (c) LS_{25}.

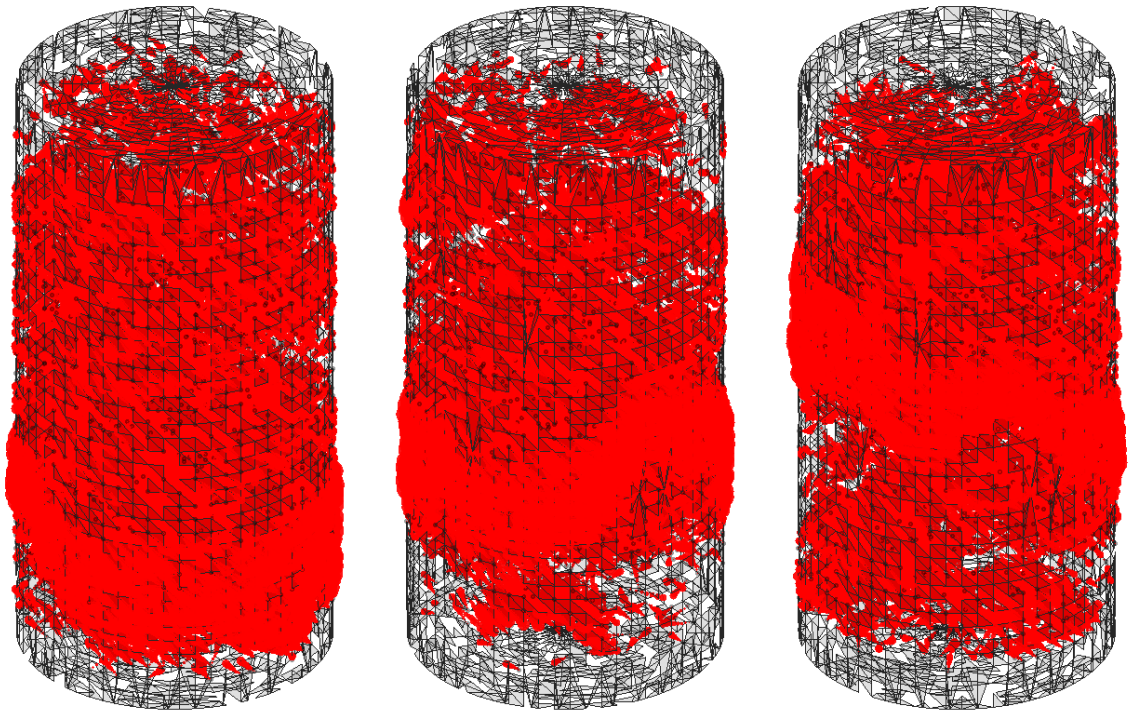


Figure 4.27: Additional UCS crack propagation and seepage response for (a) LS_0, (b) LS_{15}, and (c) LS_{25}.

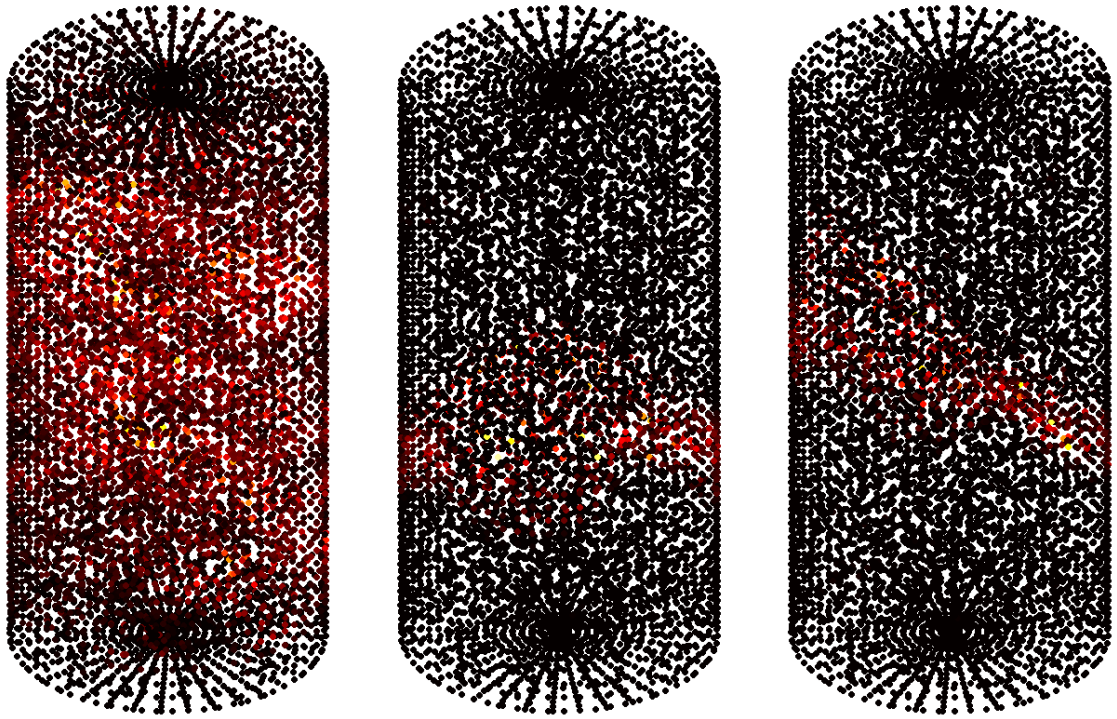


Figure 4.28: UCS aperture opening for (a) LS_0, (b) LS_{15}, and (c) LS_{25}.

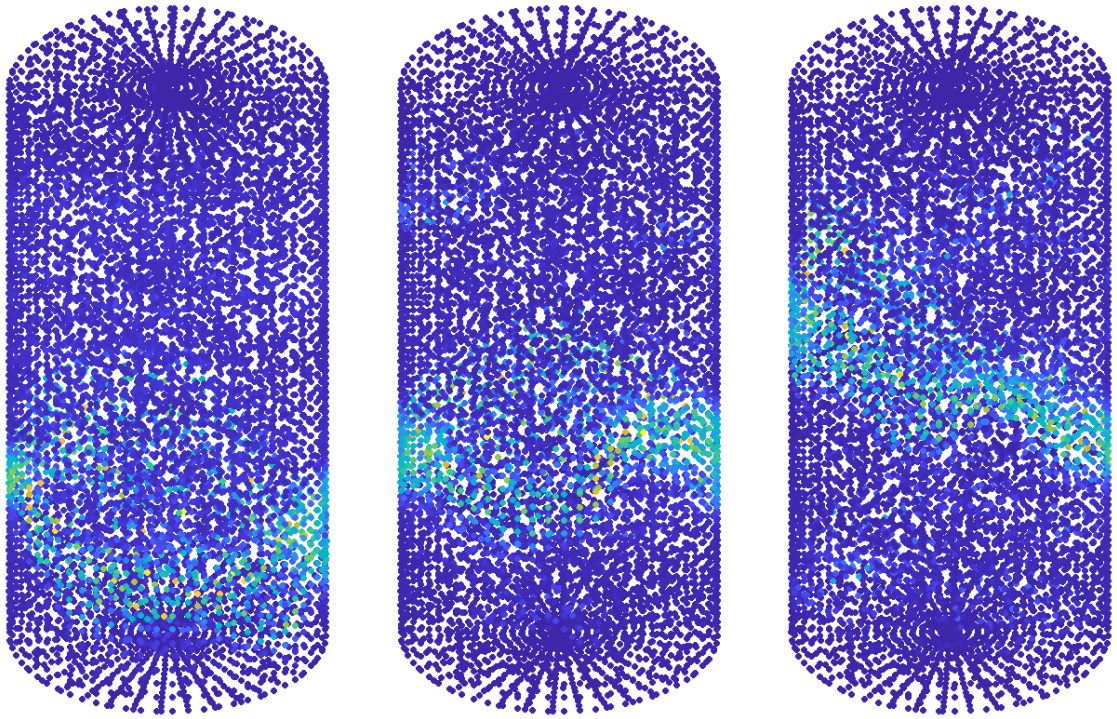


Figure 4.29: UCS crack formation and fluid flow for (a) LS_0, (b) LS_{15}, and (c) LS_{25}.

4.12 Comparison of triaxial and UCS hydraulic behaviour

The triaxial and UCS simulations show the same modelled sequence with different responses under the prescribed confinement conditions. In both calculations, hydraulic conductivity remains small during the pre-localization stage because isolated failed links do not yet form an inlet-to-outlet high-conductance path. The calculated conductivity increases after mechanically opened throats become connected. This response follows from the implemented aperture and connectivity rules and should not be interpreted as independent experimental confirmation of the physical mechanism.

The presence of confining pressure in the triaxial case restrains lateral opening and delays the development of some aperture pathways. The triaxial LEM calculation was performed under a prescribed total confining stress of 100 kPa. The PNM pressure field was solved after the mechanical aperture update. Because the calculated pore pressure was not returned to the mechanical equilibrium equation, the present model does not calculate a pore-pressure-dependent effective-stress path. The difference between the UCS and triaxial results is therefore attributed to the prescribed mechanical confinement and the resulting discontinuity topology and aperture, not to a Biot effective-stress update. In the present LEM-PNM implementation, pore pressure is imposed in the hydraulic solve, and the mechanical response is governed by the lattice fracture model under the prescribed boundary stresses and displacements. The confining pressure alters the mechanical localization pattern, and the hydraulic network responds to the resulting change in crack topology.

UCS loading permits less restrained crack opening after localization. This can lead to rapid aperture growth and increased conductivity once a connected path forms. However, the final conductivity is still not guaranteed by the absence of confinement alone. It depends on the distribution of connected apertures. The numerical outputs are consistent with this model behaviour, and the conductivity curves, aperture maps, and crack-flow visualizations should therefore be interpreted together. Stress-strain curves alone do not explain hydraulic conductivity, and aperture maps alone do not explain it unless connectivity is assessed.

4.13 Technical implications

The results of this chapter provide a traceable and problem-specific modelling chain. First, four methods were implemented and compared for the same SENB fracture problem. Second, LEM was selected because it provided the closest combined agreement with the experimental fracture-toughness trends and visible crack paths for the examined cases and supplied an explicit failed-link graph for hydraulic mapping. Third, the pore-network model was introduced after this

comparison. Fourth, the hydraulic calculation used the LEM topology and opening to update pore and throat conductance rather than applying a uniform empirical damage-permeability multiplier.

The evidence supporting the selection of LEM consists of its combined agreement with the measured initiation-toughness trends and the visible post-test paths, together with its direct representation of displacement jumps. The path comparison remains partly qualitative unless a stated image-registration and tortuosity metric is applied. The comparison therefore supports LEM for the present fracture-to-flow workflow but does not establish that LEM is universally more accurate than XFEM, STFEM, or phase-field fracture.

Figures 4.20 and 4.25 show a delayed and nonlinear increase in the calculated hydraulic conductivity because the implemented pore-network rule requires mechanically opened throats to form a connected inlet-to-outlet path. The crack-seepage figures illustrate localization of the calculated flow along connected high-conductance paths. These results are numerical predictions consistent with the model formulation. They do not independently validate the fracture-to-flow mechanism because flow through specimens fractured under the simulated UCS and triaxial loading paths was not measured.

XFEM, STFEM, phase-field fracture, and LEM therefore serve as alternative fracture representations for the SENB comparison, while LEM provides the discrete graph used in the subsequent pore-network calculation. This sequence makes the transfer from mechanical fracture output to hydraulic prediction explicit and traceable.

4.14 Chapter summary

This chapter compared XFEM, STFEM, phase-field fracture, and LEM for the two-dimensional SENB problem using the same displacement increment, nominal discretization scale, geometry families, and experimental reference quantities. Within the selected comparison measures, LEM gave the closest combined agreement with the experimental fracture-toughness trends and visible post-test paths for the cases examined. XFEM and STFEM represented sharp or tracked discontinuities, while the phase-field method represented fracture as a diffuse damage band whose conversion to a hydraulic graph would require additional assumptions.

LEM was therefore selected for the present fracture-to-flow workflow. It produced a tortuous failed-link path that was qualitatively similar to the visible post-test paths and followed the experimental K_{Ic} trends for the examined soils. The random Voronoi-Delaunay lattice reduces alignment with a regular grid, although the results remain dependent on the lattice realization, discretization, and assigned link properties. Its principal practical advantage is that it provides an explicit failed-link graph and displacement jumps for hydraulic mapping.

The LEM-based PNM then updated pore and throat conductance from the calculated mechanical opening, solved the network pressure field, and calculated equivalent hydraulic conductivity. In this implementation, the predicted conductivity evolution is controlled by the mapped aperture, assigned throat properties, conductance threshold, and inlet-to-outlet connectivity. The delayed increase in conductivity is therefore consistent with the implemented model rules and remains a prediction requiring independent fractured-specimen flow validation.

The chapter establishes a reproducible sequence for comparing fracture representations and transferring the selected mechanical output into a one-way pore-network calculation. It does not establish a fully coupled hydraulic-fracture model or independent validation of the predicted conductivity changes.

Chapter 5

Conclusions

5.1 Thesis synthesis

The present study is developed around a central limitation in conventional clay barrier design: an intact compacted clay layer may satisfy hydraulic conductivity requirements, yet a connected crack can bypass the low-permeability matrix and create a preferential contaminant transport path. The practical consequence is that hydraulic conductivity measured on an intact specimen is necessary but not sufficient for long-term containment design. A clay barrier must also resist crack initiation, limit crack propagation, and prevent the formation of interconnected aperture networks that can transmit leachate. The work therefore integrates conventional geotechnical characterization with fracture mechanics and numerical fracture-flow modelling.

Chapter 1 established the motivation for the present study by connecting PFAS-containing products, landfill disposal, leachate formation, clay liner containment, and crack-driven groundwater exposure. The motivation is not only environmental; it is mechanical. Clay liners are designed to reduce leachate percolation, but their performance is governed by the barrier's continuity. Once tensile cracks form due to desiccation, shrinkage, differential settlement, construction defects, or stress redistribution, the hydraulic response is no longer governed solely by the intact soil matrix. The barrier becomes a coupled fracture-hydraulic system.

Chapter 2 showed that the literature provides strong procedures for soil classification, compaction, hydraulic conductivity, shear strength, and consolidation, but does not provide an equally mature framework for soil fracture toughness testing, soil-specific SENB geometry correction, crack-propagation validation, or crack controlled hydraulic conductivity prediction. Linear elastic fracture mechanics provides the required crack-tip theory, but direct transfer of metallic specimen

behaviour to compacted soils is not defensible without calibration because compacted soils are low-stiffness, moisture-sensitive, heterogeneous, and quasibrittle. The review, therefore, established the need for a soil-specific experimental and numerical framework.

Chapter 3 addressed this need experimentally. A displacement-controlled SENB setup is developed for compacted clayey soils; a balanced-geometry matrix is used to evaluate size and notch effects; and a soil-specific geometry-correction function, $f(a/W)$, is developed through numerical, analytical, and experimental methods. The chapter also showed how fracture toughness, hydraulic conductivity, strength, and compressibility interact in material selection. Chapter 4 extended the same fracture parameters into numerical crack-propagation and hydraulic conductivity modelling. The developed $f(a/W)$ in Chapter 3 is retained as the basis for fracture toughness reduction in experimental and numerical comparisons, ensuring that Chapter 4 did not revert to an unverified metallic correction.

The study therefore contributes a connected framework: select clay barrier materials using conventional geotechnical criteria, measure crack initiation resistance using a soil-adapted SENB protocol, calculate corrected K_{Ic} using the developed $f(a/W)$, interpret K_{Ic} together with hydraulic conductivity and compressibility, and use a validated crack propagation model before estimating fracture-controlled hydraulic conductivity. This sequence is important because a hydraulic model attached to an unrealistic crack field may produce plausible seepage figures while still being mechanically wrong.

5.2 Experimental conclusions

The experimental programme demonstrated that Mode I fracture toughness of compacted clayey soils can be measured accurately if specimen preparation, notch formation, moisture conditioning, loading rate, load resolution, and CMOD measurement are controlled. The developed SENB system is a major outcome of the present study because compacted clay beams are weak, moisture sensitive, and prone to damage during preparation. Conventional fracture testing systems designed for metals, rocks, or concrete are not automatically suitable for soils because they often lack the low-load resolution, mould-based notch control, and CMOD sensitivity required for clayey specimens. The developed system closed this gap by combining a 10 kN load cell with 0.1 N readability, vertical displacement measurement, dual-CMOD measurement, roller supports, and moulds capable of forming a controlled notch during compaction. The measured apparent Mode-I initiation resistance varied with water content and dry density. These observations are consistent with a state-dependent unsaturated-soil response, but they do not directly demonstrate suction loss, contact lubrication, or contact softening because those quantities were not measured.

The final SENB experimental programme used a balanced 5×3 factorial geometry design with three independent replications. Specimen geometry and notch ratio were treated as controlled design factors. The geometry families used $W = 35$, 50, and 65 mm, with $B = W$ and $B = 2W$ where feasible, $S/W = 4$, $L/W = 5$, and $a/W = 0.45$, 0.50, and 0.55. All valid specimens were prepared and tested near the intended moisture-density states, with fixed loading conditions and crack propagation from the notch tip. The larger rectangular geometry $W = 65$ mm, $B = 130$ mm is attempted but excluded from the factorial analysis because self-weight made reliable handling and testing impractical. This exclusion is not a weakness in the design; it defines the upper practical boundary for SENB testing of weak compacted clay beams.

The specimen geometry study showed that maximum load is strongly affected by crack length and ligament size, whereas corrected K_{Ic} becomes substantially more stable once the soil-specific geometry correction is applied. This distinction is central to the interpretation of fracture toughness. $P_{\max}$ is a structural response of a specific beam geometry, while K_{Ic} is intended to represent material crack-initiation resistance after finite body effects are removed. The coefficient-of-variation analysis demonstrated that the $W = B = 50$ mm specimen provides the most repeatable corrected toughness values for the investigated soils. This geometry balances three requirements: it is large enough to enable representative fracture process zone development, small enough to enable repeatable soil compaction and notch formation, and practical for routine laboratory preparation.

The developed $f(a/W)$ is a principal technical contribution of the present study. The numerical route used Abaqus® contour-integral extraction of K_{I} after verifying the finite element model against the ASTM metallic benchmark. The analytical route used weight function integration to preserve the LEFM crack tip singularity and to recalibrate the finite-body amplification for measured soil elastic properties. The experimental route used changes in compliance from the load-CMOD response as an independent check. These three routes support the same conclusion: the near-tip LEFM singularity remains a valid crack-initiation description for the tested compacted soils, but the finite-body SENB amplification function must be calibrated for soil compliance. Using a metallic $f(a/W)$ without verification would obscure the distinction between material fracture resistance and specimen compliance.

The measured fracture response is controlled primarily by the mechanical state. The measured apparent Mode-I initiation resistance varied systematically with dry density and water content. Higher dry density was generally associated with higher resistance, whereas higher water content was associated with lower resistance within each tested soil series. Because matric suction, contact coordination, contact-scale stiffness, and local saturation were not measured, the results do not separate the contributions of capillary forces, density, fabric, and moisture history. Near representative compacted states, corrected fracture toughness values were approximately 0.86-0.87 kPam$^{0.5}$ for LS_0, 0.99-1.01 kPam$^{0.5}$ for LS_{15}, 0.51-0.62 kPam$^{0.5}$ for LS_{25}, and 1.70-

1.83 kPam$^{0.5}$ for FS. These values show that increasing granular content does not automatically improve the barrier response. A mixture can gain stiffness or crack resistance in one state while losing hydraulic acceptability or compressibility performance in another.

The field soil exhibited the highest wet-state fracture toughness among the investigated materials. This behaviour is consistent with a denser natural fabric, a lower void ratio, and a stronger interparticle structure than in the laboratory mixtures. However, the field soil also illustrates why fracture testing should not be interpreted in isolation. Natural fabric can improve crack resistance, but field soils may also show greater variability. The present study, therefore, treats repeatability and coefficient of variation as design-relevant indicators, not merely as statistical checks.

The nanomaterial study demonstrated that improvement strategies must be evaluated using multiple properties. A dosage that increases K_{Ic} may still be unsuitable if it increases hydraulic conductivity or produces unfavourable compressibility. The approximately 0.10% ZnO-T dosage emerged as the mechanically favourable dosage in the tested matrix, but the final material decision depends on the simultaneous response of $P_{\max}$, K_{Ic}, k, C_{r}, m_{v}, and a_{v}. This result is important for clay-barrier design because fracture resistance cannot be optimized independently of hydraulic sealing and volume-change behaviour.

The proposed K_{Ic}-k-a_{v} interrelationship provides a practical synthesis of the experimental results. The screening space defined by $k \leq 1.0 \times 10^{-9}$ m/s and $K_{\mathrm{Ic}} \geq 0.8$ kPam$^{0.5}$ identified LS_0 and FS as the most favourable barrier candidates among the investigated materials. LS_{15} is toughness-favourable but hydraulically marginal, while LS_{25} is not suitable under the combined criterion because of comparatively high hydraulic conductivity and lower fracture toughness. This interrelationship is a design-level result: it indicates that crack resistance, hydraulic conductivity, and compressibility should be treated as coupled acceptance variables.

5.3 Numerical and coupled modelling conclusions

The numerical part of the present study compared the extended finite element method, space-time finite element method, phase-field fracture method, and lattice element method using the same SENB geometry and corrected fracture-toughness framework. The comparison is based on four requirements: notch-tip crack initiation, realistic crack trajectory, agreement with experimental K_{Ic} trends, and suitability for coupled hydraulic modelling. This multi-criterion comparison is necessary because a numerical method can generate a crack yet remain unsuitable for clay-barrier design if the crack path is overly smooth, too diffuse, mesh-biased, or not hydraulically interpretable.

XFEM represented a sharp discontinuity without remeshing and provided an important benchmark for the SENB comparison. STFEM represented fracture evolution over successive pseudo-time slabs, while phase-field fracture represented the discontinuity as a diffuse damage band. For the present SENB cases and comparison criteria, LEM provided the closest combined agreement with notch-tip initiation, visible path tortuosity, and corrected K_{Ic} trends, while also supplying an explicit failed-link graph and displacement jumps for hydraulic mapping. This conclusion is specific to the implementations, parameters, discretizations, and experimental references used in this study and should not be interpreted as a universal ranking of the four methods.

In the LEM-PNM simulations, the calculated hydraulic conductivity depended on the mapped mechanical opening, assigned throat conductance, and inlet-to-outlet connectivity. Isolated failed links or non-percolating damage clusters did not produce a major calculated specimen-scale conductivity increase, whereas a connected set of opened throats produced a larger flow response. This behaviour follows from the implemented network formulation and remains to be validated against flow measurements on mechanically fractured specimens.

The UCS and triaxial simulations predicted different aperture and connectivity responses under the prescribed confinement conditions. In the UCS calculation, the absence of radial confinement allowed greater lateral opening in the numerical model, while the prescribed 100 kPa total confinement in the triaxial calculation restrained some aperture development. These are model predictions under controlled boundary conditions. Their transfer to field barriers requires calibration against stress-path-controlled and fracture-flow experiments.

The Chapter 4 validation sequence supports the use of the developed soil-specific $f(a/W)$ beyond the laboratory chapter. The same corrected SENB fracture-toughness basis used in Chapter 3 is used for numerical comparison in Chapter 4. This continuity is essential: if Chapter 4 had used a metallic correction function while Chapter 3 developed a soil-specific one, the numerical validation would have compared incompatible fracture toughness values. The present study, therefore, maintains a single fracture mechanics reduction path from experiment to simulation.

5.4 Fracture based clay barrier design methodology

The present study supports a staged design methodology for discontinuity-sensitive clay barriers. The first stage remains conventional geotechnical screening. A suitable material must satisfy classification, plasticity, gradation, compaction, hydraulic conductivity, shear strength, compressibility, and construction-quality criteria. These requirements cannot be bypassed by fracture testing. A material that fails intact hydraulic or strength requirements is not an acceptable barrier material, even if it has high fracture toughness.

The second stage is fracture-toughness characterization. The recommended routine specimen is the $W = B = 50$ mm SENB beam with $S/W = 4$, $L/W = 5$, and notch ratios in the range $a/W = 0.45$-0.55. The test should be displacement controlled, with load, vertical displacement, and dual-CMOD measurements recorded continuously. Valid tests should show notch-tip crack initiation, stable pre-peak response, and a crack path consistent with Mode I bending. K_{Ic} should be calculated using the developed soil-specific $f(a/W)$, not an unverified metallic polynomial.

The third stage is coupled material interpretation. Corrected K_{Ic}, intact hydraulic conductivity k, and coefficient of compressibility a_{v} should be evaluated together. The proposed K_{Ic}-k-a_{v} interrelationship provides a compact way to classify the trade-off between sealing capacity, crack initiation resistance, and volume-change susceptibility. For the materials investigated in the present study, the combined screening limits $k \leq 1.0 \times 10^{-9}$ m/s and $K_{\mathrm{Ic}} \geq 0.8$ kPam$^{0.5}$ provide a rational preliminary acceptance space. These limits should be refined as more field and laboratory datasets become available, but the form of the coupled check is already justified by the experimental results.

The fourth stage is improvement and optimization. Sand addition, nanomaterial addition, compaction adjustment, and field-soil selection should be evaluated based on multi-property responses. A toughness-improved mixture may become hydraulically marginal; a low-permeability mixture may remain crack sensitive; a low-compressibility mixture may still form connected cracks under shrinkage or settlement. Design should therefore seek a balanced zone rather than a maximum value of a single property.

The fifth stage is numerical fracture-flow assessment for high risk applications. Validated crack propagation should precede hydraulic conductivity prediction. The LEM-PNM framework developed in this study provides one route because it first validates the crack solver against SENB data and then uses the mechanically generated crack graph to update hydraulic connectivity. This stage is appropriate for barriers subject to high contaminant consequences, complex loading, differential settlement, or long service lives.

5.5 Original contributions

The main original contributions of this study are as follows.

1. A displacement controlled SENB laboratory testing system and mould family were developed for compacted clayey soils, with direct load, vertical displacement, and dual-CMOD measurement.
2. A balanced SENB geometry and notch-ratio programme is established, and the $W = B = 50$ mm geometry is identified as the most repeatable practical specimen size for the tested clay-barrier soils.

3. A soil-specific SENB geometry correction function, $f(a/W)$, is developed through Abaqus® contour-integral extraction, analytical weight-function derivation, and experimental compliance validation.

4. A fracture-toughness database is developed for LS_0, LS_{15}, LS_{25}, and FS over controlled moisture-density states, specimen geometries, and notch ratios.

5. Nanomaterial improvement is evaluated using fracture toughness, hydraulic conductivity, strength, and consolidation response rather than a single mechanical index.

6. A proposed K_{Ic}-k-a_v interrelationship is introduced for clay barrier screening and is used to classify the tested materials in a coupled design space.

7. XFEM, space-time FEM, phase-field fracture, and LEM were compared using the same SENB cases and reference quantities, and LEM was selected for the present fracture-to-flow workflow based on the examined comparison criteria and its explicit failed-link representation.

8. A sequential one-way LEM-PNM framework is developed to map calculated failed-link opening and connectivity to predicted equivalent hydraulic conductivity without using a uniform empirical damage-permeability multiplier.

5.6 Limitations

The results should be interpreted within the context of the tested material, geometry, and loading domain. The SENB programme focused on Mode I crack initiation and, predominantly, on Mode I crack growth. Mixed-mode fracture, cyclic loading, long-term wetting-drying, freeze-thaw degradation, chemical attack, and field-scale construction variability were not fully resolved in the present work. The LEM-PNM model provides a mechanistic framework for fracture-controlled hydraulic conductivity, but its field use requires additional calibration of aperture transfer, residual aperture, material heterogeneity, suction effects, and boundary conditions. These limitations do not diminish the contribution of the present study; they define the next level of validation required before fracture based clay barrier design becomes a routine design standard.

Matric suction was not measured or independently controlled during the SENB or UCS tests. Internal moisture uniformity and possible patchy saturation were also not examined using X-ray computed tomography or another internal imaging method. The present results are therefore state-conditioned by water content, density, and the adopted preparation procedure, but they do not provide a suction-controlled fracture law.

The present study demonstrates that fracture mechanics can be integrated into geotechnical design without replacing soil mechanics. Conventional classification, compaction, hydraulic conductivity, strength, and consolidation tests remain the foundation of clay barrier design. The missing layer is crack resistance. By adding a soil-specific SENB test, a calibrated $f(a/W)$, a coupled K_{Ic}-k-a_{v} interpretation, and validated fracture-flow modelling, clay barrier performance can be evaluated as an discontinuity-sensitive clay barrier. This shift is necessary for containment systems where a single connected fracture can dominate long-term hydraulic performance.

Under submerged and equilibrated conditions, the capillary contribution associated with unsaturated preparation would be substantially reduced or eliminated, while swelling, fabric rearrangement, drainage conditions, and transient pore pressure could alter stiffness, peak load, and apparent initiation resistance. A reduction in measured resistance is plausible but cannot be quantified from the present tests. The current mechanical models cannot predict this change because their input properties are not functions of saturation and the hydraulic pressure calculated by the PNM is not returned to the mechanical equations.

Future research scope

The present study establishes the experimental and numerical basis for fracture based clay barrier design. The following extensions would strengthen the framework and broaden its use in engineering practice.

1. **Long-term environmental cycling.** Extend the SENB, $f(a/W)$, and LEM-PNM framework to wetting-drying, freeze-thaw, thermal cycling, chemical exposure, and real landfill leachate so that degradation of K_{Ic}, k, and a_{v} can be quantified with ageing.

2. **Mixed-mode and hydraulic fracture loading.** Extend the present Mode I framework to mixed Mode I-II, shear-assisted cracking, hydraulic-fracture initiation, and combined settlement-suction loading, which are common in liners, dam cores, and tailings barriers.

3. **Field-scale validation.** Construct instrumented trial liner or clay core sections to compare field suction, settlement, crack initiation, aperture evolution, and hydraulic response with laboratory SENB parameters and LEM-PNM predictions.

4. **Microstructure-informed fracture modelling.** Combine SEM, XRD, micro-CT, pore-size distribution, and image-based fabric descriptors with LEM parameters so that anisotropy, particle bonding, pore connectivity, and nanomaterial distribution can be represented explicitly.

5. **Reliability-based design charts.** Develop probabilistic acceptance charts for K_{Ic}, k, a_{v}, compaction state, defect size, crack spacing, and construction variability so that fracture based clay barrier design can be expressed in reliability terms.

6. **Reactive contaminant transport through cracked barriers.** Couple fracture controlled hydraulic conductivity with PFAS transport, diffusion, adsorption, retardation, and leachate chemistry to quantify contaminant breakthrough through intact and fractured barrier systems.

References

Abdi, M. R., Parsapajouh, A., and Arjomand, M. A. (2008). "Effects of random fiber inclusion on consolidation, hydraulic conductivity, swelling, shrinkage limit and desiccation cracking of clays". In: *International Journal of Civil Engineering*.

Albrecht, B. A., and Benson, C. H. (2001). "Effect of desiccation on compacted natural clays". In: *Journal of Geotechnical and Geoenvironmental Engineering* 127.1, pp. 67–75. DOI: 10.1061/(ASCE)1090-0241(2001)127:1(67).

Aliha, M. R. M., and Haghighatpour, P. J. (2022). "Application of asymmetric semi-circular bend test for determining mixed mode I + II fracture toughness of compacted soil material". In: *Engineering Fracture Mechanics*. DOI: 10.1016/j.engfracmech.2022.108268.

Aliha, M. R. M., Iranmanesh, M. A., Afrasiabian, A., and Mohammadi, M. H. (2026). "Fracture toughness of clay stabilized with different additives: An experimental and theoretical study". In: *Engineering Fracture Mechanics*. DOI: 10.1016/j.engfracmech.2025.111739.

Allen, J. R. L. (1982). "On the curl of desiccation polygons". In: *Sed Geol*.

Alqahtani, I., Starr, A., and Khan, M. (2024). "Fracture Behaviour of Aluminium Alloys under Coastal Environmental Conditions: A Review". In: *Metals* 14.3, p. 336. DOI: 10.3390/met14030336.

Amarasiri, A. L., Costa, S., and Kodikara, J. K. (2011). "Determination of cohesive properties for Mode I fracture from compacted clay beams". In: *Canadian Geotechnical Journal* 48.8, pp. 1163–1173. DOI: 10.1139/t11-031.

Amarasiri, A. L., and Kodikara, J. K. (2013). "Numerical modelling of a field desiccation test". In: *Geotechnique*.

Ambati, M., Gerasimov, T., and De Lorenzis, L. (2015). “A review on phase-field models of brittle fracture and a new fast hybrid formulation”. In: *Computational Mechanics*.

Ameur, L. I., and Hattab, M. (2022). “Cracking of unsaturated clays using a newly developed small-beam bending apparatus and analysis by digital image correlation”. In: *Geomechanics for Energy and the Environment*. DOI: 10.1016/j.gete.2021.100307.

Anderson, T. L. (2017). *Fracture Mechanics: Fundamentals and Applications*. 4th ed. Boca Raton, Florida: CRC Press. DOI: 10.1201/9781315370293.

ASTM C136 (2019). *ASTM C136: Standard Test Method for Sieve Analysis of Fine and Coarse Aggregates*. Tech. rep. West Conshohocken, Pennsylvania: ASTM International.

ASTM D1557 (2021). *ASTM D1557: Standard Test Methods for Laboratory Compaction Characteristics of Soil Using Modified Effort*. Tech. rep. West Conshohocken, Pennsylvania: ASTM International.

ASTM D1586 (2022). *ASTM D1586: Standard Test Method for Standard Penetration Test and Split-Barrel Sampling of Soils*. Tech. rep. West Conshohocken, Pennsylvania: ASTM International.

ASTM D1587 (2020). *ASTM D1587: Standard Practice for Thin-Walled Tube Sampling of Fine-Grained Soils*. Tech. rep. West Conshohocken, Pennsylvania: ASTM International.

ASTM D2113 (2023). *ASTM D2113: Standard Practice for Rock Core Drilling and Sampling of Rock for Site Investigation*. Tech. rep. West Conshohocken, Pennsylvania: ASTM International.

ASTM D2166 (2024). *ASTM D2166: Standard Test Method for Unconfined Compressive Strength of Cohesive Soil*. Tech. rep. West Conshohocken, Pennsylvania: ASTM International.

ASTM D2435 (2020). *ASTM D2435: Standard Test Methods for One-Dimensional Consolidation Properties of Soils*. Tech. rep. West Conshohocken, Pennsylvania: ASTM International.

ASTM D2487 (2024). *ASTM D2487: Standard Practice for Classification of Soils for Engineering Purposes*. Tech. rep. West Conshohocken, Pennsylvania: ASTM International.

ASTM D2850 (2023). *ASTM D2850: Standard Test Method for Unconsolidated-Undrained Triaxial Compression Test on Cohesive Soils*. Tech. rep. West Conshohocken, Pennsylvania: ASTM International.

ASTM D3080 (2020). *ASTM D3080: Standard Test Method for Direct Shear Test of Soils Under Consolidated Drained Conditions*. Tech. rep. West Conshohocken, Pennsylvania: ASTM International.

ASTM D4015 (2020). *ASTM D4015: Standard Test Methods for Modulus and Damping of Soils by Resonant-Column Devices*. Tech. rep. West Conshohocken, Pennsylvania: ASTM International.

ASTM D4318 (2017). *ASTM D4318: Standard Test Methods for Liquid Limit, Plastic Limit, and Plasticity Index of Soils*. Tech. rep. West Conshohocken, Pennsylvania: ASTM International.

ASTM D4546 (2021). *ASTM D4546: Standard Test Methods for One-Dimensional Swell or Collapse of Soils*. Tech. rep. West Conshohocken, Pennsylvania: ASTM International.

ASTM D4719 (2020). *ASTM D4719: Standard Test Methods for Prebored Pressuremeter Testing in Soils*. Tech. rep. West Conshohocken, Pennsylvania: ASTM International.

ASTM D4767 (2020). *ASTM D4767: Standard Test Method for Consolidated Undrained Triaxial Compression Test for Cohesive Soils*. Tech. rep. West Conshohocken, Pennsylvania: ASTM International.

ASTM D4972 (2019). *ASTM D4972: Standard Test Methods for pH of Soils*. Tech. rep. West Conshohocken, Pennsylvania: ASTM International.

ASTM D5080 (2023). *ASTM D5080: Standard Test Method for Rapid Determination of Percent Compaction*. Tech. rep. West Conshohocken, Pennsylvania: ASTM International.

ASTM D5084 (2024). *ASTM D5084: Standard Test Methods for Measurement of Hydraulic Conductivity of Saturated Porous Materials Using a Flexible Wall Permeameter*. Tech. rep. West Conshohocken, Pennsylvania: ASTM International.

ASTM D5101 (2022). *ASTM D5101: Standard Test Method for Measuring the Soil-Geotextile System Clogging Potential by the Gradient Ratio*. Tech. rep. West Conshohocken, Pennsylvania: ASTM International.

ASTM D5311 (2020). *ASTM D5311: Standard Test Method for Load Controlled Cyclic Triaxial Strength of Soil*. Tech. rep. West Conshohocken, Pennsylvania: ASTM International.

ASTM D5434 (2020). *ASTM D5434: Standard Guide for Field Logging of Subsurface Explorations of Soil and Rock*. Tech. rep. West Conshohocken, Pennsylvania: ASTM International.

ASTM D5777 (2021). *ASTM D5777: Standard Guide for Using the Seismic Refraction Method for Subsurface Investigation*. Tech. rep. West Conshohocken, Pennsylvania: ASTM International.

ASTM D5890 (2022). *ASTM D5890: Standard Test Method for Swell Index of Clay Mineral Component of Geosynthetic Clay Liners*. Tech. rep. West Conshohocken, Pennsylvania: ASTM International.

ASTM D6243 (2022). *ASTM D6243: Standard Test Method for Determining the Internal and Interface Shear Strengths of Geosynthetic Clay Liner by Direct Shear Method*. Tech. rep. West Conshohocken, Pennsylvania: ASTM International.

ASTM D6527 (2020). *ASTM D6527: Standard Test Method for Determining Unsaturated and Saturated Hydraulic Conductivity in Porous Media by Steady-State Centrifugation*. Tech. rep. West Conshohocken, Pennsylvania: ASTM International.

ASTM D6766 (2022). *ASTM D6766: Standard Test Method for Evaluation of Hydraulic Properties Using a Flexible Wall Permeameter*. Tech. rep. West Conshohocken, Pennsylvania: ASTM International.

ASTM D6913 (2017). *ASTM D6913: Standard Test Methods for Particle-Size Distribution of Soils Using Sieve Analysis*. Tech. rep. West Conshohocken, Pennsylvania: ASTM International.

ASTM D6938 (2023). *ASTM D6938: Standard Test Methods for In-Place Density and Water Content of Soil and Soil-Aggregate by Nuclear Methods*. Tech. rep. West Conshohocken, Pennsylvania: ASTM International.

ASTM D698 (2021). *ASTM D698: Standard Test Methods for Laboratory Compaction Characteristics of Soil Using Standard Effort*. Tech. rep. West Conshohocken, Pennsylvania: ASTM International.

ASTM D7928 (2021). *ASTM D7928: Standard Test Method for Particle-Size Distribution of Fine-Grained Soils Using the Sedimentation Method*. Tech. rep. West Conshohocken, Pennsylvania: ASTM International.

ASTM D854 (2023). *ASTM D854: Standard Test Methods for Specific Gravity of Soil Solids by Water Pycnometer*. Tech. rep. West Conshohocken, Pennsylvania: ASTM International.

ASTM International (2024). *ASTM E399: Standard Test Method for Linear-Elastic Plane-Strain Fracture Toughness of Metallic Materials*. ASTM International. West Conshohocken, Pennsylvania.

ASTM-E1820 (2021). *ASTM E1820-21: Standard test method for measurement of fracture toughness*.

Atkinson, B. K. (1984). "Subcritical crack growth in geological materials". In: *Journal of Geophysical Research: Solid Earth*.

Ayad, R., Konrad, J.-M., and Souli'e, M. (1997). "Desiccation of a sensitive clay: application of the model CRACK". In: *Canadian Geotechnical Journal*.

Bai, Y., Cheng, M., Xiao, H., Li, L., Ma, Q., He, J., Yang, Y., and Deng, Y. (2025). "Desiccation cracking behavior of xanthan gum admixed clay". In: *Scientific Reports*. DOI: 10.1038/s41598-025-24356-2.

Baker, R. (1981). "Tensile strength, tension cracks, and stability of slopes". In: *Soils Found*.

Barani, O. R., and Barfar, P. (2021). "Effect of Xanthan Gum Biopolymer on Fracture Properties of Clay". In: *Journal of Materials in Civil Engineering*. DOI: 10.1061/(ASCE)MT.1943-5533.0003526.

Barenblatt, G. I. (1962). "The mathematical theory of equilibrium cracks in brittle fracture". In: *Advances in Applied Mechanics*.

Bazant, Z. P. (1984). "Size Effect in Blunt Fracture-Concrete". In: *Rock, Metal J Eng Mech-Asce*.

Bazant, Z. P. (2002). "*Scaling of Structural Strength*". In: *Scaling of Structural Strength*.

Bazant, Z. P., and Planas, J. (1998). "*Fracture and Size Effect in Concrete and Other Quasibrittle Materials*". In: *Fracture and Size Effect in Concrete and Other Quasibrittle Materials*.

Belytschko, T., and Black, T. (1999). "Elastic crack growth in finite elements with minimal remeshing". In: *International Journal for Numerical Methods in Engineering* 45.5, pp. 601–620. DOI: 10.1002/(SICI)1097-0207(19990620)45:5<601::AID-NME598>3.0.CO;2-S.

Berney, E. S., Tingle, J. S., and Newman, J. K. (2008). "Effects of desiccation on compacted clay curling". In: *Eng Geol*.

Biot, M. A. (1941). “General theory of three-dimensional consolidation”. In: *Journal of Applied Physics*.

Bishop, A. W. (1959). “The principle of effective stress”. In: *Teknisk Ukeblad*.

Blunt, M. J. (2001). “Flow in porous media: Pore-network models and multiphase flow”. In: *Current Opinion in Colloid and Interface Science* 6, pp. 197–207.

Blunt, M. J., Jackson, M. D., Piri, M., and Valvatne, P. H. (2002). “Detailed physics, predictive capabilities and macroscopic consequences for pore-network models of multiphase flow”. In: *Advances in Water Resources* 25, pp. 1069–1089.

Bolander, J. E., and Saito, S. (1998). “Fracture analyses using spring networks with random geometry”. In: *Engineering Fracture Mechanics* 61, pp. 569–591.

Borden, M. J., Verhoosel, C. V., Scott, M. A., Hughes, T. J. R., and Landis, C. M. (2012). “A phase-field description of dynamic brittle fracture”. In: *Computer Methods in Applied Mechanics and Engineering* 217-220, pp. 77–95.

Bourdin, B., Francfort, G. A., and Marigo, J.-J. (2008). “The variational approach to fracture”. In: *Journal of Elasticity*.

Bourdin, B., Francfort, G. A., and Marigo, J.-J. (2000). “Numerical experiments in revisited brittle fracture”. In: *Journal of the Mechanics and Physics of Solids* 48, pp. 797–826.

Bradley, W. H. (1933). “Factors that determine the curvature of mud-cracked layers”. In: *Am J Sci*.

Broek, D. (1982). *Elementary Engineering Fracture Mechanics*. Springer.

Buck, R. C., Franklin, J., Berger, U., Conder, J. M., Cousins, I. T., Voogt, P. de, Jensen, A. A., Kannan, K., Mabury, S. A., and Leeuwen, S. P. J. van (2011). “Perfluoroalkyl and Polyfluoroalkyl Substances in the Environment: Terminology, Classification, and Origins”. In: *Integrated Environmental Assessment and Management* 7.4, pp. 513–541. DOI: 10.1002/ieam.258.

Cai, W., Navarro, D. A., Du, J., Ying, G.-G., Yang, B., McLaughlin, M. J., and Kookana, R. S. (2022). “Increasing Ionic Strength and Valency of Cations Enhance Sorption through Hydrophobic Interactions of PFAS with Soil Surfaces”. In: *Science of the Total Environment* 817, p. 152975. DOI: 10.1016/j.scitotenv.2022.152975.

Cajuhi, T., Ziefle, G., Massmann, J., Nagel, T., and Yoshioka, K. (2024). “Modeling Desiccation Cracks in Opalinus Clay at Field Scale with the Phase-Field Approach”. In: *Conference / journal outlet on geomechanics*. DOI: 10.69631/ipj.v1i1nr8.

Camp, S., Gourc, J.-P., and Plé, O. (2010). “Landfill clay barrier subjected to cracking: Multi-scale analysis of bending tests”. In: *Applied Clay Science*. DOI: 10.1016/j.clay.2010.01.011.

Camp, S., Plé, O., and Gourc, J.-P. (2009). “Proposed Protocol for Characterizing a Clay Layer Subjected to Bending”. In: *Geotechnical Testing Journal*. DOI: 10.1520/GTJ101438.

Cengiz, C., Su, Y. Y., and Zwanenburg, C. (2025). “Flexural and Cracking Behavior of Clay Plates under Bending: Insights from Novel Tests and New Suction Parameters”. In: *Geotechnical Testing Journal*. DOI: 10.1520/GTJ20250033.

Chandler, H. W. (1984). “The use of non-linear fracture mechanics to study the fracture properties of soils”. In: *Journal of Agricultural Engineering Research*.

Cherepanov, G. P. (1967). “The propagation of cracks in a continuous medium”. In: *J Appl Math Mech*.

Costa, S., Htike, W. Y., Kodikara, J., and Xue, J. F. (2016). “Determination of j-integral for clay during desiccation”. In: *Environ Geotech*.

Costa, S., and Kodikara, J. (2012). “Evaluation of j integral for clay soils using a new ring test”. In: *Geotech Test J*.

Costa, S., Kodikara, J., and Xue, J. (2013). *J-integral as a useful fracture parameter for analysis of desiccation cracking in clayey soils*.

Coussy, O. (2004). “*Poromechanics*”. In: *Poromechanics*.

Daniel, D. E., and Wu, Y.-K. (1993). “Compacted clay liners and covers for arid sites”. In: *J Geotech Eng*.

Detournay, E. (2016). “Mechanics of hydraulic fractures”. In: *Annual Review of Fluid Mechanics*.

Detournay, E., and Cheng, A. H. D. (1993). “Fundamentals of poroelasticity”. In: *Comprehensive Rock Engineering: Principles, Practice and Projects*.

Du, Z., Deng, S., Bei, Y., Qiao, Q., Wang, B., Huang, J., Wang, Y., and Yu, G. (2014). "Sorption of perfluorooctane sulfonate (PFOS) on soils: Effects of organic matter and inorganic ions". In: *Journal of Hazardous Materials* 274, pp. 191–197.

Dugdale, D. S. (1960). "Yielding of steel sheets containing slits". In: *Journal of the Mechanics and Physics of Solids*.

Dyer, M., Utili, S., and Zielinski, M. (2009). "Field survey of desiccation fissuring of flood embankments". In: *ICE Water Management*.

Erdogan, F., and Sih, G. C. (1963). "On the crack extension in plates under plane loading and transverse shear". In: *J Basic Eng*.

Fatt, I. (1956). "The network model of porous media". In: *Transactions of the AIME* 207, pp. 144–181.

Fenton, S. E., Ducatman, A., Boobis, A., DeWitt, J. C., Lau, C., Ng, C., Smith, J. S., and Roberts, S. M. (2021). "Per- and Polyfluoroalkyl Substance Toxicity and Human Health Review: Current State of Knowledge and Strategies for Informing Future Research". In: *Environmental Toxicology and Chemistry* 40.3, pp. 606–630. DOI: 10.1002/etc.4890.

Fett, T., and Munz, D. (1997). *Stress Intensity Factors and Weight Functions*. Computational Mechanics Publications.

Francfort, G. A., and Marigo, J.-J. (1998). "Revisiting brittle fracture as an energy minimization problem". In: *Journal of the Mechanics and Physics of Solids* 46, pp. 1319–1342.

Fredlund, D. G., and Rahardjo, H. (1993). "*Soil Mechanics for Unsaturated Soils*". In: *Soil Mechanics for Unsaturated Soils*.

Fries, T. P., and Belytschko, T. (2010). "The extended/generalized finite element method: An overview of the method and its applications". In: *International Journal for Numerical Methods in Engineering* 84, pp. 253–304.

Gdoutos, E. E. (2005). *Fracture Mechanics: An Introduction*. Springer.

Glüge, J., Scheringer, M., Cousins, I. T., DeWitt, J. C., Goldenman, G., Herzke, D., Lohmann, R., Ng, C. A., Trier, X., and Wang, Z. (2020). "An Overview of the Uses of Per- and Polyfluoroalkyl Substances (PFAS)". In: *Environmental Science: Processes & Impacts* 22, pp. 2345–2373. DOI: 10.1039/D0EM00291G.

Goehring, L., Nakahara, A., Dutta, T., Kitsunezaki, S., and Tarafdar, S. (2015). *Desiccation Cracks and Their Patterns: Formation and Modelling in Science and Nature*.

Grassl, P., and Jirásek, M. (2010). "Meso-scale approach to modelling the fracture process zone of concrete subjected to uniaxial tension". In: *International Journal of Solids and Structures* 47, pp. 957–968.

Grassl, P., and Bolander, J. E. (2016). "Three-Dimensional Network Model for Coupling of Fracture and Mass Transport in Quasi-Brittle Geomaterials". In: *Materials* 9.9, p. 782. DOI: 10.3390/ma9090782.

Griffith, A. A. (1921). "The phenomena of rupture and flow in solids". In: *Philosophical Transactions of the Royal Society A*.

Gross, B., and Srawley, J. E. (1965). *Stress-Intensity Factors for Single-Edge-Notch Specimens in Bending or Combined Bending and Tension by Boundary Collocation of a Stress Function*. Tech. rep. NASA.

Guelfo, J. L., and Higgins, C. P. (2013). "Subsurface Transport Potential of Perfluoroalkyl Acids at Aqueous Film-Forming Foam (AFFF)-Impacted Sites". In: *Environmental Science & Technology* 47.9, pp. 4164–4171. DOI: 10.1021/es3048074.

Gui, Y. L., and Zhao, Z. Y. (2015). "Modelling of laboratory soil desiccation cracking using DLSM with a two-phase bond model". In: *Computers and Geotechnics*.

Gui, Y., Zhao, Z., Kodikara, J., Bui, H. H., and Yang, S. Q. (2016). "Numerical modelling of laboratory soil desiccation cracking using UDEC with a mix-mode cohesive fracture model". In: *Engineering Geology*. DOI: 10.1016/j.enggeo.2015.12.028.

Hallett, P. D., Dexter, A. R., and Seville, J. P. K. (1995). "The application of fracture mechanics to crack propagation in dry soil". In: *European Journal of Soil Science*.

Hallett, P. D., and Newson, T. A. (2001). "A simple fracture mechanics approach for assessing ductile crack growth in soil". In: *Soil Science Society of America Journal*.

Hallett, P. D., and Newson, T. A. (2005). "Describing soil crack formation using elastic-plastic fracture mechanics". In: *European Journal of Soil Science*.

Harison, J. A., Hardin, B. O., and Mahboub, K. C. (1994). "Fracture toughness of compacted cohesive soils using ring test". In: *Journal of Geotechnical Engineering*.

Health Canada (2024). *Objective for Canadian Drinking Water Quality: Per- and Polyfluoroalkyl Substances*. Official web resource. Accessed 2026-05-08.

Hewitt, P. J., and Philip, L. K. (1999). "Problems of clay desiccation in composite lining systems". In: *Eng Geol*.

Higgins, C. P., and Luthy, R. G. (2006). "Sorption of Perfluorinated Surfactants on Sediments". In: *Environmental Science & Technology* 40.5, pp. 1563–1571. DOI: 10.1021/es051800h.

Hillerborg, A., Modeer, M., and Petersson, P.-E. (1976). "Analysis of crack formation and crack growth in concrete by means of fracture mechanics and finite elements". In: *Cement and Concrete Research*.

Hirobe, S., and Oguni, K. (2017). "Modeling and numerical investigations for hierarchical pattern formation in desiccation cracking". In: *Physica D*.

Hrennikoff, A. (1941). "Solution of problems of elasticity by the framework method". In: *Journal of Applied Mechanics* 8, A169–A175.

Hu, C., Wang, L., Ling, D., Cai, W., Huang, Z., and Gong, S. (2020). "Experimental and numerical investigation on the tensile fracture of compacted clay". In: *CMES-Computer Modeling in Engineering and Sciences*. DOI: 10.32604/cmes.2020.07842.

Huang, S., Li, X., Yu, W., Zhang, X., and Du, H. (2023). "Effects of Support Friction on Mixed-Mode I/II Fracture Behavior of Compacted Clay Using Notched Deep Beam Specimens under Symmetric Fixed Support". In: *Symmetry*. DOI: 10.3390/sym15061290.

Huang, S., Li, X., Zhao, T., and Du, H. (2026). "Effect of support friction on mixed mode I-II fracture behavior of compacted clay: Numerical and experimental study". In: *Engineering Fracture Mechanics*. DOI: 10.1016/j.engfracmech.2026.111917.

Huang, S., Wang, X., Yuan, B., Liao, C., Li, X., Zhang, X., and Du, H. (2025). "Size effect on mode I fracture behavior of compacted clay with different initial crack lengths". In: *Construction and Building Materials*. DOI: 10.1016/j.conbuildmat.2025.142368.

Hughes, T. J. R., and Hulbert, G. M. (1988). "Space-time finite element methods for elastodynamics: Formulations and error estimates". In: *Computer Methods in Applied Mechanics and Engineering* 66.3, pp. 339–363. DOI: 10.1016/0045-7825(88)90006-0.

Al-Hussaini, M. M., and Townsend, F. C. (1973). “Tensile Testing of Soils: A Literature Review”. In: *U.S. Army Engineer Waterways Experiment Station report*.

Irwin, G. R. (1957). “Analysis of stresses and strains near the end of a crack traversing a plate”. In: *J Appl Mech*.

Jivkov, A. P., Hollis, C., Etiese, F., McDonald, S. A., and Withers, P. J. (2013). “A novel architecture for pore network modelling with applications to permeability of porous media”. In: *Journal of Hydrology* 486, pp. 246–258.

Julina, M., and Thyagaraj, T. (2020). “Combined effects of wet-dry cycles and interacting fluid on desiccation cracks and hydraulic conductivity of compacted clay”. In: *Engineering Geology*.

Kawai, T. (1978). “New discrete models and their application to seismic response analysis of structures”. In: *Nuclear Engineering and Design* 48, pp. 207–229.

Kaya, A. C., and Erdogan, F. (1987). “On the solution of integral equations with strongly singular kernels”. In: *Quarterly of Applied Mathematics* 45.1, pp. 105–122.

Kodikara, J., Barbour, S. L., and Fredlund, D. D. (1999). “Changes in clay structure and behaviour due to wetting and drying”. In: *Proceedings of the*.

Kodikara, J., and Choi, X. (2006). “Cracking behaviour in clay soils during drying”. In: *Can Geotech J*.

Kodikara, J., Nahlawi, H., and Bouazza, A. (2004). “Modelling of curling in desiccating clay”. In: *Can Geotech J*.

Komak Panah, A., and Yanagisawa, E. (1989). “Laboratory studies on hydraulic fracturing criteria in soil”. In: *Soils and Foundations*.

Konrad, J.-M., and Ayad, R. (1997). “An idealized framework for the analysis of cohesive soils undergoing desiccation”. In: *Canadian Geotechnical Journal*.

Krisnanto, S., Rahardjo, H., Fredlund, D. G., and Leong, E. C. (2014). “Mapping of cracked soils and lateral water flow characteristics through a network of cracks”. In: *Eng Geol*.

Lee, F. H., Lo, K. Y., and Lee, S. L. (1988). “Tension Crack Development in Soils”. In: *Journal of Geotechnical Engineering*. DOI: 10.1061/(ASCE)0733-9410(1988)114:8(915).

Lenci, S., Clementi, F., and Sadowski, T. (2012). “Experimental determination of the fracture properties of unfired dry earth”. In: *Eng Fract Mech*.

Li, J. H., Li, L., Chen, R., and Li, D. Q. (2016). “Cracking and vertical preferential flow through landfill clay liners”. In: *Engineering Geology*. DOI: 10.1016/j.enggeo.2016.03.006.

Li, K.-P., Chen, Y.-G., Li, Y.-C., Ye, W.-M., and Wang, Q. (2025). “Visualization of hydraulic fracturing in compacted bentonite: The roles of dry density, water content, and pressurization rate”. In: *Journal of Rock Mechanics and Geotechnical Engineering*. DOI: 10.1016/j.jrmge.2024.09.019.

Li, K.-p., Chen, Y.-g., Ye, W.-m., and Wang, Q. (2024). “From macro-morphology to micro-mechanics: a deep dive into hydraulic fracturing of compacted bentonite”. In: *Canadian Geotechnical Journal*. DOI: 10.1139/cgj-2023-0329.

Lin, Z. Y., Tang, C. S., Zeng, H., and Wang, Y. S. (2020). “Laboratory characterization and discrete element modeling of desiccation cracking behavior of soils under different boundary conditions (in Chinese)”. In: *Chinese J Geotech Eng*.

Lv, C., Wang, J., Huang, S., and Zhang, X. (2024). “Investigation on the size effect of compacted clay mode I fracture based on NDB specimens”. In: *Theoretical and Applied Fracture Mechanics*. DOI: 10.1016/j.tafmec.2024.104395.

Lv, C., Wang, J., Ling, H., and Huang, S. (2026). “Fracture behavior of compacted clay under mixed-mode I/II loading: Size effect analysis”. In: *Theoretical and Applied Fracture Mechanics*. DOI: 10.1016/j.tafmec.2026.105509.

Malusis, M. A., and Shackelford, C. D. (2002). “Theory for reactive clay barriers”. In: *Journal of Geotechnical and Geoenvironmental Engineering* 128.9, pp. 699–712.

Mazaheri, A. R., Delfani, N., Komasi, M., and Nasiri, M. (2021). “Experimentally Investigation of Nano Clay Effects on Leaching and Self-healing Process of Cracked Clayey Soils”. In: *Journal of Rehabilitation in Civil Engineering*. DOI: 10.22075/jrce.2020.19676.1377.

Miehe, C., Hofacker, M., and Welschinger, F. (2010). “A phase-field model for rate-independent crack propagation: robust algorithmic implementation based on operator splits”. In: *Computer Methods in Applied Mechanics and Engineering*.

Miller, C. J., and Rifai, S. (2004). “Fiber reinforcement for waste containment soil liners”. In: *Journal of Environmental Engineering*. DOI: 10.1061/(ASCE)0733-9372(2004)130:8(891).

Mitchell, J. K., and Soga, K. (2005). “*Fundamentals of Soil Behavior*”. In: *Fundamentals of Soil Behavior*.

Moës, N., and Belytschko, T. (2002). “Extended finite element method for cohesive crack growth”. In: *Engineering Fracture Mechanics* 69, pp. 813–833.

Moës, N., Dolbow, J., and Belytschko, T. (1999). “A finite element method for crack growth without remeshing”. In: *International Journal for Numerical Methods in Engineering* 46.1, pp. 131–150. DOI: 10.1002/(SICI)1097-0207(19990910)46:1<131::AID-NME726>3.0.CO;2-J.

Montgomery, D. C. (2012). *Design and Analysis of Experiments*. 8th ed. John Wiley & Sons.

Nahlawi, H., and Kodikara, J. (2002). “Laboratory experiments on desiccation cracking in thin clay layers”. In: *Can Geotech J*.

Nahlawi, H., and Kodikara, J. (2006). “Study of curling in compacted clay due to desiccation”. In: *Geotech Test J*.

National Institute of Environmental Health Sciences (2026). *Perfluoroalkyl and Polyfluoroalkyl Substances (PFAS)*. Official web resource. Accessed 2026-05-08.

Nikolić, M., Ibrahimbegović, A., and Miščević, P. (2015). “Brittle and ductile failure of rocks: Embedded discontinuity approach for representing mode I and mode II failure mechanisms”. In: *International Journal for Numerical Methods in Engineering* 102, pp. 1507–1526.

Nikolić, M., Karavelić, E., Ibrahimbegović, A., and Miščević, P. (2018). “Lattice element models and their peculiarities”. In: *Archives of Computational Methods in Engineering* 25, pp. 753–784.

Nishimura, S., and Shimizu, H. (2004). “A study of the measurement of fracture toughness in cohesive soil - relationship between the size of initial crack and diameter of specimen”. In: *Paddy and Water Environment*. DOI: 10.1007/s10333-004-0036-5.

Omidi, G. H., Thomas, J. C., and Brown, K. W. (1996). “Effect of desiccation cracking on the hydraulic conductivity of a compacted clay liner”. In: *Water, Air, and Soil Pollution* 89, pp. 91–103. DOI: 10.1007/BF00300424.

Peron, H., Hueckel, T., Laloui, L., and Hu, L. B. (2009a). “Discrete element modelling of drying shrinkage and cracking of soils”. In: *Computers and Geotechnics*.

Peron, H., Hueckel, T., Laloui, L., and Hu, L. B. (2009b). “Fundamentals of desiccation cracking of fine-grained soils: Experimental characterisation and mechanisms identification”. In: *Can Geotech J*.

Plé, O., Manicacci, A., Gourc, J.-P., and Camp, S. (2012). “Flexural behaviour of a clay layer: experimental and numerical study”. In: *Canadian Geotechnical Journal*. DOI: 10.1139/t2012-006.

Poulsen, T. G., Cai, W. L., and Garg, A. (2020). “Water evaporation from cracked soil under moist conditions as related to crack properties and near-surface wind speed”. In: *Eur J Soil Sci*.

Pouya, A., Vo, T. D., Hemmati, S., and Tang, A. M. (2019). “Modeling soil desiccation cracking by analytical and numerical approaches”. In: *Int J Numer Anal Met*.

Qiao, L., Liu, J., Li, X., Li, Q., and Xie, J. (2023). “Experimental study on Mode I fracture characteristics of compacted bentonite clay”. In: *Engineering Fracture Mechanics* 285, p. 109294. DOI: 10.1016/j.engfracmech.2023.109294.

Rahmani, M., Azzam, A., Grasley, J., Kim, Y.-R., Eun, J., and Kim, S. (2024). “Inverse characterization of shrinkage and fracture of bentonite buffer material for geological repositories of nuclear waste using an integrated DIC-FEM approach”. In: *Computers and Geotechnics*. DOI: 10.1016/j.compgeo.2024.106182.

Raoof, A., and Hassanizadeh, S. M. (2010). “A new method for generating pore-network models of porous media”. In: *Transport in Porous Media* 81, pp. 391–407.

Rayhani, M. H. T., Yanful, E. K., and Fakher, A. (2007). “Desiccation-induced cracking and its effect on the hydraulic conductivity of clayey soils from Iran”. In: *Canadian Geotechnical Journal* 44.3, pp. 276–283. DOI: 10.1139/t06-125.

Rice, J., Paris, P., and Merkle, J. (1973). *Some further results of J-integral analysis and estimates, Progress in flaw growth and fracture toughness testing*.

Rice, J. R. (1968). “A path independent integral and the approximate analysis of strain cncentrations by notches and cracks”. In: *J Appl Mech-T ASME*.

Rizvi, Z. H. (2019). “Lattice Element Method and its Application to Multiphysics”. PhD thesis. Kiel University.

Rizvi, Z. H., Nikolić, M., and Wuttke, F. (2019). “Lattice element method for simulations of failure in bio-cemented sands”. In: *Granular Matter* 21, p. 18.

Rizvi, Z., Amin, A., Arp, J. C. C., and Wuttke, F. (2022). “Fracture Toughness Mode I of Glass Fibers improved Soil”. In: *Materials Today Proceedings*. DOI: 10.1016/j.matpr.2022.04.230.

Rowe, R. K. (1998). “From the Past to the Future of Landfill Engineering Through Case Histories”. In: *International Conference on Case Histories in Geotechnical Engineering*.

Rowe, R. K. (2005). “Long-term performance of contaminant barrier systems”. In: *Géotechnique* 55.9, pp. 631–678.

Sánchez, M., Manzoli, O., and Guimarães, L. N. (2014). “Modeling 3-D desiccation soil crack networks using a mesh fragmentation technique”. In: *Computers and Geotechnics*.

Schlangen, E., and Mier, J. G. M. van (1992). “Simple lattice model for numerical simulation of fracture of concrete materials and structures”. In: *Materials and Structures* 25, pp. 534–542.

Schlangen, E., and Garboczi, E. J. (1997). “Fracture Simulations of Concrete Using Lattice Models: Computational Aspects”. In: *Engineering Fracture Mechanics* 57.2-3, pp. 319–332. DOI: 10.1016/S0013-7944(97)00010-6.

Sherard, J. L. (1986). “Hydraulic fracturing in embankment dams”. In: *Journal of Geotechnical Engineering*.

Shin, H., and Santamarina, J. C. (2011). “Desiccation cracks in saturated fine-grained soils: particle-level phenomena and effective-stress analysis”. In: *Geotechnique*.

Shirazi, S., Kazama, H., Kuwano, J., and Rashid, M. (2010). “The influence of temperature on swelling characteristics of compacted bentonite for waste disposal”. In: *EnvironmentAsia*.

Shokri, N., Zhou, P., and Keshmiri, A. (2015). “Patterns of desiccation cracks in saline bentonite layers”. In: *Transport Porous Med*.

Sih, G. C. (1974). “Strain energy density factor applied to mixed mode crack problems”. In: *Int J Fracture*.

Sih, G. C., Paris, P. C., and Irwin, G. R. (1965). “On cracks in rectilinearly anisotropic bodies”. In: *International Journal of Fracture Mechanics* 1, pp. 189–203.

Sima, J., Jiang, M. J., and Zhou, C. B. (2013). “Modeling desiccation cracking in thin clay layer using three-dimensional discrete element method”. In: *AIP Conference Proceedings*.

Sima, J., Jiang, M. J., and Zhou, C. B. (2014). “Numerical simulation of desiccation cracking in a thin clay layer using 3d discrete element modeling”. In: *Comput Geotech*.

Snow, D. T. (1969). “Anisotropic permeability of fractured media”. In: *Water Resources Research*.

Sture, S., Alqasabi, A., and Ayari, M. (1999). “Fracture and size-effect characteristics of cemented sand”. In: *Int J Fracture*.

Sukumar, N., Moës, N., Moran, B., and Belytschko, T. (2000). “Extended finite element method for three-dimensional crack modelling”. In: *International Journal for Numerical Methods in Engineering* 48, pp. 1549–1570.

Sun, Y., Shen, Z., Xu, L., Zhang, H., and Gan, L. (2024). “Review of Experimental Testing Methods of Soil Tensile Strength”. In: *Chinese Journal of Underground Space and Engineering*. DOI: 10.20174/j.JUSE.2024.04.08.

Sunderland, E. M., Hu, X. C., Dassuncao, C., Tokranov, A. K., Wagner, C. C., and Allen, J. G. (2019). “A Review of the Pathways of Human Exposure to Poly- and Perfluoroalkyl Substances (PFAS) and Present Understanding of Health Effects”. In: *Journal of Exposure Science & Environmental Epidemiology* 29, pp. 131–147. DOI: 10.1038/s41370-018-0094-1.

Tada, H., Paris, P. C., and Irwin, G. R. (1973). *The Stress Analysis of Cracks Handbook*. 3rd ed. Del Research Corporation.

Tang, C.-S., Cui, Y.-J., Tang, A.-M., and Shi, B. (2007). “Experimental evidence on the temperature dependence of desiccation cracking behavior of clayey soils”. In: *Eng Geol*.

Tang, C. S., Cui, Y. J., Shi, B., Tang, A. M., and Liu, C. (2011). “Desiccation and cracking behaviour of clay layer from slurry state under wetting-drying cycles”. In: *Geoderma*.

Tang, C. S., Shi, B., Liu, C., Suo, W. B., and Gao, L. (2011). “Experimental characterization of shrinkage and desiccation cracking in thin clay layer”. In: *Appl Clay Sci*.

Tang, C. S., Zhu, C., Leng, T., Shi, B., Cheng, Q., and Zeng, H. (2019). "Three-dimensional characterization of desiccation cracking behavior of compacted clayey soil using X-ray computed tomography". In: *Eng Geol*.

Tang, C.-S., Shi, B., Cui, Y.-J., Liu, C., and Gu, K. (2012). "Desiccation cracking behavior of polypropylene fiber-reinforced clayey soil". In: *Canadian Geotechnical Journal*. DOI: 10.1139/t2012-067.

Tao, G.-L., Guo, E., Yuan, J., Chen, Q.-S., and Nimbalkar, S. (2023). "Permeability and Cracking of Compacted Clay Liner Improved by Nano-SiO2 and Sisal Fiber". In: *KSCE Journal of Civil Engineering*. DOI: 10.1007/s12205-023-1435-8.

Terzaghi, K. (1943). "*Theoretical Soil Mechanics*". In: *Theoretical Soil Mechanics*.

Tezduyar, T. E. (1992). "Stabilized finite element formulations for incompressible flow computations". In: *Advances in Applied Mechanics* 28, pp. 1–44.

Tezduyar, T. E. (2001). "Finite element methods for flow problems with moving boundaries and interfaces". In: *Archives of Computational Methods in Engineering* 8, pp. 83–130.

Tezduyar, T. E., Behr, M., and Liou, J. (1992). "A New Strategy for Finite Element Computations Involving Moving Boundaries and Interfaces-The Deforming-Spatial-Domain/Space-Time Procedure". In: *Computer Methods in Applied Mechanics and Engineering* 94.3, pp. 339–351. DOI: 10.1016/0045-7825(92)90060-W.

Tian, B.-G., Cheng, Q., Tang, C.-S., and Shi, B. (2023). "Healing behaviour of desiccation cracks in a clayey soil subjected to different wetting rates". In: *Engineering Geology*. DOI: 10.1016/j.enggeo.2022.106973.

Trabelsi, H., Romero, E., and Jamei, M. (2012). "Crack patterns in clayey soils: Experiments and modeling". In: *International Journal for Numerical and Analytical Methods in Geomechanics*.

Trabelsi, H., Romero, E., and Jamei, M. (2018). "Tensile strength during drying of remoulded and compacted clay: The role of fabric and water retention". In: *Appl Clay Sci*.

United States Environmental Protection Agency (2025a). *Our Current Understanding of the Human Health and Environmental Risks of PFAS*. Official web resource. Accessed 2026-05-08.

United States Environmental Protection Agency (2025b). *PFAS Explained*. Official web resource. Accessed 2026-05-08.

Valvatne, P. H., and Blunt, M. J. (2004). "Predictive pore-scale modeling of two-phase flow in mixed wet media". In: *Water Resources Research* 40, W07406.

Van Marcke, P., Verleye, B., Carmeliet, J., Roose, D., and Swennen, R. (2010). "An improved pore network model for the computation of the saturated permeability of porous rock". In: *Transport in Porous Media* 85, pp. 451–476.

Wang, J. J., Zhang, H. P., Zhang, L., and Liang, Y. (2013). "Experimental study on self-healing of crack in clay seepage barrier". In: *Engineering Geology*. DOI: 10.1016/j.enggeo.2013.03.018.

Wang, J.-J., Huang, S., and Hu, J.-F. (2016). "Limit of crack depth in KIC testing for a clay". In: *Engineering Fracture Mechanics*. DOI: 10.1016/j.engfracmech.2016.08.006.

Wang, J.-J., and Liu, P. (2010). "Hydraulic fracturing in a cubic soil specimen". In: *Soil Mechanics and Foundation Engineering*. DOI: 10.1007/s11204-010-9101-9.

Wang, J.-J., Zhang, H.-P., Zhao, M.-J., and Lin, X. (2009). "Mechanisms of hydraulic fracturing in cohesive soil". In: *Water Science and Engineering*. DOI: 10.3882/j.issn.1674-2370.2009.04.009.

Wang, J.-J., Zhu, J.-G., Chiu, C. F., and Zhang, H. (2007). "Experimental study on fracture toughness and tensile strength of a clay". In: *Engineering Geology* 94.1-2, pp. 65–75. DOI: 10.1016/j.enggeo.2007.06.005.

Wang, J., Huang, S., Guo, W., Qiu, Z., and Kang, K. (2020). "Experimental study on fracture toughness of a compacted clay using semi-circular bend specimen". In: *Engineering Fracture Mechanics* 230, p. 106814. DOI: 10.1016/j.engfracmech.2019.106814.

Wang, J., Lv, C., Huang, S., and Luo, A. (2023). "Fracture process zone of Mode I in compacted clay through digital image correlation". In: *Theoretical and Applied Fracture Mechanics* 128, p. 104107. DOI: 10.1016/j.tafmec.2023.104107.

Wang, W., Rhodes, G., Zhang, W., Yu, X., Teppen, B. J., and Li, H. (2022). "Implication of Cation-Bridging Interaction Contribution to Sorption of Perfluoroalkyl Carboxylic Acids by Soils". In: *Chemosphere* 290, p. 133224. DOI: 10.1016/j.chemosphere.2021.133224.

Williams, M. L. (1957). “On the stress distribution at the base of a stationary crack”. In: *Journal of Applied Mechanics* 24, pp. 109–114.

Witherspoon, P. A., Wang, J. S. Y., Iwai, K., and Gale, J. E. (1980). “Validity of cubic law for fluid flow in a deformable rock fracture”. In: *Water Resources Research* 16, pp. 1016–1024.

Wu, X. R., and Carlsson, A. J. (1991). *Weight Functions and Stress Intensity Factor Solutions*. Pergamon Press.

Xu, J.-J., Tang, C.-S., Cheng, Q., Vahedifard, F., Liu, B., and Shi, B. (2022). “Monitoring and early detection of soil desiccation cracking using distributed fibre optical sensing”. In: *Geotechnique*.

Xu, J.-J., Tang, C.-S., Cheng, Q., Xu, Q.-l., Inyang, H. I., Lin, Z.-Y., and Shi, B. (2022). “Investigation on desiccation cracking behavior of clayey soils with a perspective of fracture mechanics: a review”. In: *Journal of Soils and Sediments*. DOI: 10.1007/s11368-021-03082-y.

Yu, Z., Eminue, O. O., Stirling, R., Davie, C., and Glendinning, S. (2021). “Desiccation cracking at field scale on a vegetated infrastructure embankment”. In: *Geotechnique Letters*.

Zhang, B., Hallett, P. D., and Zhang, G. (2008). “Increase in the fracture toughness and bond energy of clay by a root exudate”. In: *Eur J Soil Sci*.

Zhou, Y., and Rowe, R. K. (2005). “Modeling of clay liner desiccation”. In: *Int J Geomech*.

Ziegler, S., Leshchinsky, D., Ling, H. I., and Perry, E. B. (1998). “Effect of short polymeric fibers on crack development in clays”. In: *Soils and Foundations*. DOI: 10.3208/sandf.38.247.

Zimmerman, R. W., and Bodvarsson, G. S. (1996). “Hydraulic conductivity of rock fractures”. In: *Transport in Porous Media* 23, pp. 1–30.

APPENDICES

Appendix A

Experimental Procedures, State Control, Data Reduction, and Quality Assurance

A.1 Purpose and interpretation of the measured quantity

This appendix consolidates the experimental programme reported in Chapter 3 and identifies the information required for independent reproduction. It separates quantities measured directly from quantities calculated from measurements and from physical mechanisms inferred from trends. This distinction is essential because bulk water content and dry density were controlled, whereas matric suction, local saturation distribution, particle-contact coordination, and fracture-process-zone dimensions were not measured directly.

The symbol K_{Ic} is retained for continuity with the compacted-clay fracture literature. The physically precise description of the reported value is a *state-conditioned apparent Mode-I crack-initiation toughness*. It was obtained from the peak load of a displacement-controlled three-point single edge notched beam test using the adopted load-to-K_{I} reduction. It is conditional on material composition, preparation route, water content, dry density, fabric, specimen orientation, notch geometry, support condition, and loading protocol. It is not asserted to be a universal, state-independent plane-strain constant.

A compact representation is

$$K_{\mathrm{I,init}}^{\mathrm{app}} = \mathcal{F}\left(w, \rho_{\mathrm{d}}, e, S_{\mathrm{r}}, s, \text{fabric}, \text{orientation}, a/W, B/W, S/W, \dot{\delta}, \text{preparation}\right), \tag{A.1}$$

where w is gravimetric water content, ρ_{d} is dry density, e is void ratio, S_{r} is degree of saturation, s is matric suction, and $\dot{\delta}$ is displacement rate. In the experimental programme, w, ρ_{d}, specimen

geometry, and the loading sequence were controlled or recorded. Matric suction, local saturation, and directional anisotropy were not quantified.

Table A.1: Evidence classification for the experimental programme.

Quantity or mechanism	Status	Interpretation
Load, loading-point displacement, and two-sided CMOD	Measured	Recorded continuously during SENB loading
Water content, mass, specimen dimensions, and dry density	Measured at each test sample	Used to define the bulk preparation state
Specific gravity, particle-size distribution, consistency limits, compaction response, intact hydraulic conductivity, and compressibility	Measured before starting any test for all four types of soils	Determined using the ASTM standards
Peak load and initiation fracture toughness	Recorded and calculated for each test sample	Reduced from measured SENB response and specimen geometry
Matric suction, local pore pressure, and spatial saturation	Not measured	Suction-based explanations remain interpretations, not direct observations
Contact coordination, lubrication, sand percolation, and process-zone dilation	Not measured	Not treated as experimentally verified mechanisms
Fracture process zone dimensions	Not measured	No DIC, CT, or equivalent full-field measurement was performed
Compaction-induced anisotropy	Not quantified	Layered compaction may induce anisotropy; beyond the scope of the present study.

A.2 Materials, mixture definitions, and storage

A.2.1 Soil families

Four soil families were examined. LS_0 consisted of EPK kaolin clay. LS_{15} and LS_{25} contained 15% and 25% Ottawa sand, respectively, expressed as percentages of total oven-dry solid mass. FS was a field clay barrier soil. The laboratory mixtures were

$$\begin{aligned} \mathrm{LS}_0 &: 1.00\, m_\mathrm{k}, \\ \mathrm{LS}_{15} &: 0.85\, m_\mathrm{k} + 0.15\, m_\mathrm{s}, \\ \mathrm{LS}_{25} &: 0.75\, m_\mathrm{k} + 0.25\, m_\mathrm{s}, \end{aligned} \tag{A.2}$$

where m_k and m_s are the oven-dry kaolin and sand masses. Unless a test worksheet states otherwise, water content was calculated relative to the combined oven-dry mass of all solids.

The final experimental record should identify the kaolin supplier and lot, the Ottawa sand supplier, commercial grade and lot, and the sampling location and chain of custody for the field soil. Edgar Plastic Kaolin (EPK) was purchased from The Pottery Supply House (Lot No. 339661, and Ottawa sand (20-30 commercial grade) was purchased from Hoskins Scientific (Lot No. 143650, G116-HM-107). The field soil (FS) was collected by CT Soil from Windsor, Ontario and generously gifted to Dr. Dipanjan Basu. The laboratory mixtures were prepared by dry blending the EPK kaolin and Ottawa sand before water was added. The Ottawa sand was used in the dry condition and was not boiled, vacuum saturated, or separately pre-wetted before mixing.

Table A.2: Material identification and records required for reproduction.

Material	Composition	Information to retain
LS_0	100% EPK kaolin	Supplier: The Pottery Supply House; Product designation: Edgar Plastic Kaolin (EPK); Lot No. 339661
LS_{15}	85% kaolin, 15% Ottawa sand	All LS_0 fields plus Sand Supplier: Hoskins Scientific; Grade: 20-30 commercial grade; Lot No. 143650 (G116-HM-107)
LS_{25}	75% kaolin, 25% Ottawa sand	Same records as LS_{15}.
FS	Field clay-barrier soil	Sampling location: Windsor, Ontario (collected by CT Soil, chain of custody: gifted to Dr. Dipanjan Basu)

A.2.2 Particle-size distribution and consistency-limit fraction

Particle-size distributions were determined using ASTM D6913 and ASTM D7928. Liquid and plastic limits were determined using ASTM D4318. In accordance with ASTM D4318, the consistency-limit specimen was prepared from the fraction passing the No. 40 sieve (425 μm). Therefore, the reported limits for LS_{15} and LS_{25} primarily characterize the fines fraction; the sand fraction affects whole-mixture packing and compaction but is largely excluded from the consistency limit specimen.

A.2.3 First-order sand-volume and spacing estimate

Dry-mass fractions should not be interpreted directly as spatial phase fractions. A first-order bulk sand-volume fraction is

$$\phi_{s,bulk} = \frac{x_s \rho_d}{\rho_s}, \tag{A.3}$$

where x_s is dry sand mass fraction and ρ_s is sand-particle density. Using the reported maximum dry densities and $\rho_s \approx 2650\ \mathrm{kg/m^3}$, the estimated bulk sand-volume fractions are approximately 0.081 for LS_{15} and 0.138 for LS_{25}.

If equal spherical grains of representative diameter d_s are placed in equivalent cubic cells, the centre spacing and clear surface gap are

$$\lambda_c \approx d_s \left(\frac{\pi}{6\phi_{s,bulk}} \right)^{1/3}, \qquad \lambda_g = \lambda_c - d_s. \tag{A.4}$$

For an illustrative $d_s = 0.70$ mm, the centre spacings are approximately 1.30 and 1.09 mm and the clear gaps are approximately 0.60 and 0.39 mm for LS_{15} and LS_{25}, respectively. These values are geometric estimates, not image-based measurements. Unless CT or polished-section evidence is provided, the materials should be described as inclusions of sand grains in a clay-rich matrix rather than as confirmed continuous sand skeletons.

A.3 Conventional characterization and bulk-state calculations

Specific gravity was measured using ASTM D854; particle-size distribution using ASTM D6913 and ASTM D7928; consistency limits using ASTM D4318; standard Proctor compaction using ASTM D698; intact saturated hydraulic conductivity using ASTM D5084; unconfined compression using ASTM D2166; and one-dimensional consolidation using ASTM D2435.

Table A.3: Reported conventional properties used to define the experimental states.

Property	LS_0	LS_{15}	LS_{25}	FS
Specific gravity, G_s	2.62	2.63	2.64	2.71
Liquid limit (%)	68	68	68	34
Plastic limit (%)	39	39	39	16
Plasticity index (%)	29	29	29	18
Optimum water content (%)	35.89	29.57	26.84	15.82
Maximum dry unit weight (kN/m^3)	12.97	14.26	14.63	17.77
Intact saturated k (10^{-9} m/s)	0.132	1.330	6.340	0.531

Gravimetric water content, dry density, void ratio, and bulk degree of saturation were calculated as

$$w = \frac{m_{\text{wet}} - m_{\text{dry}}}{m_{\text{dry}}}, \tag{A.5}$$

$$\rho_d = \frac{m_{\text{wet}}}{V(1+w)}, \tag{A.6}$$

$$e = \frac{G_s \rho_w}{\rho_d} - 1, \qquad S_r = \frac{w G_s}{e}. \tag{A.7}$$

Equation (A.7) provides a bulk saturation estimate. It does not demonstrate spatial uniformity. Patchy saturation may result from incomplete aggregate wetting, entrapped air, sand-rich regions, or lift interfaces. No CT or other spatial saturation measurement was performed, and matric suction was neither measured nor imposed. Results are therefore indexed by measured bulk water content and dry density.

A.4 Dry preparation, batching, mixing, and moisture conditioning

The laboratory soils were prepared using the dry-preparation and compaction-control principles of ASTM D698 (ASTM D698, 2021). ASTM D698 was used to establish the water-content–dry-unit-weight relationship, optimum water content, and maximum dry unit weight. The SENB beams were then compacted in custom fracture-test moulds to the target state obtained from the ASTM D698 compaction curves. The custom SENB mould is not an ASTM D698 mould; therefore, the mould-specific lift sequence is reported separately below.

EPK kaolin and Ottawa sand were handled in the dry condition. The sand was not boiled, vacuum saturated, or separately pre-wetted before mixing. This followed the dry-mixing approach used for the laboratory mixtures. The preparation sequence was as follows.

1. Break down visible clay lumps without crushing individual mineral particles.
2. Determine the initial water content of the stored clay, sand, or field soil when the material was not oven dry.
3. Calculate the total dry mass required from the custom mould volume and the target dry density.
4. Weigh the clay and sand on a dry-mass basis. For LS_{15} and LS_{25}, the sand contents were 15% and 25% of the total dry solid mass, respectively.
5. Dry blend the clay and sand until no visible sand-rich or clay-rich zones remained.
6. Add the water equal to optimum moisture content and one-percent more to take into account of room temperature and handling drying and then gradually mix using stainless steel mixing rod (any type of rod will work). Water was not poured into one location and left unmixed.
7. Continue wet mixing until the colour and consistency were visually uniform and no dry pockets remained.
8. Place the prepared soil in a sealed container or sealed bag to limit evaporation and allow water to redistribute through the batch for 24 hours.
9. Re-mix the soil immediately before compaction and collect a representative water-content sample.

The dry-mixing must be completed within 5 minutes, wet-mixing must be completed within 15-20 minutes, and sealed for 24 hours. The mixed batch must be limited to the number of tests performed within 48 hours of curing time. Water must be sprinkled using a manual sprayer. The sealed samples must be stored in dry storage at 21-24 degrees Celsius and away from direct sunlight.

A.5 Compaction, orientation, and state verification

The target water content corresponded to the optimum moisture content, and the maximum dry density for each soil was obtained from the ASTM D698 standard Proctor compaction curves. The target density was then recorded, and the mass of soil required to fill the selected mould was calculated accordingly. This soil mass was divided into three equal layers, and each layer was compacted following the procedure specified in ASTM D698, using the same tamping rod as prescribed in the standard. Prior to compaction, a pre-formed crack element fabricated from iron was inserted in the specimen to prevent any uncontrolled deformation associated with crack formation after compaction. The density of the compacted soil was recorded to confirm the maximum dry density target. Upon completion of compaction, the sides of the mould were unscrewed, the specimen was inverted, and the bottom plate was removed. The crack insert was then carefully extracted using a pointed pair of pliers. The specimen was subsequently handled with care along its lateral surfaces and positioned on the loading platen. Displacement-controlled loading was applied in order to record the load, vertical displacement, and crack-mouth opening displacement. Once the test was completed, a small piece of soil was cut from the cracked ligament and the water content at the test was recorded The gravimetric water content was determined from a representative sample removed from the fractured ligament in accordance with ASTM D2216/D2216M using

$$w = \frac{M_{\text{wet}} - M_{\text{dry}}}{M_{\text{dry}}} \times 100\%. \tag{A.8}$$

The notch-forming insert was held in its fixed position while the soil was compacted. Soil was placed carefully around both sides of the insert so that a large void did not form at the notch. The top surface was trimmed level after the final lift. The specimen was then demoulded with support along its length to avoid bending under self-weight.

Layered compaction can cause particle alignment, lift interfaces, directional pore structure, and density gradients. The same compaction direction and notch orientation were used to improve repeatability. The degree of mechanical or hydraulic anisotropy was not measured. The test results therefore apply to the tested orientation relative to the compaction lifts. They do not demonstrate that the compacted material was isotropic.

A.6 SENB moulds, geometry, and notch formation

A.6.1 Geometry matrix

The SENB dimensions were linked through $S/W = 4$ and $L/W = 5$. The notch ratios were $a/W = 0.45$, 0.50, and 0.55.

Table A.4: SENB geometry matrix. All dimensions are in millimetres.

Specimen	W	B	L	S	$a_{0.45}$	$a_{0.50}$	$a_{0.55}$
A	35	35	175	140	15.75	17.50	19.25
B	""	70	""	""	""	""	""
C	50	50	250	200	22.50	25.00	27.50
D	""	100	""	""	""	""	""
E	65	65	325	260	29.25	32.50	35.75

A $W = 65$ mm, $B = 130$ mm geometry was attempted but excluded because self-weight and handling prevented reliable testing.

A.6.2 Fabrication drawings organized by SENB geometry

The fabrication drawings are grouped according to the geometry matrix in Table A.4. Each page contains the base plate, long wall, short end wall, loading base, and the three notch inserts used for the corresponding values of a/W. Geometry F is included for completeness because its components were fabricated, although the $W = 65$ mm, $B = 130$ mm specimen was excluded from the factorial test matrix because reliable handling and testing were not possible.

Geometry A: $W = 35$ **mm,** $B = 35$ **mm,** $L = 175$ **mm,** $S = 140$ **mm**

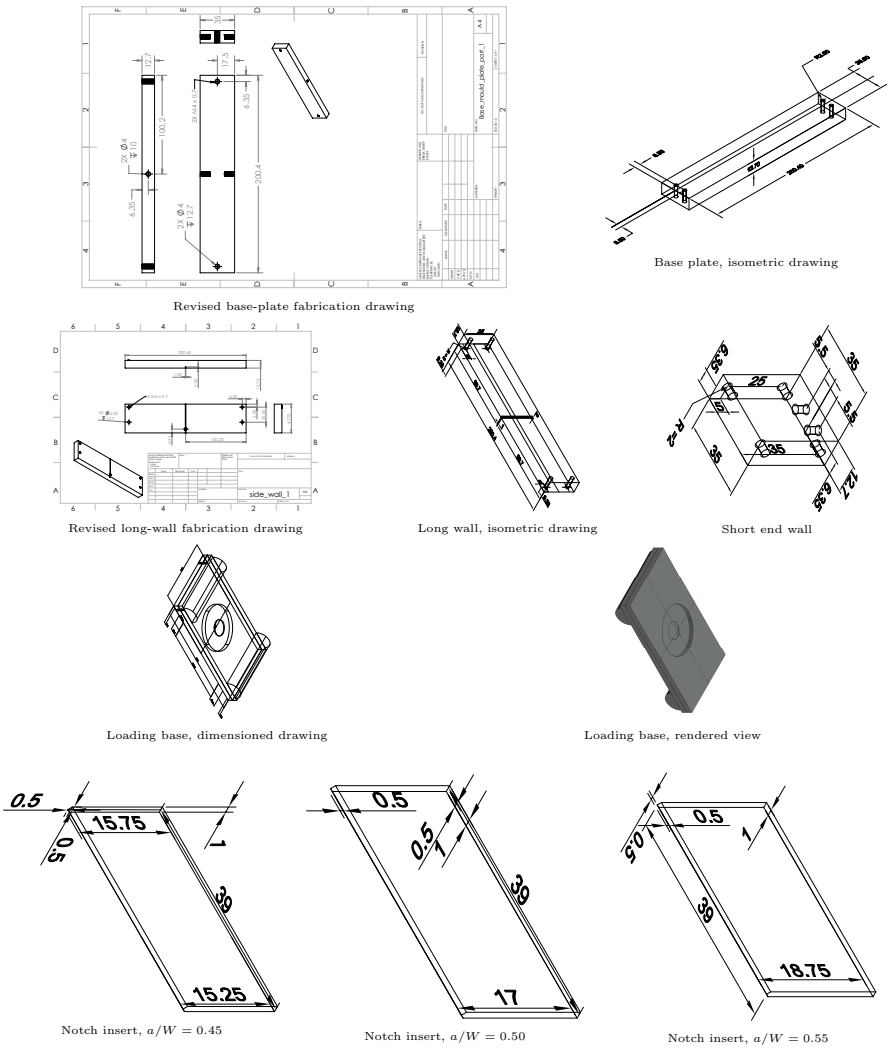
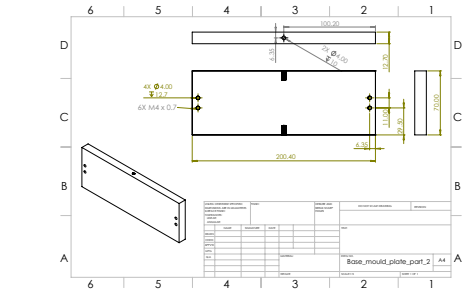
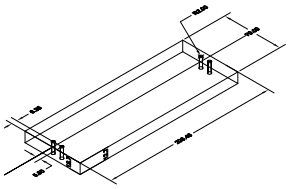


Figure A.1: Fabrication drawings for SENB Geometry A: W = 35 mm, B = 35 mm, L = 175 mm, and S = 140 mm.

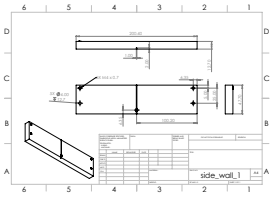
Geometry B: $W = 35$ **mm,** $B = 70$ **mm,** $L = 175$ **mm,** $S = 140$ **mm**



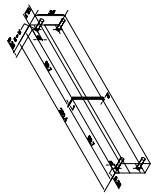
Revised base-plate fabrication drawing



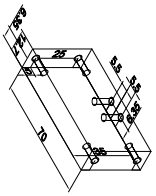
Base plate, isometric drawing



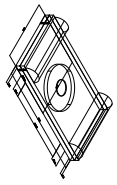
Revised long-wall fabrication drawing



Long wall, isometric drawing



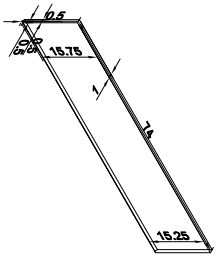
Short end wall



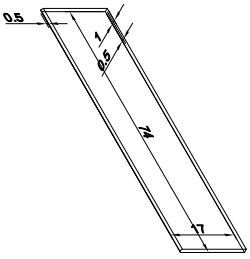
Loading base, dimensioned drawing



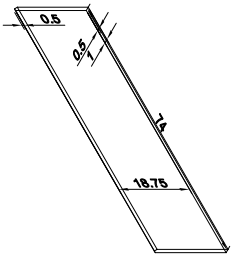
Loading base, rendered view



Notch insert, $a/W = 0.45$



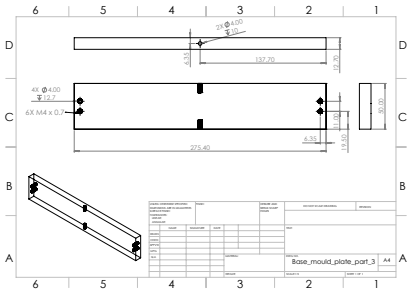
Notch insert, $a/W = 0.50$



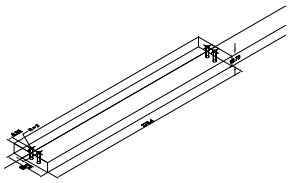
Notch insert, $a/W = 0.55$

Figure A.2: Fabrication drawings for SENB Geometry B: W = 35 mm, B = 70 mm, L = 175 mm, and S = 140 mm.

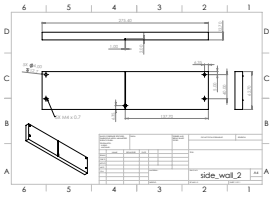
Geometry C: $W = 50$ **mm,** $B = 50$ **mm,** $L = 250$ **mm,** $S = 200$ **mm**



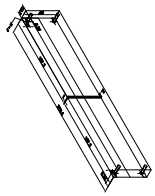
Revised base-plate fabrication drawing



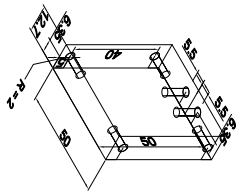
Base plate, isometric drawing



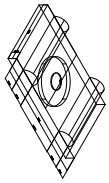
Revised long-wall fabrication drawing



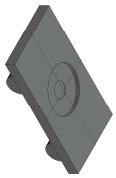
Long wall, isometric drawing



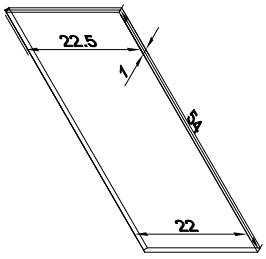
Short end wall



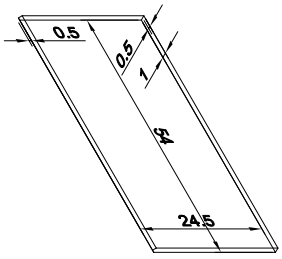
Loading base, dimensioned drawing



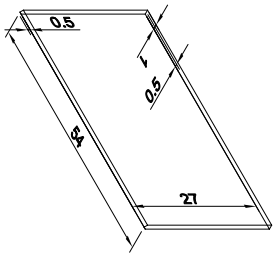
Loading base, rendered view



Notch insert, $a/W = 0.45$



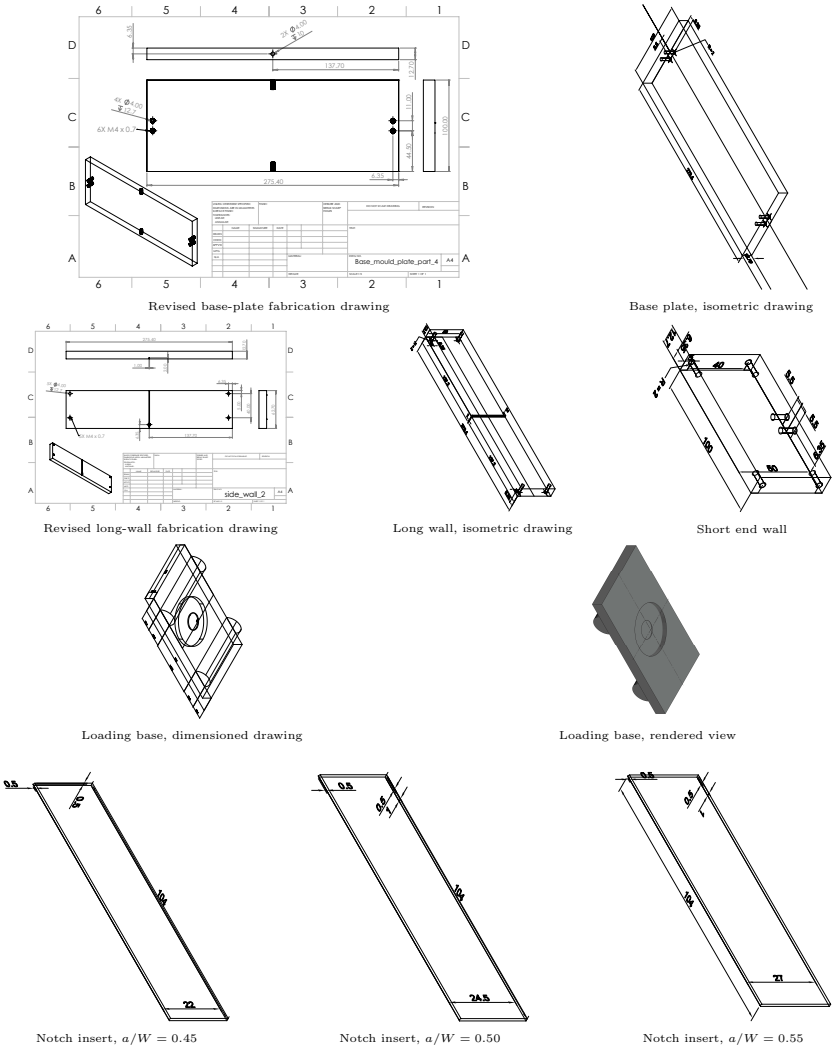
Notch insert, $a/W = 0.50$



Notch insert, $a/W = 0.55$

Figure A.3: Fabrication drawings for SENB Geometry C: W = 50 mm, B = 50 mm, L = 250 mm, and S = 200 mm.

Geometry D: $W = 50$ **mm,** $B = 100$ **mm,** $L = 250$ **mm,** $S = 200$ **mm**



Revised base-plate fabrication drawing

Base plate, isometric drawing

Revised long-wall fabrication drawing

Long wall, isometric drawing

Short end wall

Loading base, dimensioned drawing

Loading base, rendered view

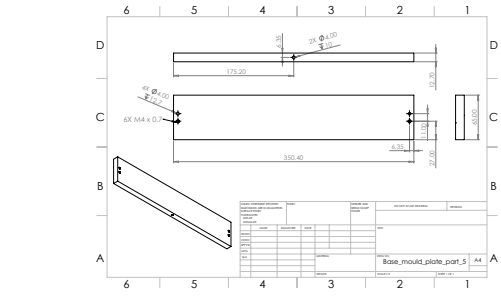
Notch insert, $a/W = 0.45$

Notch insert, $a/W = 0.50$

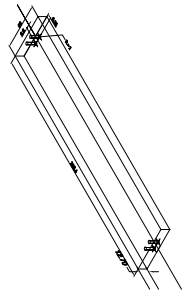
Notch insert, $a/W = 0.55$

Figure A.4: Fabrication drawings for SENB Geometry D: W = 50 mm, B = 100 mm, L = 250 mm, and S = 200 mm.

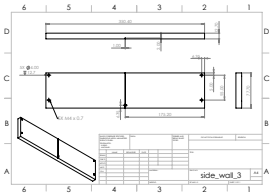
Geometry E: $W = 65$ **mm,** $B = 65$ **mm,** $L = 325$ **mm,** $S = 260$ **mm**



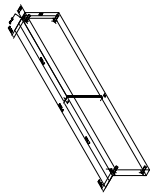
Revised base-plate fabrication drawing



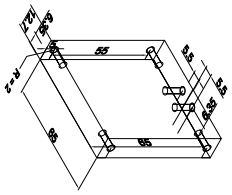
Base plate, isometric drawing



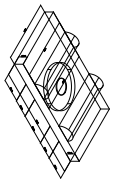
Revised long-wall fabrication drawing



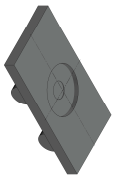
Long wall, isometric drawing



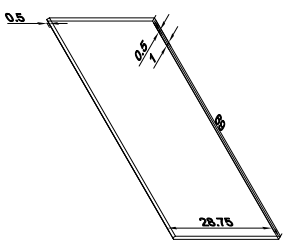
Short end wall



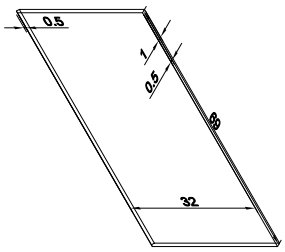
Loading base, dimensioned drawing



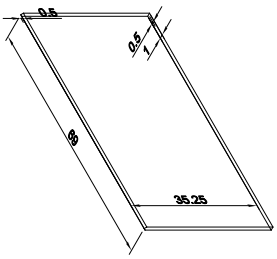
Loading base, rendered view



Notch insert, $a/W = 0.45$



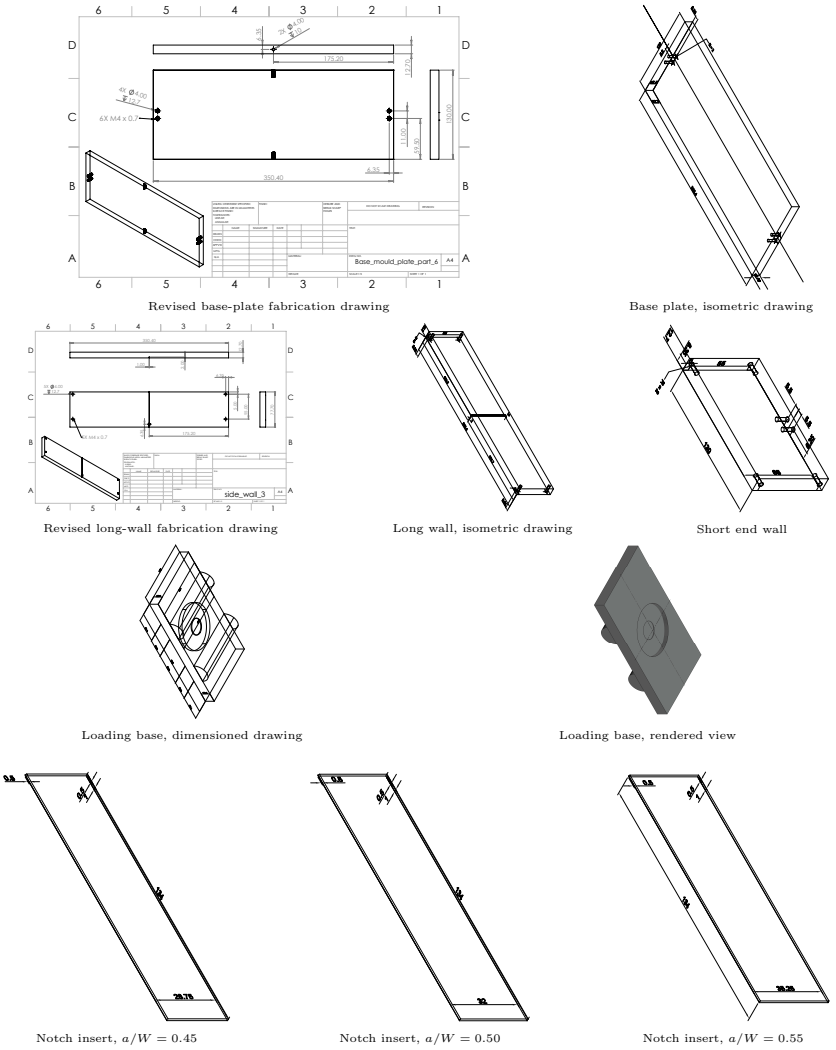
Notch insert, $a/W = 0.50$



Notch insert, $a/W = 0.55$

Figure A.5: Fabrication drawings for SENB Geometry E: W = 65 mm, B = 65 mm, L = 325 mm, and S = 260 mm.

Attempted Geometry F (excluded): $W = 65$ **mm,** $B = 130$ **mm,** $L = 325$ **mm,** $S = 260$ **mm**



Revised base-plate fabrication drawing

Base plate, isometric drawing

Revised long-wall fabrication drawing

Long wall, isometric drawing

Short end wall

Loading base, dimensioned drawing

Loading base, rendered view

Notch insert, $a/W = 0.45$

Notch insert, $a/W = 0.50$

Notch insert, $a/W = 0.55$

Figure A.6: Fabrication drawings for the attempted Geometry F: W = 65 mm, B = 130 mm, L = 325 mm, and S = 260 mm. This geometry was excluded from the factorial test matrix.

A.6.3 Rationale for three-point loading and notch range

Three-point SENB loading was selected because it provides a single central loading point, two simple supports, direct Mode-I-dominated opening at a central edge notch, compatibility with established SENB reductions, and straightforward CMOD instrumentation. Four-point bending would provide a constant-moment region and reduce shear at the notch, but requires a more complex load-spreader and additional contact controls. The objective here was to establish a reproducible baseline before increasing fixture complexity. The three-point specimen still contains finite shear and a varying bending moment; mode purity must therefore be checked from opening symmetry, crack origin, and trajectory.

The interval $0.45 \leq a/W \leq 0.55$ provides a narrow verification range around a half-depth notch. It retains a practicable remaining ligament and tests whether the corrected initiation parameter is much less notch-dependent than raw peak load. The study does not prove that $a/W = 0.50$ is universally optimal for every clay, scale, orientation, and rate.

A.6.4 Notch insert and dimensional control

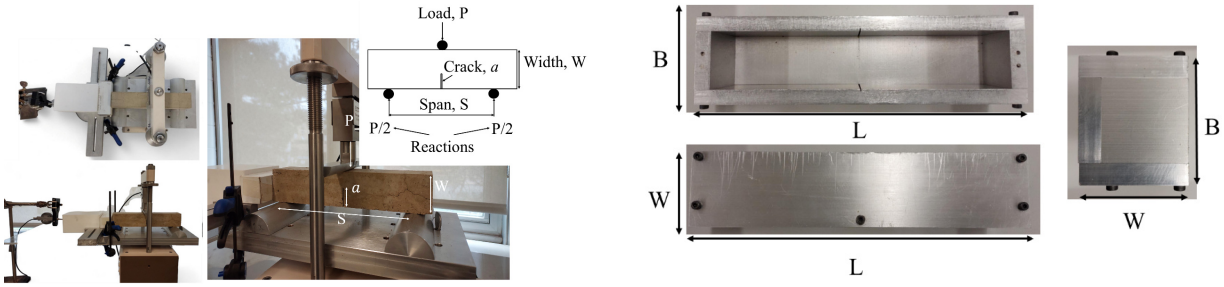
The notch was formed during compaction rather than sawn after compaction, thereby reducing post-compaction disturbance at the intended initiation location. The notch thickness was 1 mm, the crack tip had a 45-degree slant on both sides, and the notch length was defined in the geometry matrix.

A.7 SENB apparatus, loading frame, and instrumentation

The SENB apparatus used two lower roller supports and one central upper loading nose. The beam was tested with the notch facing downward so that the remaining ligament above the notch was opened by bending tension. The actuator applied vertical displacement through the loading nose. Load, loading-point displacement, and the opening at both sides of the notch mouth were recorded.

The GDS frame from the 1D consolidation test was used, and the actuator built into the GDS system was used. For further details, please refer to the GDS-1D consolidation apparatus.

The reported SENB load cell had a rated capacity of 10 kN and a display readability of 0.1 N (customized from GDS). The near-OMC SENB peak loads were commonly about 1-7 N, while the dry-state series reached larger loads, locally up to approximately 190 N. The rated load-cell



(a) Loading frame and instrumentation. **(b)** Notch-forming mould cross-section.

Figure A.7: SENB apparatus and mould used for the compacted-soil tests.

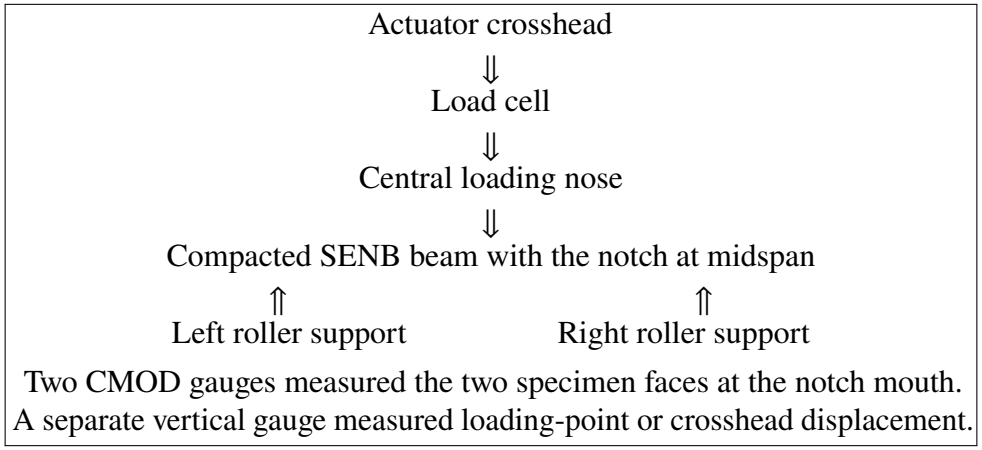


Figure A.8: Functional arrangement of the SENB loading system.

capacity was therefore much larger than most measured forces. A large rated capacity does not by itself invalidate the measurements, but suitability must be demonstrated from calibration in the actual working range, signal noise, zero drift, hysteresis, and repeatability. For example, a 0.1 N displayed increment corresponds to 5% of a 2 N load and 1.4% of a 7 N load.

Table A.5: SENB instrumentation and required calibration information.

Component	Reported specification	Purpose	Additional information required
Load cell	10 kN capacity; 0.1 N readability	Measures load and $P_{\max}$	Low-range calibration and uncertainty over approximately 1-200 N.

Table A.5 continued

Component	Reported specification	Purpose	Additional information required
Vertical displacement gauge	15 mm range; 0.001 mm readability	Measures loading-point or crosshead displacement	GDS manufactured
Left and right CMOD gauge	Sylvac; 15 mm range; 0.001 mm readability	Measures opening on one face	S233 Model (refer to Sylvac for further details)
Supports and nose	Two rollers and one central nose	Three-point bending	Rollers have 50.8 mm diameter and are made up of aluminum
Acquisition system	Continuous multichannel recording	Synchronizes load and displacement channels	Comes with GDS-1D consolidation system

A.7.1 Two-sided crack mouth opening displacement (CMOD) measurement and symmetry check

One CMOD gauge was mounted on each side of the specimen. The gauges measured the relative horizontal opening at the notch mouth. Two gauges were used because a compacted beam can rotate slightly on the supports or contact the loading nose eccentrically. A single gauge cannot separate true opening from this rotation.

The opening used for the load-CMOD curve was

$$\mathrm{CMOD} = \frac{\mathrm{CMOD_L} + \mathrm{CMOD_R}}{.} \tag{A.9}$$

A.8 SENB mounting and complete test sequence

The SENB test was completed in the following order.

1. Measure and record specimen mass, length, width, thickness, notch depth on both faces, and notch-mouth width.

2. Inspect the beam for edge damage, lift separation, drying fissures, or disturbance at the notch tip.
3. Set the support spacing to $S = 4W$. Check the span with a ruler or calliper before the test series.
4. Place the beam on the two lower rollers with the notch facing downward and centred between the supports.
5. Align the specimen centreline, notch plane, loading nose, and support midpoint.
6. Bring the loading nose into light contact with the upper surface. Apply only the seating load required to remove clearance.
7. Mount and zero the vertical displacement gauge.
8. Mount the two CMOD gauges on the two specimen faces and zero both channels.
9. Zero or tare the load channel after seating, following the laboratory data-acquisition procedure.
10. Start simultaneous recording of load, vertical displacement, left CMOD, right CMOD, and time.
11. Apply vertical displacement at a constant rate of $0.006\,\mathrm{mm\,s^{-1}}$ ($0.36\,\mathrm{mm\,min^{-1}}$).
12. Continue through peak load and the post-peak branch until the ligament had clearly separated or the residual load reached the test termination condition.
13. Stop the actuator, remove the gauges carefully, and unload the specimen.
14. Photograph both faces and the final discontinuity path. Record whether initiation occurred at the notch and whether local mixed-mode deflection, branching, support crushing, or handling damage was present.
15. Determine the final water content from representative material when this was part of the test record.

The selected rate (0.006mm/s) defines the quasi-static condition used in this study. It is not claimed to be suitable for every compacted clay liner soil. A more active or less permeable clay may have a different hydraulic redistribution time, and a faster or slower rate may change its measured response. Loading-rate sensitivity was not measured in the present programme.

The test was globally Mode-I dominated because the central notch was loaded symmetrically in three-point bending. Local deflection or branching during the post-peak stage may create mixed-mode components. The Mode-I interpretation is therefore strongest at initiation near the peak load and does not mean that every segment of the final discontinuity followed pure Mode I.

A.9 Validity and rejection criteria

A valid test should satisfy the following conditions:

(a) notch dimensions and specimen state are within predeclared tolerances;

(b) all channels remain calibrated and within range;

(c) the dominant discontinuity initiates at the notch tip;

(d) propagation occurs through the ligament without prior support crushing, edge failure, or gross torsion;

(e) the two CMOD channels satisfy the predeclared symmetry limit near initiation;

(f) the load–CMOD response provides an unambiguous initiation criterion; and

(g) post-test morphology is compatible with Mode-I-dominated opening at initiation.

A.10 SENB data reduction and uncertainty

The load-to-intensity reduction is

$$K_{\mathrm{I}} = \frac{PS}{BW^{3/2}} f\!\left(\frac{a}{W}\right), \tag{A.10}$$

and the operational initiation value is

$$K_{\mathrm{I,init}}^{\mathrm{app}} = \frac{P_{\max} S}{BW^{3/2}} f_{\mathrm{eff}}\!\left(\frac{a}{W}\right). \tag{A.11}$$

For the compliance route,

$$C(a) = \frac{\mathrm{CMOD}}{P}, \qquad G = \frac{P^2}{2B}\frac{\mathrm{d}C}{\mathrm{d}a}, \qquad K_{\mathrm{I}} = \sqrt{E'G}, \tag{A.12}$$

where

$$E' = \begin{cases} E, & \text{plane stress,} \\ E/(1-\nu^2), & \text{plane strain.} \end{cases} \tag{A.13}$$

The compliance has used best-fit trendline to smooth the plots and then follow the compliance method defined for metals.

A.11 Factorial design and statistical analysis

The feasible SENB programme used five geometries, three notch ratios, and three independently prepared replicates for each complete laboratory-soil matrix. The individual beam was the experimental unit, giving

$$N_{\text{soil}} = 5 \times 3 \times 3 = 45 \tag{A.14}$$

valid tests per complete soil matrix. Test order was randomized. The blocked factorial model was

$$Y_{ijk} = \mu + G_i + A_j + (GA)_{ij} + B_k + \varepsilon_{ijk}, \tag{A.15}$$

where G_i is geometry, A_j is notch ratio, and B_k is replicate block.

The coefficient of variation was

$$\text{COV} = 100\frac{s}{\bar{x}}, \qquad s = \sqrt{\frac{1}{n-1}\sum_{r=1}^{n}(x_r - \bar{x})^2}. \tag{A.16}$$

The coefficient of variation was calculated from the three specimen-level observations in each geometry, notch-ratio, and soil cell. Because $n = 3$, the resulting COV values are interpreted as descriptive measures of relative repeatability rather than precise estimates of population variability. No observations were excluded from the calculation. Residual plots were examined for independence, approximate normality, and variance homogeneity before the ANOVA and Tukey comparisons were interpreted.

A.12 Unconfined compression tests and elastic inputs

Unconfined compression tests were performed in general accordance with ASTM D2166/D2166M (ASTM D2166, 2024). The standard applies strain-controlled axial loading to cohesive soil that can stand without lateral support. It reports an approximate total-stress compressive strength.

The specimens were remoulded or compacted to the water-content and dry-density states listed in Table A.6. The material preparation and target state followed the same ASTM D698-based soil preparation used for the other specimens.

The UCS test and the SENB test measured different responses. UCS applied axial compression to an unconfined cylinder. The SENB test applied bending so that the ligament above the downward-facing notch opened in tension. UCS was used to obtain an operational pre-peak stiffness and strength response; it was not used as a direct tensile-fracture test.

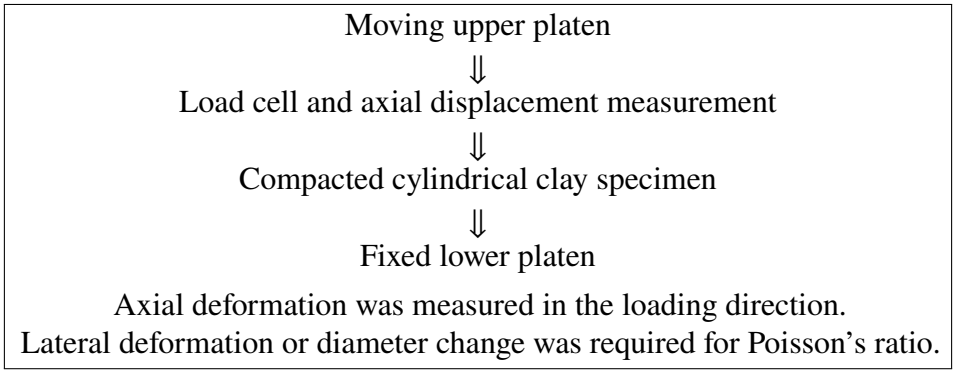


Figure A.9: Functional arrangement of the UCS test used to obtain compressive stress–strain response and the operational elastic inputs.

The complete procedure was as follows.

1. Prepare the soil at the target water content and dry density.
2. Compact or remould the cylindrical specimen (diameter-to-length ratio = 0.5, diameter = 50 mm) using the recorded mould and lift procedure.
3. Demould the specimen and measure initial height, diameter at several levels, mass, and water content.
4. Trim the ends plane and parallel so that the specimen sat centrally on the lower platen.
5. Place the specimen between the platens and centre it below the load cell.
6. Install the axial deformation gauge. Install the lateral deformation device when Poisson's ratio is determined directly.
7. Apply a small seating load, zero the channels, and begin simultaneous recording.

8. Apply strain-controlled axial loading at the recorded UCS rate until peak strength and the required post-peak deformation were reached.
9. Record the failure mode, including diagonal shear, vertical splitting, bulging or barrelling, end crushing, and evidence of platen restraint.
10. Measure final water content and specimen dimensions when included in the test plan.

Axial strain was

$$\varepsilon_a = \frac{\Delta H}{H_0}. \tag{A.17}$$

The axial displacement is recorded using the same Sylvac displacement gauge as defined above, and lateral displacement was recorded using a Vernier Calliper.

For approximately constant volume during undrained deformation, ASTM D2166 commonly uses a corrected area based on axial strain as used in this study

$$A_c = \frac{A_0}{1 - \varepsilon_a}, \qquad \sigma_a = \frac{P}{A_c}. \tag{A.18}$$

Radial strain was obtained from a measured diameter change,

$$\varepsilon_r = \frac{D - D_0}{D_0}, \tag{A.19}$$

and Poisson's ratio was evaluated from the pre-peak strain response (the readings before loading and at failure were recorded to calculate Poisson's ratio),

$$\nu_{\text{eff}} = -\frac{\Delta \varepsilon_r}{\Delta \varepsilon_a}. \tag{A.20}$$

Young's modulus was obtained as the average of a tangent, secant, and regression slope in the pre-peak range,

$$E_{\text{eff}} = \frac{\Delta \sigma_a}{\Delta \varepsilon_a}. \tag{A.21}$$

Table A.6: State-dependent operational elastic inputs reported in the thesis.

Soil	State	ρ_{d} (kg/m^3)	w (%)	ν_{eff}	E_{eff} (kPa)
LS_0	1	1315	31.58	0.322	651.6

Table A.6 continued

Soil	State	ρ_d (kg/m^3)	w (%)	ν_{eff}	E_{eff} (kPa)
""	2	1335	33.58	0.318	445.7
""	3	1355	35.58	0.315	370.9
LS_{15}	1	1425	26.58	0.270	968.1
""	2	1450	28.58	""	910.5
""	3	1475	30.58	""	849.4
LS_{25}	1	1476	23.83	0.240	465.7
""	2	1496	25.83	0.240	425.4
""	3	1516	27.83	0.239	358.9
FS	1	1787	17.35	0.199	667.8
""	2	1797	17.55	0.197	608.3
""	3	1807	17.75	""	519.6

These values are conditional on water content, density, preparation, suction state, strain range, and end restraint. They are operational inputs for the present calculations, not universal small-strain constants.

A.13 Hydraulic-conductivity procedure

Intact saturated hydraulic conductivity was measured using ASTM D5084 for a sample of diameter of 101.6 mm and length of 203.2 mm.

Table A.7: Reported intact saturated hydraulic conductivities.

Soil	k (m/s)
LS_0	1.32×10^{-10}
LS_{15}	1.33×10^{-9}
LS_{25}	6.34×10^{-9}
FS	5.31×10^{-10}

For a constant-head representation,

$$k = \frac{QL}{A\Delta h}, \tag{A.22}$$

with the exact form adapted to the implemented flexible-wall procedure. These values characterize intact saturated specimens, not flow through a mechanically generated SENB discontinuity.

A.14 One-dimensional consolidation tests

The one-dimensional consolidation tests followed ASTM D2435/D2435M (ASTM D2435, 2020). The soil specimen was laterally confined in a rigid ring and drained through porous stones. Vertical load was increased in stages while vertical deformation was recorded. This was a compression and unloading test. It was not a tension test and it was not a cyclic tension test.

The specimen diameter of approximately 49.92 mm and an initial height of approximately 19.25 mm was used. The maximum pressure of 1280 kPa was applied, and approximately 24 h at the main stress stages, and unloaded to approximately 5 kPa.

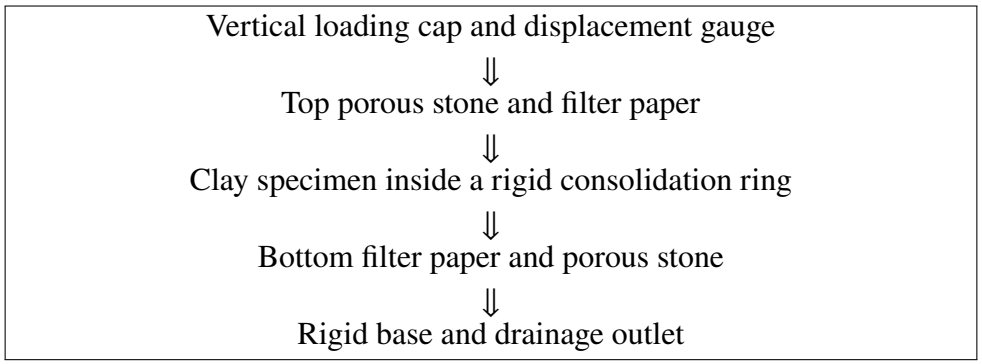


Figure A.10: Functional arrangement of the one-dimensional consolidation test.

The test sequence was as follows.

1. Prepare the soil at the optimum moisture content and maximum dry density using the ASTM D698-based mixing and compaction procedure.
2. Form or trim the specimen to fit the consolidation ring.
3. Measure initial mass, diameter, height, and water content.
4. Assemble the bottom porous stone, filter paper, specimen ring, top filter paper, porous stone, and loading cap.
5. Apply the seating stress and zero the deformation gauge after seating.

6. Apply each vertical stress increment and record deformation against elapsed time.
7. Continue each stage for the specified time or until the selected end-of-primary or deformation-rate condition was reached.
8. Increase the stress through the full loading schedule and then unload through the stated unloading schedule.
9. Determine final water content and dry mass and calculate final void ratio.

Table A.8: One-dimensional consolidation test matrix to be confirmed from the original test sheets.

Soil or treatment	Specimen state	Loading and unloading schedule	No. of Specimens
LS_0	Near the stated compaction condition	incremental loading to approximately 1280 kPa, with approximately 24 h at each main stage, followed by unloading to approximately 5 kPa; confirm the exact stress sequence from the test sheets	3
LS_{15}	Near the stated compaction condition	""	3
LS_{25}	Near the stated compaction condition	""	3
Additive-treated soils	Dosage-specific state	""	3

Vertical strain and void ratio were calculated from

$$\varepsilon_v = \frac{H_0 - H}{H_0}, \qquad e = e_0 - \Delta e. \tag{A.23}$$

For a selected stress interval,

$$a_{\mathrm{v}} = -\frac{e_2 - e_1}{\sigma'_{v,2} - \sigma'_{v,1}}, \qquad m_{\mathrm{v}} = \frac{a_{\mathrm{v}}}{1 + e_1}. \tag{A.24}$$

Different specimens can start from different initial void ratios and strains because they were prepared at different water contents, dry densities, soil compositions, or additive dosages.

Raw datasets should be immutable. The archive should contain raw files, processing scripts, processed tables, a data dictionary, and a mapping for each figure and table to its source record.

A.15 Experimental limitations and transferability

The main limitations are:

(i) suction and local saturation were not measured or controlled;

(ii) patchy saturation was not evaluated spatially;

(iii) compaction-induced anisotropy was not quantified directionally;

(iv) loading-rate dependence and drainage regime were not established;

(v) process-zone size, dilation, and pre-peak microscopic extension were not measured;

(vi) loading was monotonic and Mode-I dominated; mixed-mode, cyclic, thermal, chemical, and hydraulic-fracture conditions were outside the programme;

(vii) kaolin-dominated results require recalibration for smectitic and bentonitic barriers; and

(viii) the reported value is a state-conditioned engineering index, not a universal intrinsic constant.

Controlled saturation or submerged testing would help isolate suction-related apparent bonding, but may also produce swelling, fabric rearrangement, stiffness changes, and pore-pressure-rate effects. A submerged test at uniform hydrostatic pressure is not a hydraulic-fracture test; hydraulic fracture requires a pressure differential or pressure traction on an incipient discontinuity. The saturated response must be measured rather than inferred from bulk water content.

Appendix B

Constitutive Assumptions, Numerical Implementation, and Reproducibility

B.1 Numerical scope and coupling classification

The numerical work had two distinct purposes. First, three-dimensional linear-elastic SENB analyses, an analytical weight-function calculation, and an experimental compliance route were used to examine the load-to-K_{I} reduction for the beam family in Chapter 3. Second, the extended finite element method (XFEM), space-time finite element method (STFEM), phase-field fracture, and lattice element method (LEM) were compared for a common two-dimensional SENB problem. LEM was then extended to a three-dimensional pore-network model (PNM) to calculate conductivity changes from mechanically generated opening and connectivity.

All custom numerical codes used for the XFEM, STFEM, phase-field, LEM, and PNM analyses were developed by the author in MATLAB. The MATLAB reference documentation was consulted for programming syntax, built-in numerical functions, matrix operations, sparse solvers, data handling, and plotting. The governing formulations, discretization procedures, constitutive and fracture routines, boundary conditions, solution algorithms, coupling sequence, and post-processing procedures presented in this appendix were implemented by the author. Abaqus®/Standard 2023 was used separately for the three-dimensional SENB contour-integral analyses.

The LEM-PNM implementation is a *sequential one-way mechanical-fracture-to-flow coupling*.

Its computational chain is

$$\begin{aligned} &\text{mechanical equilibrium and link failure} \\ &\quad \longrightarrow \text{mechanical opening and failed-link graph} \\ &\quad \longrightarrow \text{hydraulic aperture and throat conductance} \\ &\quad \longrightarrow \text{pressure, flow, connectivity, and } k_{\text{eff}}. \end{aligned} \tag{B.1}$$

Pore pressure was not fed back into the mechanical equilibrium or failure criterion. The implementation is therefore not a fully two-way hydro-mechanical formulation and contains no thermal field. The term fracture-hydraulic-mechanical describes the physical context, not a monolithic three-field solver.

The SENB simulations were quasi-static. Pseudo-time in STFEM represented the load history. Inertial effects were assumed negligible, and pore-pressure migration was not solved during the SENB calculations. These choices isolate fracture-method differences but limit transfer to rapid loading, very low-permeability active clays, or pressurized in-situ discontinuities.

B.2 Common code settings and values used in the analyses

The custom XFEM, STFEM, phase-field, two-dimensional LEM, and three-dimensional LEM-PNM programs were implemented in MATLAB. The description below gives the mathematical and computational information required to understand and repeat the analyses.

The two-dimensional solvers use a consistent force-length unit system based on newtons (N) and millimetres (mm). Young's modulus is therefore supplied in $\mathrm{N\,mm^{-2}}$. The three-dimensional LEM-PNM suite uses SI units based on metres, pascals, seconds, and kilograms.

The built-in numerical settings were retained unless a value is stated below. The principal settings used for the analyses were:

1. All two-dimensional models reproduced the experimental SENB geometry. The beam length was $L = 5W$, the support span was $S = 4W$, the left and right support positions were $x = 0.5W$ and $x = 4.5W$, and the loading point was at $x = 2.5W$.

2. The initial notch was a 1 mm wide slot at the middle of the lower tensile face. The slot terminated in a triangular tip with a constant included angle, and the same tip geometry was retained across all specimen geometries and numerical grids. The notch ratios were $a/W = 0.45$, 0.50, and 0.55.

3. The nominal two-dimensional mesh or lattice spacing was 1 mm. The continuum codes used unstructured three-node triangular elements. The integrated code generated these meshes from a slightly jittered point layout. The two-dimensional LEM used the same point layout to construct its Voronoi-Delaunay network.

4. All two-dimensional SENB calculations were quasi-static and used plane stress. The imposed vertical displacement was increased by $\Delta\bar{u}_y = 0.001$ mm per nominal load step.

5. The two-dimensional cases used the experimental dry-density state, Young's modulus, Poisson's ratio, and Mode-I fracture toughness for the selected soil and specimen state. Dry density identified the experimental state; it did not enter the quasi-static equilibrium equation because inertia was not included.

6. Abaqus/CAE 2023 and Abaqus/Standard 2023 were used for the three-dimensional SENB contour-integral analyses.

7. The three-dimensional LEM-PNM specimen was a cylinder with diameter 50 mm and height 100 mm. The random-point generator used seed 17. The nominal target spacing was 1 mm; actual Delaunay edge lengths varied because the network was unstructured.

8. The three-dimensional UCS and triaxial cases were advanced in displacement control. The response was evaluated through an axial compressive stress of 100 kPa. The triaxial case also used a uniform radial confining stress of 100 kPa; the UCS case used zero radial confinement.

9. LEM-PNM cases have a uniform pore pressure of 100 kPa at both end faces. This uniform pressure did not create a hydraulic gradient and was not fed back into the mechanical equations. A separate reference network solve used a 100 kPa pressure difference to calculate equivalent hydraulic conductivity.

The same code path and numerical defaults were used for all soils unless a soil property or phase fraction was intentionally changed. This prevents a method from being improved for one soil by changing hidden numerical controls.

B.3 Stress measures and fields actually solved

For the mechanical fracture calculations,

$$\operatorname{div}\boldsymbol{\sigma} + \mathbf{b} = \mathbf{0}, \qquad \boldsymbol{\sigma} = \mathbb{C} : \boldsymbol{\varepsilon}, \qquad \boldsymbol{\varepsilon} = \frac{1}{2}\left(\nabla\mathbf{u} + \nabla\mathbf{u}^{\mathsf{T}}\right) \tag{B.2}$$

under the stated linear-elastic idealization. For unsaturated soil, a Bishop-type stress may be written as

$$\boldsymbol{\sigma}' = (\boldsymbol{\sigma} - u_a\mathbf{I}) + \chi(S_{\mathrm{r}})(u_a - u_w)\mathbf{I}, \tag{B.3}$$

and a saturated poromechanical form as

$$\boldsymbol{\sigma}' = \boldsymbol{\sigma} - \alpha_{\mathrm{B}} p\mathbf{I}. \tag{B.4}$$

Equations (B.3) and (B.4) provide theoretical context. Suction and pore pressure were not mechanical state variables in the Chapter 3 contour models or the four-method SENB comparison. In the PNM extension, pressure was solved on the hydraulic graph after the mechanical state was updated, but it did not modify stress or fracture in the same increment.

A fully coupled hydraulic-fracture analysis would require bulk poroelastic stress and fluid traction on explicitly represented discontinuity faces. These contributions must be defined without double counting. Such a two-way pressurized-fracture boundary-value problem was not solved in this thesis.

B.4 Model inventory

The numerical work used several methods because each method had a different purpose. The three-dimensional Abaqus SENB model, the analytical weight-function calculation, and the experimental compliance calculation were used to examine the relationship between the applied load and the Mode-I stress-intensity factor. These three approaches did not simulate progressive discontinuity propagation.

The XFEM, STFEM, phase-field, and two-dimensional LEM models were used to simulate initiation and propagation in the SENB specimens. The same specimen geometry, support span, notch ratio, material inputs, and displacement-controlled loading were used so that the results from the four methods could be compared on a common basis. The methods differed mainly in how they represented the discontinuity and how they updated it during loading.

The three-dimensional LEM model was subsequently linked to the pore-network model. The mechanical calculation provided the failed-link locations and link openings, while the pore-network calculation used this information to update hydraulic aperture, throat conductance, pressure, flow, and equivalent hydraulic conductivity. The hydraulic pressure calculated by the PNM was not returned to the mechanical solver. The LEM-PNM calculation was therefore a sequential one-way fracture-to-flow analysis.

Table B.1 summarizes the purpose, domain, constitutive representation, and fracture treatment of each numerical method. The table also distinguishes the methods used for stress-intensity calibration from those used for progressive fracture and hydraulic flow calculations. Except for the three-dimensional Abaqus® SENB contour-integral model, all numerical models listed in Table B.1 were implemented using MATLAB codes developed by the author.

Table B.1: Numerical models and their principal roles.

Model	Domain	Intact representation	Discontinuity representation	Principal role
Abaqus® SENB contour model	Three-dimensional beam and fixture	Homogeneous, isotropic, linear elastic	Stationary predefined seam and contour-integral extraction	Verification of the load-to-K_I reduction
Analytical weight function	SENB cross-section	Linear-elastic bending field	Edge-discontinuity weight function	Independent analytical reduction
Compliance check	SENB tests	Measured effective compliance	Change of compliance with notch length	Experimental cross-check
XFEM	Two-dimensional SENB	Plane-stress isotropic linear elasticity	Heaviside and tip enrichment with a sharp notch-connected path	Sharp-discontinuity benchmark
STFEM	Two-dimensional space-pseudo-time slabs	Plane-stress isotropic elasticity with AT2 degradation	Rate-regularized damage field and accepted notch-connected high-damage set	Load-history benchmark
Phase field	Two-dimensional SENB	Plane-stress isotropic elasticity with a tension-compression split	Diffuse AT2 damage field	Regularized topology benchmark

Table B.1 continued

Model	Domain	Intact representation	Discontinuity representation	Principal role
Two-dimensional LEM	Two-dimensional SENB	Random planar frame-link network	Progressive tensile failure of notch-connected links	Discrete path and opening benchmark
Three-dimensional lattice model	Cylindrical specimen	Normal and tangential bond stiffness on a Delaunay graph	Mixed tensile and compression-shear damage with retained aperture	Mechanical source for PNM
PNM	Co-located three-dimensional hydraulic graph	Poiseuille flow through matrix throats	Damage-dependent throat enlargement and retained hydraulic aperture	Pressure, flow, connectivity, and equivalent conductivity

The models listed in Table B.1 should not be interpreted as interchangeable solutions of the same boundary value problem. The Abaqus, analytical, and compliance approaches were used to evaluate the SENB load-to-K_I reduction, whereas XFEM, STFEM, phase-field, and LEM were used to compare progressive fracture responses. The PNM was used only after the LEM mechanical calculation and did not independently determine the location or direction of fracture. The detailed geometry, constitutive assumptions, mesh, boundary conditions, analysis steps, and solver controls for each method are presented in the following sections.

B.5 Chapter 3 Abaqus® SENB contour-integral model

B.5.1 Geometry, material idealization, and boundaries

The three-dimensional models reproduced geometries A-E in Appendix A. The common ratios were $S/W = 4$, $L/W = 5$, and $a/W = 0.45$, 0.50, and 0.55. Each beam was treated as a homogeneous, isotropic, linearly elastic solid using the measured E and ν for the selected soil state. Individual grains, compaction lifts, suction, plasticity, and a finite cohesive process zone were not represented.

The models were prepared in Abaqus®/CAE 2023 and solved with Abaqus®/Standard 2023 using a quasi-static procedure. The support and loading parts reproduced the laboratory three-point-bending fixture. They were included so that the reactions and local contact region were represented instead of applying three ideal point forces directly to the beam. The loading nose was centered above the notch. One lower support removed the remaining in-plane rigid-body translation, while the other was free in the longitudinal direction. The predefined seam faces were traction free. Solver and contact controls that were not changed explicitly were retained at the Abaqus® 2023 defaults.

Table B.2: Boundary conditions used in the Abaqus® 2023 SENB model.

Component	Adopted definition
Left support	Vertical support condition with the additional longitudinal restraint required to remove rigid translation
Right support	Vertical support condition with longitudinal release
Loading nose	Central prescribed downward displacement; reaction force obtained at the loading reference point
Beam	Full three-dimensional solid model with no material symmetry or half-model reduction
Notch and seam	Predefined seam starting at the moulded-notch tip; traction-free faces and an ordered crack front
Contact and solver	Abaqus® 2023 default controls were retained unless defined by the fixture and seam model

B.5.2 Elements, mesh, and contour paths

The beam was meshed with eight-node linear brick elements with reduced integration (C3D8R). The nominal global element size was 1 mm. The crack-front region was refined locally for the convergence study reported in Chapter 3. Element and node counts therefore varied with specimen dimensions and local refinement.

The stationary discontinuity was represented by a seam. Several contour paths were requested around the crack front. The first contour was treated cautiously because it is most sensitive to the immediate crack-front discretization. The stable outer contours were accepted when they did not show a systematic change with contour number. Their spread was evaluated as

$$\epsilon_{\text{path}} = 100\frac{\max(K_{\text{I}}^{(c)}) - \min(K_{\text{I}}^{(c)})}{\overline{K}_{\text{I}}}. \tag{B.5}$$

B.5.3 Analysis sequence

The Abaqus® calculation followed these steps:

1. Create the beam and fixture geometry for one SENB case.
2. Assign the measured elastic modulus and Poisson's ratio.
3. Create the notch seam, crack front, and crack-extension direction.
4. Define the two supports and the central loading nose.
5. Mesh the beam with C3D8R elements using a nominal 1 mm size and local crack-front refinement.
6. Apply the support restraints and the prescribed loading-nose displacement.
7. Solve the quasi-static step with Abaqus®/Standard 2023.
8. Extract reaction force, displacement, J, and K_{I} for the requested contours.
9. Check contour-path stability and mesh convergence.
10. Calculate the dimensionless load-to-K_{I} reduction for the selected a/W.

B.5.4 Benchmark and convergence

The model was first checked against a conventional SENB reference solution. The relative difference was calculated from

$$\epsilon_K = 100\frac{|K_{\mathrm{I}}^{\mathrm{FE}} - K_{\mathrm{I}}^{\mathrm{ref}}|}{K_{\mathrm{I}}^{\mathrm{ref}}}. \tag{B.6}$$

The convergence check considered the extracted K_{I}, reaction force, and beam compliance. It was not based only on visual inspection of the mesh.

B.6 Geometric function and effective calibration

In ideal homogeneous isotropic LEFM, the dimensionless SENB function is determined by geometry and boundary conditions:

$$K_{\mathrm{I}} = \frac{PS}{BW^{3/2}} f_{\mathrm{geom}}\left(\alpha, \frac{S}{W}, \frac{B}{W}, \mathrm{contact}\right), \qquad \alpha = \frac{a}{W}. \tag{B.7}$$

Material modulus changes compliance but should not be described as changing the universal near-tip singularity. The calibration used in the thesis is more transparently written as

$$f_{\mathrm{eff}}(\alpha) = \beta_{\mathrm{eff}} f_{\mathrm{geom}}(\alpha), \tag{B.8}$$

where β_{eff} is an empirical test-system or state calibration that may absorb contact compliance, finite-notch effects, process-zone effects, and the experimental reduction. It is not an intrinsic material property.

The adopted functional form is

$$f_{\mathrm{eff}}(\alpha) = \beta_{\mathrm{eff}} \sqrt{\alpha} \frac{1.99 - \alpha(1-\alpha)\left(2.095 - 3.805\alpha + 2.635\alpha^2\right)}{2(1 + 2.015\alpha)(1-\alpha)^{3/2}}. \tag{B.9}$$

Table B.3: Reported effective calibration multipliers.

Soil	Reported ν range	Numerical β_{eff}	Analytical β_{eff}
LS_0	0.315-0.322	1.320	1.190
LS_{15}	0.270	0.880	1.030
LS_{25}	0.239-0.240	1.375	1.140
FS	0.197-0.199	1.111	1.162
General	0.250	1.1715	1.141

The calibration domain is $0.45 \leq a/W \leq 0.55$, $S/W = 4$, $L/W = 5$, and the tested B/W values. Extrapolation requires renewed geometry, contact, mesh, and compliance verification.

B.7 Analytical weight function and compliance route

The analytical route used

$$K_{\mathrm{I}} = \int_0^a \sigma(y) m(a, y)\, \mathrm{d}y \tag{B.10}$$

with the uncracked bending field

$$\sigma(y) = \frac{M(W/2 - y)}{I}, \qquad M = \frac{PS}{4}, \qquad I = \frac{BW^3}{12}. \tag{B.11}$$

The weight-function source, coefficient-fitting procedure, non-dimensionalization, residual-error calculation, and calculation script are included in the numerical reproducibility archive. The compliance route used measured load-CMOD slopes over the three notch ratios. The final record states the pre-peak fitting interval, smoothing function, and numerical differentiation method used to obtain $\mathrm{d}C/\mathrm{d}a$.

The three routes share some measured inputs and are therefore cross-consistency checks rather than three statistically independent proofs.

B.8 Common two-dimensional SENB comparison

XFEM, STFEM, phase-field, and two-dimensional LEM used the same beam dimensions, notch ratios, supports, and loading position. The support and loading coordinates were

$$x_{\mathrm{L}} = 0.5W, \qquad x_{\mathrm{R}} = 4.5W, \qquad x_{\mathrm{P}} = 2.5W. \tag{B.12}$$

The left and right supports restrained vertical displacement. The left support also restrained horizontal displacement to remove rigid translation, while the right support remained free horizontally. A downward displacement was imposed at the top center. CMOD was calculated as the sum of the absolute horizontal openings on the two sides of the notch mouth.

The continuum methods used three-node triangular elements generated from a slightly jittered point layout. The nominal spacing was 1 mm. The two-dimensional LEM used the same point layout to form a Delaunay link network and bounded Voronoi cells. The starter notch was represented as a 1 mm slot with a sharp tip.

The experimental ranges supplied to the two-dimensional codes are summarized in Table B.4. The selected row depended on the soil and moisture-density state being simulated.

The dry density was used to identify the correct experimental state. It does not appear in the quasi-static elastic equilibrium equation because mass and inertia were omitted. Young's modulus and Poisson's ratio were assigned directly. For the methods that require critical fracture energy, the experimental toughness was converted using

$$G_c = \frac{K_{\mathrm{Ic}}^2}{E'}, \qquad E' = E \quad \text{for the plane-stress calculations.} \tag{B.13}$$

Table B.4: Experimental macroscopic inputs available to the two-dimensional SENB models.

Soil	ρ_d (kg m^{-3})	E (kPa)	ν	K_{Ic} (kPa$\sqrt{\mathrm{m}}$)
LS_0	1315-1355	370.9-651.6	0.315-0.322	0.86-0.87
LS_{15}	1425-1475	849.4-968.1	0.270	0.99-1.01
LS_{25}	1476-1516	358.9-465.7	0.239-0.240	0.51-0.62
FS	1787-1807	519.6-667.8	0.197-0.199	1.70-1.83

For the presented study, the fracture toughness, or the equivalent value of G_c, was entered whenever a method required a fracture resistance input. The programs also contain a strength based fallback for an incomplete input file. That fallback was not used to define the fracture toughness values reported in the thesis.

For methods requiring a tensile trigger, the same unchanged state dependent code relation was used for all soils. It was not tuned separately to improve one numerical method. Recorded outputs included load, loading displacement, left and right CMOD, CTOD, compliance, initiation step, discontinuity length, final path, and method-specific energy or damage variables.

B.9 Extended finite element method: implemented analysis steps

The XFEM formulation was implemented by the author in custom MATLAB code using a plane-stress, homogeneous, isotropic, linear-elastic representation prior to discontinuity activation. MATLAB does not provide the Heaviside enrichment, crack-tip enrichment functions, enriched degrees of freedom, or crack-tracking procedure used in this analysis as built-in XFEM options. The Heaviside jump function and the four asymptotic crack-tip branch functions were explicitly programmed and incorporated into the finite-element displacement approximation by the author. The code identifies the nodes requiring Heaviside or crack-tip enrichment, assigns the corresponding enriched degrees of freedom, evaluates the enrichment functions at the integration points, performs the required integration of elements intersected by the discontinuity, assembles the standard and enriched stiffness contributions, and updates the level-set and enrichment information as the discontinuity advances.

$$\mathbf{u}^h(\mathbf{x}) = \sum_{i\in I} N_i \mathbf{u}_i + \sum_{j\in I_H} N_j H \mathbf{a}_j + \sum_{k\in I_T} N_k \sum_{m=1}^{4} F_m \mathbf{b}_{km}. \tag{B.14}$$

The sharp discontinuity was described by level sets and could pass through the triangular background mesh.

B.9.1 Driving force and path rule

The production solver evaluated a normalized crack-driving ratio. The preferred value was obtained from a domain-form J-integral around the current tip,

$$K_{\mathrm{I}}^{J} = \sqrt{E' J}, \qquad E' = E \quad \text{for plane stress.} \tag{B.15}$$

The experimental K_{Ic} was used as resistance. A conventional SENB estimate and a local maximum-principal-tensile-stress ratio were retained as numerical fallbacks if the domain integral was not usable. Thus, the local condition

$$\frac{\sigma_1}{f_t} \geq 1 \tag{B.16}$$

was a local tensile check, while the accepted production growth ratio normally used $K_{\mathrm{I}}^{J}/K_{\mathrm{Ic}}$.

The SENB comparison was symmetric. The code therefore used a zero-kink continuation along the notch-connected centreline,

$$\theta_c = 0. \tag{B.17}$$

It did not calculate a general mixed-mode propagation angle. The crack advanced by approximately $0.67h$ during one growth event. No more than two growth events were allowed in one accepted displacement step, and the current step was re-solved after each accepted extension.

For elements intersected by the discontinuity and those containing the crack tip, a refined sub-triangular integration scheme was developed and implemented by the author in the custom MATLAB XFEM code, in which each affected triangular element was subdivided into smaller integration triangles, and the numerical quadrature was applied separately over the resulting sub-triangles. The domain used for J had a radius of at least $4h$ and was limited by the specimen boundaries and approximately $0.10W$. A small region immediately around the tip was excluded from the domain integral.

B.9.2 XFEM solution sequence

1. Generate the common SENB triangular mesh and assign E, ν, and the experimental fracture resistance.

2. Define the starter discontinuity and its level sets.

3. Identify Heaviside-enriched, tip-enriched, and cut elements.
4. Apply the support restraints and the next 0.001 mm displacement increment.
5. Assemble the standard and enriched stiffness terms using special quadrature in cut and tip elements.
6. Solve for the standard and enriched degrees of freedom.
7. Recover stresses, CMOD, CTOD, reaction force, and the local tensile-stress field.
8. Evaluate the domain J-integral and convert it to K_{I}.
9. Compare the normalized driving force with unity.
10. If growth is required, extend the notch-connected path along the symmetry line, update level sets and enrichment, and re-solve the same load step.
11. Accept the step when the driving force no longer requires another permitted extension.
12. Continue until the ligament is separated or the prescribed loading history is complete.

B.10 Space-time finite element method: implemented analysis steps

The STFEM model used the same plane-stress SENB mesh and elastic inputs as the other continuum methods. Pseudo-time ordered the load history; it was not physical time and no inertia term was retained in the reported SENB response.

Within each slab, displacement and damage were interpolated linearly,

$$\mathbf{u}(\mathbf{x},\tau) = N_1(\tau)\mathbf{u}_n + N_2(\tau)\mathbf{u}_{n+1}, \qquad d(\mathbf{x},\tau) = N_1(\tau)d_n + N_2(\tau)d_{n+1}, \tag{B.18}$$

where $N_1 = 1-\tau$, $N_2 = \tau$, and $0 \le \tau \le 1$. Two Gauss points were used over each unit pseudo-time slab.

The fracture field followed a rate-regularized AT2 form. For the 1 mm mesh and 1 mm notch, the default regularization length was

$$\ell = \max(2h, 1.5t_n) = 2\,\mathrm{mm}, \tag{B.19}$$

Table B.5: Main XFEM settings developed in the code.

Item	Adopted setting
Kinematics	Two-dimensional plane stress
Elements	Three-node triangular background elements with Heaviside and tip enrichment
Nominal spacing	1 mm
Resistance	Experimental K_{Ic}, converted from J using $E' = E$
Primary driving value	Domain J-integral; SENB and local tensile-stress fallbacks retained for numerical robustness
Path	Zero-kink continuation along the symmetry ligament
Growth update	Approximately $0.67h$ per event, at most two events per nominal load step
Inner updates	Up to eight growth/equilibrium updates in one load step
Growth tolerance	Normalized excess of 10^{-3}
Recorded results	Load, displacement, left/right CMOD, CTOD, compliance, J, K_{I}, enrichment counts, and path

where t_n is the notch width. The critical energy was obtained from the experimental toughness. The residual stiffness was $k_r = 10^{-8}$, and a small slab viscosity of $0.01G_c/\ell$ regularized the damage update.

The accepted slab-end discontinuity set was

$$\widetilde{\Gamma}^{\mathrm{ST}}_{c,n+1} = \{\mathbf{x} \in \Omega : d_{n+1}(\mathbf{x}) \geq 0.94\}\,. \tag{B.20}$$

Only the component connected to the original notch and extending ahead of the previous tip was retained. The $d = 0.88$ level was used to locate and display the tip; it was not the acceptance threshold. A notch-connected continuation safeguard prevented numerical arrest of the symmetric path. It did not create a general off-axis or mixed-mode path.

B.10.1 STFEM solution sequence

1. Generate the triangular SENB mesh and the explicit notch slot.
2. Assign E, ν, experimental G_c, ℓ, residual stiffness, and the small rate regularization.
3. Initialize the notch as a stationary diffuse damaged zone and set all other state variables to zero.

4. Transfer displacement, damage, history, and tip position from the previous slab.
5. Apply the next displacement increment over the current pseudo-time slab.
6. Assemble and solve the space-time displacement predictor.
7. Recover the static end-of-slab displacement state.
8. Evaluate the tensile energy at the time quadrature points and update the irreversible history field.
9. Assemble and solve the space-time damage predictor.
10. Recover the static end-of-slab damage state.
11. Apply damage irreversibility and retain the notch-connected high-damage set.
12. Repeat displacement and damage updates until the relative change is below tolerance.
13. Recover the final end-of-slab reaction, CMOD, CTOD, stress, strain, energy, and tip position.
14. Continue to the next slab until ligament separation.

Table B.6: Main STFEM settings used in the code.

Item	Adopted setting
Kinematics	Plane stress; linear interpolation in space and pseudo-time
Spatial mesh	Three-node triangular elements, nominal 1 mm spacing
Time integration	Unit slab with two Gauss points.
Damage model	Rate-regularized AT2 with an irreversible tensile-energy history
Regularization length	$\ell = 2$ mm for the production mesh
Residual stiffness	10^{-8}
Damage relaxation	0.90
Nonlinear limit	100 alternate iterations; relative tolerance 10^{-4}
Accepted set	Notch-connected $d \geq 0.94$; $d = 0.88$ used for tip tracking
Linear solution	Direct solution was the default; a preconditioned iterative option remained available

B.11 Phase-field method: implemented analysis steps

The phase-field model uses the Ambrosio-Tortorelli quadratic crack density functional (AT2), in which the sharp discontinuity is represented by a regularized scalar damage field and the fracture energy density contains both the local damage term and the damage gradient term.

$$\Pi(\mathbf{u}, d) = \int_{\Omega} \left[g(d)\psi_e^+(\varepsilon) + \psi_e^-(\varepsilon) \right] \, \mathrm{d}\Omega + G_c \int_{\Omega} \left(\frac{d^2}{2\ell} + \frac{\ell}{2} |\nabla d|^2 \right) \mathrm{d}\Omega - W_{\text{ext}}, \tag{B.21}$$

with

$$g(d) = (1 - d)^2 + k_r. \tag{B.22}$$

Damage irreversibility was enforced through

$$\mathcal{H}(\mathbf{x}, t) = \max_{0 \le s \le t} \psi_e^+(\varepsilon(\mathbf{x}, s)) \, . \tag{B.23}$$

The model used plane stress and the same three-node triangular mesh as the common SENB problem. For $h = 1$ mm, the default regularization length was $\ell = 2$ mm, and the residual stiffness was $k_r = 10^{-8}$. The production value of G_c was obtained from the experimental K_{Ic} using Eq. (B.13). The internal strength-based estimate was not used when fracture toughness was available.

The notch was represented by an explicit slot and a fixed $d = 1$ condition on the notch faces and tip cap. The initial diffuse notch profile was equilibrated before mechanical loading. The damage and displacement equations were solved by staggered alternate minimization. Damage was relaxed with a factor of 0.90 and was not allowed to decrease. Fully developed, notch-connected nodes were locked into the irreversible set when $d \ge 0.97$. The tip-display level was calibrated from the stationary notch profile rather than imposed as a universal material value.

B.11.1 Phase-field solution sequence

1. Generate the common SENB triangular mesh and remove the notch void.
2. Add the notch-face, notch-tip, support, and loading refinement points.
3. Assign E, ν, experimental G_c, $\ell = 2$ mm, and $k_r = 10^{-8}$.
4. Initialize the notch with $d = 1$, set $d = 0$ elsewhere, and equilibrate the diffuse notch profile.

5. Apply the next nominal displacement increment. The internal schedule may redistribute increments near propagation while retaining the same total displacement history.
6. Solve the displacement equation for the current damage field.
7. Calculate the tensile elastic energy and update the history field.
8. Solve the phase-field equation for the updated history.
9. Enforce $d_{n+1} \geq d_n$ and lock the fully developed notch-connected set.
10. Repeat the displacement and damage solves until both relative changes are below 10^{-4}, or until 100 iterations are reached.
11. Recover reaction load, CMOD, CTOD, elastic energy, fracture energy, damage field, and the displayed discontinuity path.
12. Continue until the damage band connects the notch to the upper boundary.

Table B.7: Main phase-field settings implemented in the code.

Item	Adopted setting
Kinematics	Plane stress with a tensile-compressive energy split
Elements	Three-node triangular elements for displacement and damage
Nominal spacing	1 mm
Fracture law	AT2 with experimental G_c
Regularization length	$\ell = 2$ mm
Residual stiffness	10^{-8}
Solution	Staggered displacement-damage iterations
Iteration control	Maximum 100 iterations, tolerance 10^{-4}, damage relaxation 0.90
Irreversible lock	Notch-connected nodes with $d \geq 0.97$
Recorded results	Load, CMOD, CTOD, damage, tip position, elastic energy, fracture energy, and total energy

B.12 Two-dimensional lattice element method: mesh, failure rule, and analysis steps

B.12.1 Voronoi-Delaunay network

The integrated two-dimensional comparison code generated a slightly jittered point layout with a nominal spacing of 1 mm. A Delaunay triangulation connected the points, and bounded Voronoi cells provided a local geometric scale. The resulting links did not follow a perfectly regular grid and therefore reduced directional mesh bias.

Each link was a two-node planar frame element with three degrees of freedom per node: horizontal displacement, vertical displacement, and in-plane rotation. Its elastic stiffness contained axial and bending terms. For a link of length L_e, effective area A_e, and second moment I_e,

$$A_e = B\,\bar{l}_{V,e}, \qquad I_e = \frac{B\bar{l}_{V,e}^{3}}{12}, \tag{B.24}$$

where $\bar{l}_{V,e}$ is the mean length scale obtained from the adjacent Voronoi cells.

The executable two-dimensional SENB comparison used progressive tensile link failure. The maximum tensile stress at either link end was evaluated from the axial force and bending moment,

$$\sigma_{t,e} = \max\left[0, \frac{N_e}{A_e} + \frac{|M_e| c_e}{I_e}\right], \tag{B.25}$$

and the link was eligible to fail when

$$\frac{\sigma_{t,e}}{f_t} > 1. \tag{B.26}$$

The two-dimensional comparison code did not use the full mixed tensile-shear softening law of the later three-dimensional lattice model. Instead, one notch-front candidate link was removed during one inner failure update, and the same external displacement step was re-solved. This distinction is important when comparing the two-dimensional LEM with the three-dimensional LEM-PNM formulation.

B.12.2 Two-dimensional LEM solution sequence

1. Generate the SENB point layout, boundary points, support points, loading point, and notch geometry.

2. Remove points inside the 1 mm notch slot.
3. Construct the Delaunay link network and bounded Voronoi cells.
4. Calculate each link length, orientation, effective area, and second moment.
5. Assign the experimental elastic state and the common tensile trigger used by the production code.
6. Pre-break all links that intersect the starter notch.
7. Restrain vertical motion at both supports and horizontal motion at the left support.
8. Apply the next 0.001 mm downward displacement at the central loading node.
9. Assemble and solve the frame-link equilibrium equations.
10. Recover link axial force, bending moment, and tensile-stress ratio.
11. Restrict the candidate search to unbroken links connected to the current notch front and lying near the centreline. If no such link exists, search the remaining active links.
12. Break the most highly overstressed candidate when its ratio exceeds unity.
13. Reassemble and re-solve the same load step until no new candidate fails or the inner update limit is reached.
14. Record reaction load, CMOD, CTOD, compliance, failed-link count, tip position, and the failed-link path.
15. Continue until a connected failed-link path reaches the upper boundary.

B.13 Generation of numerical LS_0, LS_{15}, and LS_{25} cases

The two-dimensional solvers did not resolve individual clay and sand grains. Each case was a homogeneous macroscopic material selected from the experimental soil-state database. Changing from LS_0 to LS_{15} or LS_{25} changed the selected experimental elastic and fracture inputs while leaving geometry, mesh, loading, and method controls unchanged.

The three-dimensional LEM-PNM code used an explicit numerical phase map. The requested percentages were treated as target nodal phase fractions. The default matrix phase was clay.

Table B.8: Main settings of the two-dimensional LEM code.

Item	Adopted setting
Point layout	Slightly jittered point grid, nominal 1 mm spacing
Network	Delaunay links with bounded Voronoi cells
Element	Two-node planar frame link with axial and bending stiffness
Failure rule	Tensile stress from axial force and end bending moment; one front link failed per inner update
Initial notch	Links crossing the 1 mm slot were pre-broken
Inner update limit	120 equilibrium-failure updates per external load step
Post-peak representation	Progressive link removal in the two-dimensional comparison code
Recorded results	Load, displacement, left/right CMOD, CTOD, work, failed-link path, and tip position

Coarser phases were assigned first in spatial clusters and the final node counts were rebalanced to the requested fractions. Thus, the generator did not convert dry-mass fractions to solid-volume fractions internally. For the soil labels used here, the target numerical phase fractions were 100/0 for LS_0, 85/15 for LS_{15}, and 75/25 for LS_{25} in terms of clay/sand nodes.

A link joining nodes of the same phase received the corresponding phase properties. A link joining unlike phases received the interface properties. The same seed, specimen geometry, load history, and network-generation rules were retained when the phase fraction was changed. The assigned percentages create clay-rich matrices containing sand inclusions; they do not by themselves prove a continuous load-bearing sand skeleton.

B.14 Three-dimensional lattice-pore-network cylinder and material parameters

The three-dimensional specimen was a cylinder with

$$D = 50\,\text{mm}, \qquad H = 100\,\text{mm}. \tag{B.27}$$

The random-number seed was 17. The scenarios used 900 interior points together with lateral, top, and bottom boundary points. A random-Poisson generator was used. The minimum target point spacing was 1 mm; because the network was random, actual Delaunay link lengths were not uniform.

A three-dimensional Delaunay tessellation was created and tetrahedra outside the cylinder were removed. Long links were removed by the fixed code-quality filter. Each remaining edge became both a mechanical bond and a hydraulic throat. The hydraulic and mechanical graphs were therefore co-located.

B.14.1 Three-dimensional bond law

The three-dimensional bond formulation was developed and implemented by the author in the custom MATLAB LEM-PNM code. It was not obtained from a MATLAB toolbox or a built-in lattice element function. Each node was assigned three translational degrees of freedom. For a bond of length L_e, characteristic area A_e, Young's modulus E_e, and shear modulus G_e, the initial normal and tangential stiffnesses were

$$k_{n,e} = \frac{E_e A_e}{L_e}, \qquad k_{s,e} = \frac{G_e A_e}{L_e}. \tag{B.28}$$

The initial tensile and shear separation limits were obtained from the bond strength, and the final limits were related to the Mode-I and Mode-II fracture energies,

$$\delta_{0t,e} = \frac{f_{t,e} L_e}{E_e}, \qquad \delta_{ft,e} = \delta_{0t,e} + \frac{2G^{\mathrm{I}}_{f,e}}{f_{t,e}}, \tag{B.29}$$

$$\delta_{0s,e} = \frac{c_e L_e}{G_e}, \qquad \delta_{fs,e} = \delta_{0s,e} + \frac{2G^{\mathrm{II}}_{f,e}}{c_e}. \tag{B.30}$$

Let d_n be the relative normal displacement and g_s the tangential slip. The tensile equivalent separation was

$$\delta_T = \sqrt{\langle d_n \rangle_+^2 + 0.25 g_s^2}. \tag{B.31}$$

Tensile and shear damage increased linearly between their respective onset and final separations. Compression raised the shear threshold through the friction angle. Damage was irreversible and was taken as the larger tensile or shear damage value. The failure mode was stored for each bond.

The mechanical aperture transferred to the hydraulic model was

$$b_{m,e} = \langle d_n \rangle_+ D_e + \psi_e g_s D_e \, I_e^{\mathrm{shear}}, \tag{B.32}$$

where D_e is bond damage, ψ_e is the link dilation coefficient, and I_e^{shear} identifies a shear-dominated damaged bond. Small closure and residual stiffnesses were retained after severe damage to keep the compressed network stable.

B.14.2 Principal phase-level defaults

Table B.9 lists the principal phase-level values stored in the supplied scenarios. They are local bond-scale inputs. They are not the specimen-scale moduli measured by UCS and should not be compared directly with Table 3.3 without homogenization.

Table B.9: Principal default phase and interface values used by the three-dimensional code.

Property	Unit	Clay	Sand
Young's modulus, E	MPa	25	120
Poisson's ratio, ν	-	0.35	0.25
Tensile strength, f_{t}	kPa	20	0
Cohesion, c	kPa	50	0
Friction angle, ϕ	degree	22	36
Void ratio, e	-	0.85	0.55
Tensile fracture energy, G_{f}^{I}	J/m^2	5	1
Shear fracture energy, G_{f}^{II}	J/m^2	20	8
Residual stiffness factor, k_{r}	-	0.05	0.03
Dilation angle, ψ	degree	0	8
Base throat scale, α_b	-	0.80	1.20
Hydraulic conductivity, k	m/s	1.0×10^{-10}	1.0×10^{-5}

The local values were held fixed when the clay/sand phase fraction changed. The resulting specimen-scale response emerged from the random network, phase arrangement, interface links, confinement, and accumulated damage.

B.15 Three-dimensional mechanical and hydraulic boundary conditions

The lower boundary layer was fixed in all three translational directions. The upper boundary layer was loaded in the axial direction. The supplied scenarios used 100 displacement-controlled steps with a nominal top displacement increment of 0.001 mm. Reaction force was divided by the original cross-sectional area to obtain axial stress. The thesis comparisons were evaluated through an axial stress of 100 kPa.

For the UCS case, the cylindrical side boundary was free and

$$\sigma_3 = 0. \tag{B.33}$$

For the triaxial case, a uniform inward radial traction was applied to the side-boundary nodes,

$$\sigma_3 = 100\,\text{kPa}. \tag{B.34}$$

The radial traction was distributed using the side area assigned to each boundary node. Confinement was established before or with the axial loading according to the scenario definition.

The actual hydraulic state used a constant pressure of 100 kPa at both top and bottom pore boundaries,

$$p_{\text{top}} = p_{\text{bottom}} = 100\,\text{kPa}. \tag{B.35}$$

Therefore, this stored pressure field did not create through-flow. To calculate equivalent hydraulic conductivity, the code solved a second reference problem using

$$p_{\text{top}}^{\text{ref}} = 0, \qquad p_{\text{bottom}}^{\text{ref}} = 100\,\text{kPa}. \tag{B.36}$$

The cylindrical side was no-flow. The reference pressure calculation was a hydraulic property evaluation and was not returned to the mechanical equilibrium equations.

Table B.10: Mechanical and hydraulic boundary conditions for the three-dimensional analyses.

Case	Mechanical boundary conditions	Hydraulic boundary conditions
UCS	Fixed lower layer; prescribed top axial displacement; radial surface free; response evaluated through $\sigma_a = 100$ kPa	Uniform stored pressure of 100 kPa at both ends; separate 0-100 kPa reference solve for k_{eff}; no-flow side
Triaxial	Fixed lower layer; prescribed top axial displacement; uniform radial confinement $\sigma_3 = 100$ kPa; response evaluated through $\sigma_a = 100$ kPa	Same hydraulic treatment as the UCS case

B.16 Pore-network equations, porosity update, and aperture mapping

The pore-network equations used in this study follow established pore-scale flow formulations. The graph representation of pores and throats, the calculation of throat conductance, and the enforcement of fluid mass conservation at each pore follow the pore-network framework introduced

by Fatt (1956) and subsequently developed by Blunt (2001), Raoof and Hassanizadeh (2010), and Jivkov et al. (2013). The laminar conductance of an approximately cylindrical matrix throat is based on the Hagen-Poiseuille relation, while the conductance assigned to an opened fracture-like throat follows the parallel-plate cubic law (Snow, 1969; Witherspoon et al., 1980; Zimmerman and Bodvarsson, 1996). The conversion from total network flow to intrinsic permeability and hydraulic conductivity follows Darcy's law. The author developed and implemented the MATLAB pore-network code, including generation of the hydraulic graph, mapping of LEM link opening to hydraulic aperture, conductance updating, pressure-matrix assembly, inlet-to-outlet connectivity checking, and the sequential LEM–PNM solution procedure.

The PNM used the same nodes and edges as the mechanical lattice. Each Delaunay edge was a hydraulic throat. The initial radius was scaled by phase type and calibrated so that the intact network reproduced the phase-fraction-based target conductivity.

For a throat of radius r_{ij}, length L_{ij}, and water viscosity μ, the Poiseuille conductance was

$$g_{ij} = \frac{\pi r_{ij}^4}{8\mu L_{ij}}. \tag{B.37}$$

The supplied scenarios used

$$\mu = 1.0 \times 10^{-3}\,\mathrm{Pa\,s}, \qquad \rho_w = 1000\,\mathrm{kg\,m^{-3}}, \qquad g = 9.81\,\mathrm{m\,s^{-2}}, \tag{B.38}$$

and an initial reference throat radius of 50 µm before phase scaling and network calibration.

Mechanical opening was converted to an irreversible hydraulic-aperture memory. A damaged link could partly close mechanically under compression, but the created flow path was not erased. In general form,

$$b_{h,ij}^{n+1} = \max\left[b_{h,ij}^{n},\ D_{ij} b_{m,ij},\ b_{r,ij}(D_{ij})\right], \tag{B.39}$$

where D_{ij} is damage and $b_{r,ij}$ is the residual aperture associated with a damaged throat. The hydraulic throat radius was enlarged using the retained aperture,

$$r_{ij} = r_{0,ij} + C_b b_{h,ij}, \tag{B.40}$$

where C_b is the unchanged code-default aperture multiplier.

The fracture void volume was calculated from link area and retained aperture,

$$V_f = \sum_e A_e b_{h,e}. \tag{B.41}$$

This value increased the fracture void ratio and irreversibly connected porosity. Matrix-throat conductance was also adjusted for the current void ratio and connected porosity ratios.

Following the standard pore-network formulation, steady fluid mass conservation was enforced at every internal pore (Blunt, 2001; Fatt, 1956; Jivkov et al., 2013; Raoof and Hassanizadeh, 2010),

$$\sum_{j \in \mathcal{N}(i)} g_{ij}(p_i - p_j) = 0, \tag{B.42}$$

which produced the sparse pressure system

$$\mathbf{A}_h \mathbf{p} = \mathbf{q}. \tag{B.43}$$

The sparse matrix system was assembled and solved in the custom MATLAB code developed by the author. The total outlet flow from the reference pressure problem was converted to intrinsic permeability and hydraulic conductivity,

$$\kappa = \frac{|Q|\mu H}{A\Delta p}, \tag{B.44}$$

$$k_{\text{eff}} = \frac{\rho_w g}{\mu}\kappa = \frac{|Q|\rho_w g H}{A\Delta p}. \tag{B.45}$$

At the available network resolution, the reported conductivity combined three consistent estimates: the direct graph solution, a void-ratio-adjusted matrix value, and a fracture-aperture estimate. The largest admissible value was retained, and conductivity was not allowed to decrease after irreversible aperture growth. This numerical closure prevents a coarse graph from losing an established flow path when a mechanically damaged bond partly recloses.

B.17 Connectivity criterion

A throat was active when its conductance exceeded the small numerical conductance threshold used by the sparse graph. The active graph was

$$\mathcal{G}^n_{\text{hyd}} = \{(i, j) \in \mathcal{E}_p : g^n_{ij} > g_{\min}\}. \tag{B.46}$$

Connected components were then calculated. A percolating path existed when at least one component contained both a top-boundary pore and a bottom-boundary pore,

$$\exists\, \mathcal{P}^n : \mathcal{V}_{\text{top}} \to \mathcal{V}_{\text{bottom}} \quad \text{through} \quad \mathcal{G}^n_{\text{hyd}}. \tag{B.47}$$

This check distinguishes isolated damaged bonds from a specimen-scale hydraulic pathway. The reported conductivity also retained a bounded aperture-based connectivity measure because a coarse random network may under-resolve an emerging fracture surface before a strict top-to-bottom graph path is formed.

B.18 Complete sequential three-dimensional lattice-PNM analysis

The full analysis was performed in the following order:

1. Read the specimen, soil phase fractions, random seed, loading case, solver controls, and hydraulic settings.
2. Generate random points inside the 50 mm by 100 mm cylinder and add boundary points.
3. Form the Delaunay tetrahedra and edge network, remove cells outside the cylinder, and apply the link-quality filter.
4. Assign clay and sand phases to nodes and classify same-phase and interface links.
5. Calculate each bond length, direction, characteristic area, normal stiffness, tangential stiffness, strength limits, fracture-energy limits, and base hydraulic property.
6. Build the co-located hydraulic throat network and calibrate its intact conductance to the phase-fraction target conductivity.
7. Initialize displacement, damage, failure mode, aperture memory, void ratio, porosity, conductance, and pressure.
8. Build the UCS or triaxial boundary conditions. For triaxial loading, apply 100 kPa radial confinement; for UCS, leave the side surface free.
9. Apply the next top displacement increment.
10. Assemble the damaged mechanical stiffness matrix.
11. Solve the mechanical equilibrium equations using the prescribed lower and upper boundary conditions.

12. Recover relative normal opening and tangential slip for every bond.
13. Evaluate tensile and compression-dependent shear damage and update the irreversible damage state.
14. Reassemble and re-solve the same external load step until the damage and aperture changes meet the inner tolerance.
15. Perform a final equilibrium solution using the converged degraded stiffness.
16. Record reaction force, axial stress, axial strain, bond damage, failure mode, and mechanical aperture.
17. Update retained hydraulic aperture and fracture void volume.
18. Update void ratio, total porosity, connected porosity, throat radius, and conductance.
19. Solve the actual pressure problem using the stored top and bottom pressures.
20. Solve the separate 0-100 kPa reference pressure problem.
21. Calculate throat flow, total outlet flow, intrinsic permeability, and hydraulic conductivity.
22. Search the active graph for top-to-bottom connectivity.
23. Store stress-strain, porosity-strain, conductivity-strain, conductivity-aperture, pressure, flow, damage, aperture, and percolation histories.
24. Continue until the requested loading history is complete.

This is a one-way sequence. The mechanical solution controls damage and aperture, and the hydraulic solution uses that state. Hydraulic pressure is not returned to the mechanical stiffness, stress, or damage equations.

B.19 Parameter provenance and calibration

The numerical inputs fall into four groups:

(a) measured macroscopic inputs used in the two-dimensional SENB models: dry-density state, E, ν, and K_{Ic};

(b) prescribed geometry and loading inputs: specimen dimensions, notch ratio, support positions, mesh size, displacement history, axial stress range, and confining stress;

(c) default local inputs in the three-dimensional lattice-PNM scenarios: phase and interface stiffness, strength, fracture energy, void ratio, and hydraulic conductivity; and

(d) numerical controls: tolerances, residual stiffnesses, quadrature, continuation safeguards, graph thresholds, and linear-solver settings.

Table B.11: Source and role of the main numerical inputs.

Input	Evidence class	Used in	Role
$E, \nu, \rho_d, K_{\mathrm{Ic}}$	Experimental	Two-dimensional SENB methods	Select the macroscopic state and fracture resistance
G_c	Calculated from experimental K_{Ic}	STFEM and phase field	Energy resistance, $G_c = K_{\mathrm{Ic}}^2/E'$
Two-dimensional tensile trigger	Unchanged code default	XFEM and LEM support logic	Local initiation or safeguard value; not reported as measured tensile strength
SENB geometry and loading	Prescribed from experiment	Abaqus, XFEM, STFEM, phase field, LEM	Common benchmark definition
Three-dimensional phase values	Scenario defaults	Lattice-PNM	Local bond and throat properties; not direct specimen-scale UCS values
Confining stress	Prescribed	Triaxial lattice-PNM	Uniform radial traction of 100 kPa
Uniform pore pressure	Prescribed scenario state	PNM	100 kPa at both end faces; no actual through-gradient
Reference pressure difference	Prescribed numerical test	PNM	100 kPa virtual drop for equivalent conductivity
Solver tolerances	Code defaults	All numerical methods	Convergence and stability

No method-specific change in the measured E, ν, or K_{Ic} was introduced to improve agreement. The phase-level three-dimensional parameters and the aperture-conductivity closure remain model inputs that require independent laboratory calibration before field prediction.

B.20 Mesh, lattice, regularization, and random-seed sensitivity

Required studies include:

(a) Abaqus® crack-front mesh and contour-range sensitivity;

(b) XFEM background mesh, enrichment radius, and crack-increment sensitivity;

(c) STFEM spatial mesh, slab size, and localization-step sensitivity;

(d) phase-field mesh h, length ℓ, residual stiffness, and extraction threshold;

(e) LEM mean link length, point density, minimum spacing, seed, and property distribution; and

(f) PNM resolution, aperture coefficient, residual aperture, conductance threshold, and pressure-solver tolerance.

For output y, successive-resolution error is

$$\epsilon_y^{(j)} = 100\frac{|y^{(j)} - y^{(j-1)}|}{|y^{(j)}|}. \tag{B.48}$$

At minimum, peak load, initiation displacement, post-peak work, path length/tortuosity, percolation step, and final k_{eff} are checked.

Random-lattice outputs are reported over several seeds:

$$\bar{y} = \frac{1}{N_R}\sum_{r=1}^{N_R} y_r, \qquad s_y = \sqrt{\frac{1}{N_R - 1}\sum_{r=1}^{N_R}(y_r - \bar{y})^2}. \tag{B.49}$$

If only one seed was used, the results represent one realization and should not be described as realization-independent.

B.21 Validation metrics and method selection

A fair comparison should use common experimental references and disclose method-specific calibration. The validation set should include:

1. peak-load error,
$$\epsilon_P = 100\frac{|P_{\max}^{\text{num}} - P_{\max}^{\text{exp}}|}{P_{\max}^{\text{exp}}}; \tag{B.50}$$
2. CMOD error at peak and over the pre-peak curve;
3. post-peak work or curve error where simulated;
4. initiation-location agreement;
5. path angle, length, tortuosity, and connectivity using a stated image-registration procedure;
6. reduced initiation-toughness error using the same load-to-K reduction; and
7. mesh/seed sensitivity and physical traceability of aperture.

LEM was selected because it provided a failed-link graph, explicit displacement jumps, and the closest combined agreement reported for the examined SENB cases. This conclusion is specific to the fracture-to-flow workflow. The hydraulic predictions were not independently validated against measured flow through specimens fractured under the simulated UCS or triaxial loading paths; they remain mechanistic predictions requiring future fracture-flow testing.

B.22 Solver controls and output reproducibility

Table B.12: Principal solver controls defined in the codes.

Method	Solution algorithm	Main tolerance or limit	Step and failure treatment
Abaqus®	Abaqus®/Standard 2023 quasi-static solution	Abaqus default convergence controls	User-defined displacement, seam, contact geometry, and mesh; remaining controls retained at defaults
XFEM	Direct solution of enriched equilibrium; repeated after growth	Growth excess 10^{-3}; at most eight inner updates	Up to two $0.67h$ growth events per nominal load step
STFEM	Alternate space-time and end-state displacement/damage solution	Relative tolerance 10^{-4}; maximum 100 iterations	Damage relaxation 0.90; notch-connected high-damage locking and continuation safeguard
Phase field	Staggered displacement-damage solution	Relative tolerance 10^{-4}; maximum 100 iterations	Damage relaxation 0.90; irreversibility and $d \geq 0.97$ notch-connected lock
2D LEM	Direct frame-network equilibrium with repeated tensile link failure	Stress ratio greater than unity; maximum 120 inner updates	One front candidate link failed in one inner update; same load step re-solved
3D mechanics	Preconditioned conjugate gradient with direct fallback	Linear tolerance 10^{-8}, maximum 4000 iterations; damage tolerance 10^{-4}	Up to 12 damage re-equilibration iterations, followed by a final equilibrium solve
PNM	Sparse pressure solution with iterative and direct fallbacks	Pressure-system tolerance 10^{-8}	Solved after every accepted mechanical step for actual and reference pressure fields

Every result file records the soil, specimen geometry, a/W, mesh or lattice size, load step, and method. The stored outputs include the global response and the local state needed to recreate each figure. Colour bars must identify the plotted variable and unit. Damage, failed link, mechanical aperture, hydraulic aperture, pore pressure, and throat flow are separate quantities and should not

be used interchangeably.

B.23 Reproducibility archive

The numerical archive should contain:

1. unit-system and notation declarations;
2. geometry and mesh/lattice generation scripts;
3. immutable production input files for every figure and table;
4. parameter files with provenance fields;
5. random seeds and generated coordinates/connectivity;
6. software, compiler/interpreter, dependency, and hardware versions;
7. convergence logs, rejected steps, warnings, and run times;
8. raw result files and post-processing scripts;
9. a manifest mapping every thesis output to inputs and results; and
10. checksums or version-control commits identifying the exact production state.

A useful naming convention is

`method_soil_geometry_aw_mesh_seed_loadcase_revision`.

For example: `LEM_LS15_C_aw050_h1mm_seedXXXX_SENB_r01`.

B.24 Numerical limitations

The numerical results must be interpreted within the following limits:

(i) the Abaqus® contour model is homogeneous, isotropic, linear elastic, and contains a stationary predefined seam;

(ii) the two-dimensional comparison is plane stress and quasi-static, and it does not solve suction, pore-pressure migration, thermal effects, or inertia;

(iii) the dry density identifies the experimental state but is not an inertial input in the two-dimensional static equations;

(iv) the symmetric XFEM path is constrained to zero-kink centreline continuation and is not a general mixed-mode model;

(v) STFEM and phase-field propagation include notch-connected continuation safeguards that are appropriate for the symmetric SENB benchmark but should not be transferred directly to arbitrary path problems;

(vi) the executable two-dimensional LEM uses progressive tensile link removal, whereas the three-dimensional lattice model uses mixed tensile and compression-shear damage;

(vii) the three-dimensional phase percentages are numerical nodal fractions and are not an internal dry-mass-to-volume conversion;

(viii) the phase-level three-dimensional values are bond-scale defaults and require homogenization before comparison with specimen-scale UCS moduli;

(ix) the LEM-PNM coupling is one-way, so pore pressure does not change mechanical stress or drive hydraulic-fracture propagation;

(x) the uniform 100 kPa pore-pressure state does not create flow; conductivity is obtained from a separate reference pressure-difference calculation;

(xi) hydraulic aperture is retained irreversibly and the reported conductivity combines graph, matrix, and fracture-aperture estimates, including a nondecreasing conductivity condition; and

(xii) chemical, thermal, cyclic, long-term ageing, and field stress-history effects are not included.

Within these limits, the codes provide a consistent comparison of four two-dimensional fracture representations and a clear one-way path from three-dimensional mechanical damage to connected hydraulic flow.